Insights From Past Sea Level and Landscapes Through the Lens of Solid Earth Ice-Sheet Interactions

Insights from past sea level and landscapes through the lens of solid Earth ice-sheet interactions

A DISSERTATION PRESENTED
BY
TAMARA PICO
TO
THE DEPARTMENT OF EARTH AND PLANETARY SCIENCES

IN PARTIAL FULFILLMENT OF THE REQUIREMENTS
FOR THE DEGREE OF
DOCTOR OF PHILOSOPHY
IN THE SUBJECT OF
EARTH AND PLANETARY SCIENCES

HARVARD UNIVERSITY
CAMBRIDGE, MASSACHUSETTS
APRIL 2019

Insights from past sea level and landscapes through the lens of solid Earth ice-sheet interactions

Abstract

Bridging geophysics, paleoclimate, and landscape studies, this interdisciplinary thesis examines critical moments during the last ice age, employing geophysical simulations of glacial isostatic adjustment and non-traditional geologic sea-level records to revise models of both ice growth and decay, with implications for global climate. In particular, by simulating river responses to solid Earth deformation over the ice age, I demonstrate that past landscapes constitute a unique and novel constraint on former ice sheets. This thesis focuses on North American ice sheets, considering both the build-up of ice sheets leading to the Last Glacial Maximum (26,000 years ago), and the subsequent disintegration phase, characterized by rapid global sea-level rise.

First, I turn to the time period of glacial build-up preceding the Last Glacial Maximum during Marine Isotope Stage 3 (60,000 to 26,000 years ago). I correct sea-level markers in the Bohai Sea, China dated to 50,000-35,000 years ago for the effects of glacial isostatic adjustment, sediment loading, and sediment compaction, and derive an estimate of peak globally averaged sea level of -37.5 m relative to present day, suggesting that global ice volumes may have increased three-fold in the 15,000 years leading into the Last Glacial Maximum. In performing these analyses, I extend the development of post-glacial sea-level theory to accurately include the effects of sediment compaction. Moreover, to partition global ice volumes during the glacial build-up phase into contributions from regional ice sheets, I analyze sea-level markers dated to 50,000-35,000 years ago at North Carolina and Virginia to infer the size and distribution of the Laurentide Ice Sheet. I conclude that the Laurentide Ice Sheet experienced a phase of very rapid growth in the 15,000 years leading into the Last

Glacial Maximum. A reduced Laurentide Ice Sheet over the time period ∼ 50,000-35,000 years ago is consistent with non-glacial deposits in eastern Canada dated to the same interval. A fast growing Laurentide Ice Sheet initiated uplift along the U.S. east coast as the solid Earth adjusted to an expanding ice load at rates of 10 mm/yr, matching or exceeding rapid tectonic uplift rates. I force a landscape evolution model with predictions of glacial isostatic adjustment, to show that a late and rapid glaciation of the Laurentide Ice Sheet is consistent with producing the eastward diversion of the Hudson River at 30,000 years ago observed in the geologic record. Moreover these simulations provide a mechanism that explains abrupt changes in river dynamics observed across the U.S. mid-Atlantic in the Delaware, Susquehanna, and Potomac rivers.

Next, I revisit two topics of considerable debate: the timing of both the expansion of the ice-free corridor between the Cordilleran and Laurentide Ice Sheet and the flooding of the Bering Strait. I use observations of the Bering Strait flooding as sea-level indicators to fingerprint a significant source of ice melt from an expanding ice-free corridor during the interval 13,000-11,500 years ago. Ice melting of this region induces a regional sea-level fall, explaining the observed two-phased flooding history of the Bering Strait. Further, this melt introduces a large freshwater flux into the Arctic, reducing the vigor of the Atlantic Meridional Overturning Circulation, and providing a trigger for the Younger Dryas cold episode (13,000-11,700 years ago).

Finally, I consider whether sediment loading has impacted the variability of sea-level markers dated to the Last Interglacial (∼ 122,000 years ago). I construct a synthetic sedimentation history over the last glacial cycle by simulating delta deposition using a diffusive model and a migrating shoreline, and correct for the effects of sediment loading on a global compilation of Last Interglacial sea-level markers. A statistical analysis, accounting for spatial autocorrelation across a compilation of 1287 Last Interglacial sea-level markers, suggests there is not a statistically significant global signal of sediment loading in Last Interglacial sea-level markers, although regionally this effect can be substantial.

Taken together, this thesis aims to define new tools for constraining the size and distribution of past ice sheets. In the concluding remarks, I summarize the research described within and explore some future directions stemming from this body of work.

Contents

Acknowledgments

The completion of this thesis is only possible because of the generous support, both material and moral, that has been made available to me at Harvard, within the Earth & Planetary Sciences department, and more specifically within Jerry Mitrovica's group. First and foremost, I owe this to my advisor, Jerry Mitrovica, who took a chance on me when I walked into his office four and a half years ago. Since then, Jerry has created a space for me to grow as a sicentist and as a researcher, but more importantly to become an engaged and inspired thinker. Jerry embodies the qualities of a true mentor, with unwavering support and enthusiasm, while pushing for critical and innovative change. Within the Mitrovica group I have found a deep and strong community.

Intellectually, I couldn't ask for a more enriching group to work with, where research interests span from the depths of the Earth to outer space, encompassing everything in between. From a human perspective, the group becomes an even more meaningful space through the encouragement, inspiration, and moral support we provide each other through daily conversation, life musings, and of course the freshest gossip. The Mitrovica group, past, present, and future, will always be my family and I am lucky to have so many fantastic academic sisters!! I need to especially thank Jacky Austermann and Harriet Lau, my older academic sisters who helped me navigate the dark cataracts of my first year both in terms of academics and the terrifying social dynamics that acompany. The group has grown since to include more amazing scientists who inspire me: Jocelyn Fuentes, a radical and thoughtful leader, Evelyn Powell, a kind, wonderful, and wide soul, Sophie Coulson, bringing cheer and practical advice, and Marisa Borreggine, whose energy is already shaking things up. The

postdocs in our group have always been supportive and encouraging, and I'm grateful to Carling Hay, Chuan Qin, Mark Hoggard, and Fred Richards for sharing their wisdom with me. Our group is lucky to have the support of Marisa Reilly, who never hesistated to take on extra work to make sure our research and opportunities to share it, went smoothly (and she deserves a serious raise!!!).

The graduate student community at EPS has been an incredible support network through the years. I am so grateful for the friendships I have forged and the mentors I have gained over my time at Harvard. When I first arrived, these senior graduate students made me feel welcome and connected me to their networks. Lady wine time brought us together to share and vent, thank you Shannon Koplitz, Katie Dagon, Katie Travis, Hannah Horowitz, Jenny Middleton, Karen Yu, Jessica Kunke, Leah Birch and others for always making my experiences feel real. Even though he was never invited to winetime, Will Steinhardt stands out as mentor and friend who was here for me since before I arrived. Will and Dan Cusworth organized *the Hard NOx* Rhino volleyball league team, which made summers fun and taught me how to play like a team. The newer graduate students have been great too: Tia Scarpelli, Aleyda Trevino, Laura Kulowski, Danny Varon, Judy Pu

My office, 200B, has changed though the years but it has remained the funnest in the department. I won't forget our margarita office party or the all the times that we sat around scheming something ridiculous. We placed third at Tasty Burger Trivia, like the team that we are. Thanks to everyone who made this work space special: Jacky, Harriet, Blake, Camille Dwyer, Evelyn Powell, Jocelyn Fuentes, Sophie Coulson, Judy Pu, Tim Clements, Jiuxin Yin, Seth Olinger, Natasha Toghramadjian.

Of this community, I am so lucky to have confidence in some of these individuals as life long friends. Anna, when we were paired together at field camp I never could have known how deep our friendship would root. I feel as though we are sisters, and I am so grateful for all the ups and downs we have spent together. Thanks for being there for me during it all, and making home a place I love to be.

As the other member of my cohort making their great escape, Rachel Silvern has been there through the whole thing. Thank you for all the moments of friendship you offered: the amazing baked goods and the willingness to have tea and listen to me cry or scream at a moments notice. Thank you for talking me through panics and stress, and for listening to me on the darker days (and the brighter days!).

I first met Athena at the 2nd floor kitchen, and she agreed to tell me about her research. When we met for tea she patiently explained what a subduction zone is, and what slabs were. Since then, Athena has inspired me as a scientist but also as an incredible (and energetic) friend. Thank you for being the best running partner, a friend who is ready to take on adventure without notice, and caring for me as a whole.

I am lucky for the friendships I made outside of EPS including Kat Heal's, Cathy Zhang's, and Lisa Lee's. Thank you Lisa for pushing standing Friday lunch over the years!

Since my first year I have been involved in HGWISE, the Harvard Graduate Women in Science & Engineering group. Through these years my views, thoughts, and goals have changed and I am lucky to have been involved in the leadership of a campus organization through which I could enact change. I want to thank the HGWISE community, past and future, that have accompanied me on my mission: Elise Wilkes, Jessica Sagers, Jeanne Gallee, Shayna Stein, Aleyda Trevino, Anna Waldeck, Kate Lachance, Sandhya Manohar. I can't wait to see where HGWISE takes it from here and I hope I get updates!

My role in HGWISE led me to connect with Prof. Sarah Richardson in Women, Gender, and Sexuality Studies. When we had a coffee hour with her and she asked us to consider how gender played a role in what subfields or research topics were valued in our field I was completely stumped. I think that question is what pushed me to sign up for her class. I am so incredibly grateful for Sarah pushing me to a secondary field - she has been an incredibly supportive mentor and so generous with her time and energy. In the sciences it is often hard to believe that someone would go out of

their way for you just because they care about your interests and your success, without any benefit to them. My life has changed because of my readings and research in feminist studies, and I am so grateful for Sarah helping me expand my world view. The space that these studies have opened to me are wide and unexplored, and without sounding too colonizing, I am so excited to create within this new area of feminist geology.

Obviously there is no way I could have gotten to this day without the tireless love of my family. My parents always wanted me to be a scientist, and now it is pretty official. Thanks Hannah for pushing me to think outside the box and challenging my stubborn assumptions. I am so lucky to have a partner to choreograph dances, plot against our parents, and drag on adventures. I love you all so much even if I also think that we are insanely stubborn and dramatic.

Kevin balances this all out, making my family seem a little more manageable and making me a more manageable person for my family to deal with. Everyday I think about how lucky I am, and this lucky feeling just accumulates over the years. Kevin, you inspire me to become whole, kinder and more thoughtful.

0

Introduction

The sediments are a sort of epic poem of the earth.
When we are wise enough, perhaps we can read in them all of past history.
For all is written here.
–Rachel Carson

For several million years, sea-level fluctuations have been driven by ice sheet growth and decay. Cycles of continental ice expansion and retreat are characterized by orbital frequencies which have been linked to variability in temperature and greenhouse gas concentrations. Over glacial timescales, climate changes correlated with ice volume variations control river evolution and sedimentation patterns. In turn, the preserved sediment archive can record the history of sea level changes, and therefore ice history. Understanding the sensitivity of ice to forcing mechanisms is key to accounting for the impact of climate change on a number of Earth system processes, including oceanic and atmospheric circulation.

This thesis uses interactions between ice sheets and the solid Earth as a lens for elucidating key

events of the last ice age. The research described within takes advantage of records of offshore sedimentation, as well as onshore river dynamics, to gain new insight into the space-time history of former ice sheets. New methods are developed, which combine traditional and non-traditional geologic sea-level indicators, with the aim of refining models of ice sheet growth and decay over the last glacial cycle. In particular, through physical modeling that is focused on the interface between landscape evolution and the cryosphere, this thesis demonstrates that landscapes provide powerful constraints on past ice sheet behavior. Ultimately, the motivation behind the studies described in each chapter is to approach ice-age sea level from somewhat unconventional angles in order to build a more complete and accurate understanding of the fundamental nature and stability of ice sheets.

The history of past glacial cover informs our understanding of the stability of ice sheets in today's changing climate. Prior to the Last Glacial Maximum (26 kyrs ago), during the glacial build-up phase, global ice volumes are particularly uncertain due to a sparsity of relevant sea-level records. Indeed, evidence of past sea level has largely been destroyed or submerged by subsequent sea-level rise during the deglaciation. Furthermore, it is challenging to reconstruct individual ice sheets because an advancing ice sheet razes evidence of previous ice margins. Oxygen isotope ratios act as a proxy for global ice volume, though the required mapping between the two is uncertain at a level of tens of meters of global sea level, and these records have reinforced the notion that ice ages are characterized by a slow glacial build-up phase followed by a rapid deglaciation. Chapters 1-5 of this thesis challenge the assumption of a slow glaciation phase. In Chapter 1, I analyze Marine Isotope Stage (MIS) 3 sea-level markers in the Yellow River Delta. In regions of high sedimentation, such as the Yellow River Delta, it is crucial to account for the impact of sediment loading and compaction when analyzing sea-level markers. I extend the theory used in ice age sea-level models to account for sediment compaction in a gravitationally self-consistent manner, and correct these sea-level markers for the effects of glacial-isostatic adjustment, sediment loading, and sediment compaction. This study demonstrates that global ice volumes more than tripled in the 15 kyrs leading into the Last Glacial

Maximum. More generally, the research highlights the utility of using sedimentary core records to constrain under-sampled periods of the ice age, and provides a template for elucidating the details of the glacial phase to unprecedented accuracy.

In Chapter 2, I turn towards MIS 3 sea-level records in North America to locate the source of the ice growth, and find that the build-up of North American ice accounts for the rapid pace of glaciation that ushered in the Last Glacial Maximum. I analyze anomalously high sea-level recorded in the U.S. mid-Atlantic dated to this same interval (50-35 kyrs ago) and show that these records can be explained by a late and substantial growth of the eastern sector of the Laurentide Ice Sheet; a result that is consistent with the existence of non-glacial deposits of MIS 3 age in this formerly glaciated region. Is such rapid growth of the Laurentide Ice Sheet in the period leading into the Last Glacial Maximum realistic? Chapter 3 approaches this issue from a glaciologic perspective. By collaborating with experts in numerical ice modeling, I find that numerical simulations of North American ice growth using a reduced MIS 3 ice sheet result in rapid rates of ice accumulation leading into the Last Glacial Maximum. Furthermore, I show that predictions of sea-level in eastern Canada are consistent with sea-level bounds associated with marine or terrestrial non-glacial deposits dated to MIS 3.

Long-term river evolution is controlled by external dynamics, such as regional tectonics, that shape the local topography crossed by the river. Yet on glacial timescales, rates of load-induced isostatic adjustment are comparable to fast tectonic uplift rates (10 mm/yr), and thus reach a level sufficient to substantially influence river courses and drainage basins. Chapters 4 and 5 explore the extent to which rivers are influenced by the glacial isostatic adjustment process. Because rivers are sensitive to changes in slope, past landscapes can faithfully record surface deformation, thereby yielding insight into past ice loading. I exploit geologic records of rivers as a novel technique for inferring the history of glaciations by quantitatively connecting evidence of past river dynamics to numerical simulations of glacial-isostatic adjustment. In Chapter 4 I force a landscape evolution model with

predictions of glacial isostatic adjustment. I show that a late and rapid glaciation of the Laurentide Ice Sheet may have driven the eastward diversion of the Hudson River 30 kyrs ago inferred from the geologic record.

In Chapter 5 I expand this work to other rivers along the U.S. east coast, and construct a more general treatment that assesses the response of a river, in terms of channel erosion or deposition, to crustal deformation reflecting glacial isostatic adjustment. The simulations I perform provide a unifying mechanism for explaining abrupt changes in river dynamics that took place across the U.S. mid-Atlantic in the Delaware and Potomac rivers from 40-15 ka. I examine the case of erosion in the Great Falls region of the Potomac using a set of cosmogenic exposure ages on abandoned bedrock terraces, which provide evidence for a large pulse of incision beginning at 40 ka. I show that the timing of incision is consistent with a substantial increase in slope driven by glacial isostatic adjustment in this region of the river channel.

In Chapter 6 I turn to examining the last deglaciation. Since the Last Glacial Maximum, sea level has risen globally as continental ice sheets deglaciated. However, the contribution to this meltwater from different ice sheets during this interval remains uncertain. Constraining these contributions is crucial for understanding a range of critical events in ice age climate, especially intervals of especially rapid sea-level rise such as Meltwater Pulse 1a (MWP-1a; 14.5 kyrs ago), when globally averaged sea-level rose 15-20 m in less than 300 yrs. Over the ice age, the solid Earth's response to the redistribution of ice and water loads produces spatially variable sea-level patterns. Therefore, sea-level records close to former ice sheets contain valuable information about the local ice-loading history.

The timing of the last separation between the major North American ice sheets is critical to paleoclimate studies as well as to arguments that an ice-free corridor served as a path for early human migration. I address this issue in Chapter 6 by using evidence of the enigmatic history of Bering Strait flooding to infer the timing of the collapse of the ice saddle between the Laurentide and Cordilleran Ice Sheet. While previous studies have suggested that melting of the ice saddle contributed signifi-

cantly to Meltwater Pulse 1a, I find that a dominant portion of this ice melted at a later time, from 13-11.5 kyrs ago. Melting of the ice saddle induces a regional sea-level fall or still-stand at the Bering Strait, 2000 km to the west, which explains the observed two-phase flooding history of the strait. The timing of this initial connection is key to accurately reconstructing past climate variability as submergence of the Bering Strait strongly modulates ocean circulation. Moreover, the melting of the ice saddle routes large volumes of freshwater directly to the Arctic, providing a trigger for the widely debated source of the Younger Dryas global cooling event (12.9-11.7 kyrs ago).

In Chapter 7 I return to the interactions between sediment loading and sea-level. I explore the impact of sedimentation on the elevation of Last Interglacial (122 ka) sea-level markers. In particular, I constructed a synthetic sedimentation history over the last glacial cycle by simulating delta deposition using a diffusive model and a migrating shoreline, and correct for the effects of sediment loading on a global compilation of Last Interglacial sea-level records. I perform a statistical analysis, which accounts for spatial autocorrelation, across a compilation of 1287 Last Interglacial sea-level markers. This analysis suggests there is not a statistically significant global signal of sediment loading in Last Interglacial sea-level markers, although regionally the impact of sediment loading can be substantial.

Finally, in Chapter 8 I summarize the main findings in the thesis. Looking beyond this thesis, I also consider possible future directions stemming from this body of research that may further expand our knowledge about past sea level and the stability of ice sheets.

1

Global ice volume during MIS 3 inferred from a sea-level analysis of sedimentary core records in the Yellow River Delta

We need a robust standpoint theory to understand the epistemic effects of systematic social differentiation, including both the effects of situated knowledge and the conditions that foster transformative criticism. I submit that these lines of analysis apply as directly to philosophy as a discipline as to any empirical science
–Alison Wylie

A version of this chapter was published with Jerry X. Mitrovica, Ken L. Ferrier, and Jean Braun in *Quaternary Science Reviews*, vol. 152, p. 72-79, 2016.

1.1 Introduction

Ice volume variations through the last glacial cycle are a direct and sensitive measure of ice age climate change, and a key input into models of glacial isostatic adjustment (GIA). These variations have been constrained using oxygen isotope records of benthic and planktic foraminifera from deep-sea sedimentary cores (Siddall et al., 2008) and a wide range of geological markers of sea level, including erosional and constructional terraces, sedimentary and biological facies, and coral reefs (Lambeck & Chappell, 2001, Yokoyama et al., 2000, Muhs et al., 2012, Hanebuth et al., 2006). However, the accuracy of ice volume inferences based on oxygen isotope records is limited by regional variability, uncertainties in the conversion from $\delta^{18}O$ related to temperature, and the mean isotopic concentration of continental ice (Siddall et al., 2008, Waelbroeck et al., 2002). Moreover, geological markers of sea-level change are spatially and temporally sparse, and estimates of ice volume based upon them must account for a variety of contaminating signals, most notably GIA (Lambeck & Chappell 2001, Lambeck et al., 2014, Milne et al., 2008). The sparsity of the record is particularly problematic for the period prior to the Last Glacial Maximum (LGM) since many markers of sea level, created during more extensive ice cover, are now submerged. For these reasons, estimates of ice volumes during the bulk of the last glaciation phase, extending from Marine Isotope Stage (MIS) 5c ($\sim$100 ka; i.e Muhs et al., 2012) through MIS 3 (60-25 ka; Siddall et al., 2008), are uncertain to within tens of meters of equivalent global mean sea level (GMSL), where GMSL is defined as the globally averaged sea-level change associated with a given change in total ice mass inventory (i.e., the volume of meltwater divided by the area of the ocean).

Constraints on ice volumes and GMSL during MIS 3 provide an illustrative case in point. Siddall et al., (2008) summarized and compared individual (e.g., Shackleton 2000) and stacked benthic records (Lisiecki & Raymo 2005), in addition to planktic records (Dannenmann et al., 2003), during this stage. As an example, over the time period 50-37 ka, peak GMSL estimates can range from -25 to

-87 m, relative to present(Siddall et al., 2008). After correcting the coral record at Huon Peninsula for the signal due to GIA and tectonic uplift, Lambeck & Chappell (2001) concluded that GMSL fell from -60 m to -80 m during the same period, while the global ice history model ICE-5G is characterized by a GMSL value within the range -87 m to -100 m across this time interval (Fairbanks & Peltier, 2006). The sea-level lowstand at the Last Glacial Maximum (LGM; 26 ka; Clark et al., 2009) reached ∼ -130 m (Yokoyama et al., 2000, Austermann et al., 2013), and therefore, within current uncertainty, global ice volume may have increased by more than a factor of 3 or by less than one-third in the 15 kyr period leading up to the LGM.

In this paper our goal is to refine estimates of global ice volume in the middle of MIS 3, from ∼50 to 37 ka, using sedimentary cores from the Yellow River Delta in the Bohai Sea of China. These cores record a transition from marine to freshwater conditions at this time that reflects a migration of the ocean margin across the area and they provide an important constraint on local sea level. We correct the inferred local sea-level history in the region for GIA-induced sea-level change using a numerical model that includes a gravitationally self-consistent treatment of the impact of sediment redistribution (Dalca et al., 2013), and reconstruct GMSL during this time interval. The analysis will explore the sensitivity of the estimate of GMSL to various inputs adopted in the GIA calculation, including the models for sediment redistribution (which incorporates erosion, deposition, and compaction), ice history, and Earth structure.

1.2 Methods

1.2.1 GIA modeling

Local sea-level changes are not simply related to fluctuations in global ice volume. Ice sheet growth and melting on a viscoelastic Earth produces a complex spatio-temporal pattern of sea level change that is dependent on the full history of the surface mass (ice, water and sediment) load. The redis-

tribution of surface loads over glacial cycles perturbs the Earth's gravitational field through crustal deformation and direct self-attraction, but the redistribution of water is, in turn, governed by this perturbation since the sea surface must remain a gravitational equipotential in a static sea-level theory. Farrell & Clark (1976) were the first to derive a gravitationally self-consistent sea-level theory – the so-called sea-level equation – under the assumption of a non-rotating Earth with fixed shoreline geometry. Their canonical work has been extended to include the effects of rotation (Milne & Mitrovica, 1996), evolving shorelines associated with local sea level changes and/or the migration of grounded, marine-based ice (Johnston, 1993; Milne et al., 1999; Lambeck et al., 2003; Kendall et al. 2005), and, most recently, sediment redistribution (Dalca et al., 2013). In the present study, we adopt the Dalca et al. (2013) sea-level theory, modified to incorporate sediment compaction, and solve it using the pseudo-spectral algorithm described in that paper. For this purpose we use a spherical harmonic truncation at degree and order 512, which represents a surface spatial resolution of $\sim$40 km.

Relative sea level (SL) is defined as the height of the equipotential that coincides with the ocean surface (G) relative to the elevation of the solid surface:

$$SL = G - (R + H + I), \tag{1.1}$$

where R is the elevation of the crust, not including sediments and grounded ice, I is the thickness of grounded ice, and H is the thickness of sediment. We will henceforth use the terms "sea level" and "relative sea level" interchangeably. We will be concerned here with perturbations in sea level and each of the components in equation (1) from an initial time t_0 to a time t_j. If we denote this perturbation by the symbol Δ, then we can write:

$$\Delta SL_j = \Delta G_j - (\Delta R_j + \Delta H_j + \Delta I_j). \tag{1.2}$$

Our sea-level predictions solve for ΔSL_j, ΔG_j and ΔR_j, given time-varying input fields ΔH_j

and ΔI_j. We prescribe the sediment redistribution, ΔH_j, as an input field computed from a database of dated sediment cores. Because these sediments have undergone compaction, we define the decompacted sediment thickness H_j at time t_j as

$$H_j = H_{present} - (h_j - \delta_j) \tag{1.3}$$

where $H_{present}$ is the sediment thickness at present to bedrock, H_j is the sediment thickness at t_j, h_j is the compacted sediment thickness deposited from time t_j to present day, and δ_j is the amount that H_j compacted from t_j to the present (see Figure 1.1 for illustration).

$H_{present}$ is obtained from a map of isopach sediment thickness to bedrock, and h_j is determined from dated sedimentary cores. We calculate the elevation difference due to decompaction, δ_j, by using the input fields h_j and $H_{present}$, and by assuming an exponential porosity depth relationship (i.e. Athy 1930; Guillocheau et al., 2012),

$$\Phi(z) = \Phi_0 e^{-\frac{z}{z_0}} \tag{1.4}$$

where Φ_0 is the surface porosity, z is depth, and z_0 is a lithology-dependent constant. By equating the sediment grain mass in the sediment column before and after compaction we may derive an expression for δ_j (details included in Appendix A):

$$\delta_j = \frac{\Phi_0 h_j (1 - e^{-\frac{H_{present}}{z_0}})}{(1 - \Phi_0 e^{-\frac{H_{present}}{z_0}})} \tag{1.5}$$

As noted above, the thickness of sediment deposited since the initial time step ($j = 0$) to time t_j is:

$$\Delta H_j = H_j - H_0. \tag{1.6}$$

This value of ΔH_j is the input into Equation 1.2.

Next, we turn to prescribing the surface mass load. In Dalca et al. (2013), the history of loading is written as

$$\Delta L_j = \rho_w \Delta S_j + \rho_I \Delta I_j + \rho_H \Delta H_j \tag{1.7}$$

where ρ_w, ρ_I, ρ_H are the (assumed constant) densities of water, ice and sediment, respectively, and ΔS_j is the change in ocean thickness. However, ρ_H is not uniform when sediment compaction is accounted for. To determine the total bulk sediment load at time step t_j we calculate the average bulk density of the decompacted sediment thickness at t_j ($\bar{\rho}_{H_j}$) and at t_0 ($\bar{\rho}_{H_0}$). Then, in place of Equation 1.7, we use the expression:

$$\Delta L_j = \rho_w \Delta S_j + \rho_I \Delta I_j + (\bar{\rho}_{H_j} H_j - \bar{\rho}_{H_0} H_0) \tag{1.8}$$

In addition, incorporating sediment compaction requires that we track the water storage capacity of the sediment pore space. To conserve total mass, any volume of water incorporated into pore space must be removed from the total ocean volume budget. In this regard, both the additional water volume accommodated into the pore space of newly deposited sediment, and the water volume expulsed from the underlying strata during compaction, must be accounted for. We track a water volume term, W_j, which is equal to the difference between newly created pore space and newly reduced pore space, and incorporate this term in the total water budget to conserve mass (Appendix A).

Finally, the contribution of sediment redistribution to sea level changes includes two components: (1) the perturbation to the crustal height, ΔR_j, and sea surface height, ΔG_j, due to deformation by the sediment load; and (2) the decompacted sediment thickness, ΔH_j, at a given time step, which is comprised of the compacted sediment thickness, h_j, and the elevation difference, δ_j, due

to compaction of underlying strata. To calculate the paleotopography, we use values for h_j derived from the constructed regional sediment redistribution model, whereas when citing predictions at the core sites we adopt the value from the core itself (see below).

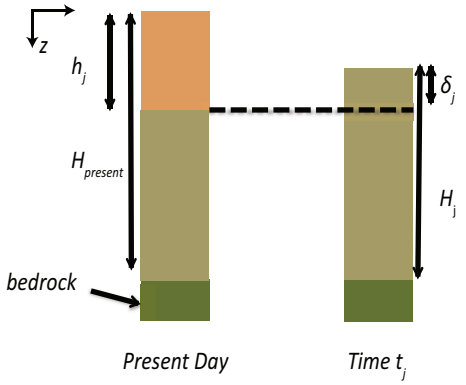

FIGURE 1.1: Schematic illustration of sediment compaction and various parameters discussed in the text.

In the initial simulation discussed below, we adopt the ICE-5G Version 1.2 model of ice history (ΔI) over the last ice age cycle (Peltier, 2004; Fairbanks and Peltier, 2006). The GMSL curve for the ICE-5G model is shown in Figure 1.2 (black line). As noted above, the model is characterized by GMSL of -87 m to -100 m during the time period 50-37 ka. ICE-5G is paired with the VM2 model for the radial profile of mantle viscoelastic structure. VM2 is characterized by a lithospheric thickness of 90 km and a mantle viscosity that increases from $\sim 5 \times 10^{20}$ Pa s in the upper mantle to $\sim 3 \times 10^{21}$ Pa s in the deep mantle, and the ICE-5G/VM2 combination is tuned to fit a global database of relative sea level histories (Peltier & Fairbanks 2006). Following this initial calculation, we will consider a suite of 300 ice histories that sample a wide range of GMSL values through the glaciation phase (Figure 1.2); We created each of the alternative ice histories by randomly sampling the range of estimated GMSL values shown by the gray shaded region in Figure 1.2; for example, each ice history is constrained to pass through the GMSL range -30 to -80 m at 44 ka (details regarding the construction of these ice histories are provided in the Supplementary Material). We will also

consider a set of alternate viscoelastic Earth models.

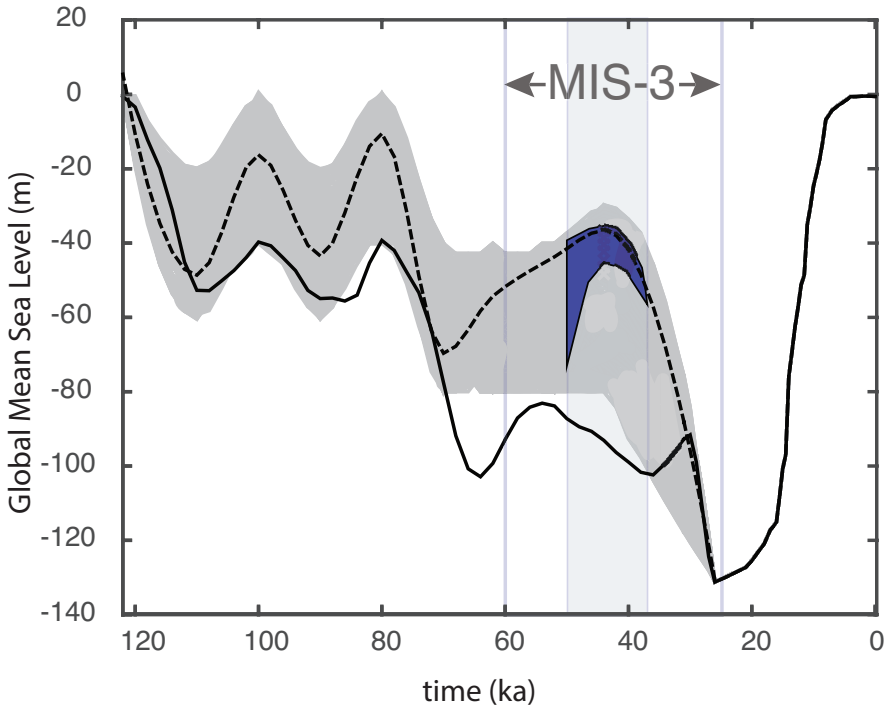

FIGURE 1.2: GMSL change associated with the ICE-5G ice history for the last glacial cycle (solid black line). The shaded region encompasses GMSL of 300 ice histories used in a sensitivity analysis described in the text. The dashed line indicates the ice history adopted in the prediction shown in Figure 1.5B. The blue shaded region indicates the full range of GMSL values within the time window 50-37 ka (shaded rectangle) that fit constraints imposed by shoreline indicators, as discussed in the text. The duration of MIS 3 is labeled on the figure.

1.2.2 Sediment redistribution models for the Yellow River Delta

We next turn our attention to the construction of a sediment redistribution model (h_j) for the Yellow River Delta region. Sediment loads perturb the predicted sea-level change due to GIA, particularly at sites close to river deltas, where large masses of sediment are deposited in prograding and receding patterns on the continental shelf in response to ice age cycles (Simms et al., 2007; Dalca et al., 2013; Ferrier et al., 2015, Wolstencroft et al., 2014).

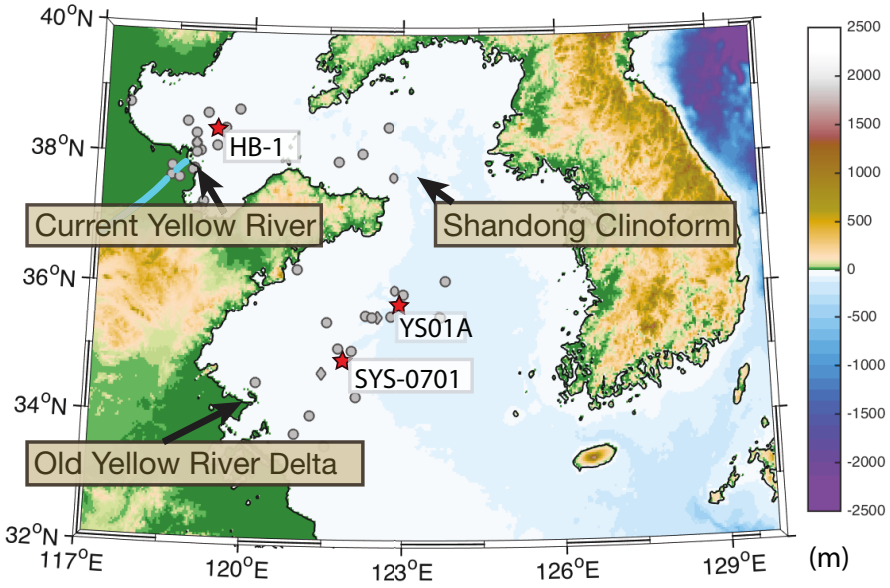

FIGURE 1.3: The location of sedimentary cores used to construct sediment transfer models. During the period 50-37 ka, core HB-1 is characterized by littoral fossils (i.e., a terrestrial environment), YSO1A by marine fossils, and SYS-0701 by a transition from marine to brackish fossils.

The shallow nature of the Bohai Sea, which has a mean depth of 20 m and a maximum depth of 70 m, makes the area highly sensitive to changes in sea level (Figure 1.3). Indeed, relatively small changes in local sea level can lead to significant migration of the shoreline and inundation or exposure of large swaths of the continental shelf. Thus, sediment cores in this region have the potential to record shoreline migration in preserved fossils that reflect the brackish or marine environments in which they were deposited. In particular, during the middle stages of MIS 3, three cores (HB-1, SYS-0701, YS01A) contain dated fossils that bound the location of the paleoshoreline (Table E.1). Specifically, fossils deposited in core HB-1 are littoral or tidal flat species and dated to cal 42.76-46.96 ka BP (2σ) and cal 41.25-44.02 ka BP (2σ), while fossils in core YS01A are shallow marine and dated to cal 39.76-41.11 ka BP (2σ). Core SYS-0701 contains a gradient of marine to brackish fossils, indicating that the shoreline was close to the core site during MIS 3, with geochronology on a pair of fossils

returning ages of cal 46.16-50.00 ka BP (2σ) and cal 44.84-49.50 ka BP (2σ) and a quartz sand near the exposure surface dated by optically stimulated luminescence (OSL) to 41 $\pm$ 4 ka (See Supplementary Material for dating and calibration methods).

Radiocarbon dates in the range of 40-50 ka are at the limit of reliability for this dating technique. Samples that return such ages may be older, and reflect contamination that would cause a radiocarbon-dead sample to give a date in this range. However, four OSL dates in this core span 41 $\pm$ 4 ka to 48 $\pm$ 5 ka from a depth of 10.19 to 22.95 m (i.e., they bound radiocarbon dates stratigraphically), and these add confidence to the radiocarbon dates. Considering the error on these dates the shoreline could have been located at this site at any point during the period 50 to 37 ka. In the results below, we will display shoreline reconstructions in the middle of this interval, at 44 ka.

Table 1.1: Geochronological data constraining paleoshoreline location. Ranges for dates derived from ^{14}C are cal ka BP (2σ).

Core name	Core depth (m)	Age (ka)	Dating method	Material dated	Reference
HB-1	35.33	41.25-44.02	^{14}C	gastropod	Liu et al., 2009
HB-1	35.33	42.76-46.96	^{14}C	mollusc shell	Liu et al., 2009
SYS-0701	10.19	41 $\pm$ 4	OSL	quartz sand	Liu et al., 2010
SYS-0701	10.70	43 $\pm$ 4	OSL	quartz sand	Liu et al., 2010
SYS-0701	15.22	45 $\pm$ 5	OSL	quartz sand	Liu et al., 2010
SYS-0701	18.41	46.16-50.00	^{14}C	mollusc shell	Liu et al., 2010
SYS-0701	20.30	44.84-49.50	^{14}C	mollusc shell	Liu et al., 2010
SYS-0701	22.96	48 $\pm$ 5	OSL	quartz sand	Liu et al., 2010
YS01A	28.65	39.76-41.1	^{14}C	foramnifera	Wang et al., 2014

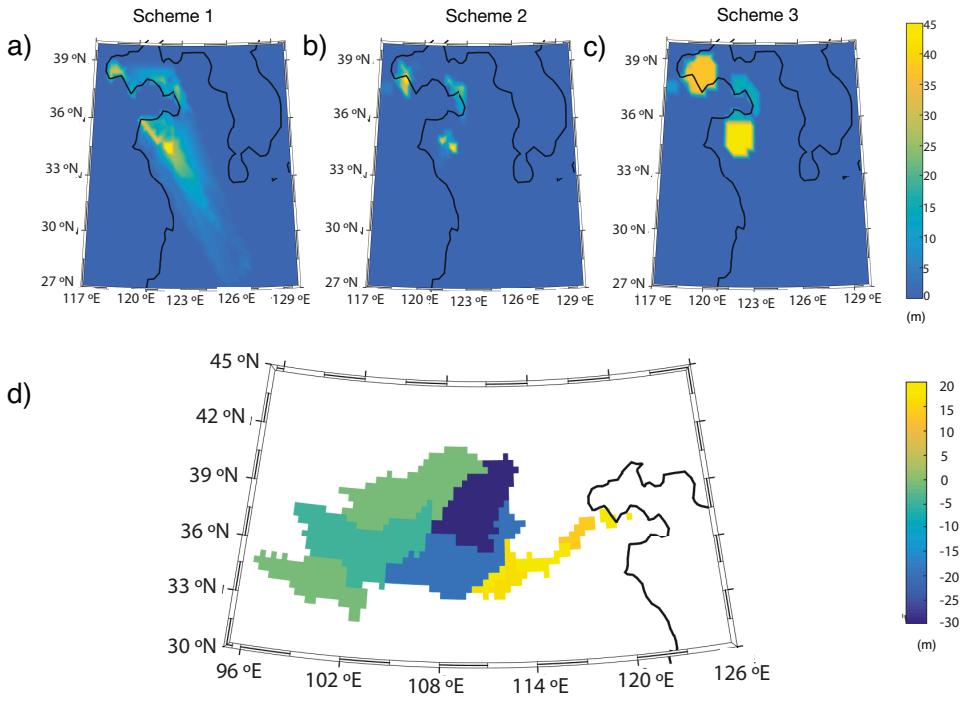

FIGURE 1.4: (a-c) Regional sediment redistribution models constructed using three interpolation schemes. a) Scheme 1: Linear interpolation between all core accumulation rates in Figure 1.3 b) Scheme 2: Linear interpolation within each depocenter region (current delta, old delta, and clinoform) individually. c) Scheme 3: Average depocenter accumulation rate is assigned uniformly in space across each depocenter. d) On-land erosion and deposition, based on present-day measurements. All frames show accumulated thicknesses over the last glacial cycle.

We constructed three different models for sediment redistribution in the region using 49 well-dated sediment cores (see Figure 1.3 for site locations) and river flux measurements in both the drainage area upstream of the Yellow River Delta and within depositional environments in the Bohai and Yellow Sea (see Supplementary Material for core database details). On-land erosion and deposition rates are calculated using river flux measurements, and erosion rates are assigned uniformly within each of six sub-basins. Accumulation rates on the continental shelf are calculated using radiocarbon or optically dated surfaces in the cores. These rates of erosion and deposition are assigned to

grids with spacing consistent with our spherical harmonic truncation at degree 512, and these grids are constructed at time steps spanning the last glacial cycle.

Sediment deposition in the region occurred in three depocenters as the river mouth avulsed between the current and old river deltas, and as ocean currents transported sediment around the Shandong peninsula. We label these depocenters as the current delta, old delta, and Shandong Clinoform. To create maps of sediment redistribution we adopt three different methods to interpolate between local accumulation rate estimates at core sites (Figure 1.4).

In Scheme 1 (Figure 1.4a), linear interpolation is employed between all core-based estimates. Because core data is sparse, and generally does not sample areas in between depocenters, Scheme 1 is likely to assign higher than actual sedimentation rates in areas outside of depocenters that are known to have low accumulation rates. Similarly, because cores do not sample the entire depocenter region, it is possible that accumulation within the depocenter is underestimated using simple interpolation. Scheme 2 (Figure 1.4b) avoids this bias by applying a linear interpolation between cores located within each of the three depocenters. However, similar to Scheme 1, this scheme also likely underestimates the amount of sediment in depocenters. Finally, in Scheme 3 (Figure 1.4c), we assign to each depocenter a uniform accumulation rate equal to the average rate in sediment cores that fall within the area. This scheme provides a more realistic representation of the total sediment load in depocenters, but it does not account for both the potentially large geographic variability in accumulation rates within each depocenter and the evolution in the areal extent of depocenters through time.

Figure 1.4d shows our model of the accumulated thickness of terrestrial erosion and deposition based on present-day river flux measurements. Our sea-level simulations must conserve mass; thus the amount of sediment eroded must equal the amount deposited. As an example, consider the last 1000 years. We assume that erosion rates, and hence deposition rates, are similar to modern values as this time period reflects the anthropogenic influence of agriculture in the region (i.e. Milliman et al. 1987, Mei-E & Zhu 1995). However, the reconstructed volume of erosion over the past 1000

years was higher than the volume of sediment deposition estimated from the core records over that period. The ratio between total eroded and deposited volume is 1.32, 5.02, and 3.09, respectively for Schemes 1, 2, and 3. To preserve the deposition volumes recorded in the sediment cores, we choose to scale erosion rates down to match the depositional record. During earlier periods such as MIS 3, where erosion rates are not constrained, we apply the same methodology; that is, we apply a unique scaling factor to each time step to conserve mass. In this process we preserve the relative contribution of each drainage sub-basin shown in Figure 1.4d. This yields a time history of erosion and deposition covering the last glacial cycle.

As a final point, we note that the three sediment models discussed above are used to define the sediment load component of the total surface mass load (equation 8) which is necessary for the calculation of the load-induced crustal deformation and sea surface perturbation (ΔR and ΔG, respectively, in equation 2). As noted above, whenever we cite sea-level results at the three core sites HB-1, YS01A and SYS-0701 (Figure 3), we use the sediment thickness of the dated core, rather than that of the sediment restribution model, to compute the change in topography associated with sediment height (ΔH_j in equation 2).

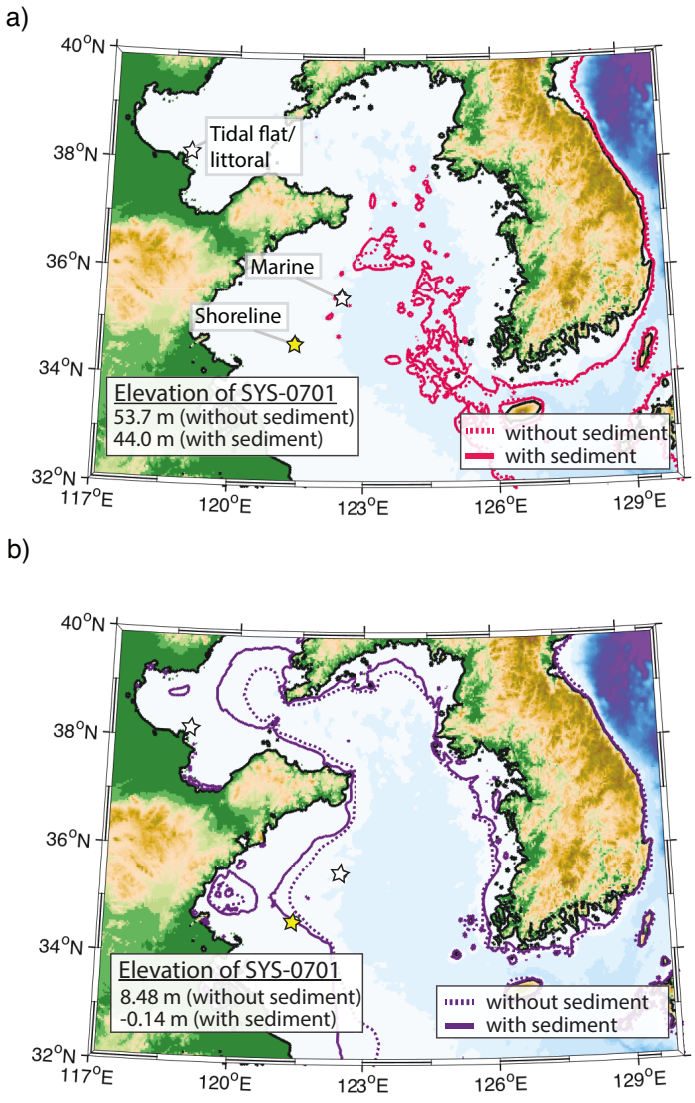

Figure 1.5: Predicted shoreline positions at 44 ka. a) Calculations based on the ICE-5G model of ice history and the VM2 viscosity profile, including (solid) and not including (dotted) sediment redistribution. The predicted elevations of the SYS-0701 core site for these simulations are 44.0 m and 53.7 m above the sea surface, respectively. The white stars label cores HB-1 and YS01A, indicating tidal-flat/littoral and marine species, respectively. The yellow star indicates the location of core SYS-0701. b) As in frame (a), except that the ice history is revised to yield the GMSL curve shown by the dotted black line in Figure 1.2. In this case, the predicted elevations of the SYS-0701 core site at 44 ka are -0.14 m and 8.48 m, respectively, for simulations with and without sediment redistribution. Details of the sediment redistribution (Scheme 3) are provided in the Methods.

We will begin by considering results based on Scheme 3 (Figure 1.4c). We consider interpolation Scheme 3 to be the most realistic model of sediment deposition in the basin since the sediments are only distributed within known areas of deposition.

We ran two ice age sea level simulations adopting the ICE-5G ice history coupled to the VM2 Earth model, one including and the other not including sediment redistribution. Figure 1.5a shows the predicted positions of the shoreline at 44 ka for these two cases. As previously noted, the fossil record at core SYS-0701 indicates that the paleoshoreline was close to the site from 50-37 ka. In contrast, the ICE-5G/VM2 predictions place the site well away from the paleoshoreline and at an elevation of either 44.0 m in the case when sediment redistribution is included, or 53.7 m for calculations that do not include the loading effect of the sediment redistribution or its compaction through time. In this regard at the site SYS-0701, our compaction model yields an estimate of δ_j of 8.04 m, based on the lithology, isopach thickness, and compacted sediment thickness accumulated since 44 ka (Figure 1.1).

The simulation shown in Figure 1.5a suggests that in order to match paleoshoreline data, relative sea level must have been $\sim$45 m higher at 50-37 ka than the value predicted by ICE-5G. This mismatch is substantial, and suggests a significant discrepancy between the true global ice volume and that of the ICE-5G history. To quantify this issue, we ran a large series of simulations that used the same Earth model (VM2) and sediment redistribution model as in Figure 1.5a, and were distinguished on the basis of the adopted ice history.

We predicted the shoreline location and the elevation of the core site SYS-0701 at 44 ka using the full suite of ice histories associated with the GMSL curves bounded by the shaded region in Figure 1.2. We then retained from this set of simulations only those results that predicted shoreline locations that: (1) were consistent with the geological settings (marine, brackish, or terrestrial) imposed by the cores YS01A, SYS-0701, and HB-1, respectively; and (2) predicted an elevation of site SYS-0701 at 44 ka within the range -3 m to 3 m, the local tidal range which bounds possible eleva-

tions for brackish deposition (as in Yokoyama et al., 2000). In Figure 1.6 we show the distribution of GMSL values associated with the subset of 46 simulations that satisfied these constraints (blue). These GMSL values range from -35.4 m to -45.5 m, (the 46 simulations have a mean of -40.0 m and a standard deviation of 2.6 m). The uncertainty reflects the sensitivity of the inference to possible errors in the ice history across the period from the LIG to MIS 3.

As an example, Figure 1.5B shows the reconstructed location of the shoreline predicted by the simulation in which GMSL during MIS 3 was raised by $\sim$ 50 m relative to the ICE-5G history, corresponding to a GMSL value of -36 m at 44 ka (black dotted line, Figure 1.2). In this case, the prediction that includes the impact of sediment redistribution accurately reconstructs the paleoshoreline close to the core site SYS-0701; the predicted elevation of the site at this time is -0.14 m. Moreover, the same prediction places core HB-1 landward of the shoreline and YS01A core in a marine setting at this time, consistent with the fossil records at these sites.

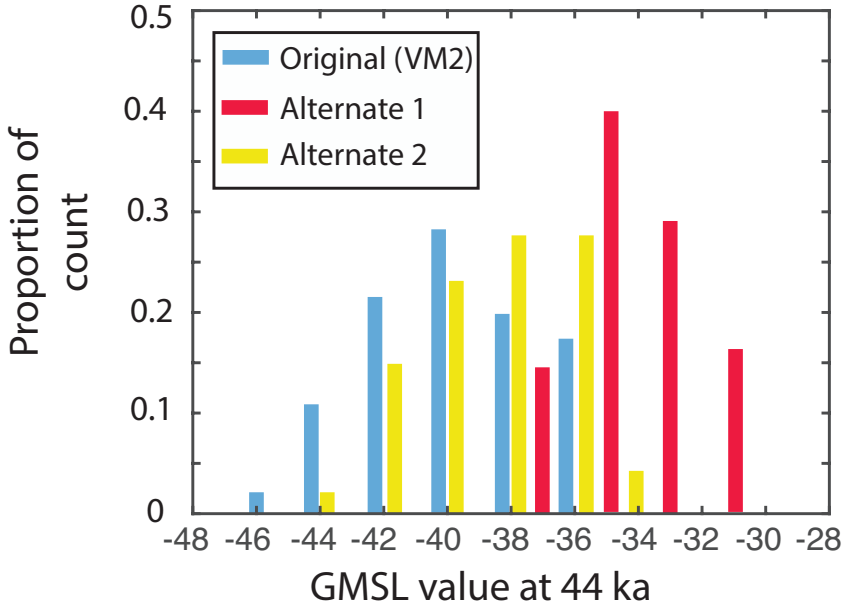

FIGURE 1.6: Distribution of GMSL values at 44 ka for simulations that predict elevations within ±3 m elevation at SYS-0701. Results are shown for Earth model VM2 (blue; values range from -35.4 to -45.5 m, with a population mean of -40.0, a standard deviation of 2.6 m, and a median of -40.0 m); Alternate model 1 (red; -30.1 to -38.0, with a population mean of -34.2, a standard deviation of 1.9 m, and a median of -34.4 m); and Alternate model 2 (yellow; -34.4 to -43.4, with a population mean of -38.5, a standard deviation of 2.4, and a median of -38.0 m). The three viscosity models yield 46, 55, and 47 runs (out of 300 each), respectively, that satisfy the bound at SYS-0701.

We next considered the sensitivity of these calculations to variations in the sediment history and Earth structure. To begin, we ran simulations in which we adopted the remaining two sediment redistribution models described in the Methods (Figure 1.4). We predict elevations of -0.2864, -1.7327, -0.1365 for the three sediment redistribution models (Scheme 1,2, and 3, respectively) at 44 ka at the core site SYS-0701. As in Figure 1.5B these were all computed using the GMSL history shown by the dotted black line in Figure 1.2, and the VM2 Earth model. The differences between the three models (∼1.6 m) thus provide a measure of the sensitivity of the predictions to uncertainties in this loading effect.

To quantify the sensitivity to the chosen Earth model we ran a series of simulations using the

same 300 ice histories, where the viscosity model VM2 was replaced by two alternate Earth models distinguished by the adopted lithospheric thickness and uniform upper and lower mantle viscosities: (1) 71 km, and 5×10^{20} Pa s and 10^{22} Pa s, consistent with several independent studies of GIA data sets (e.g., Lambeck et al., 1998; Mitrovica and Forte, 2004); and (2) 41 km, and 2×10^{20} Pa s and 5×10^{21} Pa s (consistent with the low-viscosity solution of Lambeck et al., 2014). (we refer to these as Alternate models 1 and 2, respectively.) These choices were guided, in part, by a recent analysis of Holocene relative sea level data in China which suggests that a lower mantle viscosity in excess of $5 - 10 \times 10^{21}$ Pa s is unlikely for this region (Bradley et al., 2016). The distribution of GMSL values that fall within the required elevation bounds for simulations based on the two alternate Earth models is shown in Figure 1.6 (red and yellow bars). The mean values of these distributions are -34.2 m (standard deviation of 1.9 m) and -38.5 m (standard deviation of 2.4 m), for Alternate models 1 and 2, respectively. Accounting for the variability associated with the ice history and Earth model (Figure 1.6), and sediment redistribution (-1.6 m), we infer a two sigma bound on peak GMSL in the interval 50-37 ka of -38 $\pm$ 7 m. (As we noted above, while the numerical predictions focus on the time 44 ka, errors in the timing of the shoreline migration suggest that the estimated GMSL value was obtained somewhere in the time range 50-37 ka.)

In Figure 1.7 our estimate of -38 $\pm$ 7 m for peak GMSL across the period 50-37 ka is compared with inferences from previous studies. The bounds shown for each study represent the minimum and maximum GMSL values inferred over this time interval, and the latter should be compared with our bound on peak GMSL. Our result lies at the upper range of GMSL estimates (minimum ice volume).

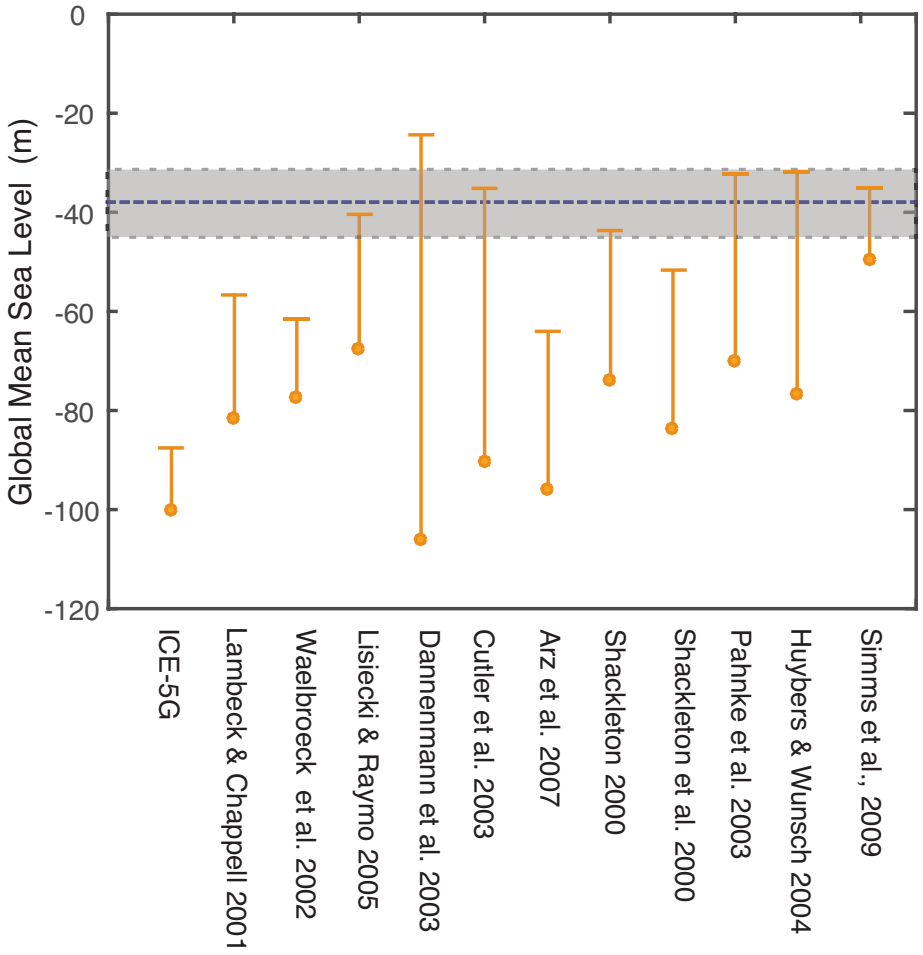

FIGURE 1.7: Estimate of peak GMSL from this study (dotted-line, shading represents the error bound) during the period 50-37 ka. Vertical lines show inferences of maximum and minimum GMSL values from previous, independent analyses (as labeled on the abscissa) summarized in Siddall et al. (2008). The bar on each is to be compared with our new inference of peak GMSL

1.4 Conclusions

Constraining ice volumes across the last glacial cycle is an important step toward a deeper understanding of ice age climate and the associated stability of ice sheets. Combining gravitationally self-consistent predictions of GIA-induced sea-level changes that accurately incorporate the effects of sediment redistribution in areas of high deposition and erosion, with dated sedimentary cores that record transitions from marine to terrestrial environments, provides a novel approach to refining existing estimates of ice volumes during the last glacial phase. We have applied this approach to estimate GMSL in the middle of Marine Isotope Stage 3, 50-37 ka, using core records in the Bohai and Yellow Sea. We conclude that peak GMSL during this time interval was in the range -38 $\pm$ 7 m, which indicates that excess (relative to present day) ice volumes increased by a factor of three in the 15 kyr period leading to LGM. In Figure 1.7 we compare this bound on GMSL to independent estimates based on mapping oxygen isotope records to global ice volumes (Waelbroeck et al., 2002, Pahnke et al., 2003, Shackleton, 2000, Lisiecki & Raymo, 2005, Dannerman et al., 2003, Cutler et al., 2003, Huybers & Wunsch, 2004, Shackleton et al., 2000, Arz et al., 2007, Simms et al., 2009) or on the sea level record at Huon Peninsula (Lambeck & Chappell 2001). Of the eleven inferences shown on the figure, the peak GMSL from six of these studies overlap with our revised estimate of GMSL.

Yokoyama et al. (2000) similarly used sea-level indicators in sediment cores, corrected for GIA, in an area of relatively low sedimentation (Bonaparte Gulf, Australia) to estimate a stable GMSL of -135 m at the LGM. With suitable well-resolved and accurately dated sedimentary core records, the approach used herein can be applied across the entire period extending from the end of MIS 5e to the LGM.

Finally, beyond global considerations of Earth system evolution during the last glacial phase, our results also have important implications for studies of local sea level in the Bohai and Yellow Sea regions. In particular, our reconstruction of shoreline evolution, consistent with available core

records, provides a key input into studies of human migration patterns in the region (D'Alpoim Guedes et al., 2015).

2

Sea-Level Records from the U.S. Mid-Atlantic Constrain Laurentide Ice Sheet Extent During Marine Isotope Stage 3

Anger is the grief of distortions between peers, and its object is change
–Audre Lorde

2.1 Introduction

Reconstructing the pace of ice growth toward the Last Glacial Maximum (LGM, 26 ka) is critical to our understanding of ice age climate and ice sheet stability. Nevertheless, global ice volume, or

A version of this chapter was published with Jerry X. Mitrovica and Jessica R. Creveling in *Nature Communications*, vol. 8, 2017.

equivalent global mean sea level (GMSL), and the corresponding geographical distribution of ice remain uncertain through Marine Isotope Stage 3 (MIS 3; 60 – 26 ka) leading into the LGM(Siddall et al., 2008; Kleman et al., 2010). Oxygen isotope records from marine sediment cores provide a proxy for global ice volume after correcting for temperature-dependent fractionation(Waelbroeck et al., 2002), however uncertainties in this correction and other complications in mapping isotope values to ice volumes have yielded estimates of peak MIS 3 GMSL that range from -30 m to -60 m relative to present day(Siddall et al., 2008). Geological records of sea level during MIS 3 are sparse because ancient markers in the far field of former ice sheets are presently submerged, while those in the near field have been erased by the subsequent advance and retreat of the major continental ice sheets(Clark et al., 1993; Dyke et al., 2002). Moreover, glacial isostatic adjustment (GIA) and tectonic uplift contaminate the present-day elevation of available sea-level records(Chappell, Ota and Berryman, 1996; Mitrovica and Milne, 2002). Studies that applied GIA modeling to fit oxygen isotope records and geological sea-level markers have published discordant inferences of peak MIS 3 GMSL, varying from -85 m(Peltier and Fairbanks, 2006) to -55 m(Lambeck and Chappell, 2001), and most recently -37.5 $\pm$ 7 m(Pico et al., 2016).

The geological markers of Pleistocene sea-level oscillations extending from Virginia to North Carolina in the Albemarle Embayment (Figure 1), on the Laurentide Ice Sheet's (LIS) peripheral bulge, require a re-evaluation of ice volume and extent during MIS 3. This record indicates that MIS 3 relative sea level (RSL) reached present-day levels from $\sim$50 – 35 ka in this region(Cronin et al., 1981; Mixon, Szabo and Owens, 1982; Parham et al., 2007, 2013; Mallinson et al., 2008; Culver et al., 2011) (Figure 1; Supplementary Table 1), but GIA calculations predict that these markers should presently be found as much as $\sim$70 m below sea level(Peltier and Fairbanks, 2006) . Tectonic uplift of the markers is insufficient to explain their present-day elevation(Doar and Kendall, 2014; Van De Plassche et al., 2014) and sediment compaction has led to only minor subsidence in this region(Brain et al., 2015). We present a new set of GIA calculations that explore the sensitivity of the predictions

to peak GMSL and LIS geometry during MIS 3. We conclude that a revised GIA model can reconcile the MIS 3 sea-level record at the Albemarle Embayment under two conditions: (1) peak GMSL reached near -40 m, and (2) the eastern sector of LIS was significantly reduced during MIS 3 compared with previous reconstructions of ice extent.

2.2 Results

2.2.1 The U.S. Mid-Atlantic Sea-level Record

The Albemarle Embayment geological record includes interfluvial, estuarine, intertidal and shallow marine lithofacies arranged in depositional sequences that record repeated sea-level highstands dated primarily by optically stimulated luminescence to MIS 5e, 5c, 5a and 3(Parham et al., 2013)(Figure 1; Supplementary Table 1). We adopt the minimum elevation of terrestrial facies and the maximum elevation of marine facies as upper and lower bounds, respectively, of MIS 5a (∼80 ka) and mid-MIS 3 (50-35 ka) sea level. For the MIS 5a data (Figure 1; Supplementary Table 1), we bound a cluster of sea-level data from 2.5 – 7 m in agreement with previous assessments of sea level records in the region(Wehmiller, Edwards and Martin-McNaughton, 2004). We assume that rare terrestrial markers found at elevations below this range do not represent a constraint on the MIS 5a highstand, but rather a lower sea level reached during late MIS 5a or MIS 4. Furthermore, calculations described below (and detailed in the Supplementary Note 3) demonstrate that RSL predictions for MIS 3 are relatively insensitive to the height of sea level during MIS 5a.

For the MIS 3 interval spanning 50 – 35 ka, three marine indicators constrain RSL to be above -0.9 m, -3 m, and -2 m(Parham et al., 2013). We thus adopt the elevation of the highest of these marine indicators, -0.9 m as the lower bound. Regarding the upper bound, three terrestrial indicators, with ages between 50 and 35 ka, show a consistent constraint on the sea-level highstand of 1 m. Two terrestrial indicators dated to earlier in this time window(Mallinson et al., 2008) are found at lower

elevations, however these may represent deposition during a time of rising sea-level rather than during the peak sea-level highstand. We adopt the terrestrial indicators at 1 m as the upper bound on sea level, yielding a range of -1 to 1 m. We apply an elevation error of $\pm$ 3 m that reflects reconstructed paleo-tidal range for the region, which may have been up to 3 times greater than the present amplitude of $\sim$1 m(Hill et al., 2011). The geological sea-level constraints we adopt below (e.g. Figure 2) incorporate these broader uncertainties.

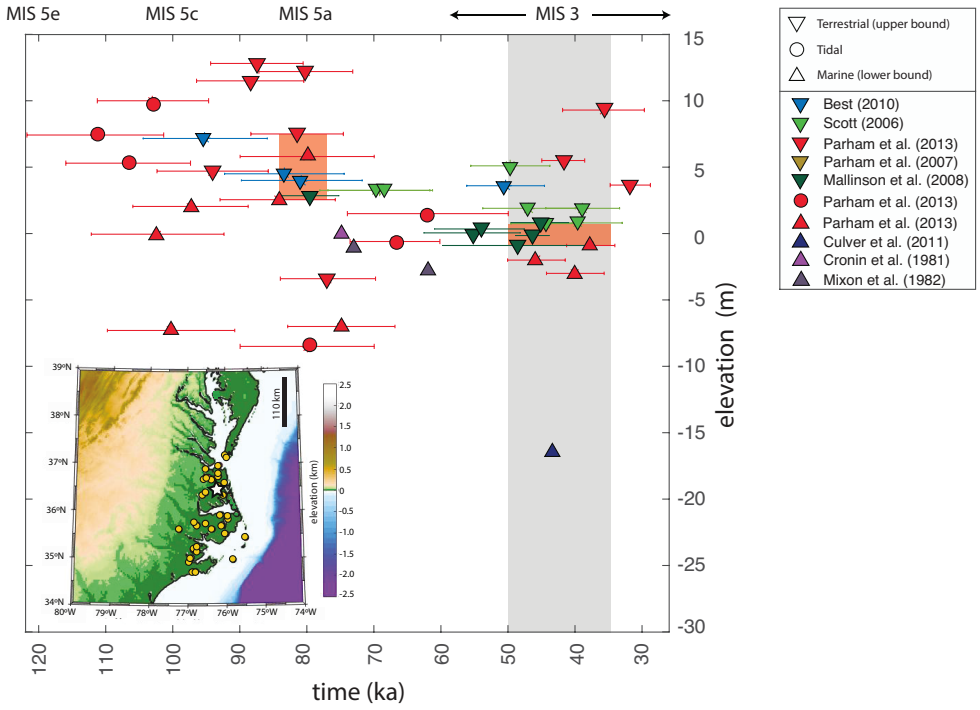

FIGURE 2.1: Present elevation of sea-level indicators from the Last Interglacial ($\sim$120 ka) to the Last Glacial Maximum ($\sim$26 ka) for the Albemarle Embayment. Field localities are shown by yellow dots on the inset map. Upward-pointing triangles represent marine indicators (lower bound), downward-oriented triangles terrestrial indicators (upper bound), and circles designate tidal facies. Marine Isotope Stages 5e, 5c, 5a and 3 are labeled at 120, 100, 80, and 60-26 ka, respectively. The shaded region covers the time interval examined within the present analysis and the orange rectangles mark the bounds on MIS 5a and MIS 3 sea level based on the plotted data (MIS 5a: 2.5 to 7.5 m; MIS 3: -1 to 1 m). The white star on the inset map marks the location of RSL predictions presented herein.

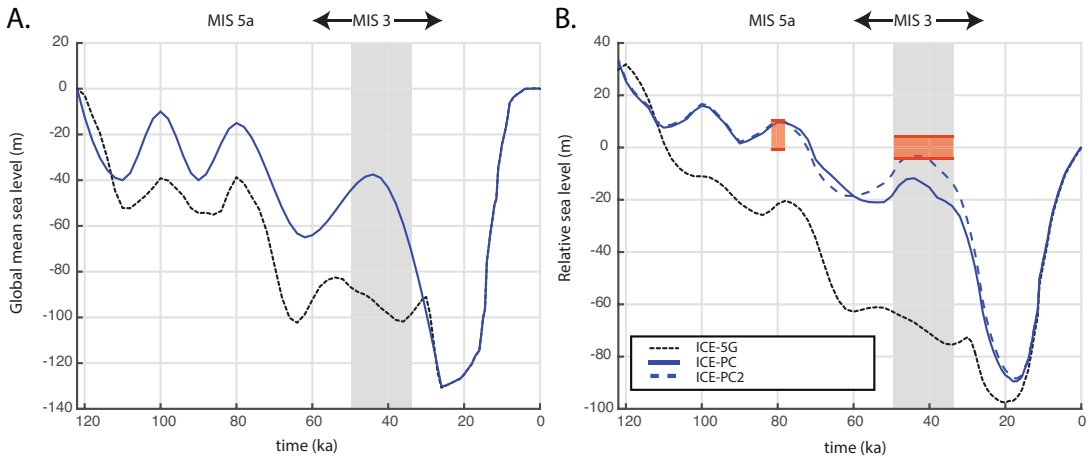

FIGURE 2.2: Global mean sea-level curves and relative sea-level prediction. A. Global mean sea level curve for Version 1.2 of ICE-5G (dotted black line) and the ICEPC (blue line) ice histories. The GMSL curve for the ICEPC2 history is identical to the curve for ICEPC. B. Relative sea level predictions for the reference site in the Albemarle Embayment based on the ICE-5G (dotted black), ICEPC (solid blue) and ICEPC2 (dashed blue; ice-free eastern sector of the Laurentide Ice Sheet from 80 ka to 44 ka) ice histories. Orange rectangles span the observational constraints on peak MIS 5a and 3 sea level including the ± 3 m paleotidal uncertainty (see Figure 1). For MIS 5a, this range is -0.5 m to 10.5 m, and at 44 ka during MIS 3 the range is -4 to 4 m. The gray shaded region spans the MIS 3 time interval examined within the present analysis

2.2.2 MODELS OF GLACIO-ISOSTATIC ADJUSTMENT

Ice sheet growth and melt produces a complex spatio-temporal pattern of sea-level change(Farrell and Clark, 1976). To predict the present elevation of sea-level markers, we perform calculations based on the sea-level theory and pseudo-spectral algorithm described by Kendall et al.(Kendall, Mitrovica and Milne, 2005) with a spherical harmonic truncation at degree and order 256. The calculations include the impact of rotation changes on sea level(Milne and Mitrovica, 1996), evolving shorelines and the migration of grounded, marine-based ice(Johnston, 1993; Milne, Mitrovica and Davis, 1999; Lambeck et al., 2003; Kendall, Mitrovica and Milne, 2005) We report RSL predictions at a representative site within the Albemarle Embayment (white star on inset of Figure 1) for a representative time (44 ka) within the middle of MIS 3 (50-35 ka). This representative site lies within the

latitudinal range of the reported geological sea-level markers used to define the bound on local peak MIS 3 sea level (Figure 1). We have found that RSL highstand predictions for this reference site differ from field locations by less than 0.5 m. We deem simulations acceptable if they satisfy the aforementioned bounds for both MIS 5a and MIS 3 (Figure 2B, orange rectangles).

Our numerical predictions require models for Earth's viscoelastic structure and the history of global ice cover. We begin by adopting an Earth model with upper and lower mantle viscosities of $0.5x10^{21}$ Pa s and 1.5 x 10^{22} Pa s, respectively; this radial profile is consistent with inferences based on globally distributed ice-age data sets(Mitrovica and Forte, 2004) and geological data along the U.S. mid-Atlantic(Potter and Lambeck, 2003; Creveling et al., 2017). Our initial GIA calculation adopts Version 1.2 of the ICE-5G ice history, characterized by a GMSL fall from -87 to -100 m throughout MIS 3(Peltier and Fairbanks, 2006) (Figure 2A; dotted black line); in this calculation, we make the standard assumption that, for any pre-LGM time step, the geometry of global ice cover was identical to the post-LGM ice distribution with the same GMSL value(Raymo et al., 2011). We explore alternatives to the GMSL history, ice geometry and viscosity profile in the discussion below. Using the combination of the ICE-5G model and Earth structure described above, we predict mid-MIS 3 sea level (at 44 ka) at the Albemarle Embayment reference site to be –67 m (Figure 2B; dotted black line), grossly misfitting (by ~70 m) the observational constraints (Figure 1). The misfit is ~25 m for the MIS 5a record (Figure 2B). The level of misfit to the MIS 3 record highlights the enigmatic nature of the sea-level record in Figure 1 and motivates the present study.

Many previous inferences of GMSL during the last glacial phase, particularly MIS 3, reconstruct higher peak sea level (smaller global ice volume) than adopted in the ICE-5G history(Lambeck and Chappell, 2001; Lisiecki and Raymo, 2009; Shakun et al., 2015). To proceed in our analysis, we revise the ICE-5G ice history on the basis of results from two recent GIA analyses. First, following the Pico et al.(Pico et al., 2016) analysis of sedimentary core records from the Bohai Sea, peak GMSL during MIS 3 is placed at -37.5 m at 44 ka. Second, we adopt GMSL values of -15 m and -10 m for MIS 5a

and 5c, respectively; these values are within bounds (5a: -18 m to 0 m, 5c: -20 m to 1 m) derived by Creveling et al.(Creveling et al., 2017) on the basis of globally distributed sea level markers from both periods. The GMSL curve for the revised ice model, ICEPC, is shown in Figure 2A (blue line). The RSL prediction based on this model (Figure 2B, solid blue) maintains the assumption that the pre-LGM global ice geometry is equivalent to the deglacial phase whenever GMSL values are equal. This prediction is consistent with observational constraints for the MIS 5a highstand, but misfits MIS 3 data. Notably, this Earth–ice model pairing predicts a peak RSL of -12 m at 44 ka, well below the observational bounds of -4 to 4 m.

We performed a suite of simulations to explore the sensitivity of our predictions to the adopted ice history. Specifically, we generated 100 synthetic ice histories in which we varied GMSL randomly across the glacial phase but confined GMSL to -37.5 $\pm$ 7 m at 44 ka(Pico et al., 2016), and to -15 m and -10 m, respectively, for MIS 5a and MIS 5c (Figure 3A, blue lines; see Supplementary Material for detailed ice history construction). Using these ice histories, we predicted RSL at the reference site within the Albemarle Embayment using the standard treatment for the pre-LGM ice distribution, i.e., that this distribution matches the post-LGM geometry when the GMSL values are the same (similar to ICEPC). In this case, the predicted RSL ranges from -26.5 to -7.5 m at 44 ka (blue lines, Figure 3B), and thus all 100 simulations predict a peak RSL that falls outside the observational constraint.

2.2.3 Revising the geometry of the Laurentide Ice Sheet during MIS 3

We next explored the impact of changing the geometry of the LIS on the local RSL predictions at the Albemarle Embayment. While few field data constrain the evolution of the LIS prior to the LGM(Clark et al., 1993; Dyke et al., 2002; Kleman et al., 2010), a recent field-based study by Dalton et al.(Dalton et al., 2016) suggests that large portions of eastern Laurentia were ice-free during MIS 3 (Figure 4). This conclusion implies limited or no ice growth from MIS 5a to MIS 3 within

large areas of the sector of the LIS closest to the Albemarle Embayment. To investigate the effect of this revised ice geometry on RSL predictions, we constructed an ice model, ICEPC2, with a GMSL history identical to that shown by the blue line in Figure 2A, but that was distinguished from the ICEPC history in the following ways: (1) the eastern sector of the LIS is ice-free from 80 to 44 ka, consistent with the conclusions of Dalton et al.34. 2016); and (2) the ice removed in this exercise, equivalent to 6.8 m of GMSL, is distributed uniformly over the western sector of the LIS, and the Cordilleran and Fennoscandian Ice Sheets. The latter resulted in an increase in ice thickness of ~170 m in each region (Figure 4; See Methods for details on ice model construction). The post-LGM ice geometry remains identical to the ICE-5G and ICEPC models, and thus we no longer assumed that global ice geometry prior and subsequent to the LGM were identical whenever the GMSL values match. The simulation, based on this revised ICEPC2 ice model and the viscoelastic Earth model discussed above, predicts a RSL of -3 m at 44 ka, consistent with the sea-level record at the Albemarle Embayment (Figure 2B).

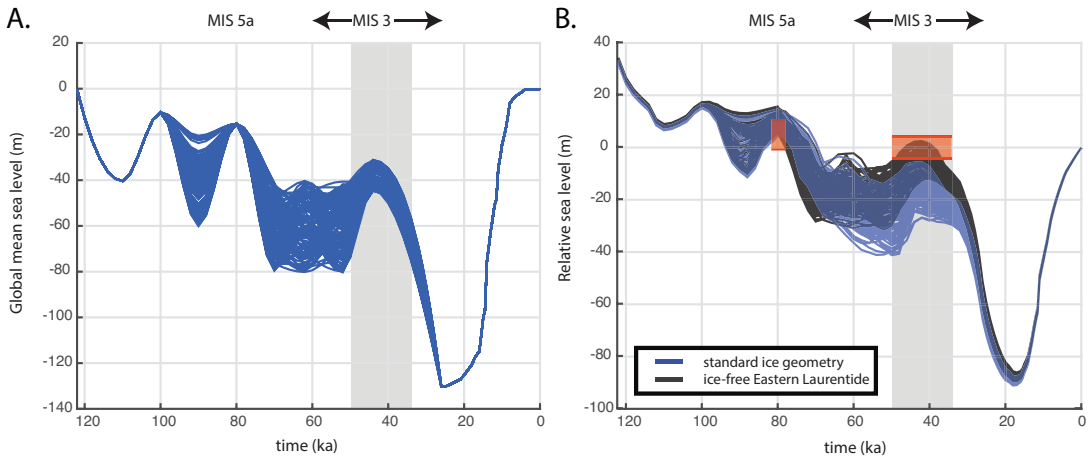

FIGURE 2.3: The effect of varying ice history on relative sea-level prediction. A. Global mean sea level curves for 100 randomly generated ice histories that pass through -37.5 $\pm$ 7 m at 44 ka (blue lines), -15 m at MIS 5a, and -10 m at MIS 5c. B. Relative sea level predictions for the Albemarle Embayment reference site based on the ice histories shown in frame A. The results of calculations that assume identical pre-LGM and post-LGM ice geometries when global mean sea level values are the same are plotted as blue lines; the calculations that assume an ice-free eastern Laurentide from 80 ka to 44 ka are shown by black lines. Orange rectangles span the adopted observational constraints on peak MIS 5a and MIS 3 sea level including the $\pm$3 m paleotidal uncertainty. The gray shaded region spans the MIS 3 time interval examined within the present analysis

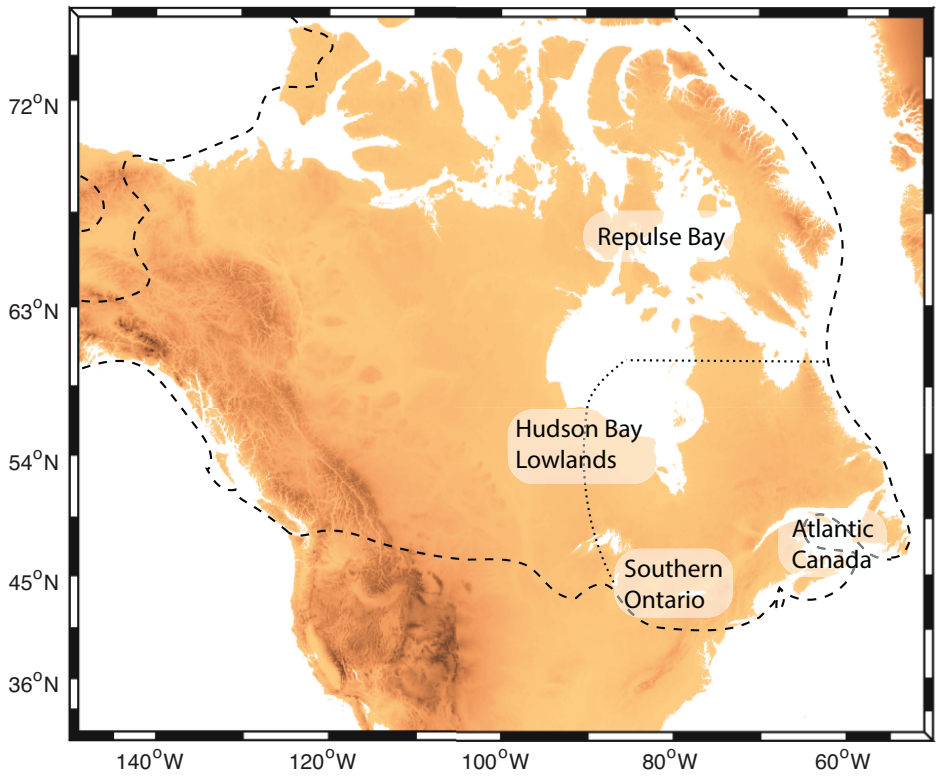

FIGURE 2.4: Geographic map showing the extent of the Laurentide Ice Sheet at LGM in the ICE-5G model (dashed black line) and the eastern extent of the ice model ICEPC2 from MIS 5a to MIS 3 (dotted black line). Repulse Bay, Hudson Bay Lowlands, Southern Ontario, and Atlantic Canada are all sites that have been reported as deglaciated at MIS 3 in Dalton et al. (2016).

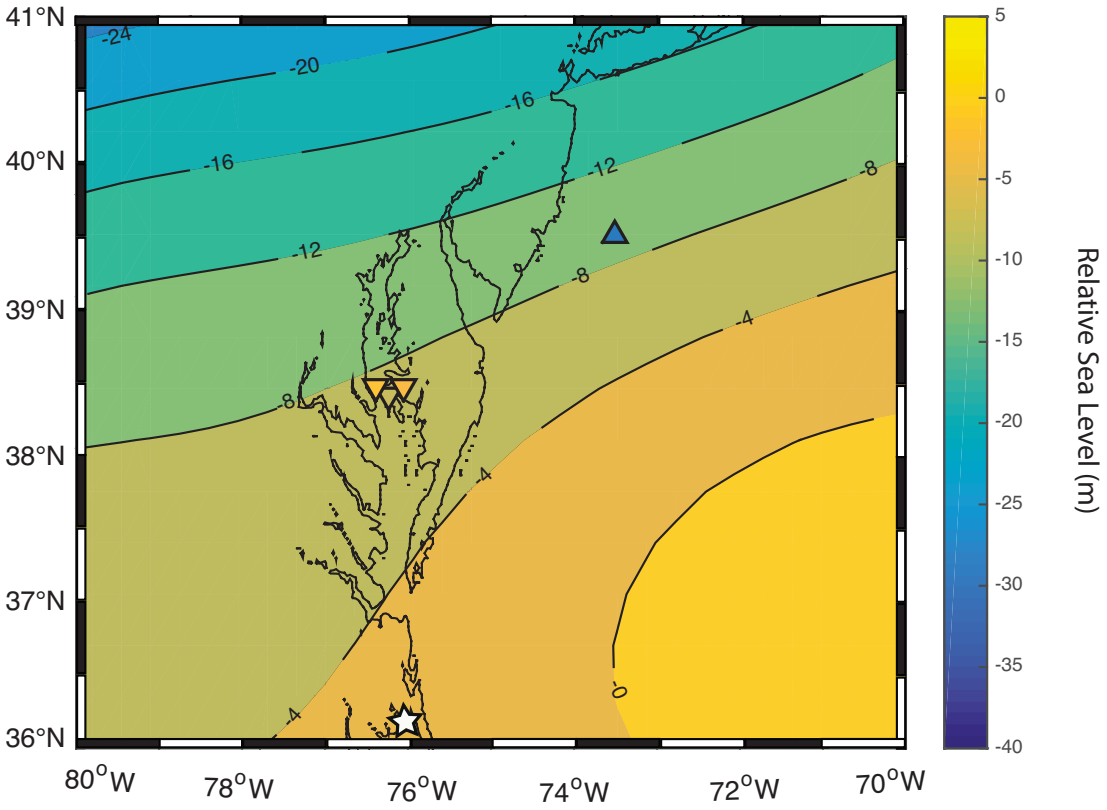

FIGURE 2.5: Map of predicted relative sea-level based on ice history ICEPC2 at 44 ka. The Albemarle Embayment site is shown by the white star. Elevation of sea level data are plotted as triangles at the Chesapeake Bay (-7.6 m, -1.7 m, -3.4 m) and the Hudson shelf (-30 m), where the color represents the elevation shown by the colorbar. Upper bounds on sea level are represented by downward pointing triangles, while lower bounds are plotted as upward pointing triangles.

2.3 Discussion

What physics underlies this improved fit to the MIS 3 sea level record in the mid-Atlantic coastal region? Crustal deformation and the direct gravitational effect of the surface load dominate sea-level predictions in this location and yield a RSL history that departs significantly from GMSL. To assess the relative contribution of each process, we decomposed the RSL prediction based on ice models ICEPC and ICEPC2 into these two components (Supplementary Figure 1). Ice model ICEPC2 is

defined by a reduced eastern sector of the LIS, and therefore a smaller surface load compared with the ICEPC model. This smaller ice load results in a reduced direct gravitational effect (expressed as a sea-level fall) and a reduced crustal deformation (a smaller upward deflection of the Earth's surface expressed as sea-level rise), compared to the ICEPC prediction. The latter effect dominates, resulting in a net sea-level rise compared to the ICEPC ice distribution and the fit evident in Figure 2B (dashed blue line). We explore the sensitivity of the RSL decomposition to variations in Earth structure in Supplementary Note 4, where we adopt the ICEPC2 ice history and consider a range of lithospheric thicknesses, and upper and lower mantle viscosities (see Supplementary Figure 2).

We performed several additional sensitivity tests related to the ICEPC2 simulation. For example, we once again randomly generated 100 simulations, and constructed ice histories with the GMSL curves shown in Figure 3A, but now assumed (as in ICEPC2) that the eastern sector of the LIS was ice-free from 80 to 44 ka. In these simulations, the predicted peak RSL at the reference site in the Albemarle Embayment ranged from -11 m to -1 m at 44 ka (black lines, Figure 3B). Nearly half (46 of 100) of these simulations yielded predictions consistent with observational constraints on the MIS 3 highstand. We also constructed ice histories in which we varied peak GMSL during MIS 5a and MIS 5c in the range of -16-0 m and -20-0 m, respectively, within bounds derived by Creveling et al.(Creveling et al., 2017), in order to test the sensitivity of the RSL predictions to this level of uncertainty. This suite of simulations perturbed the peak RSL prediction during MIS 3 by less than 0.7 m, and thus our conclusions in regard to ice cover during MIS 3 are insensitive to the GMSL values adopted for MIS 5a and 5c.

We also performed tests in which the geometry of ice removed from the eastern sector of the LIS was varied by shifting the upper latitudinal limit of the ice-free region, and by considering scenarios in which various regions within the eastern sector of the LIS remained glaciated (see Supplementary Figure 3). We conclude that increasing the ice in the eastern sector by 20% of the ice volume removed to construct the ice history ICEPC2 (or 1.5 m GMSL) from 80-44 ka, and shifting the distribution of

this ice within the sector, can lower RSL predictions by up to 3 m (Supplementary Table 2). Finally, to assess the sensitivity of the predictions to the adopted Earth model, we ran simulations in which the lower mantle viscosity was both increased and decreased by 5 x 10^{21} Pa s. The predicted RSL at 44 ka was perturbed by a maximum of 3 m at the Albemarle Embayment (Supplementary Figure 4). We also ran simulations with an additional six Earth models to assess the sensitivity of RSL predictions to lithospheric thickness and upper mantle viscosity (details in Supplementary Note 4; Supplementary Figure 5). ¬ Finally, additional constraints exist on RSL during MIS 3 at other sites along the U.S. East Coast. For example, a marine indicator at -30 m on the Hudson Shelf of age ∼45 ka provides a lower bound on sea level at this site(Sheridan et al., 2000), while terrestrial facies in the Chesapeake Bay indicate that local sea level was below approximately -7.6 m sometime during the interval 50-35 ka(Dejong et al., 2015). RSL predictions based on ice model ICEPC2 agree well with both these constraints (Figure 5).

Sea-level records from the mid-Atlantic coastal plain show that MIS 3 sea level reached present-day levels. These observations have been considered enigmatic given that previously published GIA models predict relative sea level in this region to be more than 60 m below present level at MIS 3(Doar and Kendall, 2014). However, we have shown that GIA models can be reconciled with the observational record from the Albemarle Embayment under two conditions: (1) global mean sea level during MIS 3 reached ∼ -40 m, consistent with a recent analysis of sediment core records from the Bohai Sea11. Pico et al., 2016) and within the bounds of several earlier studies(Shackleton, 2000; Cutler et al., 2003; Dannenmann et al., 2003; Pahnke et al., 2003; Huybers and Wunsch, 2004; Lisiecki and Raymo, 2005; Simms et al., 2009); and (2) the eastern sector of the Laurentide Ice Sheet remained largely ice-free over an extended period from MIS 5a through mid-MIS 3, consistent with recent field-based evidence(Dalton et al., 2016). Rigorous tests of our conclusions regarding ice extent will require improved chronological control on geological indicators of Laurentide Ice Sheet extent, as presented in, for example, Clark et al.(Clark et al., 1993), Curry et al.(Curry, 1996), Colgan

et al.(Colgan, Vanderlip and Braunschneider, 2015), and Dalton et al.(Dalton et al., 2016). Our inference, if robust, implies that the Laurentide Ice Sheet rapidly advanced during the ∼15 ky from mid-MIS 3 to the Last Glacial Maximum. Moreover, our study highlights the potential of mid-field sea-level records to constrain ice-load locations over glacial intervals where geologic evidence of ice cover is poorly preserved.

2.4 Acknowledgements

TP was supported by NSF-GRFP and Harvard University. JRC acknowledges a donation from the G. Unger Vetlesen Foundation to Oregon State University. JXM was funded by Harvard University. We thank Pippa Whitehouse and two anonymous reviewers for their constructive comments on an earlier version of this manuscript.

TP conducted simulations and analyzed results. JRC, JXM, and TP conceived the project. All authors contributed extensively to this work. TP and JXM wrote the manuscript.

The authors declare no competing financial interests.

2.5 References

Brain, M. J., Kemp, A. C., Horton, B. P., Culver, S. J., Parnell, A. C. and Cahill, N. (2015) 'Quantifying the contribution of sediment compaction to late Holocene salt-marsh sea-level reconstructions, North Carolina, USA', Quaternary Research (United States). University of Washington, 83(1), pp. 41–51. doi: 10.1016/j.yqres.2014.08.003.

Chappell, J., Ota, Y. and Berryman, K. (1996) 'Late quaternary coseismic uplift history of Huon Peninsula, Papua New Guinea', Quaternary Science Reviews, 15(1), pp. 7–22. doi: 10.1016/0277-3791(95)00062-3.

Clark, P. U., Clague, J. J., Curry, B. B., Dreimanis, A., Hicock, S. R., Miller, G. H., MBerger, G. W., Eyles, N., Lamothe, M., Miller, B. B., Mott, R. J., Oldale, R. N., Stea, R. R., Szabo, J. P., Thor-

leifson, L. H. and Vincent, J. S. (1993) 'Initiation and development of the Laurentide and Cordillean Ice Sheets following the Last Interglaciation', Quat. Sci. Reviews, 12, pp. 79–114.

Colgan, P. M., Vanderlip, C. A. and Braunschneider, K. N. (2015) 'Athens Subepisode (Wisconsin Episode) non-glacial and older glacial sediments in the subsurface of southwestern Michigan , USA', Quaternary Research. University of Washington, 84, pp. 382–397. doi: 10.1016/j.yqres.2015.09.006.

Creveling, J. R., Mitrovica, J. X., Clark, P. U., Waelbroeck, C. and Pico, T. (2017) 'Predicted bounds on peak global mean sea level during marine isotope stages 5a and 5c', Quaternary Science Reviews.

Cronin, T. M., Szabo, B. J., Ager, T. A., Hazel, J. E. and Owens, J. P. (1981) 'Quaternary climates and sea levels of the u.s. Atlantic coastal plain.', Science (New York, N.Y.), 211(4479), pp. 233–40. doi: 10.1126/science.211.4479.233.

Culver, S. J., Farrell, K. M., Mallinson, D. J., Willard, D. A., Horton, B. P., Riggs, S. R., Thieler, E. R., Wehmiller, J. F., Parham, P., Snyder, S. W. and Hillier, C. (2011) 'Micropaleontologic record of Quaternary paleoenvironments in the Central Albemarle Embayment, North Carolina, U.S.A.', Palaeogeography, Palaeoclimatology, Palaeoecology, 305(1–4), pp. 227–249. doi: 10.1016/j.palaeo.2011.03.004.

Curry, B. B. (1996) 'Absence of Glaciation in Illinois during Marine Isotope Stages 3 through 5 Absence of Glaciation in Illinois during Marine', (September 2016). doi: 10.1006/qres.1996.0040.

Cutler, K. B., Edwards, R. L., Taylor, F. W., Cheng, H., Adkins, J., Gallup, C. D., Cutler, P. M., Burr, G. S. and Bloom, a. L. (2003) 'Rapid sea-level fall and deep-ocean temperature change since the last interglacial period', Earth and Planetary Science Letters, 206(3–4), pp. 253–271. doi: 10.1016/S0012-821X(02)01107-X.

Dalton, A. S., Finkelstein, S. A., Barnett, P. J. and Forman, S. L. (2016) 'Constraining the Late Pleistocene history of the Laurentide Ice Sheet by dating the Missinaibi Formation, Hudson Bay Lowlands, Canada', Quaternary Science Reviews. Elsevier Ltd, 146, pp. 288–299. doi: 10.1016/j.quascirev.2016.06.015.

Dannenmann, S., Linsley, B. K., Oppo, D. W., Rosenthal, Y. and Beaufort, L. (2003) 'East Asian

monsoon forcing of suborbital variability in the Sulu Sea during Marine Isotope Stage 3: Link to Northern Hemisphere climate', Geochemistry Geophysics Geosystems, 4(1), p. 1001 2002GC000390. doi: 10.1029/2002GC000390.

Dejong, B. D., Bierman, P. R., Newell, W., Rittenour, T., Mahan, S., Balco, G. and Rood, D. (2015) 'Pleistocene relative sea levels in the Chesapeake Bay region and their implications for the next century', GSA Today, 25(8), pp. 4–10. doi: 10.1130/GSATG223A.1.4.

Doar, W. R. and Kendall, C. G. S. C. (2014) 'An analysis and comparison of observed Pleistocene South Carolina (USA) shoreline elevations with predicted elevations derived from Marine Oxygen Isotope Stages', Quaternary Research (United States). University of Washington, 82(1), pp. 164–174. doi: 10.1016/j.yqres.2014.04.005.

Dyke, A. S., Andrews, J. T., Clark, P. U., England, J. H., Miller, G. H., Shaw, J. and Veillette, J. . (2002) 'The Laurentide and Innuitian Ice Sheet during the Last Glacial Maximum The Laurentide and Innuitian ice sheets during the Last Glacial Maximum', Quat. Sci. Reviews, 21, pp. 9–31. doi: 10.1016/S0277-3791(01)00095-6.

Farrell, W. E. and Clark, J. A. (1976) 'On Postglacial Sea Level', Geophysical Journal of the Royal Astronomical Society, 46(3), pp. 647–667. doi: 10.1111/j.1365-246X.1976.tb01252.x.

Hill, D. F., Griffiths, S. D., Peltier, W. R., Horton, B. P. and T??rnqvist, T. E. (2011) 'High-resolution numerical modeling of tides in the western Atlantic, Gulf of Mexico, and Caribbean Sea during the Holocene', Journal of Geophysical Research: Oceans, 116(10), pp. 1–16. doi: 10.1029/2010JC006896.

Huybers, P. and Wunsch, C. (2004) 'A depth-derived Pleistocene age model: Uncertainty estimates, sedimentation variability, and nonlinear climate change', Paleoceanography, 19(PA1028). doi: 10.1029/2002PA000857.

Johnston, P. (1993) 'The effect of spatially non-uniform water loads on prediction of sea-level change', Geophysical Journal International, 114(3), pp. 615–634. Available at: http://onlinelibrary.wiley.com/doi/10.1111/j.136
246X.1993.tb06992.x/abstract.

Kendall, R. A., Mitrovica, J. X. and Milne, G. A. (2005) 'On post-glacial sea level - II. Numerical formulation and comparative results on spherically symmetric models', Geophysical Journal International, 161(3), pp. 679–706. doi: 10.1111/j.1365-246X.2005.02553.x.

Kleman, J., Jansson, K., De Angelis, H., Stroeven, A. P., H??ttestrand, C., Alm, G. and Glasser, N. (2010) 'North American Ice Sheet build-up during the last glacial cycle, 115-21 kyr', Quaternary Science Reviews. Elsevier Ltd, 29(17–18), pp. 2036–2051. doi: 10.1016/j.quascirev.2010.04.021. Lambeck, K. and Chappell, J. (2001) 'Sea level change through the last glacial cycle.', Science (New York, N.Y.), 292(5517), pp. 679–686. doi: 10.1126/science.1059549.

Lambeck, K., Purcell, A., Johnston, P., Nakada, M. and Yokoyama, Y. (2003) 'Water-load definition in the glacio-hydro-isostatic sea-level equation', Quaternary Science Reviews, 22(2–4), pp. 309–318. doi: 10.1016/S0277-3791(02)00142-7.

Lisiecki, L. E. and Raymo, M. E. (2005) 'A Pliocene-Pleistocene stack of 57 globally distributed benthic δ18O records', Paleoceanography, 20(1), pp. 1–17. doi: 10.1029/2004PA001071.

Lisiecki, L. E. and Raymo, M. E. (2009) 'Diachronous benthic□??18O responses during late Pleistocene terminations', Paleoceanography, 24(3), pp. 1–14. doi: 10.1029/2009PA001732.

Mallinson, D., Burdette, K., Mahan, S. and Brook, G. (2008) 'Optically stimulated luminescence age controls on late Pleistocene and Holocene coastal lithosomes, North Carolina, USA', Quaternary Research, 69(1), pp. 97–109. doi: 10.1016/j.yqres.2007.10.002.

Milne, G. a. and Mitrovica, J. X. (1996) 'Postglacial sea-level change on a rotating Earth: first results from a gravitationally self-consistent sea-level equation', Geophysical Journal International, 126(3), pp. F13–F20. doi: 10.1111/j.1365-246X.1996.tb04691.x.

Milne, G. A., Mitrovica, J. X. and Davis, J. L. (1999) 'Near-field hydro-isostasy: the implementation of a revised sea-level equation', Geophysical Journal International, 139, pp. 464–482. doi: 10.1046/j.1365-246x.1999.00971.x.

Mitrovica, J. X. and Forte, A. M. (2004) 'A new inference of mantle viscosity based upon joint

inversion of convection and glacial isostatic adjustment data', Earth and Planetary Science Letters, 225, pp. 177–189. doi: 10.1016/j.epsl.2004.06.005.

Mitrovica, J. X. and Milne, G. a. (2002) 'On the origin of late Holocene sea-level highstands within equatorial ocean basins', Quaternary Science Reviews, 21(20–22), pp. 2179–2190. doi: 10.1016/S0277-3791(02)00080-X.

Mixon, R. ., Szabo, B. J. and Owens, J. P. (1982) 'Uranium-Series Dating of Mollusks and Corals , arid Age of Pleistocene Deposits Chesapeake Bay Area , Virginia and Maryland Uranium-Series Dating of Mollusks and Corals , and Age of Pleistocene Deposits , Chesapeake Bay Area , Virginia and Maryland', Geological Survey Professional Paper 1067-E. Surface and shallow subsurface geologic studies in the emerged coastal plain of the Middle Atlantic States), United States Government Printing Office, Washington.

Pahnke, K., Zahn, R., Elderfield, H. and Schulz, M. (2003) '340,000-Year Centennial-Scale Marine Record of Southern Hemisphere Climatic Oscillation', Science, 16(1), pp. 10-1-10–8. doi: 10.1029/2001GB001417.

Parham, P. R., Riggs, S. R., Culver, S. J., Mallinson, D. J., Jack Rink, W. and Burdette, K. (2013) 'Quaternary coastal lithofacies, sequence development and stratigraphy in a passive margin setting, North Carolina and Virginia, USA', Sedimentology, 60(2), pp. 503–547. doi: 10.1111/j.1365-3091.2012.01349.x.

Parham, P. R., Riggs, S. R., Culver, S. J., Mallinson, D. J. and Wehmiller, J. F. (2007) 'Quaternary depositional patterns and sea-level fluctuations, northeastern North Carolina', Quaternary Research, 67(1), pp. 83–99. doi: 10.1016/j.yqres.2006.07.003.

Peltier, W. R. and Fairbanks, R. G. (2006) 'Global glacial ice volume and Last Glacial Maximum duration from an extended Barbados sea level record', Quaternary Science Reviews, 25, pp. 3322–3337. doi: 10.1016/j.quascirev.2006.04.010.

Pico, T., Mitrovica, J. X., Ferrier, K. L. and Braun, J. (2016) 'Global ice volume during MIS 3 inferred from a sea-level analysis of sedimentary core records in the Yellow River Delta', Quaternary

Science Reviews. Elsevier Ltd, 152, pp. 72–79. doi: 10.1016/j.quascirev.2016.09.012.

Van De Plassche, O., Wright, A. J., Horton, B. P., Engelhart, S. E., Kemp, A. C., Mallinson, D. and Kopp, R. E. (2014) 'Estimating tectonic uplift of the Cape Fear Arch (south-eastern United States) using reconstructions of Holocene relative sea level', Journal of Quaternary Science, 29(8), pp. 749–759. doi: 10.1002/jqs.2746.

Potter, E. K. and Lambeck, K. (2003) 'Reconciliation of sea-level observations in the Western North Atlantic during the last glacial cycle', Earth and Planetary Science Letters, 217(1–2), pp. 171–181. doi: 10.1016/S0012-821X(03)00587-9.

Raymo, M. E., Mitrovica, J. X., O/'Leary, M. J., DeConto, R. M. and Hearty, P. J. (2011) 'Departures from eustasy in Pliocene sea-level records', Nature Geosci. Nature Publishing Group, 4(5), pp. 328–332. doi: http://www.nature.com/ngeo/journal/v4/n5/abs/ngeo1118.htmlsupplementary-information. Shackleton, N. J. (2000) 'The 100,000-Year Ice-Age Cycle Identified and Found to Lag Temperature, Carbon Dioxide, and Orbital Eccentricity', Science, 289(5486), pp. 1897–1902. doi: 10.1126/science.289.5486.1897.

Shakun, J. D., Lea, D. W., Lisiecki, L. E. and Raymo, M. E. (2015) 'An 800-kyr record of global surface ocean delta18O and implications for ice volume-temperature coupling', Earth and Planetary Science Letters. Elsevier B.V., 426, pp. 58–68. doi: 10.1016/j.epsl.2015.05.042.

Sheridan, R. E., Ashley, G. M., Miller, K. G., Waldner, J. S., Hall, D. W. and Uptegrove, J. (2000) 'Offshore-onshore correlation of upper Pleistocene strata , New Jersey Coastal Plain to continental shelf and slope', 134, pp. 197–207.

Siddall, M., Rohling, E. J., Thompson, W. G. and Waelbroeck, C. (2008) 'Marine Isotope Stage 3 sea level fluctuations: data synthesis and new outlook', Hemisphere, 46(2007), pp. 1–29. doi: 10.1029/2007RG000226.1.

Simms, A. R., DeWitt, R., Rodriguez, A. B., Lambeck, K. and Anderson, J. B. (2009) 'Revisiting marine isotope stage 3 and 5a (MIS3-5a) sea levels within the northwestern Gulf of Mexico', Global

and Planetary Change. Elsevier B.V., 66(1–2), pp. 100–111. doi: 10.1016/j.gloplacha.2008.03.014.

Waelbroeck, C., Labeyrie, L., Michel, E., Duplessy, J. C., McManus, J. F., Lambeck, K., Balbon, E. and Labracherie, M. (2002) 'Sea-level and deep water temperature changes derived from benthic foraminifera isotopic records', Quaternary Science Reviews, 21(1–3), pp. 295–305. doi: 10.1016/S0277-3791(01)00101-9.

Wehmiller, J. F., Edwards, R. L. and Martin-McNaughton, J. (2004) 'Uranium-series coral ages from the US Atlantic Coastal Plain – the "' 80 ka problem '" revisited', Quaternary International, 120, pp. 3–14.

2.6 Methods

2.6.1 Ice history construction

We created 100 ice models that are distinguished from Version 1.2 of ICE-5G (Peltier & Fairbanks, 2006) by their GMSL history prior to the Last Glacial Maximum. These ice histories randomly sample GMSL values under the following constraints: At LIG, 122 ka, GMSL = 0; at 110 ka, MIS 5 d, GMSL = -40 m; at MIS 5c, GMSL = -10 m; at MIS 5a, GMSL = -15 m; during MIS 3 prior to 44 ka, GMSL varies in the range -40 m to -80 m; at 44 ka, the GMSL value is pinned within the range -37.5 $\pm$ 7m (Figure 3A). We also impose the constraint that sea level must fall between 44 ka and LGM. We produce two sets of 100 ice models from these GMSL curves. The first set is constructed by assuming that ice geometry in the pre-LGM period is identical to the time in the post-LGM period with the same GMSL value. The second set assumes that a large portion of the eastern sector of the LIS is ice-free from 80 ka to 44 ka (see Figure 4). In the latter case, the ice volume removed from the eastern sector of the LIS (equivalent GMSL of 6.8 m) is distributed over the LGM extent of the western sector of the LIS, the Cordilleran Ice Sheet, and over Fennoscandia, resulting in an increase in ice thickness of 170 m in these regions.

We note that while RSL predictions at the Albemarle Embayment are sensitive to ice geometry of the eastern LIS, these predictions will be relatively insensitive to the geographic distribution of ice cover in regions in the far-field of the mid-Atlantic U.S. East Coast. As an example, we performed a simple test in which the ice removed from the eastern sector of LIS to construct the ICEPC2 model was distributed uniformly over Fennoscandia and Antarctica (rather than over the western sector of the LIS) and found that the predicted sea level high stand at our test site at 44 ka was only perturbed by 0.6 m

3

Refining the Laurentide Ice Sheet at Marine Isotope Stage 3: A data-based approach combining glacial isostatic simulations with a dynamic ice model

Naming nature is the special business of science. Theories, models, and descriptions are elaborated names. In these acts of naming the scientists simultaneously constructs and contains nature.
–Evelyn Fox Keller

A version of this chapter was published with Leah Birch, Jamie Weisenberg, and Jerry X. Mitrovica, in *Quaternary Science Reviews*, vol. 195, p. 171-179, 2018.

3.1 Introduction

During the last glacial cycle, ice volumes fluctuated considerably leading into the Last Glacial Maximum (LGM, 26 ka; Cutler et al. 2003; Stokes et al. 2012; Lambeck & Chappell 2001). Yet determining total ice volumes over much of the growth phase is difficult because sea-level rise during the last deglaciation destroyed or submerged the majority of ancient coastlines. The Laurentide Ice Sheet contained the largest excess ice volume at the LGM, expanding over most of Canada and large swaths of the northern United States (Clark & Mix 2002). Current understanding of the space-time geometry of the Laurentide Ice Sheet build-up is limited by the sparsity of relevant observables that were preserved after the ice sheet reached its maximum extent and most prior ice margin records were erased. Calibration of numerical models aimed at simulating North American glaciation is challenged by this lack of geological constraints (Stokes 2017). In addition, uncertainties in paleoclimate conditions make it difficult to assign climatic parameters to force these ice sheet models.

A glacial isostatic adjustment (GIA) analysis of anomalously high sea-level markers along the U.S. mid-Atlantic dated to 50-35 ka suggests a late and rapid eastern Laurentide glaciation (Pico et al. 2017), and this is supported by increasingly robust evidence that the Hudson Bay Lowlands were ice-free during this same interval (Dalton et al., 2016). In this study we compare sea-level constraints associated with non-glacial deposits in eastern Canada dated to mid-Marine Isotope Stage (MIS) 3 to gravitationally self-consistent GIA sea-level predictions in order to assess the model of a reduced Laurentide Ice Sheet cover during this time interval. We reconstruct paleotopography using these GIA simulations, which we adopt to prescribe the initial basal topography for a simple numerical ice model. We explore the extent to which assumptions about Earth structure and ice cover during MIS 3 influence predicted ice-growth rates in the final stages of the glaciation phase. The ice model adopts a high-resolution topography starting at mid-MIS 3, and predicts rapid ice growth rates of 3.6 x 10^{12} m^3/yr, using a maximum mass balance of 0.4 m/yr, which is consistent with attaining LGM

ice volumes by 26 ka.

3.2 Background

3.2.1 Previous ice modeling studies

The evolution of the Laurentide Ice Sheet in the period prior to the LGM is characterized by a sparse record with poor geochronological control (Clark et al. 1993; Kleman et al. 2010). Most dynamic ice models have not been able to capture the rapid growth of ice sheets suggested by global sea-level records (i.e. at inception or MIS 5d; Charbit et al. 2013). The lack of ice margin or ice thickness constraints poses an additional limitation because these represent important boundary conditions for general circulation model (GCM) simulations (Manabe & Broccoli 1985; Roe 2001; Beghin et al. 2014; Charbit et al. 2013; Löfverström et al. 2014; Löfverström et al. 2015). Numerical models for ice evolution are sensitive to topography as well as initial ice conditions, and these are key to determining paleoclimate conditions, as it is well established that the presence of ice sheets impacts atmospheric circulation patterns (Manabe & Broccoli 1985; Roe 2001; Beghin et al. 2014; Charbit et al. 2013; Löfverström et al. 2014; Löfverström et al. 2015).

Despite these limitations, various studies have modeled the evolution of Laurentide Ice Sheet over the glaciation phase. In particular Kleman et al. (2002; 2013) forced a numerical ice sheet model with a spliced GRIP-Vostok temperature record, and inferred the climatological conditions required to predict ice margins consistent with relative ages of glacial landforms, including relict glacial lineations. Stokes et al. (2012) constructed a dynamic thermo-mechanical ice sheet model calibrated to deglacial chronologies, including records of sea-level and glacial isostatic uplift, and ran a simulation over the entire glacial cycle, comparing to geological data when available. The study found that the ice sheet became warm-based during MIS 4 after it grew substantially, and the model was able to capture rapid ice growth during inception, at MIS 5e. These simulations, which incorporated

glaciological constraints, predicted an extensive Laurentide Ice Sheet by MIS 3, with ice volumes comparable to (∼75

Although the MIS 3 glaciological record is sparse, numerical ice simulations commonly calibrate predictions using δ18O records from ocean sediment or ice cores (e.g. Charbit et al. 2007). The Laurentide Ice Sheet is assumed to have largely grown to LGM extent by ∼40 ka because the majority of oxygen isotope records show values similar to those at LGM by the middle of the glaciation phase during MIS 4 or MIS 3 (i.e., Lisiecki & Raymo 2005; Shakun et al. 2015; Waelbroeck et al. 2002). However, while benthic δ^{18} O records are a proxy for global ice volumes, they are characterized by large uncertainties associated with local ocean temperatures or salinity on the order of tens of meters of global mean sea level (Waelbroeck et al. 2002).

3.2.2 Empirical evidence

Evidence for Laurentide Ice sheet configuration prior to the LGM comprises glacial features and deposits, including till, moraines, glacial striation, and eskers, and non-glacial deposits such as marine, fluvial, or lacustrine successions (Stokes et al. 2015). In addition, glacial flow lines can be determined by analyzing satellite imagery for glacial lineations (Kleman et al. 2010). However these glacial landforms only allow relative age assignments. Ocean sediment cores record meltwater pulses indicating whether ice advanced into certain river drainage basins (Hill et al. 2006; Wickert et al. 2013). Unfortunately, MIS 3 records are typically characterized by poor chronological control given that 40-50 ka reaches the limit of radiocarbon dating. The remaining geological observations are characterized by sparse dates using methods such as optical stimulated luminescence (OSL) or cosmogenic nuclides (Dalton et al. 2016; Briner et al. 2006).

In the Atlantic region of Canada, Dredge & Thorleifson (1987) reported non-glacial deposits containing mastodon remains, peat, and marine shells during the last glacial phase. Remillard et al. (2017) dated these deposits to MIS 3, and these authors concluded that the Magdalen Islands were

deglaciated from 60-40 ka. Kleman et al. (2010) reported an Atlantic swarm (a group of lineations) that shows restricted extent, but in the absence of absolute dates they concluded these might date to MIS 5. In the St. Lawrence Lowlands there is also evidence of a restricted ice sheet during MIS 3. Clark et al. (1993) described the St. Pierre non-glacial fluvial unit, which is dated to 60-45 ka, and Dionne & Occhietti (1996) dated detrital fragments of unidentified marine shells in the eastern part of this region to 35-31 ^{14}C ka, concluding that the Laurentide Ice Sheet retreated to the southern edge of the Canadian shield at this time. In the central St. Lawrence Lowlands, Parent et al. (2015) dated plant fragments within an alluvial unit to 31.27 $\pm$ 0.20 ^{14}C ka and 33.25 $\pm$0.24 ^{14}C ka (1σ), and reported a marine unit directly overlying these terrestrial deposits, suggesting a later time of marine incursion in the west.

In southern Ontario, organic deposits were dated to 55-40 ^{14}C ka, and Bajc et al. (2015) noted that a vast region of southern Ontario might have been ice free during MIS 3 (Bajc et al. 2015; Mulligan & Bajc 2017). In the continental U.S. both glacial and non-glacial records exist, including the Roxana silt, a glacial loess with basal sediments estimated to have an age of 55 ka (Curry 1996; Clark et al. 1993). Hill et al. (2006) observed various meltwater pulses in the Gulf of Mexico from 45-28 ka signaling that the Laurentide Ice Sheet had advanced into the Mississippi drainage basin. Carlson et al. (this issue) dated wood in interbedded lacustrine and glacial till to 39.1$\pm$0.4 cal. ka in central Wisconsin, indicating that this region experienced rapid ice advance that concluded by 30.4$\pm$0.9 cal. ka. Wood et al. (2010) dated pro-glacial lake sediments in central Indiana to 40-30 ^{14}C ka and concluded that the ice margin was close to the site at that time, despite evidence that the lower peninsula of Michigan was ice free from 46-35 cal. ka. Colgan et al. (2015) dated lacustrine deposits in southwestern Michigan, and concluded that lower Michigan was ice-free from 65-29 ^{14}C ka.

Finally, a site of major importance for Laurentide Ice Sheet configuration during MIS 3 is the Hudson Bay Lowlands (HBL). This region lies between the two major ice domes (Keewatin and Quebec) inferred to exist at LGM, and is therefore a critical location for understanding the shape

and volume evolution of the Laurentide Ice Sheet (Kleman et al. 2010; Andrews 1973). Clark et al. (1993) described the non-glacial Missinaibi formation and freshwater silt in the Nelson River formation, dated to 46-30 ka using thermoluminescence dating, and noted that the HBL was possibly ice free from MIS 5a to MIS 3. Recently Dalton et al. (2016) dated these lacustrine and marine deposits, using both radiocarbon and OSL methods, to MIS 5a and mid-MIS 3, demonstrating that the HBL was likely ice-free during MIS 3, and potentially from MIS 5a through MIS 3, since there is no glacial evidence that remains from this time period. In addition, recent GIA modeling of anomalously high elevation sea-level data from the U.S. mid-Atlantic dated to mid-MIS 3 strongly suggested a reduced eastern Laurentide Ice Sheet at mid-MIS 3 and a rapid growth into the LGM (Pico et al., 2017).

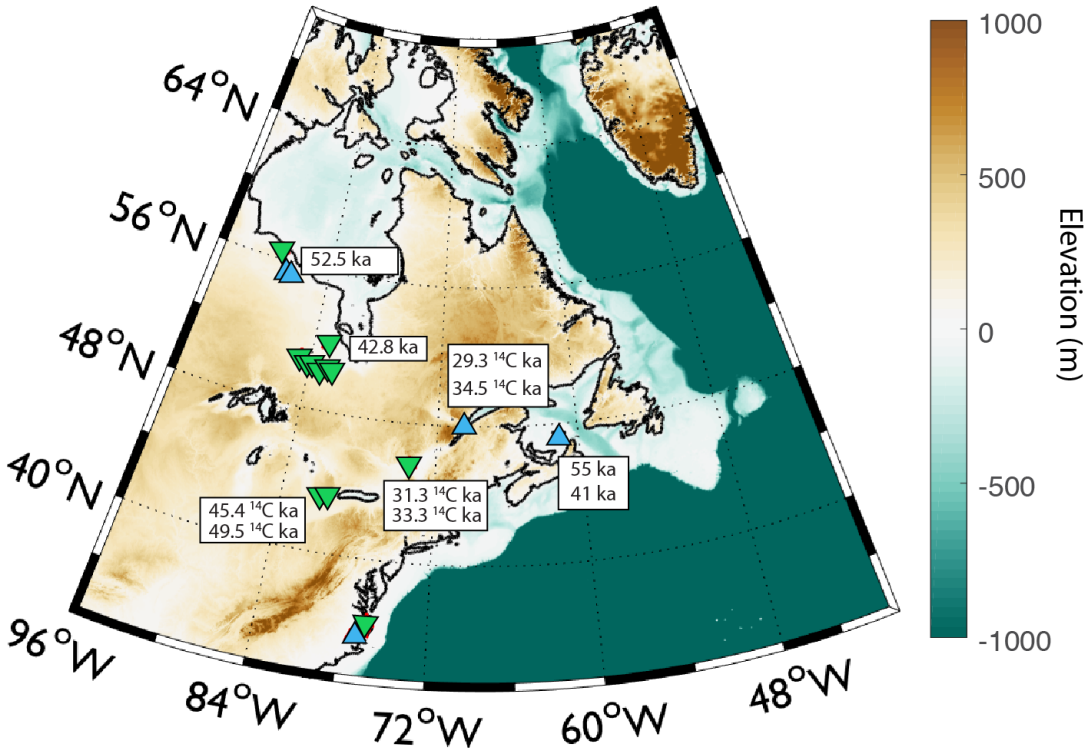

FIGURE 3.1: The location of non-glacial deposits dated to mid-MIS 3 that are discussed in the text. Upward blue triangles denote marine indicators (relative sea-level must be above this elevation) and downward green triangles denote terrestrial indicators (relative sea-level below this elevation).

3.3 METHODS

3.3.1 GIA MODELING

We reconstruct paleotopography by running GIA simulations with a prescribed ice loading history. Our calculations are based on the theory and pseudo-spectral algorithm described by Kendall et al. (2005) with a spherical harmonic truncation at degree and order 256. These calculations include the impact of load-induced Earth rotation changes on sea level (Milne & Mitrovica, 1996), evolv-

ing shorelines and the migration of grounded, marine-based ice (Johnston, 1993; Milne et al., 1999; Lambeck et al., 2003; Kendall et al., 2005). Our predictions require models for Earth's viscoelastic structure and the history of global ice cover. We adopt the viscosity profile VM2, which is designed to be paired with the ICE-5G ice history (Peltier, 2004). We will explore the sensitivity of our results to plausible variations in the Earth model.

3.3.2 Initial ice configurations

Previous work shows that dynamic ice models are sensitive to initial topography. We construct a series of initial ice configurations based on geological constraints (Dalton et al., 2016) and GIA modeling (Pico et al., 2017). Each MIS 3 ice configuration belongs to a distinct ice history spanning the entire glacial cycle (120-0 ka). An ice history spanning the entire glacial phase is necessary when predicting GIA-corrected topography, as crustal deformation will depend on the full prior history of ice loading.

The first model we constructed is based on the ICE-5G ice history (Figure 2A/B; dotted black). In our version of ICE-5G, the ice geometry during the glaciation phase is assumed to be identical to the post-LGM geometry whenever the global mean sea-level values are the same. The remaining model ice histories (ICE-PC2 and ICE-PC3) are modified from ICE-5G to be consistent with results from recent GIA analyses. In particular, following the Pico et al. (2016) analysis of sedimentary core records from the Bohai Sea, peak global mean sea level during MIS 3 is placed at -37.5 m at 44 ka in these model ice histories. Moreover, we also adopt global mean sea-level values of -15 m and -10 m for MIS 5a and 5c, respectively; these values are within bounds (5a: -18 m to 0 m, 5c: -20 m to 1 m) derived by Creveling et al. (2017) on the basis of globally distributed sea level markers from both periods. The global mean sea-level curve for ICE-PC2 and ICE-PC3 is shown in Figure 2A (blue line).

ICE-PC2 is distinguished from our version of ICE-5G in the following ways: (1) the eastern sec-

tor of the Laurentide Ice Sheet is ice-free from 80 to 44 ka; and (2) the ice removed in this exercise, equivalent to 6.8 m of global mean sea level, is distributed uniformly over the western sector of the Laurentide Ice Sheet, and the Cordilleran and Fennoscandian Ice Sheets (Figure 2C). While a uniform ice thickness in the Cordilleran Ice Sheet is unrealistic, altering its volume has minimal impact on sea level predictions in eastern Canada. Finally, in the ice history ICE-PC3 the eastern sector of the Laurentide Ice Sheet is ice-free (as in ICE-PC2) from 80-44 ka except for northern Quebec, which remains glaciated, according to retrodicted patterns of snow accumulation (e.g. Löfverström et al., 2014; See Appendix Figure 1).

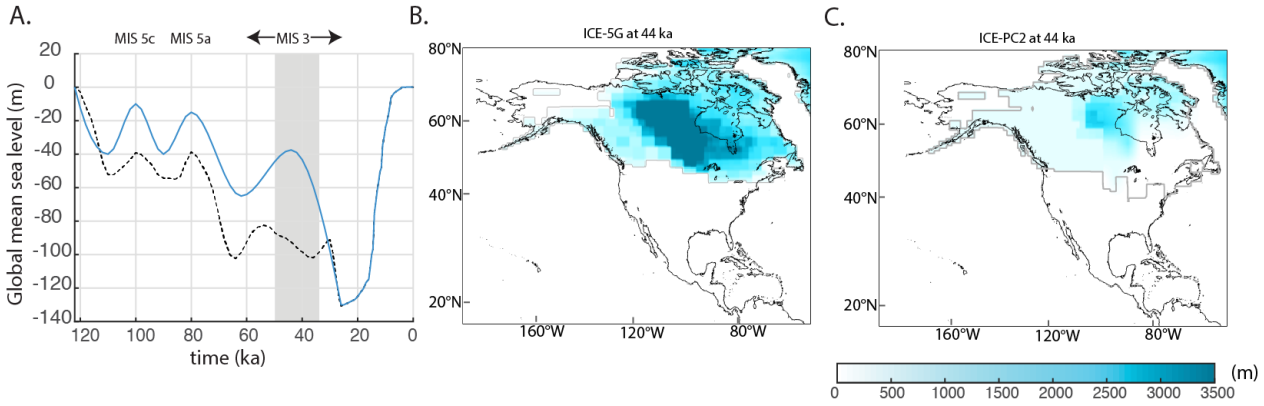

FIGURE 3.2: A. Global mean sea level history for ice history ICE-5G (dotted black) and ICE-PC2 (blue). B. Ice thickness at 44 ka for ice history ICE-5G (B) and ICE-PC2 (C). Maximum ice extent at LGM is shown by gray line in C.

3.3.3 Ice modeling

We used a simple ice flow model that reduces the three-dimensional Stokes flow equations to two dimensions using the shallow ice approximation (Cuffey & Patterson, 2010) with methodology adopted from Oerlemans (1981) as further developed in Birch et al. (2018). The resulting nonlinear diffusion equation represents ice flow by evolving ice thickness H in time based on the horizontal gradients of the surface elevation H* and the additional input of the surface mass balance G:

$$\frac{\partial H}{\partial t} = \Delta \cdot D \Delta H^* + G$$

The surface elevation (H*) is defined as

$$H^* = B + H,$$

where B is the basal topography. The non-linear shear thinning of ice flow is represented by diffusivity (D), which depends on both the ice thickness and surface elevation gradients:

$$D = AH^{m+2}[(\frac{\partial H^*}{\partial x})^2 + (\frac{\partial H^*}{\partial y})^2]^{\frac{m-1}{2}}$$

We adopted a value of m = 3 for all model simulations, which is a typical value for realistic ice simulations (Cuffey & Paterson 2010). The coefficient A, the creep parameter that influences the viscosity of the ice, is based on the temperature of the ice (i.e. colder ice flows more slowly). We adopted a value of A = 2.4x10-24 Pa-3 s-1 based on work by Cuffey & Paterson (2010), where the value of A is based on the temperature at the base of the ice sheet, near the melting point (typical of large ice sheets; Dowdeswell et al. 1997; Cutler et al. 2000; Oerlemans 2003). The basal sliding velocity is assumed to be zero. The numerical scheme used to integrate this ice model is described in Appendix 2.

The ice model requires that surface elevation (H*), ice thickness (H), and mass balance (G) be specified as inputs. The ice thickness (H) and surface elevation (H*) are derived from the initial ice configurations described above (Figure 2B/C) and the resulting paleotopography changes predicted by GIA simulations adopting the ice histories in Figure 2A. We specified a grid size of 20 km and a time step of 0.25 yr. We idealized the yearly surface mass balance (G) based on previous studies, where G increases linearly with height until an elevation plateau (Weertman 1976; Oerlemans

1989). This upper limit on the mass balance is based on the elevation desert effect, where high elevation ice sheets receive less precipitation (Mahaffy 1976; Oerlemans 2003; Birch et al. 2018; Gardner et al. 2011; Dowdeswell et al. 1997). We chose a mass balance slope, which varies as a function of height, of 1 m/yr for every 600 m of elevation gain and a maximum mass balance (net accumulation at high elevation) of 0.4 m/yr for the plateau, according to studies simulating Arctic Canadian glaciers (Dowdeswell et al. 1997; Gardner et al. 2011; Birch et al. 2017).

3.4 Results

3.4.1 Predicted topography at MIS 3

We first performed calculations with the ice history ICE-5G. The resulting paleotopography predicted at 44 ka is shown in Figure 3A. In this case, the simulation predicts that the Hudson Bay Lowlands is largely below sea level, which contradicts terrestrial markers dated to this time interval (Dalton et al., 2016). Moreover, the ice configuration at 44 ka is inconsistent with geological data described above, as ice covers many regions with ice-free markers dated to mid-MIS 3. We next adopted ice history ICE-PC2, characterized by the global mean sea-level history in Figure 2A (blue line), which has a reduced eastern sector of the Laurentide Ice Sheet until 44 ka (Figure 2C). The reconstructed topography in the ICE-PC2 simulation predicts that most of Quebec and the Hudson Bay Lowlands are terrestrial, consistent with the majority of the observational data shown in Figure 1.

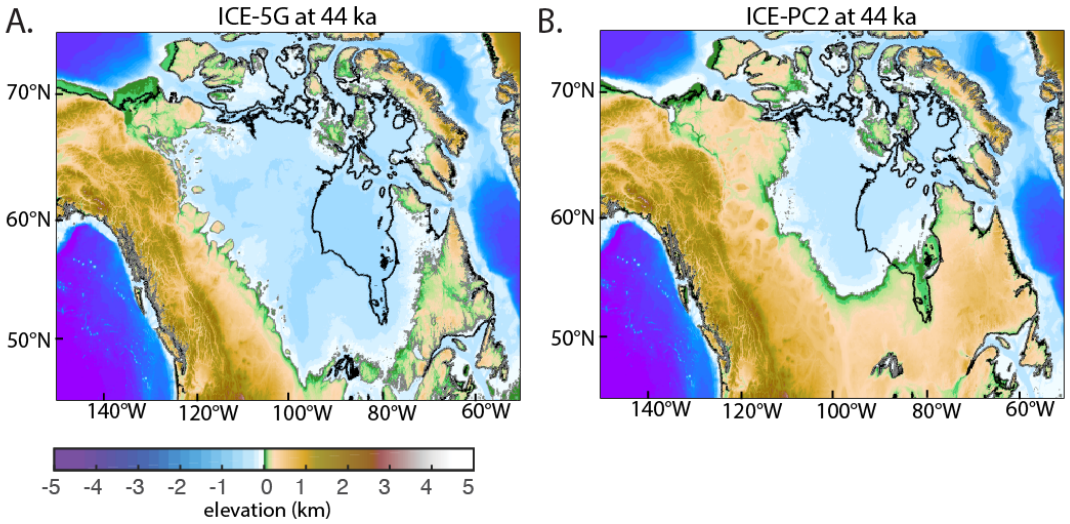

FIGURE 3.3: Predicted paleotopography at mid-MIS 3 (44 ka) using ice history ICE-5G (A) and ICE-PC2 (B).

3.4.2 COMPARING RELATIVE SEA-LEVEL PREDICTIONS WITH EMPIRICAL DATA

We next compared the predicted paleotopographies, and associated shorelines, with the geologic constraints on sea level. In particular, we examined data that specifically constrain the relative location of the shoreline with respect to the geologic marker. For example, marine sediments (Figure 4; upward triangles), including marine species such as molluscs, indicate that the shoreline is above this elevation, while fluvial deposits, peats, or lacustrine sediments are terrestrial indicators (Figure 4; downward triangles), and demonstrate the shoreline lies below this elevation. To summarize, data from the St. Lawrence River Lowlands record a transition from terrestrial to marine environment at approximately 35 ka (Parent et al. 2015; Dionne & Occhietti 1996). At the Magdalen Islands marine, terrestrial, and shoreline indicators have been dated from 60-40 ka (Remillard et al. 2017). At the Hudson Bay Lowlands recent dates obtained with OSL methods suggest a marine environment to the northwest and terrestrial environment to the southeast. Figure 5 shows the predicted relative sea level curves from 65 ka to LGM based on the ICE-PC2 ice history at the Hudson Bay Lowlands, the

St. Lawrence River Lowlands, Southern Ontario and the Magdalen Islands.

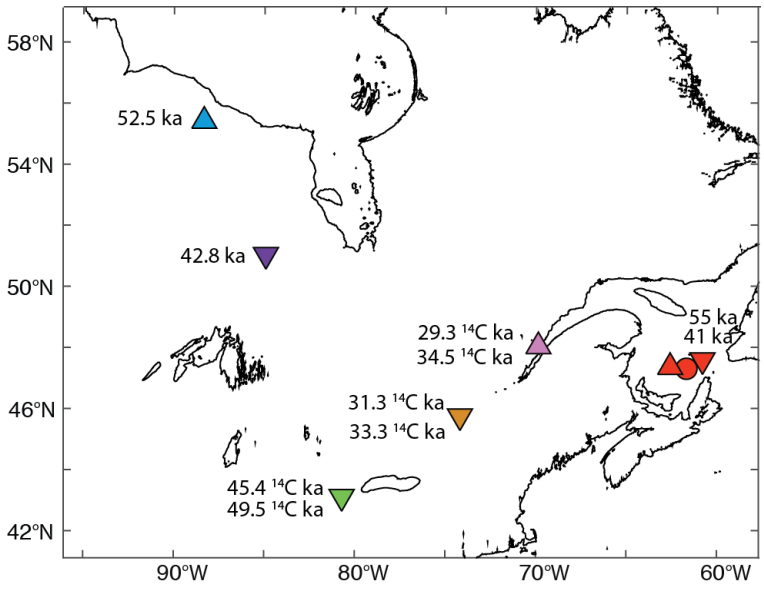

FIGURE 3.4: Location of sea-level markers in eastern Canada. Upward triangles denote marine indicators, downward triangles denote terrestrial indicators. Circles indicate a shoreline marker (data information in Appendix 1). Black lines show present-day shoreline.

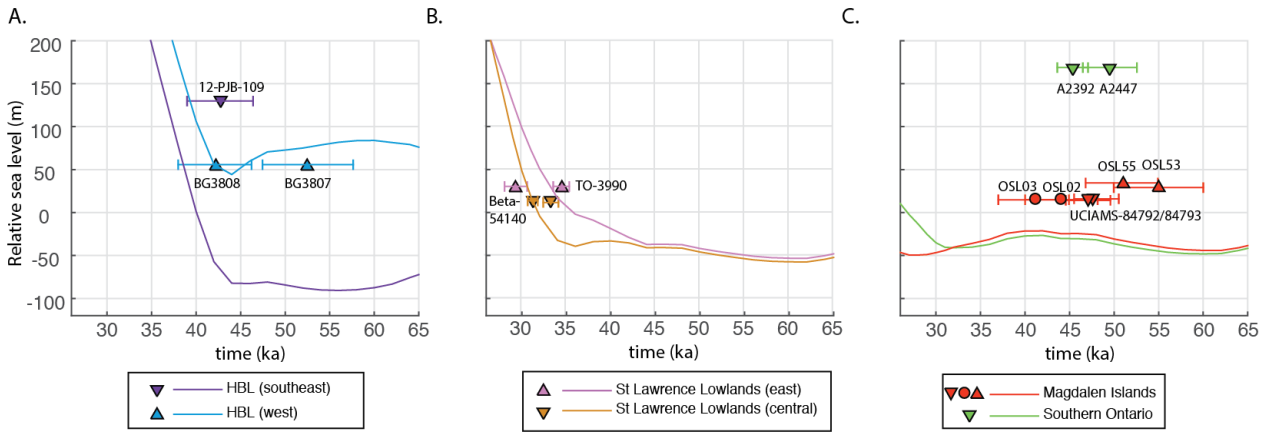

FIGURE 3.5: Relative sea level predictions adopting the ICE-PC2 ice history and VM2 Earth model compared with sea-level markers in A. Hudson Bay Lowlands B. St. Lawrence Lowlands C. Southern Ontario and Magdalen Islands. Upward triangles denote marine indicators, downward triangles denote terrestrial indicators. Circles indicate a shoreline marker (data information in Appendix 1). Location of these markers is shown in Figure 4. Labels provide identification numbers cited in original publications (as in Table 1). Age uncertainties are reported 1σ errors.

In the HBL we focused on two well-dated sites: 12-PJB-109, a terrestrial marker dated using OSL to 42.8 $\pm$ 3.75 ka at 130 m elevation at 50.87° N, 84.85 °W and Severn Marine, a marine sediment dated using OSL to 52.5$\pm$5.05 ka (BG3807) and 42.2 $\pm$4 ka (BG3808), found at 55 m elevation, at 55.43 °N, 88.2 °W (Dalton et al. 2016). We note that at the site 12-PJB-109, we adopt the OSL date since the radiocarbon dates included non-finite ages. Predicted relative sea-level curves for both sites are shown in Figure 5A. The Severn Marine site (Figure 5A; blue triangle) is predicted to be 50-150 m higher than present-day sea level, in agreement with the dated marine indicators that place sea level above 55 m from 58-38 ka. The terrestrial marker site, 12-PJB-109 (Figure 5A; purple), is predicted to be below present-day by up to 80 m from 47-38 ka, and is not predicted to experience marine flooding until $\sim$40 ka. This is consistent with the elevation of 12-PJB-109 at 130 m, indicating sea level is below this elevation.

At the eastern St. Lawrence Lowlands, predicted relative sea level is lower than present-day (sig-

naling a higher elevation of these markers) until ∼35 ka, which is consistent with fluvial deposits dated between 60-45 ka (Clark et al. 1993). The predicted marine incursion at ∼35 ka agrees with evidence of marine sediments dated to 35-31 ^{14}C ka (Dionne & Occhietti 1996). The western St. Lawerence Lowlands experiences a delayed sea-level rise relative to the eastern site. Terrestrial markers dated to 33-31 ^{14}C ka (Beta-54140, TO-3990) by Parent et al. (2015) were deposited when sea level is predicted to have risen quickly to submerge this site. The elevation of these markers is ∼14 m (Figure 5B; orange triangle), consistent with the prediction that relative sea level was 0-25 m below present-day sea level at the sites. In Southern Ontario, terrestrial markers were dated to 45.4± 1.8 ^{14}C ka (A2392) and 49.5 ± 3.1 ^{14}C ka (A2447) (Mulligan & Bajc 2017), and at this site relative sea level is predicted to be 25-40 m below present-day from 60-40 ka (Figure 5C; green triangle).

Finally we examined relative sea-level at the Magdalen Islands (Figure 5C; red circle and triangle) and found that throughout the last glacial cycle from 65-26 ka, relative sea-level is predicted to be below present-day, suggesting that there was a terrestrial environment during MIS 3, which is inconsistent with marine deposits dated from 60-45 ka (Remillard et al. 2017; Remillard et al. 2016). Furthermore, at this site shoreline markers have been dated to 50-35 ka (OSL03, OSL02, OSL55, OSL53, UCIAMS-84792/84793), and this data is similarly inconsistent with GIA predictions that suggest relative sea level at this site was well below this elevation across this time period.

These results indicate that ice history ICE-PC2 produces GIA simulations consistent with geologic records of sea level in the Hudson Bay Lowlands, and St. Lawrence lowlands, but not in the Magdalen Islands, implying that eastern Atlantic sector of the ice loading history may not be accurate.

We conclude by reiterating that these published ages to which we compare our predictions are at the limits of radiocarbon dating, and many of these chronologies include both finite and non-finite ages at the reported site. Alternative dating methods such as OSL are challenged by different uncertainties in age determination. While caution is required in using these dates, the preponderance of

MIS 3 ages in these deposits necessitates testing whether GIA-modeling is consistent with the relative sea-level markers associated with these sites.

3.4.3 Ice growth rates at MIS 3

We ran numerical simulations using the simplified ice flow model described above for 5 kyr to calculate ice growth rates. We initiated the model with the basal topography and ice thickness associated with ice history ICE-PC2 at 44 ka as shown in Figure 2C and Figure 3B, respectively, and assign a maximum mass balance (net accumulation at high elevation) of 0.4 m/yr (see Methods and Appendix 2). The resulting rate of ice growth, averaged over a 4.5 kyr period, is shown in Figure 6. Ice flows rapidly into the unglaciated Hudson Bay Lowlands, and the region over Quebec and Labrador, including the Torngat Mountains, experiences rapid glaciation. Over this 4.5 kyr time period the volume of the Laurentide Ice Sheet more than doubles, growing at a rate of 3.55×10^{12} m^3/yr, and attains a volume of 2.33×10^{16} m^3/yr by 39 ka.

Adopting the basal topography and ice thickness associated with ice history ICE-5G (Figures 2B and 3A) we predicted an ice volume growth rate of 3.75×10^{12} m^3/yr over the same region (Appendix Figure 2). A moderately higher rate of ice volume growth is predicted in the ICE-5G case compared to Figure 5 because ice thickness is greater in the ICE-5G ice history at 44 ka than in ICE-PC2 and therefore in our numerical ice simulations these high elevation regions receive the maximum mass accumulation rate.

To explore the impact of the assumed ice-loading history on predicted ice growth rates, we ran a numerical simulation in which we adopted the basal topography associated with ice history ICE-5G at 44 ka (Figure 3A), characterized by significant isostatic subsidence under a heavy Laurentide ice load, and paired this with the reduced ice thickness at 44 ka in the ICE-PC2 ice history (Figure 2C). In this simulation the initial basal topography is at a lower elevation than that associated with ICE-PC2 (Figure 3B), and therefore the predicted rates of ice volume growth are reduced to 2.46×10^{12}

m^3/yr, approximately 70% of the rate predicted using the ICE-PC2 paleotopography (Figure 3B). Thus, the Laurentide Ice Sheet is predicted to glaciate more slowly, and fewer regions experience rapid, instantaneous glaciation (Appendix Figure 3).

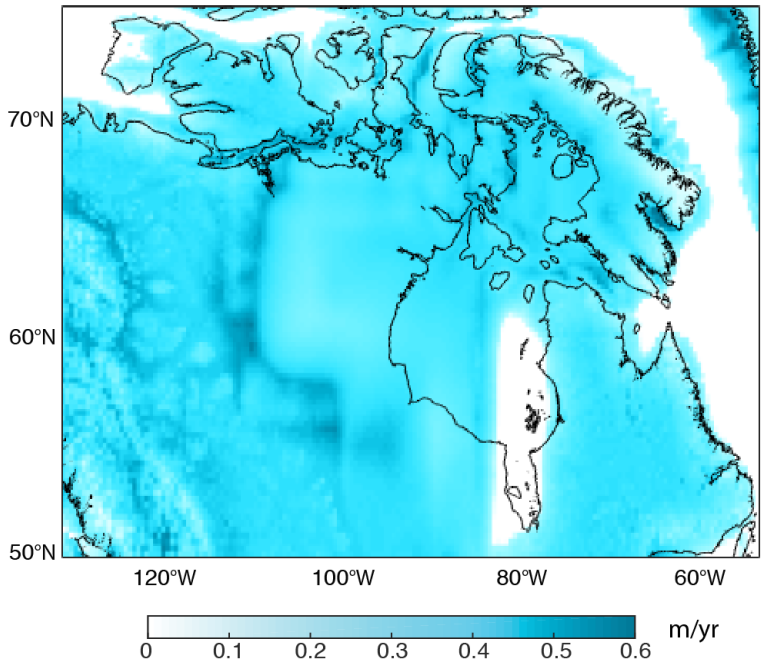

Figure 3.6: Ice growth rates averaged over 4.5 kyr using initial ice configuration ICE-PC2 at 44 ka and the paleotopography shown in Figure 3B.

3.5 Discussion

3.5.1 Climate parameters adopted in ice modeling

Climatological conditions are uncertain over much of the last glaciation phase (Charbit et al. 2007; Beghin et al. 2014; Brandefelt & Kjellstr 2011). We use values for the slope of the mass balance profile and maximum mass balance similar to those adopted in previous studies (Mahaffy 1976; Pfeffer et al. 1997; Oerlemans 2003; Cutler et al. 2000; Birch et al. 2018). In numerical simulations using the

basal topography and ice thickness associated with ICE-PC2 we varied the slope from 1m/yr per 300 m to 1m/yr per 3000 m (a value of 1 m/yr per 600 m was adopted in above simulations). We found that the perturbation to the mass balance slope resulted in similar ice spreading rates, and thus ice volume growth rates are relatively insensitive to this parameter. In contrast, ice volume growth rates are highly sensitive to the value of maximum mass balance; reducing the maximum mass balance by 50

Precipitation patterns, and therefore the realistic mass balance, likely varied substantially geographically and through time because the growth of large ice sheets alters atmospheric circulation through changes in stationary wave patterns (Roe & Lindzen 2001). However, while it is simplistic to model the variable climatology over the Laurentide Ice Sheet with a single mass balance, we believe that our numerical simulations demonstrate that the predicted ice growth from 44-39 ka in the case of a reduced Laurentide Ice Sheet extent (Figure 2C) is sufficiently rapid to attain LGM ice volumes by 26 ka. We note, in this regard, that the maximum mass balance values adopted here are similar to those calculated at high elevations in the Arctic region at present day (Dowdeswell et al. 1997). In our simulations, we assume that accumulation patterns maintained the Torngat Mountains region in ice-free conditions until 44 ka, but later atmosphere circulation changes caused the region to glaciate rapidly. Nevertheless we explored simulations that initiate with a glaciated Torngat Mountains in ice model ICE-PC3 (Appendix Figure 5A/B).

To accurately model the evolution of the Laurentide Ice Sheet over the MIS 3 period from 44 ka to 26 ka it will be necessary to realistically simulate changes in climatology associated with a delayed growth during the glaciation phase, an evolution that has previously not been taken into consideration (i.e. Charbit et al. 2007). In particular, the significantly reduced mid-MIS 3 Laurentide Ice Sheet inferred from the non-glacial deposits in Figure 1 and GIA simulations shown in Figure 4 may point to a distinct regime of atmospheric circulation across early MIS 3 relative to LGM. In order to explain that the regions containing some of the thickest ice at LGM were ice-free at MIS 3, precip-

itation patterns must have been quite different than those considered in previous modeling of the glaciation phase. Furthermore our simulations suggest that the prior history of ice loading during MIS 4 may impact the Laurentide Ice Sheet volume growth rate at MIS 3. Future studies should assess the likelihood of a substantially reduced Laurentide Ice Sheet over much of the glaciation phase from MIS 5a to MIS 3.

3.5.2 Sensitivity to assumptions of ice thickness and Earth model

Next we assessed the sensitivity of our results to a change in the ice distribution and Earth model adopted in GIA simulations. First we considered the alternate ice history ICE-PC3, characterized by the same global mean sea-level history as ICE-PC2 (Figure 2A; blue), but distinguished on the basis of the spatial distribution of ice during MIS3. In this ice history, at 44 ka, much of Quebec, including the Torngat Mountains, is glaciated, with an ice-free swatch over the Hudson Bay region. Running our numerical simulations using the basal topography and ice thickness associated with the ICE-PC3 ice history (Appendix Figure 5A/B) we predicted ice volume growth rates of 3.36×10^{12} m^3/yr, with a total ice volume of 2.33×10^{16} m^3 by 39 ka. These values are negligibly different from the ICE-PC2 based simulation in Figure 5.

We also tested the sensitivity of our predictions to the choice of Earth model adopted in GIA simulations. We predicted paleotopography at 44 ka using ice history ICE-PC2 and an Earth model characterized by an upper and lower mantle viscosity of 5×10^{20} Pa s and 5×10^{21} Pa s, respectively, and a lithospheric thickness of 48 km (Appendix Figure 5C and D). The resulting predictions of ice growth indicated that using an alternative Earth model does not impact modeled spreading rates of the ice sheet. In particular, we predict rates of 3.61×10^{12} m^3/yr, with a total ice volume of 2.36×10^{16} m^3 by 39 ka in this case.

A rapid growth of the Laurentide Ice Sheet late in the glacial build-up phase drives a delayed growth of the Laurentide peripheral bulge in GIA simulations, and this could potentially influence

estimates of global ice volumes at the LGM. While the majority of sites used to determine global sea level at the LGM (∼26 ka) are located in the far-field (i.e. Cutler et al. 2003; Stokes et al. 2012; Lambeck & Chappell 2001), sites in the intermediate-field of the Laurentide Ice Sheet should be corrected for GIA using an updated MIS 3 ice history prior to considering implications for global ice volumes. For example, we found that at Barbados, a key site used to reconstruct LGM global ice volumes (Peltier & Fairbanks, 2006), GIA simulations adopting the Earth model VM2 and the standard ice history ICE-5G (Peltier & Fairbanks, 2006) predicted that relative sea level is more than 3 m lower at LGM (26 ka) compared to the GIA simulations adopted in Pico et al. (2017), which are based on an ice history characterized by rapid Laurentide Ice Sheet growth. Thus, if we correct the Barbados RSL record for GIA effects with an ice history characterized by a late and rapid Laurentide Ice Sheet, a larger global ice volume (equivalent to ∼3 m global mean sea level) would be required to reconcile that record.

3.6 Conclusion

This study was motivated by recent work suggesting a Laurentide Ice Sheet of limited extent during mid-MIS 3. In particular, we investigate the robustness of the recently proposed Laurentide Ice Sheet configuration by comparing GIA predictions based upon it to RSL bounds implied by non-glacial deposits in the near-field of the Laurentide Ice Sheet. The resulting agreement lends support for arguments of a reduced Laurentide Ice Sheet during MIS 3, and potentially over much of the glaciation phase, implying a rapid growth of the ice sheet leading into the LGM.

Finally, we ran a simple numerical ice simulation to assess whether it is feasible to predict ice growth rates that are consistent with achieving LGM ice volumes in a 15 ky period from mid-MIS 3 to the LGM. We demonstrate, using mass balance values similar to those calculated in the present-day Arctic region, that our numerical ice simulations predict sufficiently rapid ice growth rates at 44 ka during mid-MIS 3 to reconcile the necessary growth towards LGM volumes.

3.7 References

Andrews, J.T., 1973. The Wisconsin Laurentide Ice Sheet□: Dispersal Centers , Problems of Rates of Retreat , and Climatic Implications. Arctic and Alpine Research, 5, pp.185–199.

Bajc, A.F. et al., 2015. Geology and paleoecology of a Middle Wisconsin fossil occurrence in Zorra Township , southwestern Ontario , Canada. Canadian Journal Earth Sciences, 19(April), pp.1–19.

Beghin, P. et al., 2014. Interdependence of the growth of the Northern Hemisphere ice sheets during the last glaciation: The role of atmospheric circulation. Climate of the Past, 10(1), pp.345–358.

Birch, L., Cronin, T. & Tziperman, E., 2018. The Role of Regional Feedbacks in Glacial Inception on Baffin Island□: The Interaction of Ice Flow and Meteorology. Climate of the Past, (revised June), pp.1–28.

Birch, L., Cronin, T. & Tziperman, E., 2017. Glacial inception on Baffin Island: The role of insolation, meteorology, and topography. Journal of Climate, 30(11), pp.4047–4064.

Charbit, S. et al., 2007. Numerical reconstructions of the Northern Hemisphere ice sheets through the last glacial-interglacial cycle To cite this version□: of the Past Numerical reconstructions of the Northern Hemisphere ice sheets through the last glacial-interglacial cycle. Climate of the Past, 3, pp.15–37. Charbit, S. et al., 2013. The Cryosphere Influence of ablation-related processes in the build-up of simulated Northern Hemisphere ice sheets during the last glacial cycle. The Cryosphere, 7, pp.681–698.

Clark, P.U. et al., 1993. Initiation and development of the Laurentide and Cordillean Ice Sheets following the Last Interglaciation. Quat. Sci. Reviews, 12, pp.79–114.

Clark, P.U. & Mix, A.C., 2002. Ice sheets and sea level of the Last Glacial Maximum. Quaternary Science Reviews, 21, pp.1–7.

Colgan, P.M., Vanderlip, C.A. & Braunschneider, K.N., 2015. Athens Subepisode (Wisconsin

Episode) non-glacial and older glacial sediments in the subsurface of southwestern Michigan , USA. Quaternary Research, 84, pp.382–397.

Cuffey, K.M. and Paterson, W.S.B., 2010. The physics of glaciers., Academic Press. Cutler, K.B. et al., 2003. Rapid sea-level fall and deep-ocean temperature change since the last interglacial period. Earth and Planetary Science Letters, 206(3–4), pp.253–271.

Cutler, P.M. et al., 2000. A numerical investigation of ice-lobe-permafrost interaction around the southern Laurentide ice sheet. Journal of Glaciology, 46(153), pp.311–325.

Dalton, A.S. et al., 2016. Constraining the Late Pleistocene history of the Laurentide Ice Sheet by dating the Missinaibi Formation, Hudson Bay Lowlands, Canada. Quaternary Science Reviews, 146, pp.288–299.

Dionne, J. & Occhietti, S., 1996. Apercu du Quaternaiare a L 'Embouchure Du Saguenay, Quebec. Geographie Physique et Quaternaire, 50(1), pp.5–34.

Dowdeswell, J.A. et al., 1997. The Mass Balance of Circum-Arctic Glaciers and Recent Climate Change. Quaternary Research, 48(1), pp.1–14.

Dredge, L.A. & Thorleifson, L.H., 1987. The Middle Wisconsinan History of the Laurentide Ice Sheet. Geographie Physique et Quaternaire, 41(2), p.215–235.

Gardner, A.S. et al., 2011. Sharply increased mass loss from glaciers and ice caps in the Canadian Arctic Archipelago. Nature, pp.6–9.

Hill, H.W. et al., 2006. Laurentide Ice Sheet meltwater and abrupt climate change during the last glaciation. Paleoceanography, 21, pp.1–9.

Kleman, J. et al., 2010. North American Ice Sheet build-up during the last glacial cycle, 115-21 kyr. Quaternary Science Reviews, 29(17–18), pp.2036–2051.

Kleman, J. et al., 2013. Pre-LGM northern hemisphere ice sheet topography. Climate of the Past, 9(5), pp.2365–2378.

Kleman, J., Fastook, J.L. & Stroeven, A.P., 2002. Geologically and geomorphologically con-

strained numerical model of Laurentide Ice Sheet inception and build-up. Quaternary International, (September).

Lambeck, K. & Chappell, J., 2001. Sea level change through the last glacial cycle. Science (New York, N.Y.), 292(5517), pp.679–686.

Lisiecki, L.E. & Raymo, M.E., 2005. A Pliocene-Pleistocene stack of 57 globally distributed benthic□ δ18O records. Paleoceanography, 20(1), pp.1–17.

Löfverström, M. et al., 2014. Evolution of the large-scale atmospheric circulation in response to changing ice sheets over the last glacial cycle. Climate of the Past, 10, pp.1453–1471.

Löfverström, M., Liakka, J. & Kleman, J., 2015. The North American Cordillera — An Impediment to Growing the Continent-Wide Laurentide Ice Sheet. Journal of Climate, 28(2004), pp.9433–9450.

Mahaffy, M.W., 1976. A three-dimensional numerical model of ice sheets: Tests on the Barnes Ice Cap, Northwest Territories. Journal of Geophysical Research, 81(6), pp.1059–1066. Available at: http://doi.wiley.com/10.1029/JC081i006p01059.

Manabe, S. & Broccoli, A.J., 1985. The Influence of Continental Ice Sheets on the Climate of an Ice Age. Journal of Geophysical Research, 90, pp.2167–2190.

Marshall, S. & Clark, P.U., 2002. Basal temperature evolution of North American ice sheets and implications for the 100-kyr cycle. Geophysical Research Letters, 29(24).

Marshall, S.J., 2002. Modelled nucleation centres of the Pleistocene ice sheets from an ice sheet model with subgrid topographic and glaciologic parameterizations. , 96, pp.125–137.

Mulligan, R.P. & Bajc, A.F., 2017. The pre-Late Wisconsin stratigraphy of southern Simcoe County , Ontario□: implications for ice sheet buildup , decay , and Great Lakes drainage evolution 1. Canadian Journal Earth Sciences, 21(January), pp.1–21.

Oerlemans, J., 2003. A quasi-analytical ice-sheet model for climate studies To cite this version□: Nonlinear Processes in Geophysics A quasi-analytical ice-sheet model for climate studies. Nonlinear

processes in Geophysics, 10, pp.441–452.

Oerlemans, J., 1989. On the Response of Valley Glaciers to Climatic Change. Glacier Fluctuations and Climatic Change, pp.353–371.

Parent, M. et al., 2015. Mid-Wisconsinan Fluvial and Marine Sediments In the Central St. Lawrence Lowlands - Implications for Glacial and Deglacial Events in the Appalachian Uplands. In GSA Northeastern Section - 50th Annual meeting.

Pfeffer, W.T. et al., 1997. Numerical modelling of the late glacial Laurentide advance of ice across Hudson strait:insights into terrestrial and marine geology, mass balance, and calving flux. Paleoceanography, 12(1), pp.97–110.

Pico, T. et al., 2016. Global ice volume during MIS 3 inferred from a sea-level analysis of sedimentary core records in the Yellow River Delta. Quaternary Science Reviews, 152, pp.72–79.

Pico, T., Creveling, J.R. & Mitrovica, J.X., 2017. Sea-level records from the U.S. mid-Atlantic constrain Laurentide Ice Sheet extent during Marine Isotope Stage 3. Nature Communications, 8(May), p.15612. Remillard, A. et al., 2017. Relative sea-level changes and glacio-isostatic adjustment on the Magdalen Islands archipelago (Atlantic Canada) from MIS 5 to the late Holocene. Quaternary Science Reviews, 171, pp.216–233.

Remillard, A.M. et al., 2016. Chronology and stratigraphy of the Magdalen Islands archipelago from the last glaciation to the early Holocene: new insights into the glacial and sea-level history of eastern Canada. Boreas, 45(4), pp.604–628.

Roe, G., 2001. The Mutual Interaction between Continental-Scale Ice Sheets and Atmospheric Stationary Waves. Journal of Climate, 14, pp.1450–1465.

Shakun, J.D. et al., 2015. An 800-kyr record of global surface ocean delta18O and implications for ice volume-temperature coupling. Earth and Planetary Science Letters, 426, pp.58–68.

Stokes, C.R., 2017. Deglaciation of the Laurentide Ice Sheet from the Last Glacial Maximum. Cuadernos de Investigacion Geografica, 43(2), pp.377–428.

Stokes, C.R. et al., 2015. On the reconstruction of palaeo-ice sheets□: Recent advances and future challenges. Quat. Sci. Reviews, 125.

Stokes, C.R., Tarasov, L. & Dyke, A.S., 2012. Dynamics of the North American Ice Sheet Complex during its inception and build-up to the Last Glacial Maximum. Quaternary Science Reviews, 50, pp.86–104. Available at: http://dx.doi.org/10.1016/j.quascirev.2012.07.009.

Waelbroeck, C. et al., 2002. Sea-level and deep water temperature changes derived from benthic foraminifera isotopic records. Quaternary Science Reviews, 21(1–3), pp.295–305.

Weertman, J., 1976. Milankovitch solar radiation variations and ice age ice sheet sizes. Nature, 261(5555), pp.17–20.

Wickert, A.D. et al., 2013. Gradual demise of a thin southern Laurentide ice sheet recorded by Mississippi drainage. Nature, 502(7473), pp.668–71.

Wood, J.R. et al., 2010. Lacustrine sediments in Porter Cave , Central Indiana , USA and possible relation to Laurentide ice sheet marginal positions in the middle and late Wisconsinan.

Palaeogeography, Palaeoclimatology, Palaeoecology, 298(3–4), pp.421–431. Available at: http://dx.doi.org/10.1016/j.palaeo

Yokoyama, Y., Lambeck, K. & Deckker, P. De, 2000. Timing of the Last Glacial Maximum from observed sea-level minima. Nature, 406(August), pp.1998–2001.

4

Glacial Isostatic Adjustment Deflects Path of Hudson River

4.1 Introduction

The Laurentide Ice Sheet reached its maximum extent over the last glacial cycle at the Last Glacial Maximum (26 ka; Clark et al. 2009). Evidence of ice-sheet extent during the glaciation phase preceding the Last Glacial Maximum is obscured by the subsequent retreat of the ice sheet, and is poorly preserved in the geological record (Dyke et al., 2002; Clark et al., 1993; Kleman et al., 2010). Geochronological constraints on ice-sheet history are difficult to obtain because much of the last ice age is beyond the age limit of radiocarbon dating, and the remaining geologic observations are characterized by sparse dates using methods such as optical stimulated luminescence (OSL) or cos-

A version of this chapter was published with Jerry X. Mitrovica, Jean Braun, and Ken L. Ferrier in *Geology*, issue. 7, p. 1-4, 2018.

mogenic nuclides (Dalton et al., 2016; Briner et al., 2006). These limitations extend to other regions that were glaciated across the last ice-age cycle, and they pose a serious challenge to studies of glacial isostatic adjustment (GIA) prior to the Last Glacial Maximum, in addition to hindering our understanding of the dynamics of ice-sheet growth. However, it should be possible to gather insight into ice-sheet histories by examining well-dated evidence of landscape evolution in unglaciated regions proximal to continental glaciation. GIA produces geographically variable crustal uplift and subsidence rates that reach many tens of m/ky, a level sufficient to control river drainage patterns (Wickert et al., 2013; Wallinga et al., 2004; Wickert 2016) and delta morphology (Whitehouse et al., 2007).

The diversion of the Hudson River during the latest phase of Marine Isotope Stage 3 (MIS 3; 60-26 ka; Siddall et al. 2008) is an example of landscape evolution that has been connected – albeit speculatively – to crustal deformation related to the growth of the Laurentide Ice Sheet and, in particular, the dynamics of its peripheral bulge (Knebel et al., 1979; Carey et al., 2005). The river was diverted eastward from its ancestral channel (dashed black line; Figure 1), which has been dated to 40-30 ka using radiocarbon (14C) and amino acid racemization dating (Knebel et al., 1979; Carey et al., 2005) and mapped by seismic reflection surveys (Christensen et al., 2013; Carey et al., 2005; Santra et al., 2013). Though this river diversion ~30 ka has been attributed to ice-age processes, this hypothesis has not been tested using process-based models of either GIA or landscape evolution.

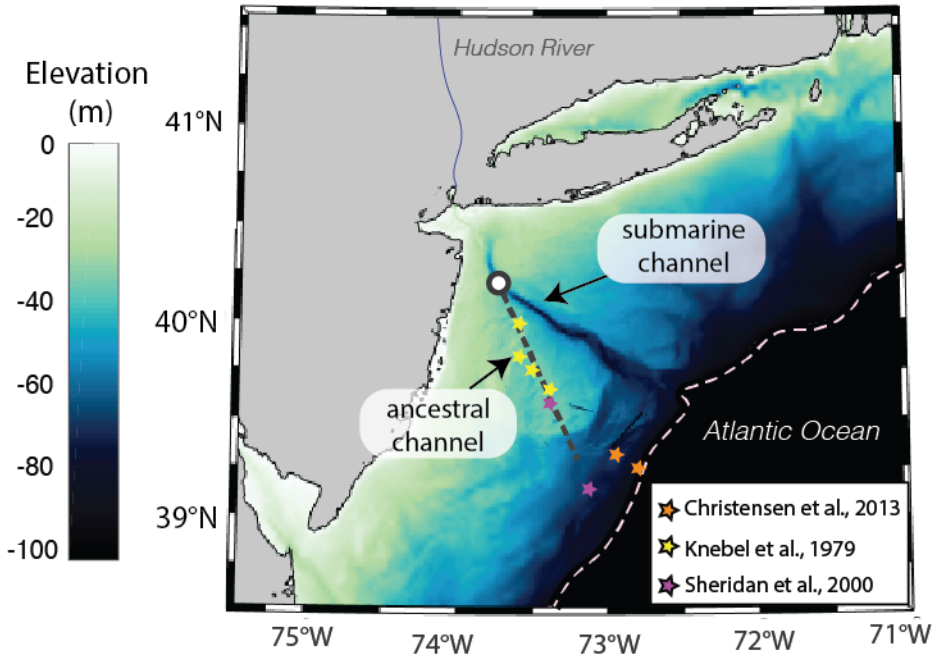

FIGURE 4.1: Present-day bathymetry on the Hudson shelf. Colored stars indicate sites with dated deposits along the ancestral Hudson River, whose approximate path is shown by dash-dotted black line. The white circle indicates the likely location of the river diversion. The dashed white line is the shoreline reconstruction at 26 ka based on calculations using ice model ICE-PC2. The thin, solid blue lines within the continental interior are schematic locations of present-day river paths.

Predicting how GIA modulates these river processes requires knowledge of the history of ice growth over North America prior to the Last Glacial Maximum. Glacial geologists have mapped out terminal moraines tracing the maximum extent of the Laurentide Ice Sheet at the Last Glacial Maximum: the Erie and Lake Champlain lobes entered Pennsylvania from the northwest and northeast,

respectively, forming a triangular-shaped ice-free region between the two ice lobes (Braun 2004). Ice advanced to its maximum position in southern New England at 27-20 ka (Balco & Schaefer 2006); however, little evidence remains in New England of ice extent during the build-up phase (Ridge 2004; Corbett et al., 2017). Pre-Last Glacial Maximum configurations of the Laurentide Ice Sheet have been constructed by Clark et al. (1993) on the basis of extensive stratigraphic records, and by Kleman et al. (2010) using a wide range of geomorphic evidence (eskers, ribbed moraines, ice-flow traces, and glacial striations). Nevertheless, given the uncertainties in chronology discussed above, it has not been possible to identify a spatially and temporally precise Laurentide Ice Sheet configuration during MIS 3. Recently, Dalton et al., (2016) inferred delayed glaciation of the eastern sector of the Laurentide Ice Sheet by dating non-glacial deposits in the region to 50-37 ka using OSL, uranium-thorium (U-Th), and 14C chronometers. They concluded that the Hudson Bay Lowlands was possibly ice-free from MIS 5a (100 ka) through mid-MIS 3 ($\sim$40 ka).

In this study we predict crustal deformation using GIA simulations based on a suite of possible ice sheet histories and viscoelastic Earth structures, and use the predicted changes in topography to drive a landscape evolution model that allows river networks to evolve under spatially variable uplift. We use these results to explore the extent to which GIA may have controlled the diversion of the Hudson River.

4.2 Methods

4.2.1 Glacial Isostatic Adjustment & Ice Histories

Ice-sheet growth and decay drive a complex pattern of sea-level (or equivalently, topographic) change. In the following simulations, we perform sea-level calculations based on the theory and pseudo-spectral algorithm described by Kendall et al., (2005) with a spherical harmonic truncation at degree and order 256. These calculations include the impact of load-induced Earth rotation changes on sea

level (Milne & Mitrovica 1996), evolving shorelines, and the migration of grounded, marine-based ice (Johnston 1993; Milne et al., 1999; Lambeck et al., 2003; Kendall et al., 2005). In our primary GIA calculations, we adopt an Earth model with a lithospheric thickness of 96 km and upper and lower mantle viscosities of 0.5 x 1021 Pa s and 1.5 x 1022 Pa s, respectively. This model is consistent with recent GIA studies involving data from the U.S. Atlantic coastal plain (Potter & Lambeck 2003; Pico et al., 2017; Creveling et al., 2017). In the Supplementary Material, we consider the sensitivity of our results to these Earth model parameters.

We construct a series of ice histories spanning the last glacial cycle that are used as input to the GIA simulations. In one case, we adopt the global ice history ICE-5G (Peltier, 2004) across the last glacial cycle with two important modifications. The original Version 1.2 of the ICE-5G history assumes that prior to 26 ka the ice sheet perimeter was fixed at the maximum perimeter. Our version adopts the same global mean sea level variation as ICE-5G (Figure 2A; dotted black line), but we make the common assumption that the geographic distribution of ice before 26 ka is the same as that afterwards , during the last deglaciation, for a given global ice volume (Raymo et al., 2011). Furthermore we revise the ICE-5G Last Glacial Maximum ice distribution to spatially resolve ice lobes described in the Dyke 2004 Last Glacial Maximum reconstruction (Briner et al., 2006; Supplementary Figure 1A). We will refer to this model as modified ICE-5G.

Many previous inferences of global mean sea level during the last glacial phase, and particularly during MIS 3, reconstruct higher sea levels (i.e., smaller global ice volume) than the ICE-5G history (e.g., Lambeck & Chappell, 2001; Pico et al., 2016; Creveling et al., 2017). Moreover, a recent GIA analysis demonstrated that anomalously high sea-level markers dated to 50-35 ka along the U.S. mid-Atlantic are reconciled by adopting a significantly reduced eastern Laurentide Ice Sheet compared to the modified ICE-5G reconstruction, and concluded that this sector underwent especially rapid growth from 44-26 ka (Pico et al., 2017). Motivated by these studies, as well as non-glacial deposits dated to mid-MIS 3 in eastern Laurentia (Dalton et al., 2016), we construct an alternate ice

history which we denote as ICE-PC2. This ice history differs from "modified ICE-5G" by adopting a global mean sea level history consistent with recent constraints on peak sea-level highstands across the glacial phase. In particular, these constraints suggest that global ice volumes reached above -20 m global mean sea level during both MIS 5a and 5c (∼100 ka and ∼80 ka, respectively; Creveling et al., 2017) and they tripled from 44 ka to 26 ka (Pico et al., 2016). The resulting global mean sea level curve is shown in Figure 2A. In ICE-PC2 the eastern sector of the model Laurentide Ice Sheet is ice-free from 80-44 ka, and this region glaciates rapidly leading into the Last Glacial Maximum from 44 ka to the 26 ka (Supplementary Figure 1D).

Finally, we construct three other ice models that provide variations in ICE-PC2 history to explore the sensitivity of river network evolution to the modeled ice history. These are denoted as ICE-PC, ICE-PC3 and ICE-PC4, and they are described in detail in Supplementary Note 1.

4.3 Results

4.3.1 Glacial Isostatic Adjustment Predictions

To begin, we predict the change in topography over the last glacial cycle using the modified ICE-5G model (dotted line, Figure 2A; Peltier & Fairbanks, 2006). The global mean sea level curve associated with the modified ICE-5G history is characterized by ice volumes that reach near-Last Glacial Maximum values by ∼65 ka, i.e., prior to the beginning of MIS 3 (Figure 2A). Because the solid Earth response to pre-65 ka ice load variations has largely equilibrated by 30 ka, our modified ICE-5G-based calculation predicts low rates of crustal deformation (∼1 m/ky) and no pronounced regional west-to-east tilting from 32 ka to 26 ka (Figure 2B). The observed eastward diversion of the Hudson River during this time period implies contemporaneous deformation in the region, with a decreasing gradient in crustal uplift rates from west to east, a pattern that is not predicted with the modified ICE-5G history.

We next perform GIA simulations adopting the ice history ICE-PC2, characterized by a rapid drop in global mean sea level from 44-26 ka (Figure 2A). The average rate of change in topography predicted by this simulation from 32-26 ka is characterized by west-to-east tilting of the crust, which is particularly pronounced in the region bounding the predicted shorelines at 26 and 32 ka (dotted lines in Figure 2C; vertical displacement rates at 1 kyr intervals across this time window are shown in Supplementary Figure 2).

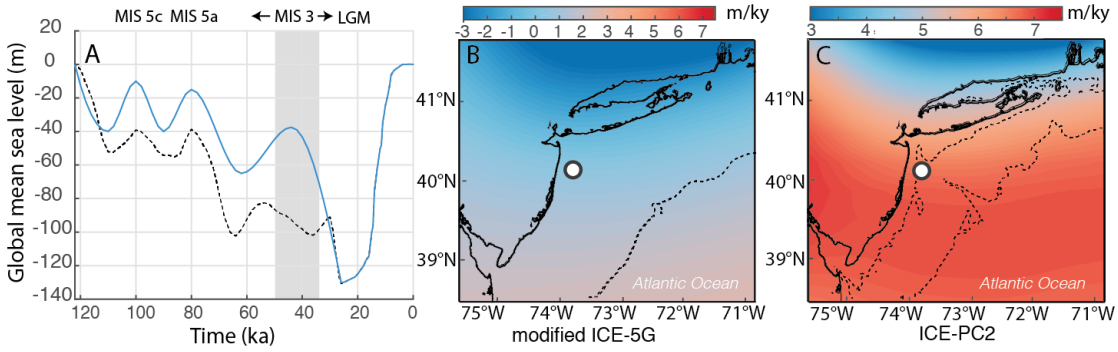

FIGURE 4.2: A. Global mean sea level change predicted with the modified ICE-5G history (dotted black) and the suite of ICE-PC histories (solid blue). The gray bar shows the interval from 50-35 ka, the time period the relative sea-level highstand is dated to. The Last Glacial Maximum (LGM; 26 ka) is labeled. B, C. Average rate of vertical displacement over the time interval 32-26 ka associated with GIA in the region of interest computed using the (B) modified ICE-5G and (C) ICE-PC2 ice histories. The dotted-black lines on each frame denote the reconstructed shoreline locations at 32 and 26 ka. The lower sea-level shoreline represents 26 ka, and in case (B) the shorelines at 32 and 26 ka are nearly coincident. The white circle marks the likely location of river diversion. Note distinct colorbar in B,C.

4.3.2 Landscape Response to Glacial Isostatic Adjustment

Next, we explore how the landscape responds to the predicted GIA-induced deformation fields. Rivers respond through increased erosion or deposition to base level changes (including changes in the position of the shoreline) during glacial cycles, and numerous studies have focused on the response of coastal landscapes to globally uniform sea-level variations (Fagherazzi et al., 2004; Meijer 2002). Here, however, we focus on the response of rivers to GIA-induced crustal deformation.

To highlight these effects, our landscape evolution simulations drive river network evolution only through fluvial processes in both transport- and detachment-limited rivers, and do not include coastal processes such as delta formation.

We perform simulations of landscape evolution using a generalized initial topography in the Hudson River region at the onset of the simulation (32 ka) because topography at this time was dissimilar to that of today. In particular, at ∼13 ka, the Hudson River drained a catastrophic flood from pro-glacial Lake Iroquois, which led to up to 40 m of incision in the present-day channel and the deposition of debris flows in the surrounding regions of the shelf (Uchupi et al., 2001; Donnelly et al., 2005; Thieler et al., 2007; Rayburn et al., 2005). As a consequence, maps of present-day elevation are a poor representation of the landscape at the time of the diversion of the Hudson River. Our model is instead initiated using a regional synthetic reconstruction of topography on a grid with a uniform spacing of 30 arc-seconds (∼ 1 km; Figure 3A; Supplementary Note 4) that is characterized by a north-south gradient similar to the general trend on the Hudson shelf (1 m/km); this yields paleo-Hudson River drainage that flows from north to south, consistent with paleoflow directions ∼30 ka recorded in the stratigraphic record (i.e. Carey et al., 2005; Figure 1). Our goal in establishing the initial field of topography described above is to assess the general trends in the evolution of a North-South flowing river in this location when subject to deformation due to GIA.

The location of river paths on the synthetic topography is shown in Figure 3B, and the largest rivers (measured by drainage area > 10×10^7 m^2) are shown in green. There are nine such rivers and ten additional ("intermediate"; > 5×10^7 m^2) rivers (blue; Figure 3B). To explore whether GIA may have been responsible for the diversion of the Hudson River and whether this connection favors certain ice histories, we focus on the response of this synthetic river network to topographic changes predicted by each of the GIA simulations. Our measure of performance in this regard will be the number of large and intermediate rivers diverted during the period 32 ka to 26 ka.

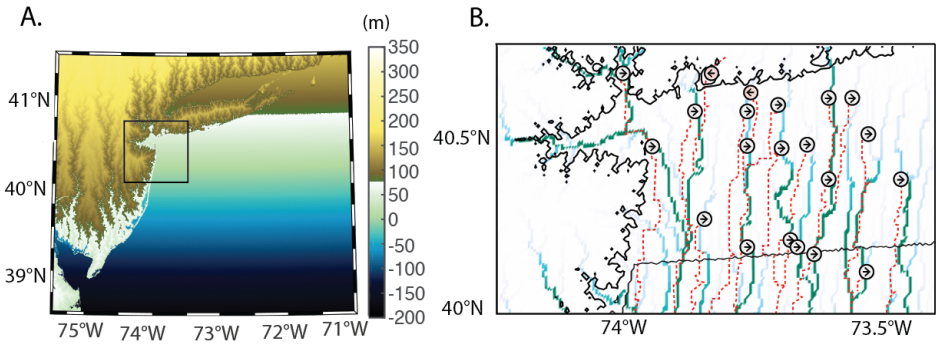

FIGURE 4.3: Figure 3 | A. The regional reconstruction of topography used to initialize the landscape evolution simulations at 32 ka. The black box outlines the region used in landscape evolution simulations. B. River drainage patterns within the boxed region of frame (A), illustrating the location of 9 large rivers in green.

To quantify river network responses to GIA-induced crustal deformation, we adopt the Channel-Hillslope Integrated Landscape Development (CHILD) landscape evolution model, which includes parameterizations for both detachment-limited and transport-limited processes (Tucker et al. 2001; Tucker, 2010), both of which may influence river evolution in the study region. We drive CHILD simulations by applying time-variable uplift rates drawn from the GIA predictions from 32 to 26 ka (Supplementary Figure 2) to the initial topography, and compute the responses in the resulting river network. Supplementary Table 1 lists the parameter values adopted for these simulations, and Supplementary Note 5 reviews the fluvial and hillslope processes applied in CHILD. In Supplementary Note 6 we describe additional simulations aimed at assessing the sensitivity of river diversions to the relative strength of detachment-limited and transport-limited conditions. These sensitivity tests revealed that the number of modeled river diversions is relatively insensitive to the adopted values for the sediment transport coefficient and the critical shear stress, implying that the modeled river diversions are not sensitive to the relative dominance of detachment-limited or transport-limited conditions.

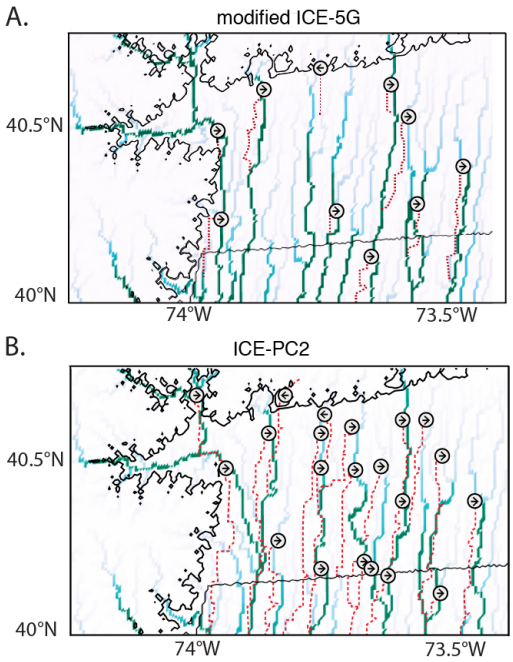

FIGURE 4.4: River drainage pattern computed using CHILD after the initial topography in Figure 3A is perturbed by regional GIA predicted using (A) ice model modified ICE-5G (Figure 2B) and (B) ICE-PC2 (Figure 2C). Darker colors are used to highlight relatively larger rivers. Eastward and westward diversions are labeled by arrows. Dashed red lines show the original paths of these rivers prior to the imposition of the GIA deformation field (Figure 3B). The thin black line represents the shoreline position (as in Figure 3A/B) adopted in the landscape evolution model at the start of the simulation.

Driving the landscape evolution model with the vertical displacement field produced by ice history ICE-PC2 (Figure 2C), and adopting the erodibility parameters described in the Supplementary Note 5, predicts that all 9 large rivers and 6 intermediate rivers are diverted eastward by 6 ky after the onset of the simulation at 32 ka (a total of 19 sites of eastward diversion and 2 sites of westward diversion along 17 rivers; gray and pink circles; Figure 4B). This trend is consistent with the eastward diversion of the Hudson River preserved in the geological record. In contrast, only 6 large rivers and 1 intermediate river are diverted eastward when the simulation is driven by deformation associated with the modified ICE-5G simulation using the same Earth model and erodibility parameters (total

of 9 sites of eastward diversion and 1 site of westward diversion along 16 rivers; gray and pink circles; Figure 4A).

4.4 Discussion

Analogous predictions for additional ice histories and Earth models are shown in Supplementary Figures 3-6. The number of predicted river diversions is primarily sensitive to the adopted upper mantle viscosity of the Earth model, as the peripheral bulge is largely accommodated in this depth of the mantle. In particular, the predicted west-east topographic gradient increases as one weakens the upper mantle, leading to more river diversions.

We note that the predicted west-to-east pattern of deformation does not reflect the broader geometry of the Laurentide Ice Sheet peripheral bulge, which spans the greater part of the United States, but is due to a superimposed, smaller scale peripheral bulge formed by the Erie ice lobe (Supplementary Figure 1A; Dyke et al., 2002). The tilting caused by the late and rapid growth of the Laurentide Ice Sheet and its associated ice lobes could have been sufficient to have affected other rivers along the U.S. east coast, including the Delaware River, a connection that warrants further study.

4.5 Conclusion

Previous studies have speculated that the eastward diversion of the Hudson River at ~30 ka was driven by changes in topography associated with ongoing GIA (e.g., Knebel et al., 1979; Carey et al., 2005). Our modeling of both GIA and the associated river network evolution provides strong quantitative support for this hypothesis. An eastward diversion requires that the GIA field introduce a west-to-east tilting of topography. Our simulations indicate that this tilting would have been a natural consequence of a rapid, late growth of the eastern Laurentide Ice Sheet before the Last Glacial Maximum. These simulations suggest the Hudson River likely was diverted during the sea-level fall as the shoreline passed through the region of maximum west-east tilting from 32-26 ka. Our

simulations ignore shallow coastal processes including backwater effects and autogenic avulsions; incorporating these effects may increase the likelihood of diversions.

Our results demonstrate that solid-Earth deformation over Pleistocene glacial cycles can be an important influence on landscape evolution in regions without glacial cover, particularly at the periphery of former ice sheets where information about past river evolution can refine estimates of glaciation rates.

4.6 References

Balco, G. & Schaefer, J.M., 2006. Cosmogenic-nuclide and varve chronologies for the deglaciation of southern New England. Quaternary Geochronology, 1(1), pp.15–28.

Braun, D.D., 2004. The Glaciation of Pennsylvannia, USA. In J. Ehlers, P. L. Gibbard, & P. D. Hughes, eds. Quaternary Glaciations - Extent and Chronology: A Closer Look.

Briner, J., Gosse, J. & Bierman, P.R., 2006. Applications of cosmogenic nuclides to Laurentide Ice Sheet history and dynamics Applications of cosmogenic nuclides to Laurentide Ice Sheet history. Geological Society of America Special Papers, 415(October 2014), pp.29–41.

Carey, J.S. et al., 2005. Glacially-influenced late Pleistocene stratigraphy of a passive margin: New Jersey's Record of the North American ice sheet. Marine Geology, 218(1–4), pp.155–173.

Christensen, B.A. et al., 2013. The Last Glacial: Insights from continuous coring on the New Jersey continental shelf. Marine Geology, 335, pp.78–99. Available at: http://dx.doi.org/10.1016/j.margeo.2012.10.015.

Clark, P.U. et al., 1993. Initiation and development of the Laurentide and Cordillean Ice Sheets following the Last Interglaciation. Quat. Sci. Reviews, 12, pp.79–114.

Clark, P.U. et al., 2009. The Last Glacial Maximum. Science (New York, N.Y.), 325(5941), pp.710–4. Available at: http://www.ncbi.nlm.nih.gov/pubmed/19661421 [Accessed July 10, 2014].

Corbett, L.B. et al., 2017. Cosmogenic nuclide age estimate for Laurentide Ice Sheet recession from the terminal moraine , New Jersey , USA , and constraints on latest Pleistocene ice sheet his-

tory. Quaternary Research, 87, pp.482–498.

Creveling, J.R. et al., 2017. Predicted bounds on peak global mean sea level during marine isotope stages 5a and 5c. Quaternary Science Reviews, 163, pp.193–208. Available at: http://www.sciencedirect.com/science/article/p

Dalton, A.S. et al., 2016. Constraining the Late Pleistocene history of the Laurentide Ice Sheet by dating the Missinaibi Formation, Hudson Bay Lowlands, Canada. Quaternary Science Reviews, 146, pp.288–299. Available at: http://dx.doi.org/10.1016/j.quascirev.2016.06.015.

Donnelly, J.P. et al., 2005. Catastrophic meltwater discharge down the Hudson Valley□: A potential trigger for the Intra-Allerød cold period. Geology, 33(2), pp.89–92.

Dyke, A.S., 2004. An outline of North American Deglaciation with emphasis on central and northern Canada. In J.Ehlers & P.L.Gibbard, eds. Quaternary Glaciations-Extent and Chronology: Part II: North America. pp. 373–424.

Dyke, A.S. et al., 2002. The Laurentide and Innuitian Ice Sheet during the Last Glacial Maximum The Laurentide and Innuitian ice sheets during the Last Glacial Maximum. Quat. Sci. Reviews, 21, pp.9–31. Fagherazzi, S., Howard, A.D. & Wiberg, P., 2004. Modeling fluvial erosion and deposition on continental shelves during sea level cycles. Journal of Geophysical Research, 109(F3), p.F03010. Available at: http://doi.wiley.com/10.1029/2003JF000091 [Accessed October 20, 2014].

Johnston, P., 1993. The effect of spatially non-uniform water loads on prediction of sea-level change. Geophysical Journal International, 114(3), pp.615–634. Available at: http://onlinelibrary.wiley.com/doi/10.1111/j.1365-246X.1993.tb06992.x/abstract.

Kendall, R.A., Mitrovica, J.X. & Milne, G.A., 2005. On post-glacial sea level - II. Numerical formulation and comparative results on spherically symmetric models. Geophysical Journal International, 161(3), pp.679–706. Available at: http://gji.oxfordjournals.org/cgi/doi/10.1111/j.1365-246X.2005.02553.x.

Kleman, J. et al., 2010. North American Ice Sheet build-up during the last glacial cycle, 115-21 kyr. Quaternary Science Reviews, 29(17–18), pp.2036–2051. Available at: http://dx.doi.org/10.1016/j.quascirev.2010.04.021.

Knebel, H.J., Wood, S.A. & Spiker, E.C., 1979. Hudson River□: Evidence for extensive migration on the exposed continental shelf during Pleistocene time. Geology, 7(May), pp.254–258.

Lambeck, K. et al., 2003. Water-load definition in the glacio-hydro-isostatic sea-level equation. Quaternary Science Reviews, 22(2–4), pp.309–318.

Lambeck, K. & Chappell, J., 2001. Sea level change through the last glacial cycle. Science (New York, N.Y.), 292(5517), pp.679–686.

Meijer, X.D., 2002. Modelling the drainage evolution of a river-shelf system forced by Quaternary glacio-eustasy. Basin Research, 14, pp.361–377.

Milne, G.A., Mitrovica, J.X. & Davis, J.L., 1999. Near-field hydro-isostasy: the implementation of a revised sea-level equation. Geophysical Journal International, 139, pp.464–482.

Milne, G. a. & Mitrovica, J.X., 1996. Postglacial sea-level change on a rotating Earth: first results from a gravitationally self-consistent sea-level equation. Geophysical Journal International, 126(3), pp.F13–F20. Available at: http://gji.oxfordjournals.org/cgi/doi/10.1111/j.1365-246X.1996.tb04691.x.

Peltier, W.R. & Fairbanks, R.G., 2006. Global glacial ice volume and Last Glacial Maximum duration from an extended Barbados sea level record. Quaternary Science Reviews, 25(23–24), pp.3322–3337.

Pico, T. et al., 2016. Global ice volume during MIS 3 inferred from a sea-level analysis of sedimentary core records in the Yellow River Delta. Quaternary Science Reviews, 152, pp.72–79. Available at: http://dx.doi.org/10.1016/j.quascirev.2016.09.012.

Pico, T., Creveling, J.R. & Mitrovica, J.X., 2017. Sea-level records from the U.S. mid-Atlantic constrain Laurentide Ice Sheet extent during Marine Isotope Stage 3. Nature Communications, 8(May), p.15612. Available at: http://www.nature.com/doifinder/10.1038/ncomms15612.

Potter, E.K. & Lambeck, K., 2003. Reconciliation of sea-level observations in the Western North Atlantic during the last glacial cycle. Earth and Planetary Science Letters, 217(1–2), pp.171–181.

Rayburn, J.A., Knuepfer, P.L.K. & Franzi, D.A., 2005. A series of large , Late Wisconsinan melt-

water floods through the Champlain and Hudson Valleys , New York State , USA. Quat. Sci. Reviews, 24, pp.2410–2419.

Raymo, M.E. et al., 2011. Departures from eustasy in Pliocene sea-level records. Nature Geosci, 4(5), pp.328–332. Available at: http://dx.doi.org/10.1038/ngeo1118.

Santra, M. et al., 2013. Latest Pleistocene Sediment Wedge on the New Jersey Outer Continental Shelf - Forced Regressive Paleo-Hudson Delta□? Marine Geology, 339(August), pp.57–70.

Siddall, M. et al., 2008. Marine Isotope Stage 3 sea level fluctuations: data synthesis and new outlook. Hemisphere, 46(2007), pp.1–29. Available at: http://www.agu.org/pubs/crossref/2008/2007RG000226.shtml.

Thieler, E.R. et al., 2007. A catastrophic meltwater flood event and the formation of the Hudson Shelf Valley. Palaeogeography, Palaeoclimate, Palaeoecology, 246, pp.120–136.

Tucker, G.E. et al., 2001. An object-oriented framework for distributed hydrologic and geomorphic modeling using triangulated irregular networks. , 27, pp.959–973.

Uchupi, E. et al., 2001. Drainage of late Wisconsin glacial lakes and the morphology and late Quaternary stratigraphy of the New Jersey – southern New England continental shelf and slope Drainage of late Wisconsin glacial lakes and the morphology and England continental shelf and. Marine Geology, 172, pp.117–145.

Wallinga, J. et al., 2004. Allogenic forcing of the late Quaternary Rhine - Meuse fluvial record□: the interplay of sea-level change , climate change and crustal movements. Basin Research, pp.535–547.

Whitehouse, P.L., Allen, M.B. & Milne, G. a., 2007. Glacial isostatic adjustment as a control on coastal processes: An example from the Siberian Arctic. Geology, 35(8), p.747. Available at: http://geology.gsapubs.org/cgi/doi/10.1130/G23437A.1 [Accessed October 5, 2014].

Wickert, A.D. et al., 2013. Gradual demise of a thin southern Laurentide ice sheet recorded by Mississippi drainage. Nature, 502(7473), pp.668–71. Available at: http://www.ncbi.nlm.nih.gov/pubmed/24172978.

Wickert, A.D., 2016. Reconstruction of North American drainage basins and river discharge since

the Last Glacial Maximum. Earth Surface Dynamics, 4(4), pp.831–869.

5

The Influence of Glacial Isostatic Adjustment on U.S. East Coast Rivers

5.1 Introduction

The growth and decay of continental ice sheets deform the solid Earth on the ~10^5-year timescales associated with Late Pleistocene glacial-interglacial cycles. This process has produced up to 10 mm/yr of crustal vertical motion hundreds of kilometers away from Late Pleistocene ice cover (Mitrovica & Milne, 2002; Whitehouse et al., 2007), matching or exceeding tectonic rock uplift rates in these regions (i.e. Moucha et al., 2008). Previous studies show that this process of glacial isostatic adjustment (GIA) produces sufficient crustal deformation to control rates of river incision (Wickert et al., 2019)), river drainage patterns (Wickert, 2016), river diversions (Pico et al., 2018), and delta accumu-

A version of this chapter is under review as a manuscript coauthored with Jerry X. Mitrovica, Taylor Perron, and Ken L. Ferrier in *Earth & Planetary Science Letters*

lation rates (Whitehouse et al., 2007).

Because ice sheets blanketing North America contained the largest excess ice volume at the Last Glacial Maximum (LGM, 26-20 ka; Clark et al. 2009), the U.S east coast experienced high rates of GIA-induced crustal deformation (∼10 mm/yr), as it is located on the formerly uplifted region, or peripheral bulge, surrounding the Laurentide Ice Sheet. The eastern Laurentide Ice Sheet began growing rapidly around 50-35 ka, according to inferences from sea-level markers along the U.S. mid-Atlantic coast (Pico et al., 2017), and initiated uplift along the U.S. east coast as the solid Earth adjusted to an expanding ice load. During the peripheral bulge growth phase, various rivers along the U.S. east coast, including the Hudson, Potomac, Susquehanna, and Delaware, experienced major changes in their evolution. Although deglaciation was rapid after the LGM, the eastern sector of the Laurentide Ice Sheet remained a major ice load until the early Holocene (∼11 ka; Dyke, 2004), such that subsidence rates from 20 to 10 ka in the U.S. mid-Atlantic region were slower than GIA-induced uplift rates during the peripheral bulge growth phase. Here we investigate the potential role of GIA-driven crustal deformation in the evolution of these four major rivers on the U.S. Atlantic coastal plain.

5.2 Background

5.2.1 U.S. east coast rivers during peripheral bulge growth

Transitions in river dynamics are recorded in the Hudson, Delaware, Susquehanna, and Potomac Rivers during the period ∼40-10 ka. In the ancestral Hudson River, sediment cores and seismic reflection surveys record an eastward diversion at ∼30 ka (Carey et al., 2005; Knebel et al., 1979). Sediment cores sampling fluvial deposits in the lower reaches of the Delaware River record a switch from incision to aggradation in an estuarine and organic-rich environment from 40 to 25 ka (Stanford et al., 2016). Stanford et al. (2016) argue that the Delaware River fully diverted eastward to the Rari-

tan drainage basin after 25 ka based on correcting the shallow present-day profile of the Delaware River with a linearly projected forebulge reconstructed from proglacial lake shorelines. In contrast to aggradation in the Delaware, an incisional pulse occurred in the Susquehanna and Potomac Rivers from 30 to 14 ka and 33 to 13 ka, respectively, with erosion rates more than doubling compared to those in the previous interval (Bierman, 2015; Reusser et al., 2006, 2004). Reusser et al. (2006) argue that this pulse of incision reflected a wider regional change in river dynamics rather than an increase in glacial meltwater flux, given that erosion rates in the partly glaciated Susquehanna and the unglaciated Potomac were comparably high during the incision pulse.

Each of these transitions – whether a diversion or a change in the rate of incision or aggradation – has been interpreted as a consequence of crustal deformation associated with the growth of the peripheral bulge of the Laurentide Ice Sheet. Studies of the Delaware and Hudson River have speculated that the peripheral bulge played an important role in the shift to aggradation in the Delaware (Stanford et al., 2016) and the eastward diversion of the Hudson (Knebel et al., 1979). Pico et al. (2018) forced a landscape evolution model with numerical predictions of GIA and found that crustal uplift caused by a rapid growth of the Laurentide Ice Sheet is consistent with an eastward diversion of the Hudson River at ∼30 ka. The high incision rates in the Potomac and Susquehanna from ∼30 to 15 ka have been qualitatively linked to regional changes in precipitation, rapid base-level fall, or uplift of the peripheral bulge (Reusser et al., 2006).

Here we test whether GIA can quantitatively explain the observed trends in river regime (incision vs. aggradation) in the Susquehanna, Potomac and Delaware Rivers. We reconstruct topography based on GIA simulations to determine changes to river channel slope and drainage area in each of these rivers. We then estimate the resulting perturbation to sediment transport capacity and compare these changes to the recorded changes in sedimentation and erosion rates.

5.2.2 GIA and ice history constraints from 120 to 26 ka

The growth and decay of continental ice sheets drive a complex pattern of sea-level (or equivalently topographic) change. In the simulations discussed herein, we perform GIA calculations based on the theory and pseudo-spectral algorithm described by Kendall et al. (2005) with a spherical harmonic truncation at degree and order 256. These calculations include the impact of load-induced Earth rotation changes on sea level (Milne & Mitrovica, 1996) as well as evolving shorelines and the migration of grounded, marine-based ice (Johnston, 1993; Kendall et al., 2005; Lambeck et al., 2003; Milne et al., 1999). Our predictions require models for Earth's viscoelastic structure and the history of global ice cover. We use an Earth model with upper and lower mantle viscosities of 0.5 x 10^{21} Pa s and 1.5 x 10^{22} Pa s, respectively; these values are consistent with inferences from GIA analyses of sea-level highstands along the U.S. mid-Atlantic extending from Marine Isotope Stages (MIS) 5 to 3 (Creveling et al., 2017; Pico et al., 2017; Potter & Lambeck, 2003).

A major challenge in selecting an ice history across the glacial build-up phase is the sparsity of geologic data constraining global mean sea level (GMSL) and continental ice extent. During the glacial build-up phase, global sea level was lower than it is today, and subsequent sea-level rise during the last deglaciation (26 ka to present) destroyed or submerged the majority of sea-level records. In addition, as the Laurentide Ice Sheet grew to its maximum extent at the LGM, it destroyed most evidence of prior ice margins (Clark et al., 1993; Dyke et al., 2002). Recent GIA modeling studies have refined the pace of global sea-level fall leading into the LGM (Pico et al., 2016), and an analysis of sea-level data on the U.S. east coast (Pico et al., 2017) supports field evidence for a late and rapid glaciation of the eastern sector of the Laurentide Ice Sheet (Dalton et al. 2016; Carlson et al., 2018). In the following simulations we revise the standard ICE-5G ice history (Peltier & Fairbanks 2006; black line in Figure 1C) in accordance with these recent analyses to construct an ice model we term ICE-PC2. We use a peak GMSL value during MIS 3 of -37.5 m at 44 ka (Pico et al., 2016). Second, we

use GMSL values of -15 m and -10 m for MIS 5a (80 ka) and 5c (100 ka), respectively; these values are within bounds (5a: -18 m to 0 m, 5c: -20 m to 1 m) derived by Creveling et al. (2017) on the basis of globally distributed sea level markers from both periods (blue; Figure 1B). Finally we require that the eastern section of the Laurentide Ice Sheet is ice-free from 80 to 44 ka, and grows rapidly to its LGM extent as in Pico et al. (2018). GIA simulations are primarily sensitive to total loads, and therefore predictions for the U.S. east coast are robust to changes in the ice margin geometry of ICE-PC2.

Our aim is to determine the extent to which GIA processes, in particular the growth of the peripheral bulge of the Laurentide Ice Sheet, exerted control on the abrupt transitions in river dynamics recorded during the last glacial cycle along the U.S. east coast. We model GIA-corrected topography during the interval when major geomorphic changes are recorded in U.S. mid-Atlantic rivers. Specifically, we use ice history ICE-PC2 and focus on topographic changes from 36 to 20 ka, as this period encompasses maximum rates of crustal deformation due to the growth of the peripheral bulge of the Laurentide Ice Sheet. These rates are characterized by a general north-south gradient in uplift, in addition to lateral variations caused by the distribution of ice lobes and the effect of ocean loading near the coasts (Pico et al., 2018). Ice lobes extending south from the main Laurentide Ice Sheet represent local loads that superimpose smaller peripheral bulges on the longer wavelength peripheral bulge that extends across the entire United States (Figure 1A).

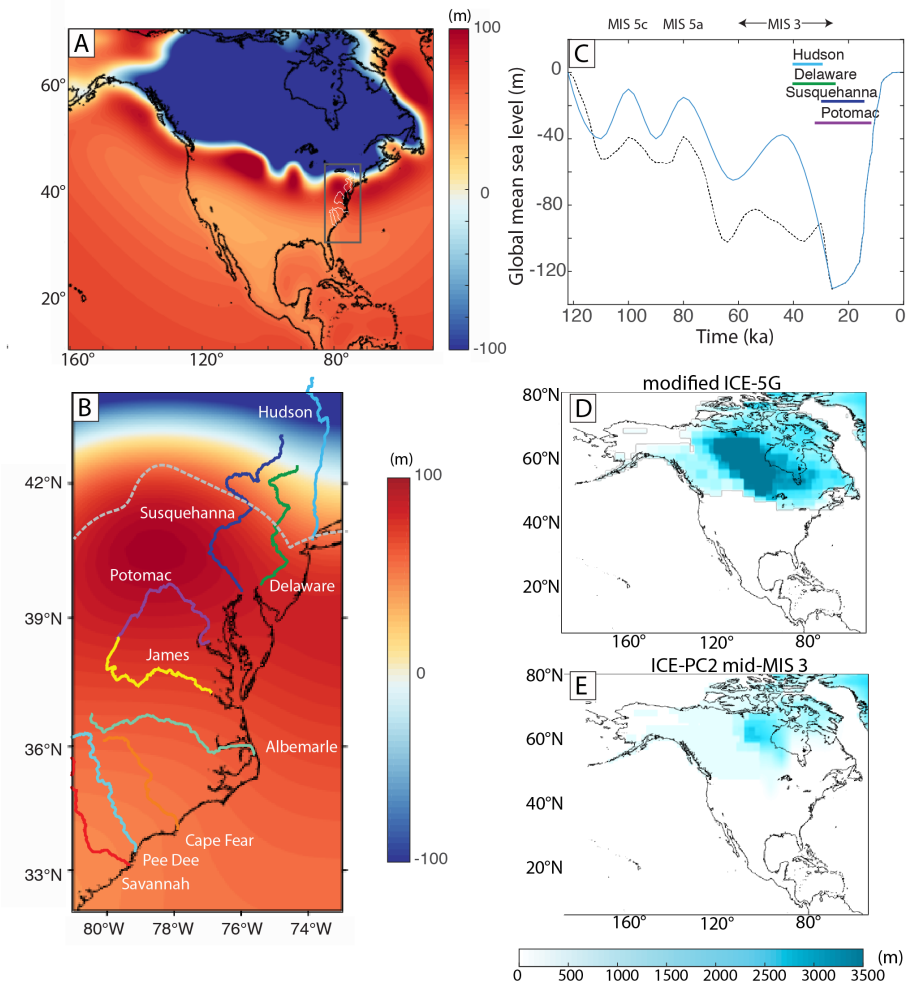

FIGURE 5.1: A. Predicted topographic changes from 36 to 20 ka using ice history ICE-PC2 (uplifted regions in red) over North America. Rectangle indicates the region shown in B, where major U.S. east coast rivers are labeled. The approximate extent of ice at the Last Glacial Maximum is shown by the dashed gray line. C. Global mean sea level history for ice history ICE-5G (dotted black) and ICE-PC2 (blue). Horizontal lines indicate dates of observed river dynamic changes in labeled rivers. Remaining two frames show the geographic extent of ice at 44 ka (mid-MIS 3) in (D) ICE-5G and (E) ICE-PC2.

5.3 Methods: GIA effects on river channels

The tendency of a riverbed to erode or aggrade depends on the sediment transport capacity of the river (Qc) relative to the sediment supply from upstream (Qs). If the transport capacity of a river reach exceeds the upstream sediment supply, the bed will erode. If the upstream sediment supply exceeds the transport capacity, the bed will aggrade. Both sediment supply and transport capacity may have varied in U.S. mid-Atlantic rivers from 36 to 20 ka during the time interval of peripheral bulge growth. For example, changing patterns of glacial and periglacial erosion could have altered sediment supply volume or grain size through time, and changing precipitation patterns (and ice melting, in the case of glaciated basins) could have altered sediment transport capacity. Given the lack of detailed information about sediment supply and climate variability from 36 to 20 ka in the study region, we focus on perturbations to sediment transport capacity associated with GIA, and neglect changes in sediment supply or precipitation-induced changes in sediment transport capacity. For simplicity we ignore the non-linear influence of sediment cover in the channel (Sklar & Dietrich, 2001, 2004) and a threshold for bedrock incision (Snyder et al., 2003). We test whether modeled GIA-induced changes in transport capacity can explain the sign of observed changes in fluvial sedimentation (erosion vs. aggradation).

Effects of slope and drainage area on sediment transport capacity

The sediment transport capacity Qc of a river reach depends on the bed shear stress. In studies of long-term river profile evolution, it is common to use expressions for runoff, river channel hydraulic geometry, and steady, uniform open-channel flow of an effective water discharge to relate the bed shear stress to the upstream drainage area (A) and the local channel bed slope (S), yielding (e.g., Willgoose et al., 1991; Howard et al., 1994)

$$Qc = kAmSn$$

, (1)

where k is a transport coefficient and the exponents m and n are constants. We assume that k, m and n remain constant and use GIA-driven changes in slope and drainage area to calculate the perturbation to sediment transport capacity Qc for each river from 36 to 20 ka. The right-hand side of Equation 1 has the same form as the channel incision rate in the stream power equation for bedrock channel incision (Howard & Kerby, 1983; Seidl & Dietrich, 1992; Whipple & Tucker, 1999). We therefore use the product AmSn as a generic proxy for either sediment transport capacity or bedrock incision rate. For cases in which a bedrock channel experienced a change in incision rate, we set m = 0.5 and n = 1, consistent with estimated values worldwide that typically put m/n close to 0.5 (Harel et al. , 2016) and more generally in the range 0.35-0.6 (Whipple & Tucker, 1999). For cases in which a channel experienced aggradation or erosion of sediment, we set m = 1.5 and n = 1, consistent with field data (e.g., Massong & Montgomery, 2000) and with previous estimates that suggest (m - 1)/n □ 0.5 for transport-limited channels (Whipple & Tucker, 2002).

To calculate the change in sediment transport capacity or bedrock incision rate from Equation 1, we first modeled the GIA-induced changes in river channel slope and drainage area for the rivers shown in Figure 1A. We then calculated fractional changes in the sediment transport capacity or bedrock incision rate of these rivers during the growth of the peripheral bulge from 36 to 20 ka using the modeled changes in channel slope and drainage area (Equation 2). For a change in transport capacity (Qc), for example,

$$\frac{\Delta Q_c}{Q_{c,36ka}} = \frac{A_{20ka}^m S_{20ka}^n}{A_{36ka}^m S_{36ka}^n} - 1$$

Although we use the quantity on the right-hand side of Equation 2 as a proxy for either a change in bedrock incision rate or a change in transport capacity, hereafter we refer to this quantity as ΔQc/Qc for simplicity.

5.3.1 Calculating the impact of GIA on slope and drainage area

We used steepest-descent flow routing to identify river flow paths and compute drainage areas. We used the HydroSHEDS North America 30-second resolution void-filled DEM (Lehner et al., 2008) and filled lakes and depressions to obtain continuous paths of descent to the ocean (Barnes et al., 2014). We identified major rivers by tracing the steepest-descent directions along the path of maximum drainage area. Next, we extracted modern river profiles starting at the drainage divide for the Hudson, Delaware, Susquehanna, and Potomac (Figure 2). We then calculated reconstructed river profiles at 36 and 20 ka by applying the same flow routing algorithms to the void-filled and sink-filled topography at 36 and 20 ka, where upstream distance was measured from the modern coastline, before and after the GIA-induced crustal deformation shown in Figure 1A.

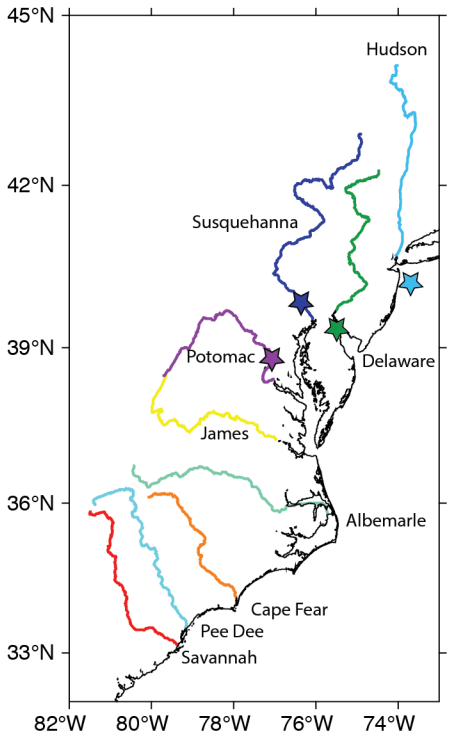

FIGURE 5.2: A. Present-day channel paths of major rivers along the U.S. east coast. Locations of published observations of river changes at ~40-10 ka are shown by stars.

Predicted river channel locations varied from 36 to 20 ka as a result of GIA-induced topographic changes (Appendix Figure 1). Therefore, we sought to compare slopes and drainage areas on the respective channel location for each time. In the following calculations we used the upstream distance (measured from the modern coastline) to compare slope and drainage area changes. Then we mapped these changes onto the 36 ka river path (calculated starting from the modern coastline). Because the sinuosity of rivers may have changed from 36 to 20 ka, a given upstream distance may not represent the same location on both river channels. We compared the upstream distance on each location of the river channel, and showed that these differed by less than 10 km, except in the upper reaches of the Susquehanna and the Delaware (Appendix Figure 2). Some rivers, including the Albe-

marle, experienced small-scale avulsions or meanders in the modeled topography from 36 to 20 ka. These path changes have a small impact (< 4 km) on the upstream distance calculated at each location (Appendix Figure 2), and comparing slopes at these sites can result in short-scale variations as the channel location switches.

5.3.2 Changes in slope

We used the modeled crustal deformation field shown in Figure 1A to produce a map of the fractional change in river channel slope from 36 to 20 ka for all rivers in Figure 2. First, we reduced noise associated with short-wavelength variations in the reconstructed topography by applying a 20 km-window smoothing filter to the river elevation profiles. We then calculated slope using a 10 km baseline and found the fractional change in slope from 36 to 20 ka as (S20 ka – S36 ka) / S36 ka. Because the rivers turn sharply through the smooth field of GIA-induced topographic changes, our calculations indicate sudden changes in slope along the rivers in certain locations (Figure 4A). The filtering we applied does not affect the GIA signal, since the smoothing window is considerably smaller than the wavelength of the GIA-induced crustal deformation field.

5.3.3 Changes in drainage area

We computed the percent change in drainage area along each river using the topography predicted from our GIA simulations at 36 ka and 20 ka. In Figure 3 we present maps of drainage basins at 36 and 20 ka. To estimate total changes in drainage area due to GIA-induced deformation alone, rather than additionally including the effects of changes in drainage area due to coast migration resulting from sea-level change, we calculated the total drainage area at the shoreline predicted at 36 ka using ice history ICE-PC2 (Appendix Table 1). At every location along the channel, we then calculated fractional changes in upstream drainage area as (A20 ka – A36 ka) / A36 ka.

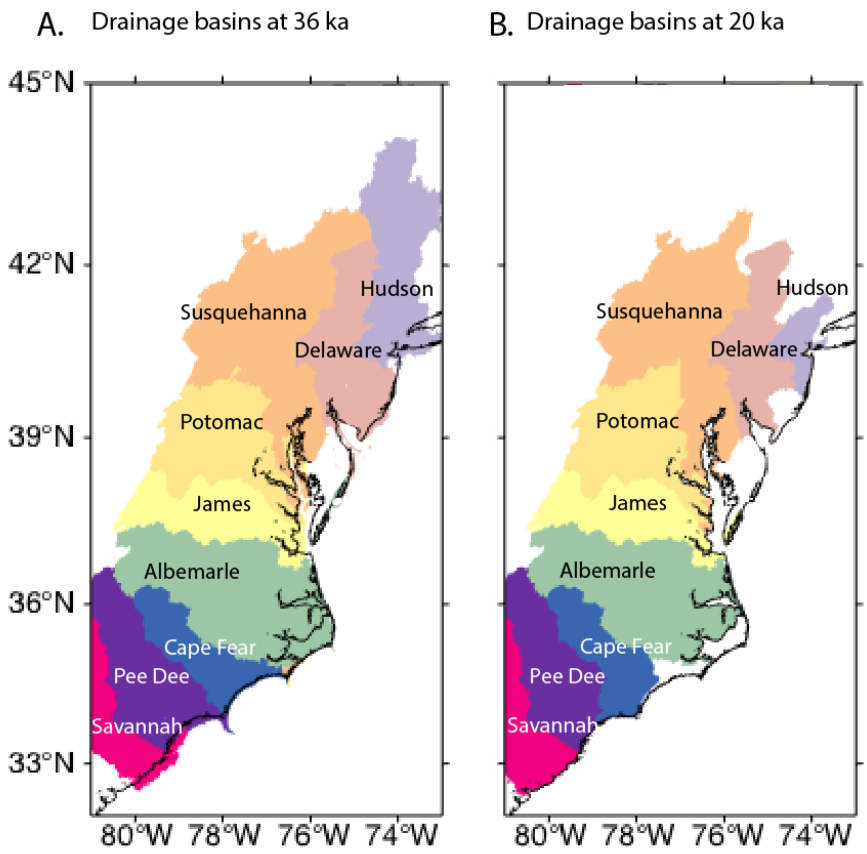

FIGURE 5.3: Drainage basins at 36 ka (A) and 20 ka (B) using the reconstructed paleotopography driven by ice history ICE-PC2.

5.4 Results & Discussion: GIA effects on river channels

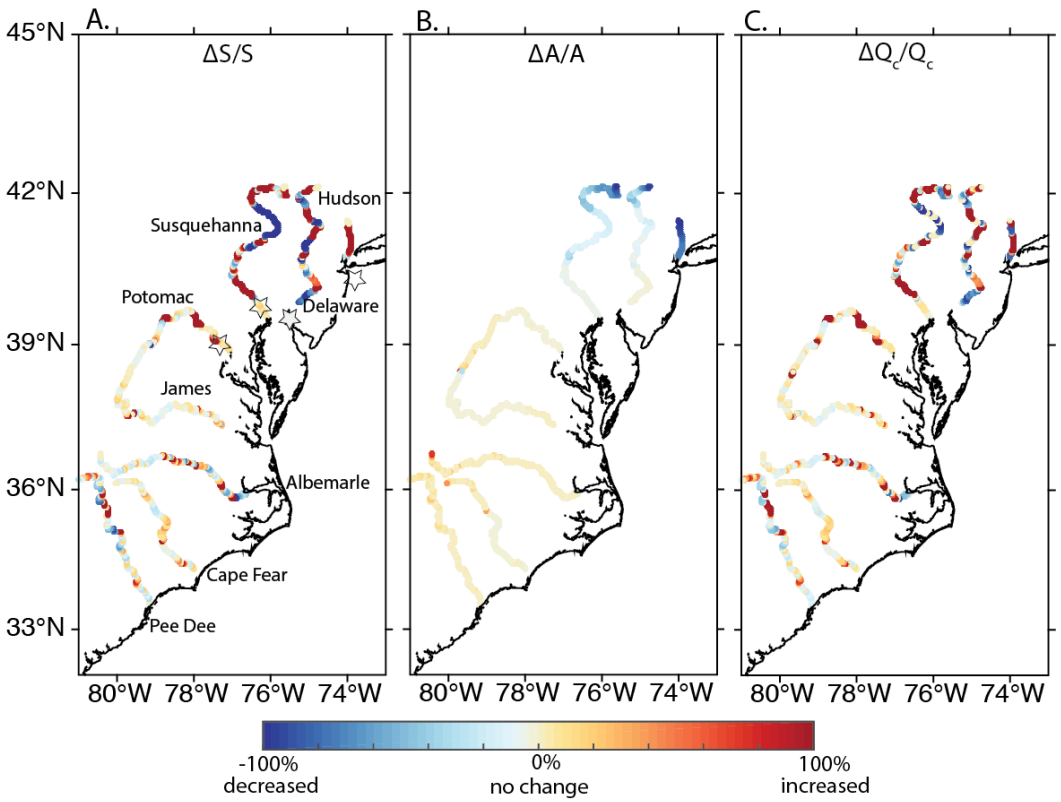

Figure 5.4: GIA-induced percent changes from 36 to 20 ka in (A) channel slope (S) (B) drainage area (A) and (C) sediment transport capacity Qc, driven by ice history ICE-PC2 (Figure 1A). Stars indicate locations of published observations of river changes at ~40-10 ka.

5.4.1 Impact of GIA on river channel slopes

Figure 4A shows regions where the slope steepens (warm colors) and where slope shallows (cool colors). GIA-induced changes in slope are a result of the channel crossing through the crustal deformation field in Figure 1A, in addition to changes in channel location, and are not simply correlated with proximity to the ice load.

While many stretches of rivers show little change in slope, with values close to 0%, several rivers show large percent differences in channel slope. In the Potomac River, channel slope increases significantly in the 100 km stretch upstream of the modern coastline (Figure 4A). This includes a prominent peak within this stretch of river, where slope increases by 370%, corresponding well with the location ~25 km upstream of the modern coast where rapid erosion rates have been measured (Reusser et al., 2004).

In contrast to the GIA-driven increase in channel slope in the Potomac, the Delaware River channel slope shallows in the first 70 km upstream of the modern coastline (Figure 4A). The slope decrease is -20% at the modern coastline, near the site in the Delaware Bay that records increased deposition (Stanford et al. 2016). The change in slope ranges from a maximum of -97% at a site 25 km upstream to 0% at a site 68 km upstream from the modern coastline. The Hudson River's slope is predicted to increase sharply, although the channel locations at 36 and 20 ka differ substantially (see Appendix Figure 1), since a portion of the Hudson's drainage basin was modeled as temporarily captured by another river during the growth of the peripheral bulge. Finally, we note there is no slope change in the Susquehanna near a location ~35 km upstream where increased incision rates were measured by Reusser et al. (2004). Instead, the modeled channel slope within the Susquehanna only changes starting 80-100 km upstream of the modern coastline (Figure 4A), with slopes increasing by as much as 300%.

5.4.2 Impact of GIA on drainage area

Major reductions in drainage area occur along the Hudson, Delaware, and Susquehanna Rivers, (Figure 4B), while the other rivers in the study area experience minor changes in drainage area. In the case of the Hudson River, the total drainage area at the 36 ka coastline is reduced by a factor of 5, from 5.3x104 at 36 ka to $1.1x10^4$ km^2 at 20 ka (Appendix Table 1). This change in drainage area occurs because GIA-induced crustal deformation causes a large displacement of the drainage divide

that defines the basin boundary (see Appendix Figure 1 for predicted channel locations at 36 and 20 ka; Figure 3). The Susquehanna River total drainage area is similarly displaced by the growth of the peripheral bulge, although by only ~7%, from 10.1×10^4 to 9.4×10^4 km^2 (Appendix Table 1).

5.4.3 Impact of GIA on sediment transport capacity

We calculated changes to Qc using Equation 2, based on the calculated changes to channel slope and drainage area (Figure 4A/B). Figure 4C shows a map of percent changes to Qc for the rivers in Figure 2.

Without estimates of sediment supply rate Qs from 36 to 20 ka, we cannot quantify the magnitude of Qc relative to Qs, and therefore we cannot determine whether the study rivers were likely to have eroded or aggraded during this time period. However, we can gain insight by considering the simple scenario in which Qc and Qs are in balance at 36 ka everywhere along each river's length and in which Qs remains steady from 36 to 20 ka. In this scenario, an increase in Qc would imply a tendency to erode the riverbed, whereas a decrease in Qc would imply a tendency to deposit sediment and aggrade. Under these conditions, the zones of increased transport capacity (warm colors in Figure 4C) would be expected to have eroded from 36 to 20 ka, whereas the blue zones would be expected to have aggraded. Calculations using m = 1.5, the case associated with transport-limited channels, are shown in Appendix Figure 3. Changes to Qc in the transport-limited case are only substantially different from the detachment-limited case in rivers with large changes in drainage area, because only in those cases does the different value of m have a substantial effect. We next discuss how our model calculations compare to existing observations for each river.

5.4.4 The Hudson and Delaware Rivers

Modeled transport capacity Qc in the Hudson River sharply increases from 20 to 60 km upstream of the modern coastline, though at the modern coastline modeled Qc is reduced by 98% (Figure 4C).

Because the Hudson's drainage area is drastically reduced, it is the only river with substantially different results using the transport-limited exponents (Appendix Figure 3): in this case, modeled Qc is reduced throughout the entire 0-80 km stretch upstream of the modern coastline. A modeled decrease in slope by 30% near the modern coastline is compounded by a drastic reduction of drainage area (Figure 3). The latter result is consistent with a model of GIA-driven displacement of drainage divides throughout North America over the last deglaciation (Wickert, 2016). To the extent that reductions of both slope and drainage area imply an increased tendency to aggrade, this result is consistent with evidence of an eastward diversion of the Hudson River ~30 ka (Carey et al., 2005) given that increased aggradation would shallow slopes and make diversions more likely. On the other hand, it is possible that drainage area reduction lowered upstream sediment supply, a factor we do not consider here. Landscape evolution model simulations forced by GIA predictions replicate this recorded eastward diversion (Pico et al., 2018).

In the lower reaches of the Delaware River (0-65 km upstream of the modern coastline), modeled transport capacity Qc is reduced by ~10-98% (Figure 4C). Our predictions of Qc reductions are in line with observations of increased aggradation from 40-25 ka in the lower reaches of the Delaware (Stanford et al. 2016). Our modeling indicates a reversed slope may have occurred in the Delaware from 20-35 km upstream of the modern coastline, which supports the suggestion that GIA-induced slope changes, in conjunction with increased aggradation, might have reversed local channel slope and induced a major avulsion (Stanford et al., 2016). Confirming an eastward diversion of the Delaware River near Trenton into the Raritan drainage basin will require additional data such as provenance studies on sediment cores near the mouth of the Raritan.

5.4.5 The Susquehanna and Potomac Rivers

Modeled changes in transport capacity Qc peak at various locations along the Potomac River (Figure 4C), coinciding with regions where the slope steepened (Figure 4A) as the channel crosses a gra-

dient in the GIA-induced crustal deformation field (Figure 1A). Modeled Qc increased by 360% at this peak, resulting in a more than doubling of the sediment transport capacity. Erosion rates measured ∼25 km upstream of the modern coastline show that incision rates from 33 to 13 ka increased by at least a factor of two relative to those in the period 85-33 ka (Reusser et al., 2004). To the extent that increases in sediment transport capacity imply an increased tendency for river incision, our model is consistent with this accelerated incision in the Potomac.

The modeled transport capacity Qc in the Susquehanna increases from 36 to 20 ka in a stretch along the lower reaches (beginning 80 km upstream of the modern coastline) and decreases in its upper reaches (Figure 4C). Nevertheless, the region where transport capacity more than doubles (warm colors) does not coincide with the location 35 km upstream of the modern shoreline where measurements indicate an incisional pulse (Reusser et al., 2006). At this location, our model shows no change in Qc (Figure 4). Our simulations suggest that a mechanism other than GIA, such as meltwater associated with the glaciated region of the Susquehanna, may be responsible for the observed increase in erosion rates from 30-14 ka.

To investigate other possible explanations for the differing responses of the Potomac and Susquehanna, we consider regional factors that could have influenced both drainage basins, including the time-dependent response to base level fall and changes in precipitation. We calculate the transit time, τ, for a knickpoint to propagate from base level to a distance x upstream as (Royden & Perron, 2013; Goren, 2016)

$$\tau(x) = \int_0^x \frac{dx'}{kAx'^m}$$

In solving this equation, we use k = 2.5 x10^{-6} yr^{-}1 and m = 0.5, as in Miller et al. (2013), and the parameter x is the along-channel distance upstream of the modern shoreline. Following this approach, we estimate a value for τ of 50 ky for the Potomac at a location 25 km upstream from

the modern coastline, and 33 ky for the Susquehanna at a location 35 km upstream of the modern coastline (Appendix Figure 4). Thus, for this value of k, if knickpoints had been generated at the coast at the LGM (26 ka), they should still be downstream of the locations of accelerated incision on the Potomac and Susquehanna, implying that propagation of coastally-generated knickpoints could not have driven the observed changes in incision rate. We stress, however, that if the relevant k value for the lower reaches of these rivers were higher than the one we applied by a factor of 3-5, or if knickpoint propagation were accelerated by factors not accounted for in the stream power law (e.g., changes in sediment supply or grain size), then knickpoints could have propagated past the locations of accelerated incision within the relevant time window, implying that the observed changes in incision rate could have been generated by knickpoint propagation.

Another argument against knickpoint-driven accelerated incision is that the coastal topography is not conducive to generating knickpoints. The continental shelf offshore of these modern-day river mouths in Chesapeake Bay is broad and low-gradient, such that even a large fall in local sea level would result in a relatively small vertical perturbation in the river profile. Large knickpoints are thus unlikely to form at these river mouths, even under large changes in sea level.

We consider it less likely that the observed increases in river incision were caused by changes in river water discharge. If bedrock river incision, the mechanism inferred for both the Potomac and Susquehanna Rivers, scales with the square root of basin-averaged precipitation rate, as previous studies suggest (e.g., Ferrier et al., 2013), then the observed doubling in river incision rate would require precipitation to have quadrupled. Pollen records and global circulation models, however, suggest that the U.S. mid-Atlantic was cooler and drier leading into the Last Glacial Maximum than during the Holocene (Leigh et al., 2004), and thus river water discharge was likely lower.

Although our analysis is consistent with the hypothesis that GIA-induced crustal deformation influenced the evolution of several US mid-Atlantic rivers substantially, additional factors beyond those considered here could have altered patterns of channel incision and aggradation. The extent

and location of ice and permafrost could also have altered erosion rates and processes in rivers, as well as affecting sediment supply (Herman et al., 2011; West et al., 2013). Furthermore, and calculating sediment transport capacity in glaciated regions would require considering different regimes of erosion and sediment transport. In our study area, this is particularly relevant for the Hudson, Delaware, and Susquehanna rivers, which were either almost entirely glaciated (Hudson) or glaciated in their northern halves (Delaware and Susquehanna) at the LGM (Figure 1B).

5.4.6 Sensitivity to Earth and ice models

Modeled crustal deformation using GIA simulations are sensitive to the choice of ice history and Earth viscosity structure. We assess the sensitivity of our results to these model inputs by considering an alternate Earth model and ice history. In particular, we adopt an Earth structure characterized by upper and lower mantle viscosities of 0.2 x10^{21} Pa s and 5 x10^{22} Pa s, respectively, i.e., a model with a weaker upper mantle and stiffer lower mantle relative to the Earth model adopted in simulations shown in Figure 1 (Figure 5A). Predicted percent slope change (and transport capacity) are of larger magnitude using this Earth model, but trends in each river are similar (Figure 5C; Appendix Figure 5).

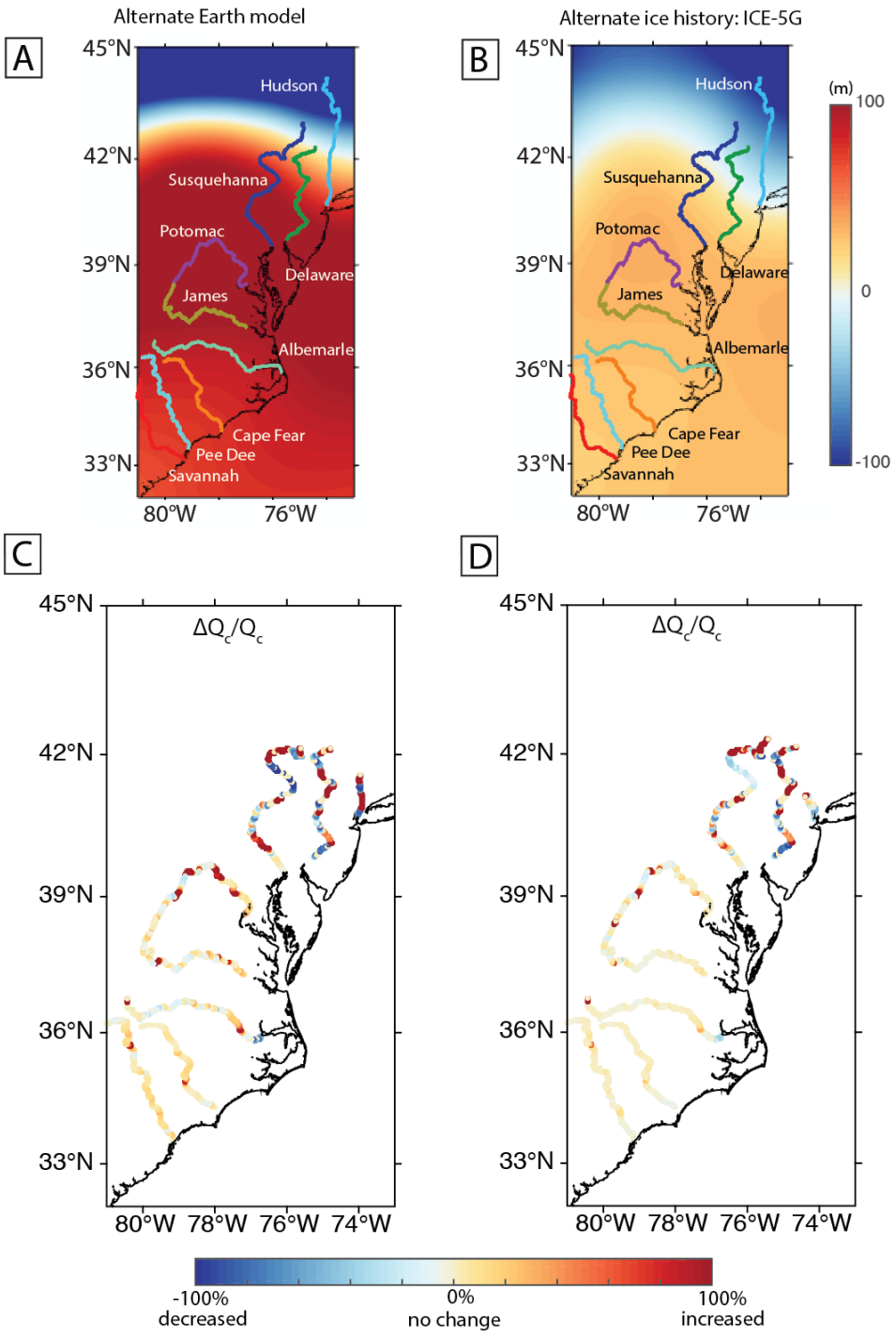

FIGURE 5.5: Topographic change from 36 to 20 ka predicted using an alternate Earth model (A) or ice history ICE-5G (B). Percent change in transport capacity using alternate Earth model (C) and alternate ice history ICE-5G (D).

We assess the sensitivity of our results to the selected ice history by performing GIA simulations with ice history ICE-5G (Peltier & Fairbanks, 2006). In the ICE-5G ice history (Figure 1B), the Laurentide Ice Sheet grows steadily over the glacial phase such that by 36 ka, the predicted topography is largely in isostatic equilibrium (Figure 5B). In this case, we find that the predicted changes in channel slope and transport capacity are minor for most rivers. The Delaware and Susquehanna Rivers are exceptions to this general trend (Figure 5D; Appendix Figure 6). The Delaware is predicted to have a reduction in Qc (Figure 5D), similar to the results using ice history ICE-PC2 (Figure 4C). In contrast to the results in Figure 4, the Potomac shows no change to Qc (Figure 5D). Similarly, the Susquehanna shows no change to Qc at the location of observation (Figure 5D). To the extent that changes in Qc indicate changes in erosion and deposition, the topographic changes predicted using ICE-5G are consistent with the observed aggradation in the Delaware, but are not consistent with the observed incision in the Potomac.

The improved fit with the Potomac observations of the ICE-PC2 history, used in the main results and constrained by sea-level records along the U.S. mid-Atlantic, supports an increasing body of evidence for a rapidly growing eastern Laurentide Ice Sheet, beginning ~50-35 ka (Carlson et al., 2018; Dalton et al., 2019; Dalton et al., 2016; Pico et al., 2017).

5.5 Conclusion

In this study, we explored the impact of the Laurentide peripheral bulge growth on rivers along the U.S. mid-Atlantic during the last glacial cycle. Our GIA simulations produced crustal deformation rates on the order of 10 mm/yr along the U.S. mid-Atlantic during the phase of peripheral bulge growth near the end of the last glaciation. Using this GIA model, we calculated changes to river channel slope and drainage area over the time period of particularly rapid peripheral bulge growth (36-20 ka) and used these changes to calculate perturbations to sediment transport capacity or bedrock incision rate in river channels. We then explored connections between these model

calculations and previously documented transitions in river dynamics in the Hudson, Delaware, Susquehanna, and Potomac Rivers during the interval of peripheral bulge growth. Assuming that sediment supply did not change significantly over this time, we found that GIA-driven changes in sediment transport capacity or bedrock incision rate are consistent with the observed patterns of aggradation in the Delaware, incision in the Potomac, and a diversion in the Hudson River, but are inconsistent with an erosional pulse observed in the Susquehanna. Our analyses add to a growing body of evidence showing that GIA-induced crustal deformation can drive river evolution over millennial timescales.

5.6 Acknowledgements

We appreciate thoughtful discussions with P. Bierman, which improved the content of this manuscript. T.P. acknowledges funding from NSF-GRFP. T.P. and J.X.M acknowledge funding from Harvard University. J.T.P. thanks Harvard University for a sabbatical stay. K.L.F. acknowledges support from NSF grant EAR-1525922 and ACS-PRF grant 58209-DNI8.

5.7 References

Barnes, R., Lehman, C., & Mulla, D. (2014). Priority-Flood: An Optimal Depression-Filling and Watershed-Labeling Algorithm for Digital Elevation Models. Computers and Geosciences, 62(2), 117–127.

Bierman, P. (2015). The incision history of the Great Falls of the Potomac River—The Kirk Bryan field trip. Geological Society of America, Field Guid(40), 1–10. http://doi.org/10.1130/2015.0040(01)

Carey, J. S., Sheridan, R. E., Ashley, G. M., & Uptegrove, J. (2005). Glacially-influenced late Pleistocene stratigraphy of a passive margin: New Jersey's Record of the North American ice sheet. Marine Geology, 218(1–4), 155–173. http://doi.org/10.1016/j.margeo.2005.04.006

Carlson, A. E., Tarasov, L., & Pico, T. (2018). Rapid Laurentide ice-sheet advance towards southern last glacial maximum limit during marine isotope stage 3. Quaternary Science Reviews, 196, 118–123. http://doi.org/10.1016/j.quascirev.2018.07.039

Clark, P. U., Clague, J. J., Curry, B. B., Dreimanis, A., Hicock, S. R., Miller, G. H., … Vincent, J. S. (1993). Initiation and development of the Laurentide and Cordillean Ice Sheets following the Last Interglaciation. Quat. Sci. Reviews, 12, 79–114.

Clark, P. U., Dyke, A. S., Shakun, J. D., Carlson, A. E., Clark, J., Wohlfarth, B., … McCabe, a M. (2009). The Last Glacial Maximum. Science (New York, N.Y.), 325(5941), 710–4. http://doi.org/10.1126/science.1172873

Creveling, J. R., Mitrovica, J. X., Clark, P. U., Waelbroeck, C., & Pico, T. (2017). Predicted bounds on peak global mean sea level during marine isotope stages 5a and 5c. Quaternary Science Reviews, 163, 193–208. http://doi.org/10.1016/j.quascirev.2017.03.003

Dalton, A. S., Finkelstein, S. A., Barnett, P. J., & Forman, S. L. (2016). Constraining the Late Pleistocene history of the Laurentide Ice Sheet by dating the Missinaibi Formation, Hudson Bay Lowlands, Canada. Quaternary Science Reviews, 146, 288–299. http://doi.org/10.1016/j.quascirev.2016.06.015

Dalton, A. S., Finkelstein, S. A., Forman, S. L., Barnett, P. J., Pico, T., & Mitrovica, J. X. (2019). Was the Laurentide Ice Sheet significantly reduced during Marine Isotope Stage 3□? Geology, 47(2), 111–114.

Dyke, A. S. (2004). An outline of North American Deglaciation with emphasis on central and northern Canada. In J.Ehlers & P.L.Gibbard (Eds.), Quaternary Glaciations-Extent and Chronology: Part II: North America (pp. 373–424).

Dyke, A. S., Andrews, J. T., Clark, P. U., England, J. H., Miller, G. H., Shaw, J., & Veillette, J. . (2002). The Laurentide and Innuitian Ice Sheet during the Last Glacial Maximum The Laurentide and Innuitian ice sheets during the Last Glacial Maximum. Quat. Sci. Reviews, 21, 9–31. http://doi.org/10.1016/S0277-3791(01)00095-6

Ferrier, K. L., Huppert, K. L., & Perron, J. T. (2013). Climatic control of bedrock river incision.

Nature, 496(7444), 206–209. http://doi.org/10.1038/nature11982

Goren, L. (2016). A theoretical model for fluvial channel response time during time-dependent climatic and tectonic forcing. Geophysical Research Letters, (1), 753–763. http://doi.org/10.1002/2016GL070451

Harel, M., Mudd, S. M., & Attal, M. (2016). Global analysis of the stream power law parameters based on worldwide Be denudation rates. Geomorphology, 268, 184–196. http://doi.org/10.1016/j.geomorph.2016.05.035

Herman, F., Beaud, F., Champagnac, J., Lemieux, J., & Sternai, P. (2011). Glacial hydrology and erosion patterns□: A mechanism for carving glacial valleys. Earth and Planetary Science Letters, 310(3–4), 498–508. http://doi.org/10.1016/j.epsl.2011.08.022

Howard, A. D., Dietrich, W. E., & Seidl, M. A. (1994). Modeling fluvial erosion on regional to continental scales. Journal of Geophysical Research, 99.

Howard, A. D., & Kerby, G. (1983). Channel changes in badlands. Geological Society of America Bulletin, 94(June), 739–752.

Johnston, P. (1993). The effect of spatially non-uniform water loads on prediction of sea-level change. Geophysical Journal International, 114(3), 615–634. Retrieved from http://onlinelibrary.wiley.com/doi/10.1111/j.1365-246X.1993.tb06992.x/abstract

Kendall, R. A., Mitrovica, J. X., & Milne, G. A. (2005). On post-glacial sea level - II. Numerical formulation and comparative results on spherically symmetric models. Geophysical Journal International, 161(3), 679–706. http://doi.org/10.1111/j.1365-246X.2005.02553.x

Knebel, H. J., Wood, S. A., & Spiker, E. C. (1979). Hudson River□: Evidence for extensive migration on the exposed continental shelf during Pleistocene time. Geology, 7(May), 254–258.

Lambeck, K., Purcell, A., Johnston, P., Nakada, M., & Yokoyama, Y. (2003). Water-load definition in the glacio-hydro-isostatic sea-level equation. Quaternary Science Reviews, 22(2–4), 309–318. http://doi.org/10.1016/S0277-3791(02)00142-7

Lehner, B., Verdin, K., & Jarvis, A. (2008). New global hydrography derived from spaceborne elevation data. Eos, Transactions, AGU, 89(10), 93–94.

Leigh, D. S., Srivastava, P., & Brook, G. A. (2004). Late Pleistocene braided rivers of the Atlantic Coastal Plain , USA. Quat. Sci. Reviews, 23, 65–84. http://doi.org/10.1016/S0277-3791(03)00221-X

Massong, T. M., & Montgomery, D. R. (2000). Influence of sediment supply, lithology, and wood debris on the distribution of bedrock and alluvial channels. GSA Bulletin, (5), 591–599.

Miller, S. R., Sak, P. B., Kirby, E., & Bierman, P. R. (2013). Neogene rejuvenation of central Appalachian topography□: Evidence for differential rock uplift from stream pro fi les and erosion rates. Earth and Planetary Science Letters, 369–370, 1–12. http://doi.org/10.1016/j.epsl.2013.04.007

Milne, G. a., & Mitrovica, J. X. (1996). Postglacial sea-level change on a rotating Earth: first results from a gravitationally self-consistent sea-level equation. Geophysical Journal International, 126(3), F13–F20. http://doi.org/10.1111/j.1365-246X.1996.tb04691.x

Milne, G. A., Mitrovica, J. X., & Davis, J. L. (1999). Near-field hydro-isostasy: the implementation of a revised sea-level equation. Geophysical Journal International, 139, 464–482. http://doi.org/10.1046/j.1365-246x.1999.00971.x

Mitrovica, J. X., & Milne, G. a. (2002). On the origin of late Holocene sea-level highstands within equatorial ocean basins. Quaternary Science Reviews, 21(20–22), 2179–2190. http://doi.org/10.1016/S0277-3791(02)00080-X

Moucha, R., Forte, A. M., Mitrovica, J. X., Rowley, D. B., Quéré, S., Simmons, N. A., & Grand, S. P. (2008). Dynamic topography and long-term sea-level variations□: There is no such thing as a stable continental platform. Earth and Planetary Science Letters, 271, 101–108. http://doi.org/10.1016/j.epsl.2008.03.056

Peltier, W. R., & Fairbanks, R. G. (2006). Global glacial ice volume and Last Glacial Maximum duration from an extended Barbados sea level record. Quaternary Science Reviews, 25, 3322–3337. http://doi.org/10.1016/j.quascirev.2006.04.010

Pico, T., Birch, L., Weisenberg, J., & Mitrovica, J. X. (2018). Refining the Laurentide Ice Sheet at Marine Isotope Stage 3□: A data-based approach combining glacial isostatic simulations with a dynamic ice model. Quaternary Science Reviews, 195, 171–179. http://doi.org/10.1016/j.quascirev.2018.07.023

Pico, T., Creveling, J. R., & Mitrovica, J. X. (2017). Sea-level records from the U.S. mid-Atlantic constrain Laurentide Ice Sheet extent during Marine Isotope Stage 3. Nature Communications, 8(May), 15612. http://doi.org/10.1038/ncomms15612

Pico, T., Mitrovica, J. X., Braun, J., & Ferrier, K. L. (2018). Glacial isostatic adjustment deflects the path of the ancestral Hudson River. Geology, (7), 1–4.

Pico, T., Mitrovica, J. X., Ferrier, K. L., & Braun, J. (2016). Global ice volume during MIS 3 inferred from a sea-level analysis of sedimentary core records in the Yellow River Delta. Quaternary Science Reviews, 152, 72–79. http://doi.org/10.1016/j.quascirev.2016.09.012

Potter, E. K., & Lambeck, K. (2003). Reconciliation of sea-level observations in the Western North Atlantic during the last glacial cycle. Earth and Planetary Science Letters, 217(1–2), 171–181. http://doi.org/10.1016/S0012-821X(03)00587-9

Reusser, L., Bierman, P., Pavich, M., Larsen, J., & Finkel, R. (2006). An Episode Of Rapid Bedrock Channel Incision During The Last Glacial Cycle , Measured With 10Be. American Journal of Science, 306(February), 69–102.

Reusser, L. J., Bierman, P., Finkel, R., Bierman, P. R., Pavich, M. J., & Zen, E. (2004). Rapid Late Pleistocene Incision of Atlantic Passive-Margin River Gorges of Atlantic Passive-Margin. Science, 305(July). http://doi.org/10.1126/science.1097780

Royden, L., & Perron, J. T. (2013). Solutions of the stream power equation and application to the evolution of river longitudinal pro fi les. Journal of Geophysical Research□: Earth Surface, 118(May), 497–518. http://doi.org/10.1002/jgrf.20031

Seidl, M. A., & Dietrich, W. E. (1992). The Problem of Channel Erosion into Bedrock. Functional Geomorphology, 101–124.

Sklar, L. S., & Dietrich, W. E. (2001). Sediment and rock strength controls on river incision into bedrock, (12), 1087–1090.

Sklar, L. S., & Dietrich, W. E. (2004). A mechanistic model for river incision into bedrock by

saltating bed load, 40, 1–22. http://doi.org/10.1029/2003WR002496

Snyder, N. P., Whipple, K. X., Tucker, G. E., & Merritts, D. J. (2003). Importance of a stochastic distribution of floods and erosion thresholds in the bedrock river incision problem. Journal of Geophysical Research, 108(B2), 2117. http://doi.org/10.1029/2001JB001655

Stanford, S. D., Witte, R., Braun, D., & Ridge, J. (2016). Quaternary fluvial history of the Delaware River. Geomorphology.

Stanford, S. D., Witte, R. W., Braun, D. D., & Ridge, J. C. (2016). Quaternary fluvial history of the Delaware River, New Jersey and Pennsylvania, USA: The effects of glaciation, glacioisostasy, and eustasy on a proglacial river system. Geomorphology, 264, 12–28. http://doi.org/10.1016/j.geomorph.2016.04.002

West, N., Kirby, E., Bierman, P., Slingerland, R., Ma, L., Rood, D., & Brantley, S. (2013). Regolith production and transport at the Susquehanna Shale Hills Critical Zone Observatory , Part 2□: Insights from meteoric 10 Be. Journal of Geophysical Research□: Earth Surface, 118, 1877–1896. http://doi.org/10.1002/jgrf.20121

Whipple, K. X., & Tucker, G. E. (1999). Dynamics of stream-power river incision model. Journal of Geophysical Research, 104(August), 661–674.

Whipple, K. X., & Tucker, G. E. (2002). Implications of sediment-flux-dependent river incision models for landscape evolution. Journal of Geophysical Research, 107.

Whitehouse, P. L., Allen, M. B., & Milne, G. a. (2007). Glacial isostatic adjustment as a control on coastal processes: An example from the Siberian Arctic. Geology, 35(8), 747. http://doi.org/10.1130/G23437A.1

Wickert, A. D. (2016). Reconstruction of North American drainage basins and river discharge since the Last Glacial Maximum. Earth Surface Dynamics, 4(4), 831–869. http://doi.org/10.5194/esurf-4-831-2016

Wickert, A. D., Anderson, R. S., Mitrovica, J. X., Naylor, S., & Carson, E. C. (2019). The Mississippi River records glacial-isostatic deformation of North America. Science Advances, (January), 1–8.

Willgoose, G., Bras, R. L., & Rodriguez-Iturbe, I. (1991). A Coupled Channel Network Growth and Hillslope Evolution Model 1. Theory. Water Resources Research, 27(7), 1671–1684.

6

Sea-level fingerprinting of the Bering Strait flooding history detects the source of the Younger Dryas climate event

6.1 Introduction

The timing of the last separation between the major North American ice sheets is central to paleoclimate studies as well as to arguments that an ice-free corridor served as a path for early human migration. However, efforts to constrain the history of retreat between the Laurentide and Cordilleran ice sheets have been limited by sparse geologic observations(Dyke, 2004). Glacial isostatic adjustment due to the disintegration of this ice saddle and removal of its mass load on the continent would in-

A version of this chapter is under review as a manuscript coauthored with Jerry X. Mitrovica, and Alan C. Mix in *Nature Geoscience*

duce a local sea-level fall and exert an important influence on sea level in the Bering Strait(Gomez et al., 2015), ∼2000 km to the west. Submergence of the Bering Strait modulates ocean circulation as it provides a return pathway for relatively low-salinity Pacific waters to the North Atlantic via the Arctic Ocean(Hu et al., 2010). The timing of this initial connection is thus a key issue in reconstructing past ice extent, as well ocean and climate variability. However, this timing remains contentious; observations in sediment cores support an ∼11.5 ka submergence of the Bering Strait(Keigwin et al., 2006; Hill and Driscoll, 2008; Jakobsson et al., 2017), whereas other lines of evidence based on marine species dispersal suggest a connection 2 ky earlier, at 13.3 ka (Dyke et al., 1996; Dyke and Savelle, 2001; England and Furze, 2008).

Here we reconcile these apparently contradictory datasets related to the inundation of the Bering Strait using a gravitationally self-consistent relative sea-level simulation based on an ice history that sources a substantial contribution of meltwater from the western Laurentide Ice Sheet (LIS) and the Cordilleran Ice Sheet (CIS), in the region west of 110°W, from 13-11.5 ka. Our proposed ice-melting scenario is consistent with the hypothesis that discharge of freshwater into the Arctic slowed thermohaline circulation and triggered the Younger Dryas cold episode(Tarasov and Peltier, 2006), an abrupt climate event associated with a reduced Atlantic Meridional Overturning Circulation, from 12.9-11.7 cal ka(Carlson, 2010). Our sea-level reconstructions predict an evolution of regional shorelines that provides a key boundary condition for studies of the first peopling of the Americas(Clark, Mitrovica and Alder, 2014).

6.2 Observations Of Bering Strait Resubmergence

Current understanding of the timing of the Bering Shelf resubmergence during the last deglaciation is based on dated sediment cores that record local subaerial or marine environments, as well as geochemical shifts implying a change in ocean connectivity (Table 1; see Methods & Supplementary Material 8.1-8.6 for radiocarbon calibration). The present sill depth at the Bering Strait is 53 m. If

we assume minimal vertical displacement due to longer-term tectonic, erosion, and sedimentation effects (see Supplementary Material 1) local sea level must have reached this elevation for the Arctic and Pacific oceans to be connected.

Elias et al.(Elias et al., 1996) dated terrestrial peat at a current water depth of 45.0 m on the Beringian continental shelf to 12.9 +0.08/-0.09 (1σ) cal ka at Site 85-69 (red triangle; Figure 1; Figure 2), suggesting inundation of the Bering Strait later than this time. A transgressive flooding surface in core JPC10 from the Chukchi Shelf was analyzed by Hill et al.(Hill and Driscoll, 2008), and an age of 10.9 +0.25/-0.24 (1σ) cal ka was measured 1 m above the flooding surface at -59.2 m, though it was not possible to directly date the surface (orange triangle; Figure 1; Figure 2). In nearby core VBC03, a shell contained within a mud clast was dated to 12.6 +0.9/-1.1 (1σ) cal ka at 60.4 m depth(Hill and Driscoll, 2008), suggesting that relative sea level in the vicinity was higher than this depth by this time (orange triangle; Figure 1; Figure 2). Keigwin et al.(Keigwin et al., 2006) inferred a rapid change from estuarine to open marine conditions at 12.0 +0.5 /-0.4 (1σ) cal ka from an increase in δ18O values above a flooding surface in sediment core JPC02 in Hope Valley, just north of Bering Strait, at 53.5 m depth (overlapping open and filled blue triangle; Figure 1; Figure 2). Jakobsson et al.(Jakobsson et al., 2017) inferred an ~11 ka inundation based on a sharp increase in measured δ^{1}3Corg and bio silica content, proxies for increased marine organic carbon input and Pacific influence, respectively, which was dated to 10.9+0.5/-0.2 (1σ) cal ka in core 4PC-1 from 120 m deep in Herald Canyon (overlapping open and filled teal squares; Figure 1; Figure 2). Observations by Keigwin et al.(Keigwin et al., 2006), and Jakobsson et al.(Jakobsson et al., 2017) point to a flooding event of age 11-11.5 ka, and suggest that prior to this time the Bering Strait sill separated the Pacific from the Arctic Ocean.

The initial appearance of Pacific species in the Arctic provides an independent constraint on the timing of the Bering Strait inundation. Dyke & Savelle(Dyke and Savelle, 2001) and Dyke et al.(Dyke et al., 1996) found species endemic to the Pacific on raised beach terraces in the Canadian

Arctic, specifically bowhead whale bones and the mollusk Macoma (Limecola) balthica, and dated these specimens, respectively, to 10.9 $\pm$0.1 (1σ) cal ka, and 12.6+0.1/-0.9 (1σ) cal ka (open green, purple; Figure 2). More recently, England & Furze(England and Furze, 2008) dated three samples of Cyrtodari kurriana, a mollusk species likely migrating from the North Pacific, on Banks Island, Canada to 13.0 $\pm$0.1, 13.3 $\pm$0.6, 13.5 $\pm$0.1 (1σ) cal ka (yellow circles; Figure 2) demonstrating that a Pacific-Arctic connection existed at least 2 ky earlier than suggested by sediment cores that capture a transition indicating the submergence of the Bering Strait.

These two lines of evidence, sediment core records and species dispersal, point to initial times of Bering Strait inundation of $\sim$11.5 ka and $\sim$13.3 ka, respectively, separated by nearly 2 ky. While the absolute timing in both datasets depends on the reservoir ages for radiocarbon dates (see Supplementary Material 8), the relative timing does not. These apparently contradictory datasets suggest the possibility of a double opening of the Bering Strait, implying a local sea-level fall or stillstand from 13-11.5 ka, an interval when globally averaged sea level rose at a pace in excess of 10 m/ky(Lambeck et al., 2014). In the next section, we explore whether ice-melting scenarios exist that produce a geographically variable sea-level history in the Bering Strait region consistent with this entire set of observations.

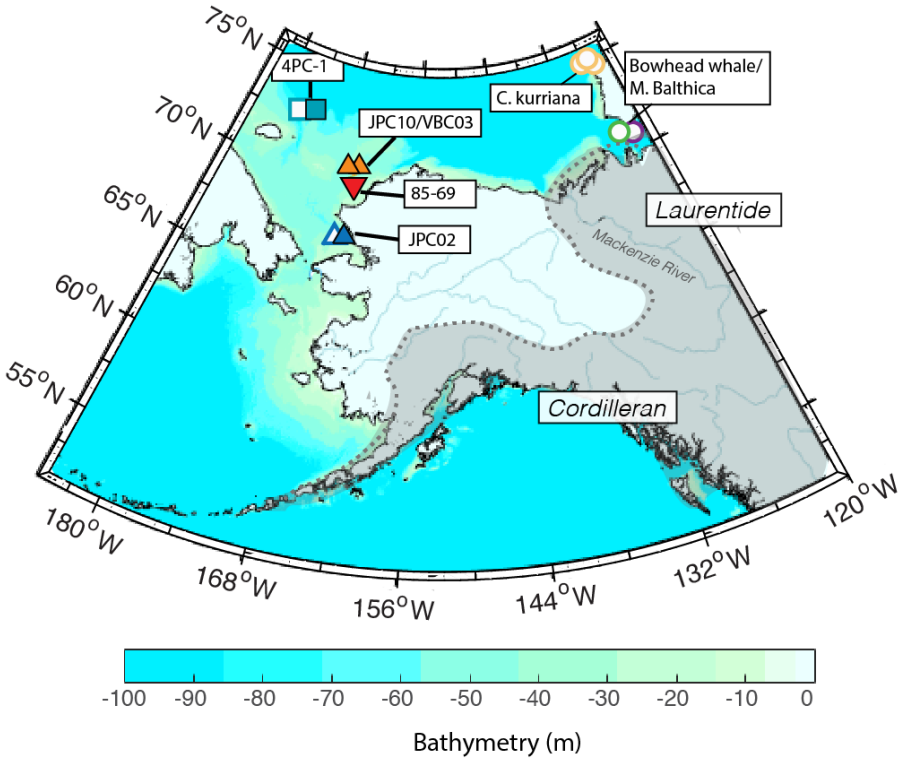

FIGURE 6.1: Bathymetry in the Bering Shelf region from ARDEM (Danielson et al., 2015). Locations of observations constraining the timing of the Bering Strait resubmergence are shown by circles, triangles, and squares, which correspond to markers in Figures 2 and 4. Pacific species found on uplifted beach terraces were collected on Victoria and Banks Island, Canada (Dyke et al., 1996; Dyke and Savelle, 2001; England and Furze, 2008). Dotted gray line and shaded region shows schematic of Last Glacial Maximum ice margin (Dyke(2004)).

6.3 Refining Ice Melt Histories and Reconstructing Local Sea Level

6.3.1 Initial GIA modeling

The melting of ice sheets across the last deglaciation drove a complex spatio-temporal pattern of sea-level change due to deformational, gravitational and rotational effects of glacial isostatic adjustment

(GIA). The following simulations are based on the sea-level theory and pseudo-spectral algorithm described by Kendall et al.(Kendall, Mitrovica and Milne, 2005). These predictions require models for Earth's viscoelastic structure and the history of ice cover. We begin by adopting the global ice history ICE-6G(Peltier, Argus and Drummond, 2015) (black line; inset, Figure 3) coupled with an Earth model characterized by a lithospheric thickness of 48 km and upper and lower mantle viscosities of 5x1020 Pas and 5x1021 Pas, respectively (see Methods). Using the standard ice model ICE-6G, relative sea level (RSL) at the Bering Strait is predicted to reach present-day sill depth at 11.5 ka, consistent with observations in sediment cores but inconsistent with evidence of an earlier connection at 13.3 ka (black dotted line; Supplementary Figure 1).

6.3.2 Geological evidence & climate-ice and sea-level modeling of LIS/CIS retreat

Sea level in the vicinity of the Bering Strait is sensitive to the melting history of the CIS and the western LIS. Radiocarbon (squares; Figure 4), luminescence (circles; Figure 4), and cosmogenic dating (triangles; Figure 4) have established minimum ages of ice retreat in this region(Gowan, 2013; Huntley, Hickin and Lian, 2017; Menounos et al., 2017; Munyikwa, Rittenour and Feathers, 2017). While there is evidence for ice-free conditions within the former saddle region by 15 ka(Munyikwa, Rittenour and Feathers, 2017), details of the timing, rate, and geometry of the saddle disintegration require refinement in order to understand the history of GMSL sourced from the eastern CIS and western LIS over the deglaciation. We use a compilation of 818 ages constraining the deglaciation of this region in our construction of ice-melt scenarios that are consistent with the inundation record at the Bering Strait(Gowan, 2013; Huntley, Hickin and Lian, 2017; Menounos et al., 2017; Munyikwa, Rittenour and Feathers, 2017) (Figure 4; see Supplementary Material 7 for detailed discussion of ages).

Pulses of meltwater recorded in marine sediment cores provide additional constraints on the

timing and location of ice ablation in the Cordilleran region. Taylor et al(Taylor, Hendy and Pak, 2014) noted early deglacial retreat of marine margins of the Southwest CIS between 17.5 and 15.5 ka. Davies et al.(Davies et al., 2011) and Praetorius et al.(Praetorius et al., 2016) observed similar early melting, with the retreat of the western CIS from its marine termination near ∼14.8 cal ka and an increased freshwater influence in sediment cores in the Gulf of Alaska from 14.7-13.8 cal ka.. In the Siberian Arctic, Spielhagen et al.(Spielhagen, Erlenkeuser and Siegert, 2005) observed a freshwater peak in cores near 13 cal ka. Freshening in the Arctic near the Mackenzie delta, a direct outflow path from the former saddle region, is similarly observed in foraminiferal Δ18O data from 12.9-12.2 cal ka(Keigwin et al., 2018) and from 12.7-11.6 cal ka(Andrews and Dunhill, 2004; Leydet et al., 2018) (see Supplementary Material 6 for updated ^{14}C reservoir ages). Furthermore, regional seismic data and sedimentation patterns suggest a flood of meltwater at this time(Hillaire-marcel et al., 2013; Keigwin et al., 2018; Lakeman et al., 2018).

An ice-sheet modeling study(Gregoire, Payne and Valdes, 2012) predicted a rapid collapse of this ice sheet sector equivalent to a global mean sea level (GMSL) rise of ∼10.5 m in 0.5 ky, at a mean rate of 7.1 m/ky over 2 ky. Although the main pulse of melting occurred at 11.6 ka in model time, it was assumed to have been coincident with MWP-1a (14.5 ka)(Gregoire, Payne and Valdes, 2012). We evaluate this assumption in light of sea-level observations on the Bering Shelf.

Melting of the CIS-LIS saddle results in a local sea-level rise in the Bering Strait region significantly smaller than the global average, as ice-sheet melting produces a near-field component of sea-level fall due to a loss of gravitational attraction between the ocean and ice mass and crustal uplift due to ice unloading(Gomez et al., 2015). Thus, a substantial melting of the CIS/western LIS extending from 13-11.5 ka could have been sufficient to produce a sea-level fall or stillstand over this period. We hypothesize that such an event would reconcile observations of a possible double opening of the Bering Strait, and would be consistent with other glaciological, geomorphological, and sea-level evidence during this time interval.

6.3.3 Modification to ICE-6G: Fitting observations in the Bering Strait

We construct a hypothetical alternate ice model (GI-31) by modifying the deglaciation geometry of the ICE-6G model while requiring that the total ice volume (or GMSL) history of that model be preserved in order to satisfy far-field sea-level constraints (see inset, Figure 3, and Supplementary Material 9). We delay ice loss in the CIS/western LIS region within the zone west of 110°W, preserving the ICE-6G ice distribution at 15 ka in this specific region until 13 ka. The ice distribution from 15-13 ka is modified to be consistent with the median ages reported in a large dataset (n= 818) constraining the deglaciation chronology of this region. In particular, we require that regions with minimum ages older than 13 ka must be ice-free by 13 ka in the GI-31 ice history (Figure 4). A comparison with previously published ice models(Gregoire, Payne and Valdes, 2012; Peltier, Argus and Drummond, 2015; Gowan et al., 2016) and a map showing time steps of ice cover from 13 to 11.5 ka is included in Supplementary Figure 2/3.

We source 14.3 m of GMSL rise from 13-11.5 ka from the CIS/western LIS region, which results in a total rate of GMSL rise from North American Ice Sheets (black and gray lines; Figure 3) of 9.5 m/ky from 13-11.5 ka, slightly higher than the ICE-6G rate of 9.2 m/ky over the same interval. To maintain a total GMSL curve that matches the ICE-6G history we revise this history such that melting of the Antarctic Ice Sheet (AIS) equivalent to a GMSL rise of 5.7 m from 13-11 ka, and melting of the Fennoscandian Ice Sheet (FIS) equivalent to a GMSL rise of 5.3 m previously inferred to occur from 13-11.5 ka, are assumed to occur earlier, during MWP-1a (~14.5-14.0 ka; dashed red and blue lines; Figure 3; See Supplementary Material 4.4 for discussion on MWP-1a sources).

The ice model ICE-6G sources a large melt contribution across MWP-1a from a rapid ice margin retreat between the CIS and LIS equivalent to 6.9 m GMSL from 14.5-14 ka, and a total of 10.6 GMSL from 15-13 ka at a mean rate of 6.1 m/ky(Peltier, Argus and Drummond, 2015). This ice model also sources 10.2 m GMSL from the eastern LIS across MWP-1a from 14.5-14 ka, and a total of

17.4 m GMSL from 15-13 ka. In contrast, ice model GI-31 sources 0 m GMSL from the CIS/western LIS from 14.5-14 ka across MWP-1a, and a total of 2.4 m GMSL from 15-13 ka. The ice model GI-31 sources 10.2 m GMSL from the eastern LIS across MWP-1a, from 14.5-14 ka, and a total of 21.8 m GMSL from 15-13 ka. The only source of meltwater from 13-11.5 ka in the GI-31 ice model is the CIS/western LIS (dashed black line; Figure 3).

The RSL prediction adopting ice model GI-31 at the Bering Strait sill (65.5 °N, 168.7 °W) exceeds the present-day sill depth at ~13.3 ka with a value of -51.6 m at 13 ka, and remains near this elevation until 11.5 ka (increasing to -50.3 m), after which RSL increases rapidly (black line; Figure 2). This sea-level stillstand occurs due to a combination of a local sea-level fall due to gravitational and deformation effects added to the GMSL change produced by the input ice history (Supplementary Figure 4).

Next, we consider predictions of RSL at each core site plotted in Figure 1. We note that RSL varies substantially (>10 m) throughout the Bering Shelf region due to the strong gradient in gravitational and deformation effects in the near field of the CIS/western LIS region (Supplementary Figure 5). Therefore, RSL at each site exceeds the local present-day sill depth at different times (inset; Figure 2), and this temporal variability is consistent with constraints imposed by the datasets summarized in Figure 2. For example, at site 4PC-1, rapid sea-level rise started at 11.5-11 ka as the Bering Strait sill deepened, consistent with the increase in Pacific water influence observed by Jakobsson et al.(Jakobsson et al., 2017) (teal squares; Figure 2). Moreover, RSL at the site VBC03/JPC10 is just above -60 m at 13.3 ka (orange line; Figure 2) while RSL at the site 85-69 is below -45 m at 12.9 ka (red line; Figure 2).

Our calculations predict RSL to be higher near the sill than in the surrounding regions, explaining discrepancies in reported RSL elevations (see Figure 2) that are not reconciled using the standard ICE-6G history (i.e., JPC10/VBC03; Supplementary Figure 1). Most significantly, GI-31 predicts a first breach of the sill by 13 ka. Even a shallow inundation at the sill would allow dispersal of shallow-

water mollusk species with a planktonic larval stage, and this can explain the early appearance of Pacific mollusk species in the Arctic. Total inundation of the Bering Strait does not occur in the simulation until 11.5 ka, explaining the later date for biosilica accumulation, which requires a sill depth great enough for substantial northward flows of Pacific water (Figure 2).

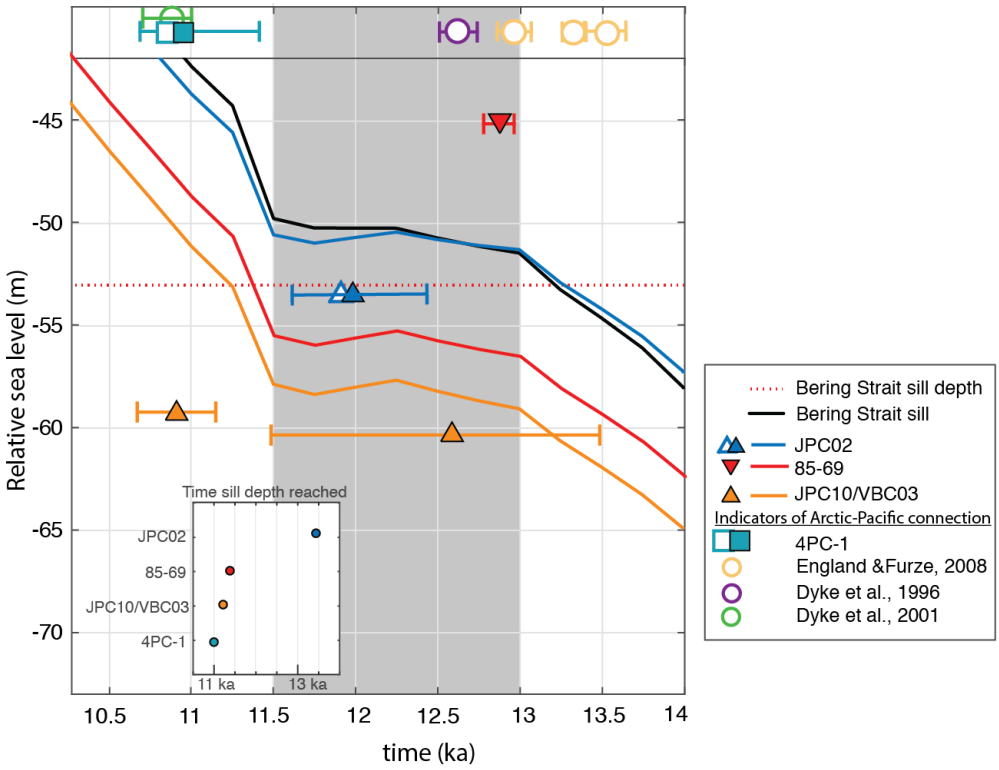

FIGURE 6.2: Relative sea-level predictions for sites in the Bering Strait region compared with observations on the timing of Bering Strait resubmergence. Predictions at the Bering Strait sill are shown by the black line. Present-day sill depth is shown by horizontal dotted red line at -53 m. Upward-pointing triangles denote dates on marine deposits, implying relative sea level higher than the plotted elevation. Downward-pointing triangles denote terrestrial deposits, implying relative sea level lower than the plotted elevation. Open circles are observations signaling an open connection at the Bering Strait (e.g. Pacific species found in the Arctic), which requires that Bering Strait had flooded sufficiently for tidal flows to allow species dispersal in a planktonic larval (veliger) stage, whereas squares are observations signaling significant flows through the Bering Strait. Error bars represent 1 σ uncertainties (see Supplementary Material). Overlapping filled and open squares or triangles represent geochemical evidence of a transition from a closed to a significantly open connection at the Bering Strait between the Arctic and Pacific Oceans with net northward water flows. The gray rectangle highlights the interval from 13-11.5 ka. The blue, red, and orange lines show relative sea-level histories at the corresponding site of observation (Figure 1) using ice history GI-31.

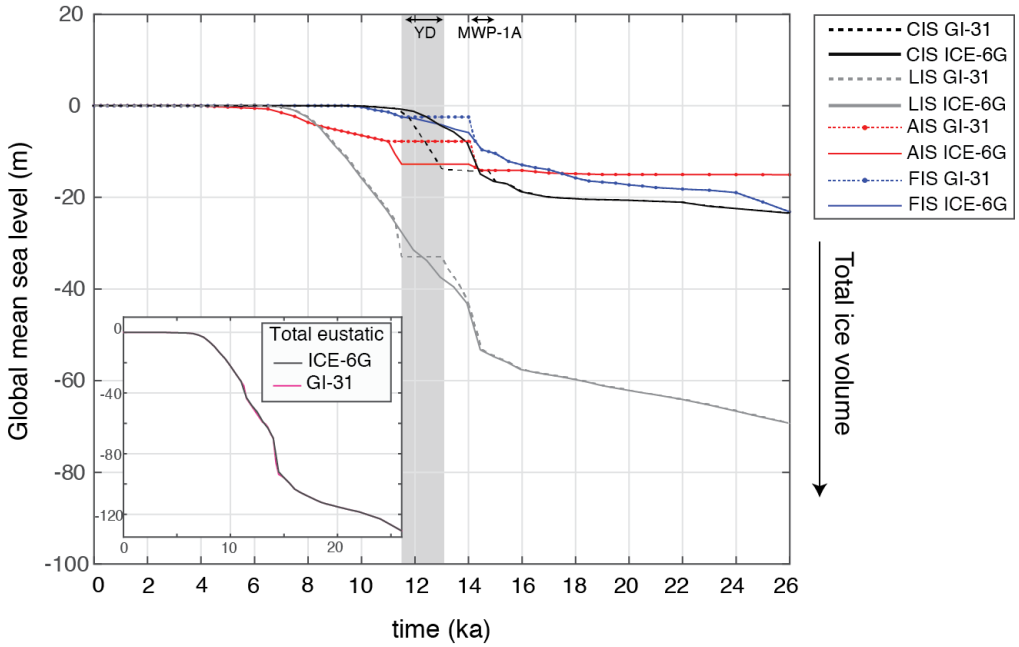

FIGURE 6.3: Eustatic contributions of each ice sheet. Cordilleran and western Laurentide Ice Sheet (CIS) in black, Laurentide Ice Sheet (east of 110°W; LIS) in gray, Fennoscandian Ice Sheet (FIS) in blue, and Antarctic Ice Sheet (AIS) in red, for both ICE-6G (solid) and an alternate ice model GI-31 (dashed). The shaded gray rectangle highlights the interval 13-11.5 ka. The Younger Dryas (YD; 12.9-11.7 ka) and Meltwater Pulse 1A (MWP-1A; 14.5-14 ka) are labeled. The inset compares total global eustatic histories for ICE-6G (gray) and GI-31 (pink), which differ by less than 2 m from 13-11.5 ka.

6.3.4 SENSITIVITY TESTS

We construct two additional ice histories that sample the range of ice-melting scenarios consistent with the age uncertainties associated with our data compilation. We adopt the 2σ error minimum (GI-34; "older scenario"; Supplementary Figure 6A) and maximum (GI-30; "younger scenario"; Supplementary Figure 6B) ages and use these as constraints to refine the ice-melting scenario from 13-11.5 ka. These reconstructions result in a smaller (12.6 GMSL) and larger (15.1 GMSL) ice volume loss in the CIS/western LIS region for the older and younger age scenario, respectively, over the 13-11.5 ka interval, and result in a RSL rise of 1.7 m and 1.2 m, respectively, from 13-11.5 ka at the Bering

Strait sill.

We test the robustness of these results to variations in the regional distribution and duration of ice melt by constructing a series of alternate ice models. Simulations varying the timing of sub-regions of melting within the period 13-11.5 ka suggest that a RSL stillstand at the Bering Strait required melting in the northwest region of CIS/western LIS over the entire duration of 13-11.5 ka (Supplementary Figure 7B). We also performed calculations that explored the sensitivity of sea-level predictions to the total mass flux from the CIS-LIS region, the AIS, FIS, and eastern LIS. These simulations indicate that the predicted RSL stillstand is robust to different relative contributions of these far-field ice sheets to MWP-1a (Supplementary Figure 7B).

We also assessed the sensitivity of the RSL predictions in the Bering Strait region to the adopted Earth model by varying the lithospheric thickness and upper and lower mantle viscosities. We found that while the Earth model modulates the amplitude of RSL, the total sea-level rise from 13-11.5 ka is robust, varying by less than 0.7 m. This insensitivity is a consequence of the dominance of gravitational and elastic deformation effects (Supplementary Figure 8).

There are a variety of data sets that can be brought to bear to refine the spatial geometry of ice loss local to the region of saddle melting, including the present-day elevation of proglacial lake shorelines and site-specific relative sea level histories(Gowan et al., 2016). Since the ICE-6G ice history was not tuned to fit most of these records, the ice model GI-31 based upon it would not be expected to fit such data sets. In the Supplement (see Supplementary Material 10) we adopt the model NAICE(Gowan et al., 2016) that was, in contrast, tuned to fit these data sets and demonstrate that introducing the delay in saddle melting necessary to reconcile the Bering Strait sea level record does not introduce a misfit to the lake and relative sea level data in the vicinity of the ice loss (Supplementary Figures 14/15/16/17).

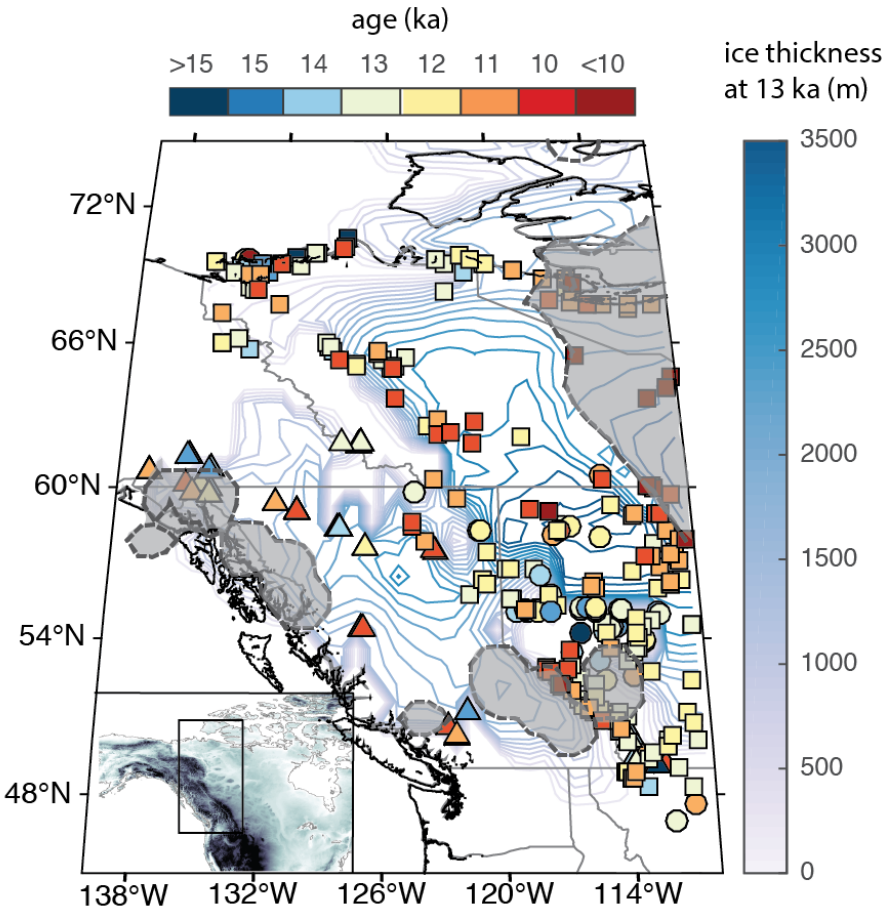

FIGURE 6.4: Ice melting scenario from 13-11.5 ka. Contours represent ice thickness at 13 ka in the GI-31 ice history (right-hand colorbar). Squares represent calibrated radiocarbon ages on organic material postdating ice loss, circles represent luminescence ages on aeolian dune deposits, and triangles represent cosmogenic ages on moraines, including cirque and valley moraines (see Supplementary Figure 8). The GI-31 ice distribution from 15-13 ka is consistent with the median ages reported in this dataset (n= 818) constraining the deglaciation chronology of this region. For any dates that round to 13 ka, we ensure that these sites become ice free in the time step from 13 ka to 12.75 ka. Interior colors represent ages rounded to nearest integer (top colorbar). Dashed gray lines with gray shading represent the limits of ice extent at 11.5 ka. Inset shows map area in black rectangle.

6.4 Conclusion

We refine the timing and geometry of RSL change in the Bering Strait during the last deglaciation by constructing an ice history within the CIS and western LIS that is consistent with available land dates. Our ice sheet reconstructions, which maintain fits to sea-level records in the far-field (Supplementary Material 9), yield sea-level predictions that reconcile disparate and previously enigmatic datasets recording the inundation history of the Bering Shelf. Our inferred ice-melting scenarios source substantial meltwater from the retreat between the Cordilleran and Laurentide Ice Sheets from 13-11.5 ka in the region west of 110°W, potentially initiated by marine retreat of the ice sheet (Supplementary Figure 17). Part of the freshwater flux from this ice-mass loss (0.11 Sv over 13-11.5 ka) would have freshened the subpolar North Atlantic and may have been sufficient to suppress deepwater convection and thereby initiate Younger Dryas cooling(Murton et al., 2010; Condron and Winsor, 2012; Ivanovic et al., 2017). The end of the meltwater flux may have also had a role in terminating the anomalous Younger Dryas cooling and triggering the onset of early Holocene warmth(Liu et al., 2009).

6.5 Acknowledgements

We are grateful to R. Ackert for insightful discussions regarding chronology methods. T.P was supported by NSF-GRFP. J.X.M and T.P. acknowledge funding from Harvard University.

6.6 References

Andrews, J. T. and Dunhill, G. (2004) 'Early to mid-Holocene Atlantic water influx and deglacial meltwater events , Beaufort Sea slope , Arctic Ocean', Quaternary Research, 61, pp. 14–21. doi: 10.1016/j.yqres.2003.08.003.

Bauch, H. A., Mueller-lupp, T., Taldenkova, E., Spielhagen, R. F. and Kassens, H. (2001) 'Chronol-

ogy of the Holocene transgression at the North Siberian margin', Global and Planetary Change, pp. 125–139.

Carlson, A. E. (2010) 'What Caused the Younger Dryas Cold Event□?', Geology, 38(4), pp. 383–384. doi: 10.1029/95PA02643.Liu.

Clark, J., Mitrovica, J. X. and Alder, J. (2014) 'Coastal paleogeography of the California-Oregon-Washington and Bering Sea continental shelves during the latest Pleistocene and Holocene: Implications for the archaeological record', Journal of Archaeological Science. Elsevier Ltd, 52, pp. 12–23. doi: 10.1016/j.jas.2014.07.030.

Condron, A. and Winsor, P. (2012) 'Meltwater routing and the Younger Dryas', PNAS, 109(49), pp. 1–6. doi: 10.1073/pnas.1207381109.

Coulthard, R. D., Furze, A. J., Piewnkowski, F. C., Nixon and England, J. (2010) 'New marine DeltaR values for Arctic Canada', Quaternary Geochronology, 5, pp. 419–434.

Danielson, B. S. L., Dobbins, E. L., Jakobsson, M., Johnson, M. A. and Thomas, J. (2015) 'Sounding the Northern Seas', Eos, (December 2015), pp. 1–8.

Davies, M. H., Mix, A. C., Stoner, J. S., Addison, J. A., Jaeger, J., Finney, B. and Wiest, J. (2011) 'The deglacial transition on the southeastern Alaska Margin□: Meltwater input , sea level rise , marine productivity , and sedimentary anoxia', Paleoceanography, 26, pp. 1–18. doi: 10.1029/2010PA002051.

Dyke, A. S. (2004) 'An outline of North American Deglaciation with emphasis on central and northern Canada', in J.Ehlers and P.L.Gibbard (eds) Quaternary Glaciations-Extent and Chronology: Part II: North America, pp. 373–424.

Dyke, A. S., Dale, J. E., Mcneely, R. N., Dyke, A. S., Dale, J. E., Mcneely, R. N., Division, S. and Survey, G. (1996) 'Marine Molluscs as Indicators of Environmental Change in Glaciated North America and Greenland During the Last 18000 Years', Geographie Physique et Quaternaire, 50(2), pp. 125–184.

Dyke, A. S. and Savelle, J. (2001) 'Holocene History of the Bering Sea Bowhead Whale (Balaena

mysticetus) in Its Beaufort Sea Summer Grounds off Southwestern Victoria Island , Western Canadian Arctic', Quaternary Research. doi: 10.1006/qres.2001.2228.

Elias, S., Short, S., Nelson, H. and Birks, H. (1996) 'Life and times of the Bering land bridge', Nature, 382(July).

England, J. H. and Furze, M. F. A. (2008) 'New evidence from the western Canadian Arctic Archipelago for the resubmergence of Bering Strait', Quaternary Research, 70(1), pp. 60–67. doi: 10.1016/j.yqres.2008.03.001.

Gomez, N., Gregoire, L. J., Mitrovica, J. X. and Payne, A. J. (2015) 'Laurentide-Cordilleran Ice Sheet saddle collapse as a contribution to meltwater pulse 1A', Geophysical Research Letters, (42), pp. 3954–3962. doi: 10.1002/2015GL063960.Received.

Gowan, E. J. (2013) 'An assessment of the minimum timing of ice free conditions of the western Laurentide Ice Sheet', Quaternary Science Reviews. Elsevier Ltd, 75, pp. 100–113. doi: 10.1016/j.quascirev.2013.06.001.

Gowan, E. J., Tregoning, P., Purcell, A., Montillet, J. and Mcclusky, S. (2016) 'A model of the western Laurentide Ice Sheet , using observations of glacial isostatic adjustment', Quaternary Science Reviews. Elsevier Ltd, 139, pp. 1–16. doi: 10.1016/j.quascirev.2016.03.003.

Gregoire, L. J., Payne, A. J. and Valdes, P. J. (2012) 'Deglacial rapid sea level rises caused by ice-sheet saddle collapses.', Nature. Nature Publishing Group, 487(7406), pp. 219–22. doi: 10.1038/nature11257.

Hill, J. C. and Driscoll, N. W. (2008) 'Paleodrainage on the Chukchi shelf reveals sea level history and meltwater discharge', Marine Geology, 254, pp. 129–151. doi: 10.1016/j.margeo.2008.05.018.

Hillaire-marcel, C., Maccali, J., Not, C. and Poirier, A. (2013) 'Geochemical and isotopic tracers of Arctic sea ice sources and export with special attention to the Younger Dryas interval', Quaternary Science Reviews. Elsevier Ltd, 79, pp. 184–190. doi: 10.1016/j.quascirev.2013.05.001.

Hu, A., Meehl, G. A., Otto-bliesner, B. L., Waelbroeck, C., Han, W., Loutre, M., Lambeck, K., Mitrovica, J. X. and Rosenbloom, N. (2010) 'Influence of Bering Strait flow and North Atlantic

circulation on glacial sea-level changes', Nature Geoscience. Nature Publishing Group, 3(2), pp. 118–121. doi: 10.1038/ngeo729.

Huntley, D. H., Hickin, A. S. and Lian, O. B. (2017) 'The pattern and style of deglaciation at the Late Wisconsinan Laurentide and Cordilleran ice sheet limits in northeastern British Columbia', Canadian Journal of Earth Sciences, 75(August 2016), pp. 52–75.

Ivanovic, R. F., Gregoire, L. J., Wickert, A. D., Valdes, P. J. and Burke, A. (2017) 'Collapse of the North American ice saddle 14,500 years ago caused widespread cooling and reduced ocean overturning circulation', Geophysical Research Letters, 44(1), pp. 383–392. doi: 10.1002/2016GL071849.

Jakobsson, M., Pearce, C., Cronin, T. M., Backman, J., Anderson, L. G., Björk, G., Coxall, H., Boer, A. De, Mayer, L. A., Mörth, C., Rattray, J. E., Stranne, C., Semilietov, I. and Regan, M. O. (2017) 'Post-glacial flooding of the Beringia Land Bridge dated to 11 , 000 cal yrs BP based on new geophysical and sediment records', Climate of the Past. doi: 10.5194/cp-2017-11.

Johnston, P. (1993) 'The effect of spatially non-uniform water loads on prediction of sea-level change', Geophysical Journal International, 114(3), pp. 615–634. Available at: http://onlinelibrary.wiley.com/doi/10.1111/j.136
246X.1993.tb06992.x/abstract.

Keigwin, L. D., Donnelly, J. P., Cook, M. S., Driscoll, N. W. and Brigham-grette, J. (2006) 'Rapid sea-level rise and Holocene climate in the Chukchi Sea', Geology, (10), pp. 861–864. doi: 10.1130/G22712.1.

Keigwin, L. D., Klotsko, S., Zhao, N., Reilly, B., Giosan, L. and Driscoll, N. W. (2018) 'Deglacial floods in the Beaufort Sea preceded Younger Dryas cooling', Nature Geoscience. Springer US. doi: 10.1038/s41561-018-0169-6.

Kendall, R. A., Mitrovica, J. X. and Milne, G. A. (2005) 'On post-glacial sea level - II. Numerical formulation and comparative results on spherically symmetric models', Geophysical Journal International, 161(3), pp. 679–706. doi: 10.1111/j.1365-246X.2005.02553.x.

Lakeman, T. R., Pie, A. J., Nixon, F. C., Furze, M. F. A., Blasco, S., Andrews, J. T. and King, E. L. (2018) 'Collapse of a marine-based ice stream during the early Younger Dryas chronozone , western

Canadian Arctic', Geology, 46(3), pp. 211–214.

Lambeck, K., Purcell, A., Johnston, P., Nakada, M. and Yokoyama, Y. (2003) 'Water-load definition in the glacio-hydro-isostatic sea-level equation', Quaternary Science Reviews, 22(2–4), pp. 309–318. doi: 10.1016/S0277-3791(02)00142-7.

Lambeck, K., Rouby, H., Purcell, A., Sun, Y., Sambridge, M., Bard, E., Mitrovica, J. X. and Clark, P. U. (2014) 'Sea level and global ice volumes from the Last Glacial Maximum to the Holocene', PNAS, 111(43), pp. 15296–15303. doi: 10.1073/pnas.1411762111.

Lambeck, K., Smither, C. and Johnston, P. (1998) 'Sea-level change , glacial rebound and mantle viscosity for northern Europe', Geophysical Journal International, pp. 102–144.

Leydet, D. J., Carlson, A. E., Teller, J. T., Breckenridge, A., Barth, A. M., Ullman, D. J., Sinclair, G., Milne, G. A., Cuzzone, J. K. and Caffee, M. W. (2018) 'Opening of glacial Lake Agassiz ' s eastern outlets by the start of the Younger Dryas cold period', Geology, 46(2), pp. 155–158.

Liu, Z., He, F., Brady, E. C., Tomas, R., Clark, P. U., Carlson, A. E., Curry, W., Brook, E., Erickson, D., Jacob, R., Kutzbach, J. and Cheng, J. (2009) 'Transient Simulation of Last Deglaciation with a New Mechanism for Bølling-Allerød Warming', 413(July), pp. 310–315.

McNeely, R., Dyke, A. S., and R, S. J. . (2006) 'Canadian Marine Reservoir Ages, Preliminary Data Assessment, Ottawa', Geological Survey of Canada, pp. 1–3.

Menounos, B., Goehring, B. M., Osborn, G., Margold, M., Ward, B., Bond, J., Clarke, G. K. C., Clague, J. J., Lakeman, T., Koch, J., Caffee, M. W., Gosse, J., Stroeven, A. P., Seguinot, J. and Heyman, J. (2017) 'Supplement: Cordilleran Ice Sheet mass loss preceded climate reversals near the Pleistocene Termination', Science, 358(6364), pp. 781–784. doi: 10.1126/science.aan3001.

Milne, G. a. and Mitrovica, J. X. (1996) 'Postglacial sea-level change on a rotating Earth: first results from a gravitationally self-consistent sea-level equation', Geophysical Journal International, 126(3), pp. F13–F20. doi: 10.1111/j.1365-246X.1996.tb04691.x.

Milne, G. A., Mitrovica, J. X. and Davis, J. L. (1999) 'Near-field hydro-isostasy: the implemen-

tation of a revised sea-level equation', Geophysical Journal International, 139, pp. 464–482. doi: 10.1046/j.1365-246x.1999.00971.x.

Mitrovica, J. X. and Forte, A. M. (2004) 'A new inference of mantle viscosity based upon joint inversion of convection and glacial isostatic adjustment data', Earth and Planetary Science Letters, 225, pp. 177–189. doi: 10.1016/j.epsl.2004.06.005.

Munyikwa, K., Rittenour, T. M. and Feathers, J. K. (2017) 'Temporal constraints for the Late Wisconsinan deglaciation of western Canada using eolian dune luminescence chronologies from Alberta', Palaeogeography, Palaeoclimatology, Palaeoecology. Elsevier B.V., 470, pp. 147–165. doi: 10.1016/j.palaeo.2016.12.034.

Murton, J. B., Bateman, M. D., Dallimore, S. R., Teller, J. T. and Yang, Z. (2010) 'Identification of Younger Dryas outburst flood path from Lake Agassiz to the Arctic Ocean', Nature, 464(April). doi: 10.1038/nature08954.

Pearce, C., Varhelyi, A., Wastegård, S., Muschitiello, F. and Barrientos, N. (2017) 'The 3 . 6 ka Aniakchak tephra in the Arctic Ocean□: a constraint on the Holocene radiocarbon reservoir age in the Chukchi Sea', pp. 303–316. doi: 10.5194/cp-13-303-2017.

Peltier, W. R., Argus, D. F. and Drummond, R. (2015) 'Space geodesy constrains ice age terminal deglaciation: The global ICE-6G-C (VM5a)model', Journal of Geophysical Research: Solid Earth, 119. doi: 10.1002/2014JB011176.Received.

Praetorius, S., Mix, A., Jensen, B., Froese, D., Milne, G., Wolhowe, M., Addison, J. and Prahl, F. (2016) 'Interaction between climate , volcanism , and isostatic rebound in Southeast Alaska during the last deglaciation', Earth and Planetary Science Letters. Elsevier B.V., 452, pp. 79–89. doi: 10.1016/j.epsl.2016.07.033.

Reimer, P. J., Bard, E., Bayliss, A., Beck, J. W., Blackwell, P. G., Bronk, C., Caitlin, R., Hai, E. B. and Edwards, R. L. (2013) 'Intcal13 and marine13 radiocarbon age calibration curves 0 – 50,000 years cal bp', Radiocarbon, 55(4).

Spielhagen, R. F., Erlenkeuser, H. and Siegert, C. (2005) 'History of freshwater runoff across the Laptev Sea (Arctic) during the last deglaciation', Global and Planetary Change, 48, pp. 187–207. doi: 10.1016/j.gloplacha.2004.12.013.

Tarasov, L. and Peltier, W. R. (2006) 'A calibrated deglacial drainage chronology for the North American continent□: evidence of an Arctic trigger for the Younger Dryas A calibrated deglacial drainage chronology for the North American continent□: evidence of an Arctic trigger for the Younger D', Quaternary Science Reviews, 25(September 2014), pp. 659–688. doi: 10.1016/j.quascirev.2005.12.006.

Taylor, M. A., Hendy, I. L. and Pak, D. K. (2014) 'Deglacial ocean warming and marine margin retreat of the Cordilleran Ice Sheet in the North Pacific Ocean', Earth and Planetary Science Letters. Elsevier B.V., 403, pp. 89–98. doi: 10.1016/j.epsl.2014.06.026.

Wolf, L. W., Mccaleb, R. C., Stone, D. B. and Klemperer, S. L. (2002) 'Crustal structure across the Bering Strait , Alaska□: Onshore recordings of a marine seismic survey', Geological Society of America Special Papers, pp. 25–37.

6.7 Methods

6.7.1 Radiocarbon date calibration

The calculation of Arctic ^{14}C ages is somewhat uncertain north of the Bering Strait. Published reservoir ages range from ∼450 to 900 yrs (i.e., ΔR from 50 to 500 yr (Bauch et al., 2001; Jakobsson et al., 2017; Pearce et al., 2017)). The value used in 4PC-1 is relatively low, $\Delta R = 50 + 100$ yr(Jakobsson et al., 2017) for the early inundation period based on assumed sea level; if a higher value is used, the inferred date for sea-level rise there could be as young as 10 ka. In contrast, the reservoir age used for the mollusks in the Canadian Archipelago is 1140 yr (ΔR=740 (McNeely, R., Dyke, A. S., and R, 2006)); if a younger reservoir age is applied there, the first appearance of Pacific fauna in the Arctic could be as old as 14 ka. It is unlikely that plausible changes in reservoir age could collapse the spread

of dates toward a single unified value.

Given these uncertainties we recalibrate ^{14}C raw ages in order to present data consistently throughout the text. We assign a reservoir age anomaly (ΔR) of 320$\pm$ 50 yr to post-inundation Canadian Arctic ^{14}C dates according to modern (pre-bomb) mollusk calibrations done by Coulthard et al.(Coulthard et al., 2010). On the Arctic side of the Bering Strait for dates between 12,000-10,000 yrs ^{14}C we assign a ΔR = 250 $\pm$ 200 yr. This reservoir age correction is selected as an intermediate between likely ΔR values prior to an Arctic-Pacific connection (ΔR = 60 $\pm$ 40) and likely values post Bering Strait flooding (ΔR = 350$\pm$120). See Supplementary Material 6.1-6.6 for a detailed discussion of these reservoir ages. We use the Marine13 or Intcal13 for marine and terrestrial deposits, respectively(Reimer et al., 2013). See Table 1 for a compilation of data.

7

The Influence of Sediment Loading on Last Interglacial Sea-Level Markers

7.1 Introduction

Refining the magnitude of excess ice melting at the Last Interglacial (LIG; ~122 ka Dutton and Lambeck, 2012) informs assessments of the stability of ice sheets in response to today's warming climate, and it relies on correcting sea-level records for local processes of vertical displacement (i.e. Creveling et al., 2015; Austermann et al., 2017; Dendy et al., 2017). Sediment loading is one such process potentially contaminating the sea-level record. While regional studies have shown sediment can influence sea-level on glacial timescales (Simms et al., 2007, 2013; Wolstencroft et al., 2014; Ferrier et al., 2015; Pico et al., 2016), in this article we pose the question globally: to what extent does sediment

A version of this chapter is under preparation as a manuscript coauthored with Jerry X. Mitrovica, Jacqueline Austermann, Ken L. Ferrier, and Alessio Rovere

loading control the variability of Last Interglacial sea-level observations, and where are these effects most substantial?

To answer these questions, we construct a global history of sedimentation over the last glacial cycle, and use a gravitationally self-consistent model of glacial-isostatic adjustment (GIA) to predict sea-level change as a result of sediment loading. We then compare our predictions to a global compilation of 1287 sea-level observations using a robust linear regression model that accounts for spatial autocorrelation. We investigate whether there is a statistically-significant relationship between our modeled sea-level change and the elevation of sea-level observations globally, or at passive or active tectonic margins. This analysis has implications for estimates of long-term uplift rates at tectonically-active margins based on the elevation of Last Interglacial sea-level highstands (e.g., Radtke et al., 2006; Muhs et al., 2012; Simms et al., 2015). Moreover, our results will quantify the extent to which sediment loading may impact estimates of peak globally averaged sea level during the LIG that have included sea-level markers at tectonically active sites such as Barbados (Kopp et al., 2009, 2013).

7.2 Methods

7.2.1 Observations: LIG dataset

We use a database of 1753 measured elevations of LIG sea-level markers. Where multiple measurements were made at a single location, we retain the peak value, which results in a final dataset of 1287 observations. This global sea-level database is compiled from previously published LIG sea-level markers (Ferranti et al., 2006; Kopp et al., 2009; Pedoja et al., 2014; Hibbert et al., 2016), and includes markers on passive (354) and active (933) tectonic margins. Each marker is assigned an associated indicative range, and we explore the uncertainty associated with the elevation of the sea-level marker by running our analyses using both the upper and lower bound reported in this database.

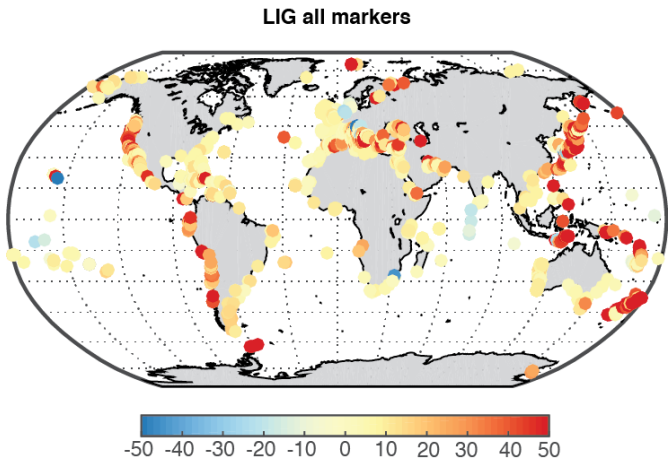

FIGURE 7.1: Elevation of Last Interglacial sea-level markers at 1287 sites (see text)

7.2.2 OBSERVATIONS: TECTONIC UPLIFT RATES

At active tectonic margins, paleo sea-level records are commonly used to derive estimates of long-term uplift or subsidence rates. As an example, a typical procedure uses marine terraces dated to the LIG to infer long-term tectonic uplift rates, and these rates are then adopted to correct for paleo-shorelines dated to other periods (e.g. MIS 5a/5c, MIS 11)(Chappell, Ota and Berryman, 1996; Radtke et al., 2006). However, choosing a reference LIG sea-level value is complicated by uncertainty in the magnitude and timing of peak GMSL, as well as the significant geographic variability in the elevation of LIG markers associated with local processes, such as GIA (Creveling et al., 2015, Simms et al., 2015, Lambeck & Chappell 2001). An additional confounding factor contributing to variability in LIG shoreline elevations is the sea-level change due to sediment loading. Since erosion rates often scale with uplift (Perron, 2017), tectonically uplifting margins tend to produce high volumes of sediment, which are ultimately transported to the oceans. The impact of this mass flux may be important to consider when estimating the uplift rate of marine terraces.

To illustrate this issue, we compile marine terrace data from Simms et al. (2015) and Radtke et al.,

(2006) and estimate the effect of sediment loading on estimates of long-term tectonic uplift rates in two regions: the North American west coast and Barbados.

7.2.3 Modeling: Glacial isostatic adjustment

Sea level varies spatially in response to the redistribution of surface mass loads, including ice, water, and sediment, as ice sheets grow and decay over a glacial cycle. We perform calculations based on the theory and pseudo-spectral algorithm described by Kendall et al. (2005) with a spherical harmonic truncation at degree and order 512. These calculations include the impact of load-induced Earth rotation changes on sea level (Milne and Mitrovica, 1996; Mitrovica et al., 2005), evolving shorelines, and the migration of grounded, marine-based ice (Johnston, 1993; Milne et al., 1999; Lambeck et al., 2003; Kendall et al., 2005), and they incorporate a gravitationally self-consistent treatment of sediment loads (Dalca et al., 2013, Pico et al., 2016, Ferrier et al., 2017).

7.2.4 Modeling: Constructing global sedimentation history over the last glacial cycle

In order to construct a sediment loading history since the LIG we adopt a global compilation of modern river flux measurements (776 rivers; total suspended sediment reported in Milliman & Farnsworth, 2011). River fluxes varied over the course of the glacial cycle. However, at present there is insufficient data on rivers globally to assess the time history of sediment delivery to the ocean for most rivers over the last glacial cycle. As a consequence, in this study we assume that sediment flux is uniform through time. Improving this model of sediment loading will require detailed studies of each river that incorporate erosional and depositional records over the last glacial cycle, including accumulation rates based on sediment cores (as in Ferrier et al., 2015; Pico et al., 2016).

We model the riverine sedimentation since the LIG by simulating marine river deposition using a diffusive model applied to the case of a migrating shoreline. We adopt shoreline predictions from

a GIA simulation based on Earth model VM2 and the ice history ICE-PC2 based on a suite of constraints on global ice volume histories during MIS 5a, 5c, and MIS 3 (Creveling et al., 2017, Pico et al., 2016, Pico et al., 2017). The model is run with 200 year time steps over 100,000 years, and the river mouth (sediment flux source) evolves with the shoreline, the position of which is determined by searching for the nearest coastline node at every time step. To simulate marine deposition, we adopt an Alternating Direction Implicit (ADI) method for solving the diffusion equation, including the sediment flux as a source term and a diffusion constant of $1x10^6$ m^2/yr (Fagherazzi and Overeem, 2007). Diffusion of sediment occurs solely in ocean regions, as determined by the predicted shoreline location. This simulation of marine deposition results in a relatively realistic approximation of the geometry of sedimentation, where large deltaic depocenters build up, and more diffusive regions of deposition occur near mountainous areas drained by small rivers. To conserve mass, we uniformly remove a layer of sediment from each continental drainage basin with a volume equivalent to the sediment flux deposited in the oceans. This procedure accounts for density difference between marine (1750 kg/m^3) and terrestrial sediments (2650 kg/m^3) (Bahr et al., 2001). The resulting sediment erosion and deposition over the last glacial cycle is shown in Figure 2.

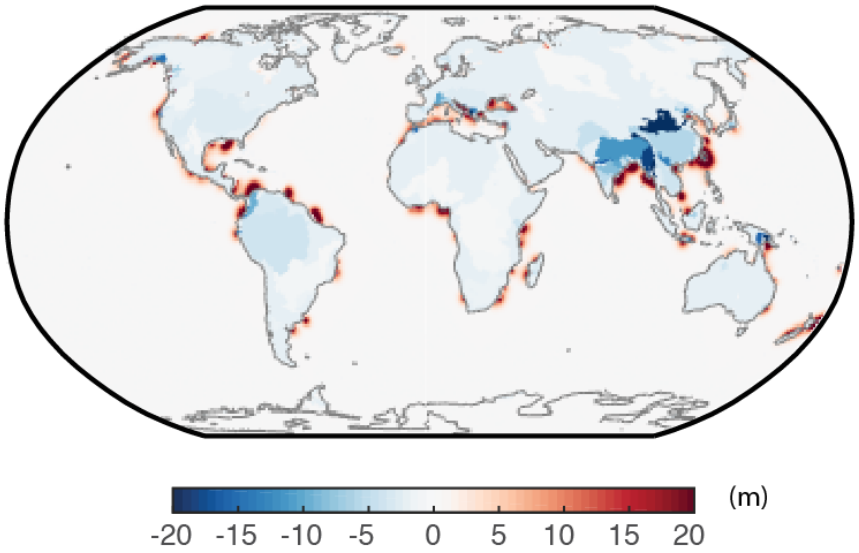

FIGURE 7.2: Cumulative modeled sediment transfer from 122 ka to 0 ka.

7.3 Results

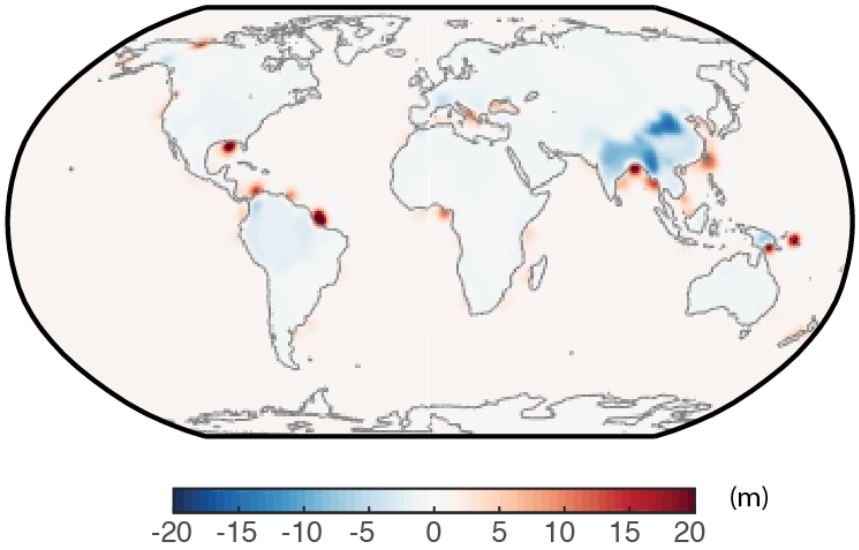

Figure 7.3: Modeled sea level change due to sediment loading from 122 ka to 0 ka relative to the LIG. Positive values are areas where sediment loading has caused an increase in sea level since the LIG.

7.3.1 Sea-level response to sediment loading

Using the sedimentation redistribution construction described above, we derive a time-varying sediment loading history since the LIG. We then perform GIA simulations that adopt this history, and in this case, we ignore ice load changes in order to isolate the effect of sedimentation. The resulting sea-level change due to sediment loading since the LIG is shown in Figure 3.

Sites susceptible to sediment loading experience a sea-level rise in response to this loading. Therefore, the present-day elevation of LIG sea-level markers would be lower than one would predict in the absence of sediment loading (Figure 4). We would then expect a negative correlation between predicted sea-level change due to sediment loading and the elevation of LIG sea-level markers.

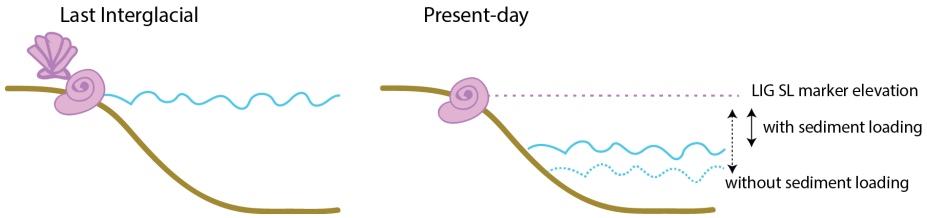

Figure 7.4: Schematic diagram shows (A) sea level at the LIG and (B) the observed elevation of a LIG SL marker for a site with sediment loading (solid line) and without sediment loading (dotted line). The observed elevation would be lower at a site with high sediment loading because sea level has increased due to loading from the LIG to present.

The largest sediment loading sea-level signals are located near major river deltas, and these sea-level effects are highly localized. However, sediment loading associated with small rivers that drain uplifting mountain ranges can also drive relatively large (5-10 m) sea-level changes along active tectonic margins.

7.3.2 Statistical analysis

We are interested in determining whether predicted spatial variability of sea-level changes due to sediment loading is reflected in the observed elevation of LIG sea-level markers. LIG sea-level markers

sampled at different locations are not independent from each other, and to account for this we build a regression model that incorporates spatial autocorrelation. We account for whether a site is tectonically active, in addition to estimating the sea-level change due to GIA associated with ice loading since the LIG. We first run a least squares regression model, $Y = X\beta + \epsilon$, where Y is the observed elevation of LIG sea level markers, and X includes the following predictor variables: 1) a variable of the mean-centered predicted sea-level change due to sediment loading (X_{SLsed} ; calculated from Figure 3), 2) a dummy (binary) variable that categorizes active and passive margin sites (X_{active}), where active sites are assigned a value of one and passive sites are assigned a value of zero, 3) an interaction term ($X_{interact}$) where active margin sites are set equal to XSLsed, the predicted sea-level change variable, and 4) a GIA term that is calculated from the average of 70 Earth models (X_{GIA} ; see Appendix). In order to account for spatial autocorrelation, we calculate the residuals from this model and use these to construct an autocovariate variable (X_{ac}) that is a distance-weighted function of the neighboring response values. The distance range of neighbors is set by fitting a semivariogram to the residuals and calculating the range, which yields a value of 5.44 km. Next we use a linear model that uses MM-estimation to perform an analysis that is robust to outliers. This model includes the above predictor variables (X_{SLsed}, X_{active} $X_{interact}$ X_{GIA}) and the autocovariate variable X_{ac}, which accounts for spatial autocorrelation.

In Figure 5 we plot the elevation of LIG sea-level markers against the predicted sea-level change for passive (blue) and active (pink) margins. The estimated relationship is shown by the pink and blue lines, and the shaded regions in the figure represent the calculated error bars in the regression for each. The estimated β coefficients for each variable are shown in Appendix Table 1. As discussed in the context of Figure 4, we expect a negative to exist between the observations and the prediction. In the case of passive margins there is no clear relationship between their predicted signal from sediment loading and the elevation of sea-level markers (slope = -0.138$\pm$0.305; p = 0.651; Figure 5). For active margins, there is a weak, yet significant positive relationship ((slope = 1.169$\pm$0.739; p

$=3.72\text{x}10^{-14}$) between the two. By analyzing the interaction term, we also determine that the slope describing the relationship between marker elevation and predicted sea level for sites on active margins is significantly (95% confidence level) different (β =1.307±0.434; p=0.00265) than the slope for passive margins.

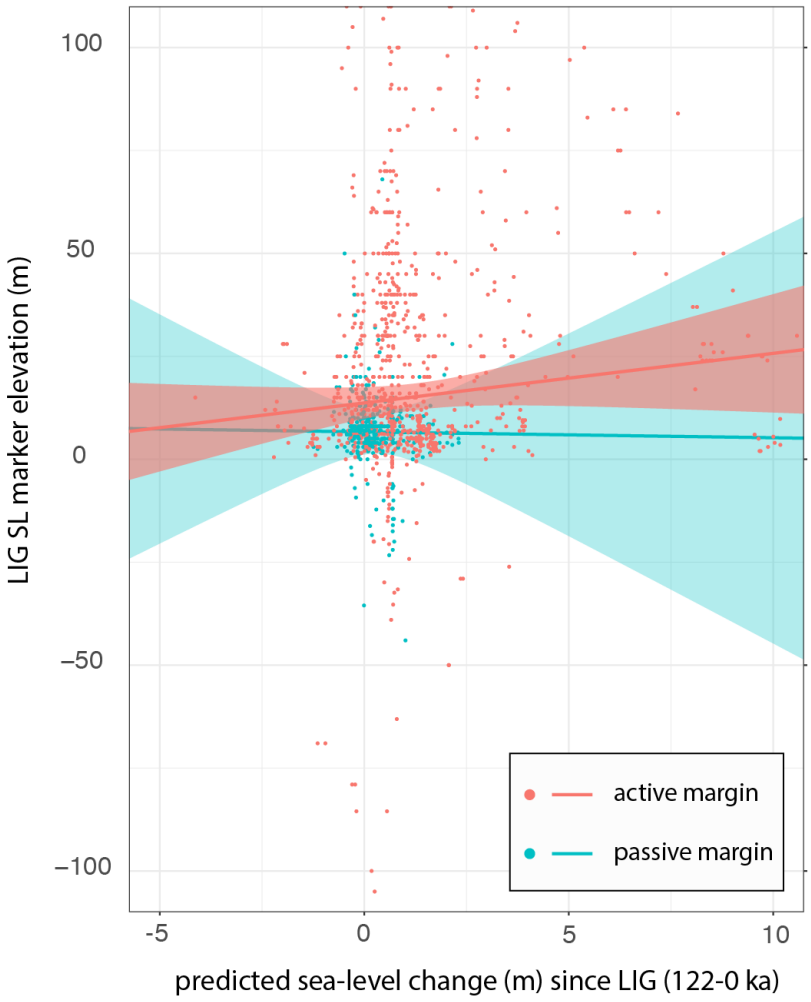

FIGURE 7.5: Correlation between predicted sea-level change due to sediment loading and the observed elevation of LIG sea-level markers (active sites – pink dots; passive sites – blue dots). Shaded regions represent error bars on each regression.

We performed analyses with the upper and lower bound elevations of LIG sea-level markers and found that the relationship between predicted sea level and observed LIG sea-level markers was unchanged (Appendix Table 2/3). We also performed sensitivity tests where we altered the lithospheric thickness, and upper and lower mantle viscosity while retaining the sedimentation history in Figure 2. We found that the calculated correlation coefficients were nearly identical (Appendix Table 4-8).

7.4 Discussion

We have explored the impact of sediment loading on sea level over the last glacial cycle by: (1) generating a pattern of sediment deposition using a model of river delta evolution since the LIG and adopting modern day river sediment fluxes; and (2) running a gravitationally self-consistent sea level solver developed in the ice age community.

A statistical analysis indicates that our predictions of sea-level change due to sediment loading do not correlate strongly with the observed elevation of 1287 LIG sea-level markers. At active margins, there is a statistically significant positive relationship between elevation and predicted sea-level, whereas simple physical arguments suggest that the correlation should be negative. This positive correlation likely reflects the dominance of tectonic uplift at these sites because rates of uplift are not explicitly accounted for in our model. Though estimates of tectonic uplift exist at many sites, these estimates are largely based on the same Last Interglacial sea-level markers, and using them would introduce circularity in our analysis.

Given the current database, it will be challenging to detect any globally coherent trend for the influence of sediment loading on LIG sea level. Future improvements in this dataset may ultimately reveal a signal of sediment loading on the elevation of LIG sea-level markers. However, we note that the accuracy of our model predictions is limited by our assumption of a constant sediment flux and our method of constructing the geometry of deposition. Finally, while we have not detected global coherency between or predicted sediment loading signal and observations, the impact such loading

may nevertheless be important at passive margin sites (our estimates range from -1.24 m to 16.27 m) where the elevation of LIG sea-level markers have been measured. This signal should thus be accounted for before these data sets are used, for example, to infer peak global mean sea level during the LIG.

7.4.1 Implications for derived tectonic uplift rates in western United States/Barbados

Since sediment loading effects are most significant at active tectonic margins, this contribution should be accounted for in estimating tectonic uplift rates based on the elevation of LIG sea-level markers. Along the Pacific coast of the United States, sea level is perturbed by up to 10 m due to sediment loading (Figure 3), comparable in magnitude to the impact of GIA since the LIG (8-14 m; Simms et al., 2015). We have recalculated the GIA-corrected tectonic uplift rates published in Simms et al. (2015) using the predictions described above to correct for sediment loading and find that doing so changes the predicted tectonic uplift rates at these sites by as much as 16

The tectonic uplift rate at Barbados has been estimated from the elevation of MIS6-5 sea-level markers (Fairbanks, 1989) by assuming that peak global mean sea level reached 6 m during the LIG (Radtke et al., 2006). This uplift rate has subsequently been used to correct sea-level records in this region for tectonic effects, including the deglacial sea-level portion of the record which is widely-used as a global ice volume curve in paleoclimate, GIA, and ice modeling communities. At this site, we predict that sea level since the LIG has increased by 4 m due to sediment loading, and accounting for this signal increases the inferred tectonic uplift rate by 7

Revising tectonic uplift rates is important for our understanding of long-term tectonics in these regions. However, an accurate assessment of uplift rates is also important for estimating global mean sea level changes based on geological markers at these sites. Key sea level sites used in this effort (Huon Peninsula, Barbados, Vanuatu) are within active tectonic margins, in part because they have the potential to preserve shoreline features through uplift (Chappell, Ota and Berryman, 1996;

Cabioch and Ayliffe, 2001; Radtke et al., 2006). It is essential to consider the impact of sediment loading on sea level in these regions because sites of tectonic uplift are often associated with high rates of marine sedimentation. Indeed, accurate reconstructions of LIG sea-level with the goal of determining long-term uplift rates becomes even more imperative when extrapolating these uplift rates to older shorelines, such as MIS 11 (Raymo and Mitrovica, 2012).

7.5 Conclusion

The elevation of LIG sea-level markers is highly variable, and previous studies have not considered how the effects of sediment loading have influenced this variability on a global scale. We explore this variability by simulating deltaic deposition in 776 rivers over a full glacial cycle and computing the resulting sea-level change due to sediment loading at 1287 sites in a database of LIG sea-level markers. The analysis, based on a regression model that accounts for spatial autocorrelation and is robust to outliers, indicates that there is no statistically-significant signal of sediment loading on the observed elevation of LIG sea-level markers. Nevertheless, local changes in sea level due to sediment loading can be substantial and we show that accounting for this signal can alter the inferred uplift rates in tectonically active regions such as Barbados and the North American Pacific coast.

7.6 Acknowledgements

We want to thank P. Huybers for insightful discussions and Steven at the Institute for Quantitative Social Sciences for advice on statistical modeling. J. Weisenberg performed a literature review on this topic as an undergraduate researcher.

7.7 References

Austermann, J., Mitrovica, J. X., Huybers, P. and Rovere, A. (2017) 'Detection of a dynamic topography signal in last interglacial sea-level records', Science Advances, 3(7), p. e1700457. doi: 10.1126/sciadv.1700457.

Bahr, D. B., Hutton, E. W. H., Syvitski, J. P. M. and Pratson, L. F. (2001) 'Exponential approximations to compacted sediment porosity profiles', Computers and Geosciences, 27(6), pp. 691–700. doi: 10.1016/S0098-3004(00)00140-0.

Cabioch, G. and Ayliffe, L. K. (2001) 'Raised Coral Terraces at Malakula, Vanuatu, Southwest Pacific, Indicate High Sea Level During Marine Isotope Stage 3', Quaternary Research, 56, pp. 357–365. doi: 10.1006.

Chappell, J., Ota, Y. and Berryman, K. (1996) 'Late quaternary coseismic uplift history of Huon Peninsula, Papua New Guinea', Quaternary Science Reviews, 15(1), pp. 7–22. doi: 10.1016/0277-3791(95)00062-3.

Creveling, J. R., Mitrovica, J. X., Hay, C. C., Austermann, J. and Kopp, R. E. (2015) 'Revisiting tectonic corrections applied to Pleistocene sea-level highstands', Quaternary Science Reviews. Elsevier Ltd, 111, pp. 72–80. doi: 10.1016/j.quascirev.2015.01.003.

Dendy, S., Austermann, J., Creveling, J. R. and Mitrovica, J. X. (2017) 'Sensitivity of Last Interglacial sea-level high stands to ice sheet con fi guration during Marine Isotope Stage 6', Quaternary Science Reviews. Elsevier Ltd, 171, pp. 234–244. doi: 10.1016/j.quascirev.2017.06.013.

Dutton, A. and Lambeck, K. (2012) 'Ice Volume and Sea Level During the Last Interglacial', Science, 337(6091), pp. 216–219. doi: 10.1126/science.1205749.

Fagherazzi, S. and Overeem, I. (2007) 'Models of Deltaic and Inner Continental Shelf Landform Evolution', Annual Review of Earth and Planetary Sciences, 35(1), pp. 685–715. doi: 10.1146/annurev.earth.35.031306.140128.

Fairbanks, R. G. (1989) 'A 17,000 year glacio-eustatic sea level record: Influence of glacial melting rates on the Younger Dryas event and deep-ocean ciruclation', Nature.

Ferranti, L., Antonioli, F., Mauz, B., Amorosi, A., Dai, G., Mastronuzzi, G., Orru, P., Pappalardo, M., Radtke, U., Renda, P., Romano, P. and Sanso, P. (2006) 'Markers of the last interglacial sea-level high stand along the coast of Italy□: Tectonic implications', Quaternary International, 146, pp. 30–54. doi: 10.1016/j.quaint.2005.07.009.

Ferrier, K. L., Mitrovica, J. X., Giosan, L. and Clift, P. D. (2015) 'Sea-level responses to erosion and deposition of sediment in the Indus River basin and the Arabian Sea', Earth and Planetary Science Letters. Elsevier B.V., 416, pp. 12–20. doi: 10.1016/j.epsl.2015.01.026.

Hibbert, F. D., Rohling, E. J., Dutton, A., Williams, F. H., Chutcharavan, P. M., Zhao, C. and Tamisiea, M. E. (2016) 'Coral indicators of past sea-level change□: A global repository of U-series dated benchmarks', Quaternary Science Reviews. Elsevier Ltd, 145, pp. 1–56. doi: 10.1016/j.quascirev.2016.04.019.

Kopp, R. E., Simons, F. J., Mitrovica, J. X., Maloof, A. C. and Oppenheimer, M. (2009) 'Probabilistic assessment of sea level during the last interglacial stage.', Nature, 462, pp. 863–867. doi: 10.1038/nature08686.

Kopp, R. E., Simons, F. J., Mitrovica, J. X., Maloof, A. C. and Oppenheimer, M. (2013) 'A probabilistic assessment of sea level variations within the last interglacial stage', GJI, pp. 711–716. doi: 10.1093/gji/ggt029.

Lambeck, K. and Chappell, J. (2001) 'Sea level change through the last glacial cycle.', Science (New York, N.Y.), 292(5517), pp. 679–686. doi: 10.1126/science.1059549.

Milne, G. a. and Mitrovica, J. X. (1996) 'Postglacial sea-level change on a rotating Earth: first results from a gravitationally self-consistent sea-level equation', Geophysical Journal International, 126(3), pp. F13–F20. doi: 10.1111/j.1365-246X.1996.tb04691.x.

Mitrovica, J. X., Wahr, J., Matsuyama, I. and Paulson, A. (2005) 'The rotational stability of an ice-age earth', Geophysical Journal International, 161(2), pp. 491–506. doi: 10.1111/j.1365-246X.2005.02609.x.

Muhs, D. R., Simmons, K. R., Schumann, R. R., Groves, L. T., Mitrovica, J. X. and Laurel, D. (2012) 'Sea-level history during the Last Interglacial complex on San Nicolas Island, California: Implications for glacial isostatic adjustment processes, paleozoogeography and tectonics', Quaternary Science Reviews. Elsevier Ltd, 37, pp. 1–25. doi: 10.1016/j.quascirev.2012.01.010.

Pedoja, K., Husson, L., Johnson, M. E., Melnick, D., Witt, C., Pochat, S., Nexer, M., Delcaillau, B., Pinegina, T., Poprawski, Y., Authemayou, C., Elliot, M., Regard, V. and Garestier, F. (2014) 'Coastal staircase sequences re fl ecting sea-level oscillations and tectonic uplift during the Quaternary and Neogene', Earth Science Reviews. Elsevier B.V., 132, pp. 13–38. doi: 10.1016/j.earscirev.2014.01.007.

Peltier, W. R., Argus, D. F. and Drummond, R. (2015) 'Space geodesy constrains ice age terminal deglaciation: The global ICE-6G_C (VM5a)model', Journal of Geophysical Research: Solid Earth, 119. doi: 10.1002/2014JB011176.Received.

Perron, J. T. (2017) 'Climate and the Pace of Erosional Landscape Evolution', Annual Review of Earth and Planetary Sciences, 45(1), p. annurev-earth-060614-105405. doi: 10.1146/annurev-earth-060614-105405. Pico, T., Mitrovica, J. X., Ferrier, K. L. and Braun, J. (2016) 'Global ice volume during MIS 3 inferred from a sea-level analysis of sedimentary core records in the Yellow River Delta', Quaternary Science Reviews. Elsevier Ltd, 152, pp. 72–79. doi: 10.1016/j.quascirev.2016.09.012.

Radtke, U., Schellmann, G., Radtket, U. and Schellmann, G. (2006) 'Uplift History along the Clermont Nose Traverse on the West Coast of Barbados during the Last 500,000 Years-Implications for Paleo-Sea Level Reconstructions Stable', Journal of Coastal Research, 22(2), pp. 350–360. doi: 10.2112/05-0439.1.

Raymo, M. E. and Mitrovica, J. X. (2012) 'Collapse of polar ice sheets during the stage 11 interglacial', Nature. Nature Publishing Group, 483(7390), pp. 453–456. doi: 10.1038/nature10891.

Simms, A. R., Anderson, J. B., DeWitt, R., Lambeck, K. and Purcell, A. (2013) 'Quantifying rates of coastal subsidence since the last interglacial and the role of sediment loading', Global and Planetary Change. Elsevier B.V., 111, pp. 296–308. doi: 10.1016/j.gloplacha.2013.10.002.

Simms, A. R., Lambeck, K., Purcell, A., Anderson, J. B. and Rodriguez, A. B. (2007) 'Sea-level history of the Gulf of Mexico since the Last Glacial Maximum with implications for the melting history of the Laurentide Ice Sheet', Quaternary Science Reviews, 26, pp. 920–940. doi: 10.1016/j.quascirev.2007.01.001.

Simms, A. R., Rouby, H., Lambeck, K., Géologie, L. De, École, D., Supérieure, N. and Cnrs, U. M. R. (2015) 'Marine terraces and rates of vertical tectonic motion□: The importance of glacio-isostatic adjustment along the Pacific coast of central North America', (Xx), pp. 1–14. doi: 10.1130/B31299.1.

Waelbroeck, C., Labeyrie, L., Michel, E., Duplessy, J. C., McManus, J. F., Lambeck, K., Balbon, E. and Labracherie, M. (2002) 'Sea-level and deep water temperature changes derived from benthic foraminifera isotopic records', Quaternary Science Reviews, 21(1–3), pp. 295–305. doi: 10.1016/S0277-3791(01)00101-9.

Wolstencroft, M., Shen, Z., Tornqvist, T. E., Milne, G. A. and Kulp, M. (2014) 'Understanding subsidence in the MIssissippi Delta', 44(0). doi: 10.1002/2013JB010928.Received.

8

Conclusions and Future Work

If we recognize, however, that knowledge is shaped by the assumptions, values, and interests of a culture and that, within limits, one can choose one's culture, then it's clear that as scientists/theorists we have a choice.
–Patricia Hill Collins

A great deal of work remains necessary to fully understand the dynamics and stability of ice sheets, and how these interact with the oceans, atmosphere, and land. The primary motivation behind this thesis was to improve constraints on past ice sheets by approaching critical moments of the last ice age using unconventional sea level indicators. In Chapter 1, I used modeling of glacial isostatic adjustment, sediment loading, and sediment compaction to determine a likely value of globally-averaged sea level during Marine Isotope Stage 3. This work suggested a rapid pace of global glaciation in the 15 thousand years preceding the Last Glacial Maximum. Next, in Chapter 2, I found that much of this ice volume growth took place in North America, as the eastern Laurentide Ice Sheet glaciated rapidly. In Chapter 3, I assessed whether a rapid late growth of the Laurentide Ice

Sheet was physically plausible by performing numerical simulations with a dynamic ice sheet model. I found that these simulations predicted rates that were consistent with reaching Last Glacial Maximum ice volumes in 15 kyr. I am currently collaborating with experts in 3D ice modeling (Ruth Anne Halberstadt, UMass Amherst) and atmospheric dynamics (Dr. Leah Birch, Woods Hole Research Center) to understand the climatic regime during Marine Isotope Stage 3 that maintained ice-free conditions in eastern Canada.

Chapter 4 and 5 turn to a coupling between landscape evolution and glacial isostatic adjustment. In Chapter 4, I demonstrated that glacial isostatic adjustment may have played an important role in the eastern diversion of the Hudson River ~30,000 years ago by forcing a landscape evolution model to respond to crustal deformation imposed by different ice loading histories. I then expanded this work to other U.S. east coast rivers in Chapter 5. By calculating the perturbation to channel slope and upstream drainage area due to glacial isostatic adjustment during the growth of the Laurentide peripheral bulge, I predicted changes in sediment transport capacity along each river's profile. I then compared these predictions to the observed change in river dynamics in four major rivers: the Hudson, Delaware, Susquehanna, and Potomac River, finding that in all cases, with the exception of the Susquehanna, it was possible to predict the correct trend towards erosion or deposition evident in the geological record. I am currently working, in collaboration with Prof. Paul Bierman (University of Vermont), to expand this research by performing a detailed analysis of the Great Falls region in the Potomac River. This work indicates that the location of abandoned terraces dated to MIS 3 coincide with a location where the river transverses perpendicular to the gradient of uplift imposed by glacial isostatic adjustment (Bierman et al., in prep.).

In Chapter 6 I explored a critical event in the North American deglaciation: the timing of melt of the ice saddle connecting the Cordilleran and Laurentide Ice Sheets. I showed that the observed two-phase flooding of the Bering Strait can be used as a sea-level constraint to fingerprint the location and timing of melt in the saddle region. Using this constraint suggests a substantial mass of

ice melted from 13,000 to 11,500 years ago. The timing of the melting has important implications for global climate, as it would lead to a large influx of freshwater into the Arctic Ocean during the Younger Dryas cooling episode, acting as a trigger for this cold event.

I am currently following up on the Bering Strait project by investigating the stability of an ice stream of the Laurentide Ice Sheet 13,000 years ago. Recently, ice-rafted debris in marine sediment cores indicate that the Amundsen Ice Stream, flowing from the western Laurentide Ice Sheet, collapsed in less than 400 years 13,000 years ago. The stability of ice streams is strongly dependent on the slope of the underlying topography, and it is understood that a positive feedback of ice retreat occurs for ice streams underlain by a retrograde slope (known as the Marine Ice Sheet Instability hypothesis). In collaboration with Prof. Alex Robel (Georgia Tech) and Evelyn Powell (Harvard), I am using a simple ice flow model to demonstrate that a collapse of the Amundsen Ice Stream at this time is most consistent with the slope of an underlying bed slope that would have been produced by the ice history proposed in Chapter 6, characterized by substantial melting of the ice saddle from 13,000 to 11,500 years ago. Another implication of the research described in Chapter 6 involves the reconstruction of paleoceanography. I am collaborating with Marisa Borreggine (Harvard) to understand how our revised prediction of Bering Strait sea-level, and the associated connectivity of the Arctic and Pacific oceans, relates to the observed timing of anoxic or hypoxic events in nearby basins.

In Chapter 7 I returned to the question of sediment loading and sea level. I investigated whether the impact of sediment loading on sea level could, in part, explain the variability of the elevation of Last Interglacial sea-level markers. I found that there is no statistically significant global signal of sediment loading in a dataset comprising 1287 sea-level markers, although the regional impact of sediment loading on Last Interglacial sea level records can be substantial.

Each chapter of this thesis explores a key moment during the last ice-age and uses non-traditional measures of sea level to gain insight into the size and distribution of past ice sheets. In particular, this thesis represents a new direction in ice age research that bridges the fields of geomorphology,

geodynamics, and paleoclimate, and that uses past landscapes as an novel sea-level indicator. Future research will further develop these connections, exploring how landscapes and other geologic markers can serve as tools to infer surface deformation produced by past ice loading.

A

Chapter 1 Supplement

A.1 Sediment compaction

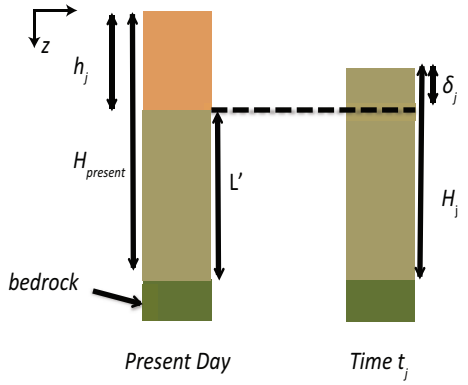

Figure A.1: Schematic illustration of sediment compaction and various parameters discussed in the text. The depth, z, is defined to be 0 at the surface and it increases downward in the column.

To estimate the effect of compaction on our paleo-topography elevations, we assume a porosity profile that follows an exponential porosity-depth relationship (Athy, 1930):

$$\Phi(z) = \Phi_0 e^{-\frac{z}{z_0}}$$

where Φ_0 is the surface porosity, z is the depth, and z_0 controls the length scale of the porosity reduction with depth.

Consider the two columns in Figure A.1: the one at left pertains to the present day and the other to an arbitrary time in the past, t_j. At present day there is a thickness of sediment h that has accumulated since the time of interest t_j, and a thickness of sediment beneath this to the bedrock, $L' = H_{present} - h_j$. At the time t_j, there is a thickness H_j of sediments to bedrock. The difference $H_j - L'$ is denoted as δ_j. A general expression for volume in a core from the top of the sediment downward at time t_j is:

$$Volume = A \int_0^{H_j} (1 - \Phi(z))dz$$

where A is the cross-sectional area of the column.

The mass of sediment grains in the column H_j and column L' must be equal, and since we assume that the grain density remains constant over time, we can equate the volumes in these two columns. This yields:

$$A \int_0^{H_j} (1 - \Phi(z))dz = A \int_0^{L'+h_j} (1 - \Phi(z))dz - A \int_0^{h_j} (1 - \Phi(z))dz$$

$$\int_0^{H_j} (1 - \Phi(z))dz = \int_0^{h_j} (1 - \Phi(z))dz + \int_h^{L'+h_j} (1 - \Phi(z))dz - \int_0^{h_j} (1 - \Phi(z))dz$$

$$\int_0^{H_j}(1-\Phi(z))dz = \int_{h_j}^{L'+h_j}(1-\Phi(z))dz$$

If we substitute $\delta_j = H_j - L'$, we obtain an expression for δ:

$$\delta_j = \Phi_0 z_0[1 - e^{-\frac{L'}{z_0}}(e^{-\frac{\delta_j}{z_0}} - e^{-\frac{h_j}{z_0}}) - e^{-\frac{h_j}{z_0}}]$$

Assuming that both δ_j and $h_j << z_0$, we can approximate this as

$$\delta_j = \frac{\Phi_0 h_j(1 - e^{-\frac{L'}{z_0}})}{(1 - \Phi_0 e^{-\frac{L'}{z_0}})}$$

To illustrate how we estimated δ_j, it will help to consider the procedure for decompaction at a single sediment core, SYS-0701. For this purpose, we choose the following values: Φ_0 = 0.63, the surface porosity (Guillocheau et al., 2012); z_0 = 3.7 km, appropriate for clay (Guillocheau et al., 2012); h_j = 19.3 m, the average thickness of the core between dates cal 46.97 ka BP and cal 48.48 ka BP, Liu et al. 2010); and $H_{present}$ = 1.68 km, the total thickness of the sediment column (Divins, 2003). From these values we estimate a compaction δ_j of 8.04 m for this site. In a similar manner, we can calculate δ_j over the entire region of study by using the sediment thickness h_j from the sediment redistribution models and a map of isopach sediment thickness to bedrock (Divins, 2003).

Sediment loads are calculated according to the equation:

$$\Delta L_j = \rho_w \Delta S_j + \rho_I \Delta I_j + (\bar{\rho}_{Hj} H_j - \bar{\rho}_{H0} H_0)$$

where the average bulk sediment density $\bar{\rho}_H$ over a given depth is based on the average porosity, $\bar{\Phi}(z)$, such that

$$\bar{\rho}_H = \rho_s - (\rho_s - \rho_w)\bar{\Phi}(z)$$

And $\bar{\Phi}(z)$ is defined as

$$\bar{\Phi}(z) = \frac{1}{z_2 - z_1} \int_{z_1}^{z_2} \Phi(z) = \frac{z_0 \Phi_0 (e^{-\frac{z_1}{z_0}} - e^{-\frac{z_2}{z_0}})}{z_2 - z_1}$$

This can be written as the integral from depth 0 to H_j:

$$\bar{\Phi}(z) = \frac{1}{H_j} \int_{0}^{H_j} \Phi(z) = \frac{-\Phi_0 z_0 (e^{-\frac{H_j}{z_0}} - 1)}{H_j}$$

If we substitute this expression into our equation for average density we obtain:

$$\bar{\rho}_{H_j} = \rho_s + (\rho_s - \rho_w) \frac{\Phi_0 z_0 (e^{-\frac{H_j}{z_0}} - 1)}{H_j}$$

Finally, the water volume storage capacity term is equal to the difference between newly created pore space and newly reduced pore space:

$$W_j = \int_{0}^{H_j} \Phi(z) dz - \int_{0}^{H_0} \Phi(z) dz$$

B

Chapter 2 Supplement

B.1 Supplementary Note 1: Sea-level data

In Supplementary Table 1 we list the elevation data from the U.S. mid-Atlantic coast used in Figure 1 to derive constraints on peak sea level during MIS 5a (80 ka) and mid-MIS 3 (50-35 ka). Parham et al.(Parham et al., 2013) compiled previously published data and assigned depositional environments to observed facies in cores and outcrops. In Figure 1, and Supplementary Table 1, markers are labeled as terrestrial, marine, or tidal. All dates are based on OSL except those noted as U-series, AAR (amino-acid racemization), or C14. Marine limiting samples GH25, GH15, MYK01 are dated to 37.7 $\pm$ 3.6 ka, 40 $\pm$ 4.3 ka, and 45.8 $\pm$ 4.3 ka, respectively; these records constrain RSL from 50-35 ka to being above -0.9 m, -3 m, and -2 m, respectively, as these correspond to shallow marine facies. GH 15/25 is a shelly muddy sand and has mollusk shell fragments, whereas MYK01 is a shelly sand in which Melita has been observed (interpreted as a shallow marine/shoreline complex). Qtp-1 and TCK-19 are terrestrial limiting samples, both at 0.8 m elevation dated to 39.6 $\pm$ 6.6 ka and 45.3$\pm$

4.3 ka, respectively, and correspond to quartz lithofacies, identified by Parham et al.(Parham et al., 2013) as terrestrial (see Scott et al.(Scott et al., 2010)). These two samples represent the minimum elevation of terrestrial sea-level indicators whose age uncertainties span 50-35 ka. We therefore conclude that RSL was in the range -1 to 1 m from 50-35 ka (as in Figure 1). The data of MIS 5a age from the mid-Atlantic coast of the U.S. suggest that local relative sea level (RSL) was between +2.55 and +7.5 m. Ages determined by Parham et al.(Parham et al., 2013) include samples FNB-02 and GH10, which are dated to 84.4 $\pm$ 8.6 ka and 81.5 $\pm$ 6.9 ka, at elevations of 2.55 m and 7.5 m respectively. FNB-02 is a marine limiting indicator, corresponding to a shelly muddy sand, interpreted as shallow marine. GH10-01 is a terrestrial-limiting indicator in a sand facies, interpreted as "shoreline complex"(Parham et al., 2013). While other sea level markers are lower than this range during this time interval, given the associated large age uncertainties, we assume the higher range represents the MIS 5a highstand. Moreover, this sea-level highstand is in agreement with previous studies of MIS 5a RSL in the region(Wehmiller, Edwards and Martin-McNaughton, 2004).

We add an uncertainty of $\pm$ 3 m to the elevation of these sea-level indicators since the tidal range may have been different in the past relative to the Holocene. For instance, Hill et al.(Hill et al., 2011) (2011) showed that the tidal range of the mid-Atlantic U.S. coast might have been 2-3 times the magnitude at 9 ka. Present day tidal range in the region is $\sim$1 m(Titus, J., & Wang, no date), and we thus assign a maximum value of $\pm$ 3 m to account for the possible paleo tide range.

B.2 Supplementary Note 2: Decomposing Sea Level Change into Deformational and Direct Gravitational Effects

Relative sea level (RSL) can be decomposed into global mean sea level (GMSL) plus a term associated with glacial isostatic adjustment (GIA):

TABLE B.1: Supplementary Table 1: Sea-level data

Sample No.	Elevation (m)	Age (ka)	Age error (ka)	Indicator type	Analytical technique	Latitude	Longitude	Reference
FS181	9.3	35.8	6.1	terrestrial	OSL	35.609	-77.217	(Moore, 2009)
KNL02	5.5	41.8	3.2	terrestrial	OSL	35.022	-76.898	(Parham et al., 2013)
GH23-01	3.65	31.8	3	terrestrial	OSL	36.717	-76.529	(Parham et al., 2013)
GH25-01	-0.9	37.7	3.6	marine	OSL	36.699	-76.359	(Parham et al., 2013)
GH15-01	-3	40	4.3	marine	OSL	35.737	-76.534	(Parham et al., 2013)
MYK-01	-2	45.8	4.3	marine	OSL	36.532	-76.177	(Parham et al., 2013)
TCK-17	0.345	54.3	6.7	terrestrial	OSL	36.270	-75.911	(Mallinson et al., 2008)
TCK-19	0.826	45.3	4.3	terrestrial	OSL	36.335	-75.907	(Mallinson et al., 2008)
HS-02	-0.15	46.4	2.5	terrestrial	OSL	36.343	-76.064	(Mallinson et al., 2008)
HS-03	-0.9	48.9	10.9	terrestrial	OSL	36.343	-76.064	(Mallinson et al., 2008)
RI-03	0.05	55.4	7.2	terrestrial	OSL	35.939	-75.718	(Mallinson et al., 2008)
DR-2	1.5	62	12	tidal	OSL	35.930	-76.165	(Parham et al., 2013)
qw-1	1.9	46.9	6.9	terrestrial	OSL	37.162	-75.980	(Scott, 2006)
qw-2	1.9	38.9	5.5	terrestrial	OSL	37.162	-75.980	(Scott, 2006)
qts-1	5.1	49.7	5.9	terrestrial	OSL	36.895	-76.515	(Scott, 2006)
qtp-1	0.8	39.6	6.6	terrestrial	OSL	36.577	-76.037	(Scott, 2006)
qtp-2	0.75	44.4	5.2	terrestrial	OSL	36.577	-76.037	(Scott, 2006)
cr-08-gp1b	3.6	50.4	5.8	terrestrial	OSL	34.729	-76.861	(Best, 2010)
c-1	-2.8	62	2	marine	U-series	36.975	-76.172	(Mixon, Szabo and Owens, 1982)
ELP-05	-0.6	66.9	6.7	tidal	OSL	35.857	-75.952	(Parham et al., 2013)
SS-2 exp	2.85	79.81	4.55	terrestrial	OSL	34.977	−75.830	(Mallinson et al., 2008)
FNB-02	2.55	84.4	8.6	marine	OSL	34.982	-76.945	(Parham et al., 2013)
CR-08-GP3	4	80.8	9	terrestrial	OSL	34.729	-76.861	(Best, 2010)
CR-08-GP5	4.5	83.4	8.92	terrestrial	OSL	34.729	-76.861	(Best, 2010)
GH18-01	-3.4	76.9	7.1	terrestrial	OSL	35.620	-76.357	(Parham et al., 2013)
GH2-01	11.5	88.5	8	terrestrial	OSL	35.167	-76.851	(Parham et al., 2013)
MLD01-02a	-7	74.9	8	marine	OSL	35.509	-76.001	(Parham et al., 2013)
MLD01-02b	-8.5	80	10	tidal	AAR	35.509	-76.001	(Parham et al., 2013)
GH8-02	12.2	80.2	7	terrestrial	OSL	35.732	-76.815	(Parham et al., 2013)
GH10-01	7.5	81.5	6.9	terrestrial	OSL	35.715	-76.757	(Parham et al., 2013)
TT-01	12.81	87.5	6.9	terrestrial	OSL	36.346	-76.602	(Parham et al., 2013)
qnb-1	3.25	69.3	7.6	terrestrial	OSL	37.195	-76.005	(Scott, 2006)
qnb-2	3.25	69.7	8.4	terrestrial	OSL	37.195	-76.005	(Scott, 2006)
GH26,30,33	5.8	80	10	marine	AAR	35.726	-76.099	(Parham et al., 2013)
C-2	-1	73	4	marine	U-series	36.742	-76.188	(Mixon, Szabo and Owens, 1982)
4	0	75	5	marine	U-series	36.788	-76.196	(Cronin et al., 1981)
GH20-01	4.7	94.1	8.3	terrestrial	OSL	36.392	-76.530	(Parham et al., 2013)
CR-08-GP4	7.16	95.2	9.25	terrestrial	OSL	34.729	-76.861	(Best, 2010)
GH12-01	5.3	106.7	9.3	tidal	OSL	35.703	-76.755	(Parham et al., 2013)
GH24-01	2.04	97.4	8.6	marine	OSL	36.729	-76.453	(Parham et al., 2013)
GH5-01	-0.05	102.3	9.9	marine	OSL	35.179	-76.771	(Parham et al., 2013)
EDP-03	10	103	8.3	tidal	OSL	35.250	-76.771	(Parham et al., 2013)
ELP-01	-7.3	100.3	9.5	marine	OSL	35.900	-75.963	(Parham et al., 2013)
GH1-01	7.42	111.6	10.2	tidal	OSL	35.182	-76.857	(Parham et al., 2013)
BC-02	11.1	130	10.8	tidal	OSL	35.756	-76.830	(Parham et al., 2013)
OBX-12	-16.25	43.2	0.48	marine	14 C	35.439	-75.486	(Culver et al., 2011)

$$RSL = GMSL + GIA$$

and the GIA term can be further decomposed into sea level contributions from crustal deformation (including the gravitational perturbation associated with this deformation; R) and the direct gravitational effects of the surface mass load (G_D):

$$GIA = R + G_D$$

Figure S1 shows the decomposition of RSL predictions at our reference site in the Albemarle Embayment region (white star, Figure 1) into the three terms GMSL, R and GD. Results are shown for simulations based on ice histories ICEPC and ICEPC2. Delaying the growth of ice in the eastern sector of the Laurentide Ice Sheet (LIS) until MIS 3 (44 ka), suppresses deformational effects, yielding a higher RSL prediction for the ICEPC2 model at 44 ka relative to the ICEPC simulation. The relative contribution of crustal deformation to predicted RSL will be a function of the Earth model, and in particular the values adopted for lithospheric thickness and lower and upper mantle viscosities. Using the Earth model described in the main text, we noted that crustal deformation dominates the RSL signal compared to direct gravitational effects. We explore the sensitivity of this decomposition to variations in Earth structure by running simulations for additional Earth models. In Supplementary Figure 2, results are shown for predictions in which the following parameter ranges are considered: (A) lithospheric thickness from 72 - 127 km; (B) lower mantle viscosity from [5-30] x 10^{21} Pa s; and (C) upper mantle viscosity from [0.3-1] x 10^{21} Pa s. We note that several of these Earth models predict local RSL values that lie outside the observational bound at MIS 3 (Supplementary Figure 2, orange box). For predictions that are consistent with this bound, the crustal deformation signal is larger than the signal from direct gravitational effects of the surface mass load

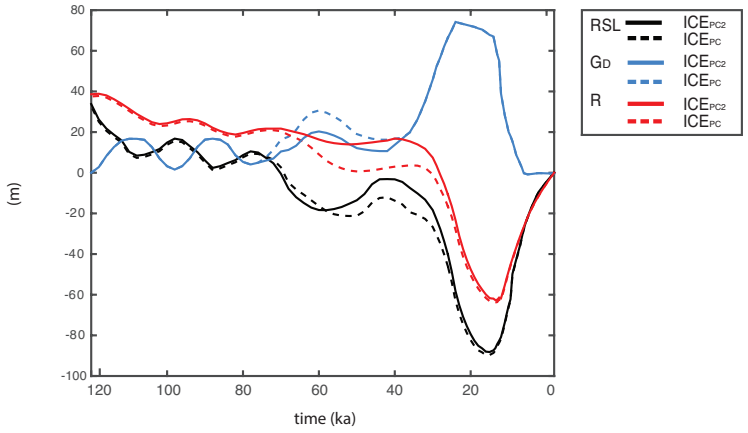

FIGURE B.1: Decomposition of RSL predictions (black lines) at location shown by white star (Figure 1) is based on the ice histories ICEPC2 (solid lines) and ICEPC (dashed lines) into contributions from deformation (R; red lines) and direct gravitational attraction of the surface mass load (G_D; blue lines).

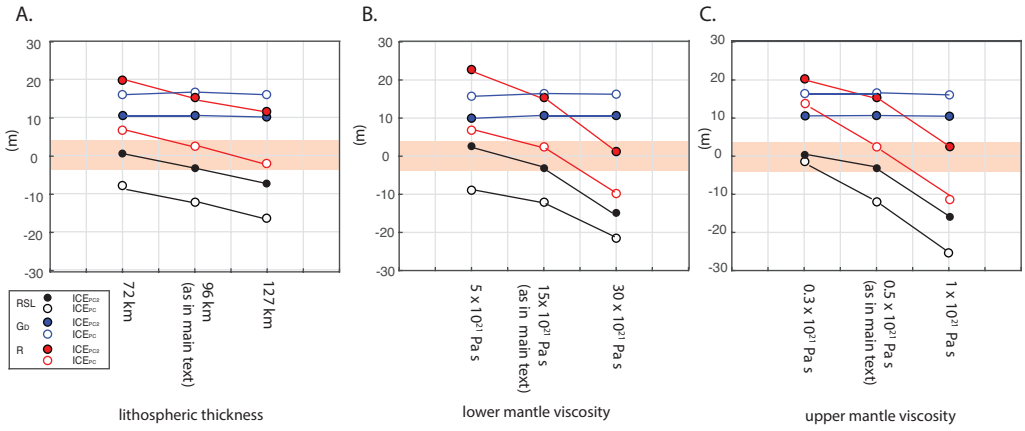

FIGURE B.2: Decomposition of RSL predictions (black) at location shown by white star (Figure 1) is based on the ice histories ICEPC2 (solid circles) and ICEPC (white circles) into contributions from deformation (R; red) and direct gravitational attraction of the surface mass load (GD; blue) for six additional Earth models where we perturb A. the lithospheric thickness B. lower mantle viscosity C. upper mantle viscosity. The orange box denotes the observational sea-level bounds (Figure 1).

B.3 Supplementary Note 3: Sensitivity to ice history and geographic distribution

To test the sensitivity of our simulations to the GMSL values at MIS 5a and MIS 5c, we constructed ice histories as described above, with the exception that we allowed GMSL to range from -16 to 0 m at 80 ka (MIS 5a), and from -20 to 0 m at 100 ka (MIS 5c). We ran simulations with 100 of these ice models and found that the predicted RSL at 44 ka is perturbed by no more than ~0.7 m.

Next we explored the sensitivity of sea-level predictions in the Albemarle Embayment region to variations in the ice cover over the eastern sector of the LIS (Figure S3). Specifically, we: (1) shifted the northern latitudinal boundary of the no-ice zone in eastern Laurentia from 60 °N (ICEPC2) to 57°N (ICEPC3) and 55°N (ICEPC4); and (2) modified the location of ice in eastern Laurentia, such that Newfoundland and Northern Quebec are glaciated (Geometry 1,2, and 3). For this series of ice geometries, we include one ice history where Baffin Island is glaciated (Geometry 1), and two where the southern portion of the island is not (Geometries 2 and 3). The latter two ice geometries are distinguished by their latitudinal bounds: in Geometry 2, ice cover extends to 51°N in the eastern sector of the LIS, whereas in Geometry 3 it extends to 52°N. Supplementary Table 2 gives the change in ice volume compared with the standard assumption of ice distribution for each ice model listed, and the resulting relative sea level predicted.

Table B.2: Supplementary Table 2: Prediction of relative sea level at 44 ka based on a variety of ice models

Ice model	Difference in ice volume (m GMSL)	Relative Sea Level
ICEPC	0	-12
ICEPC2	6.8	-3.1
ICEPC3	5.3	-3.8
ICEPC4	4.2	-5.1
Geometry 1	5.3	-6.3
Geometry 2	6.1	-5.8
Geometry 3	6.53	-3.8

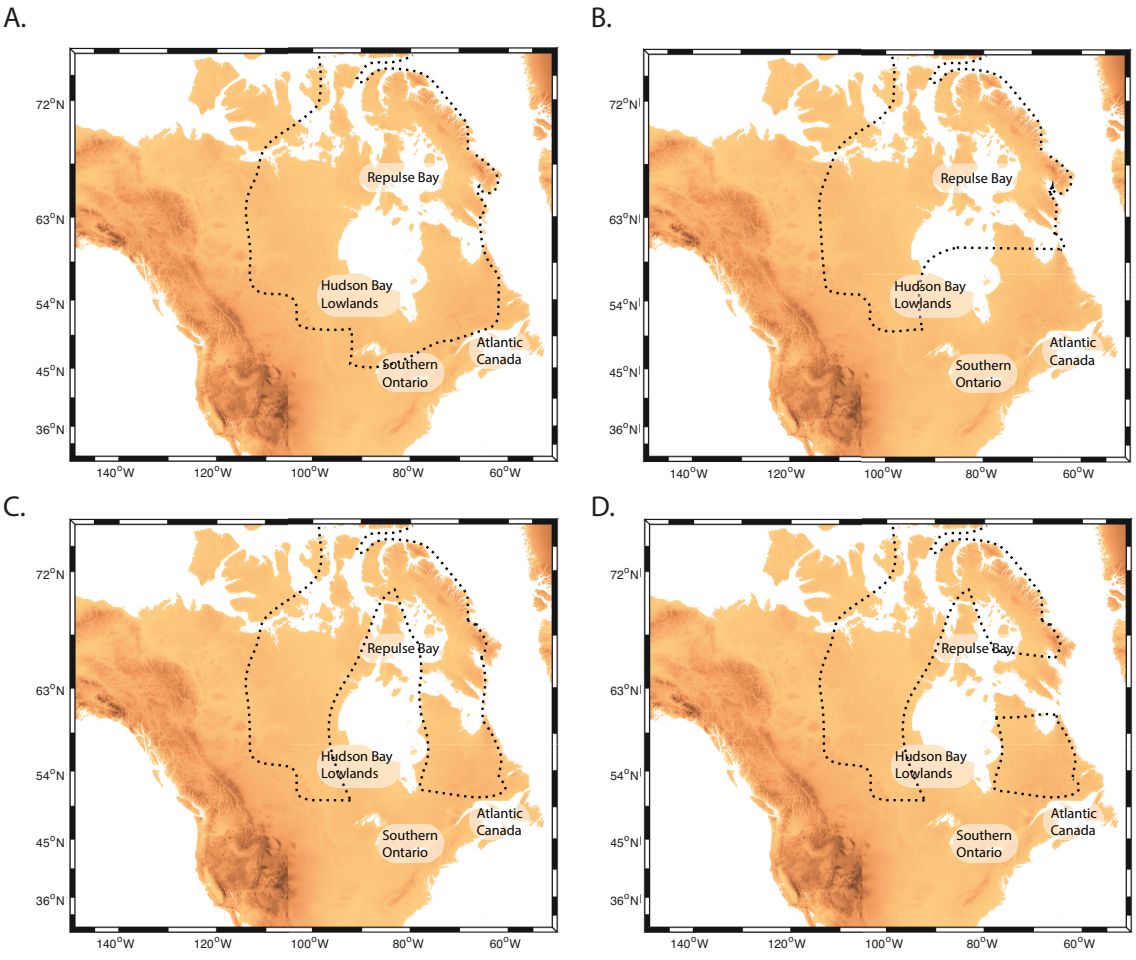

Figure B.3: Geographic distribution of ice cover for various ice models. A. ICEPC (standard ice distribution, as in Figure 2 and 3B) B. ICEPC2 (alternate ice distribution, as in Figure 2 and 3B). ICEPC3 and ICEPC4 are distinguished by the latitudinal extent of ice cover over the eastern sector of the LIS (see text). C. Geometry 1. D. Geometry 2 & 3 (these two models are distinguished by the latitudinal extent of ice cover - see text). In frames B-D, the difference in ice volume between the given ice model and model ICEPC in eastern Laurentia is distributed uniformly over the LGM extent of western Laurentia, the Cordilleran Ice Sheet, and Fennoscandia.

B.4 Supplementary Note 4: Earth model sensitivity

We ran a large suite of simulations in which we adopted ice histories with the GMSL curves shown in Figure 3A. The calculations, shown in Figure 3B, were based on an Earth model with upper and lower mantle viscosities of 0.5 x 10^{21} Pa s and 15 x 10^{21} Pa s, respectively. These runs yielded predicted peak RSL values within the Albemarle Embayment region during MIS 3 that ranged from -28.6 to -5.7 m when pre- and post-LGM ice geometries were assumed to match when GMSL values were equal (as in ice model ICEPC) and -14.8 m to 2.4 m when it was assumed that the eastern sector of the LIS remained ice free in an extended period leading to MIS 3 (as in ice model ICEPC2). When we reran these calculations using an Earth model in which the lower mantle viscosity was increased to 2 x10^{22} Pa s, the above ranges were perturbed upwards by ∼1.5 m. Decreasing the lower mantle viscosity to 10^{22}Pa s, perturbed the above RSL range downwards by ∼3 m (Supplementary Figure 3).

To explore the sensitivity of our results to other Earth model parameters, we ran simulations using a suite of Earth models where we varied values of the lithospheric thickness and upper and lower mantle viscosity. The resulting RSL predictions for MIS 3, based on the ice model ICEPC2 (Figure 2A), for the representative site in Albemarle Embayment (white star, Figure 1) are plotted in Figure S5. In the figure, results are shown for predictions in which the following Earth model parameters were adopted: (A) lithospheric thickness of 72 km (dark blue), 96 km (white) and 127 km (pink); (B) upper mantle viscosity of 0.3x10^{21} Pa s (dark blue), 0.5x10^{21} Pa s (white), and 1x10^{21} Pa s (pink); and (C) lower mantle viscosity of 5x10^{21} km (dark blue), 15x10^{21} Pa s (white) and 30x10^{21} Pa s (pink).

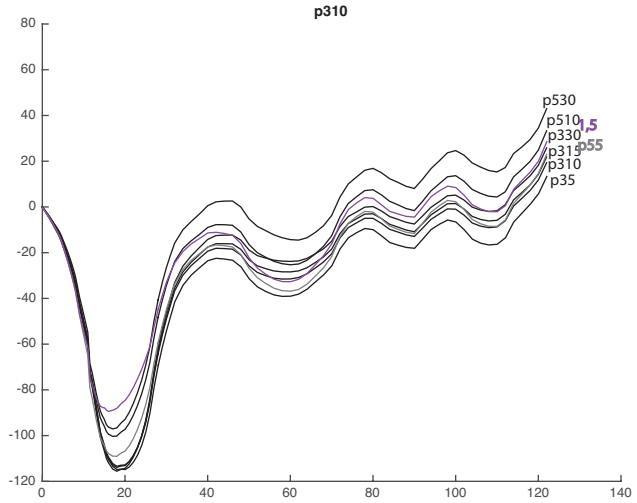

FIGURE B.4: Range of RSL highstand predictions during MIS 5a and MIS 3 based on simulations with the GMSL scenarios in Figure 3A and a lower mantle viscosity of either 10^{22} Pa s (pink rectangle) or 2 x 10^{22} Pa s (blue rectangle). The black rectangles indicate the range of RSL values predicted in main text (lower mantle viscosity of 1.5 x 10^{22} Pa s; Figure 3B). The orange bars at 80 ka and 44 ka show the observational constraints (Figure 1). All calculations are based on ice models that assume that the eastern sector of the LIS remained ice free in the period 80-44 ka (similar to the ICEPC2 model).

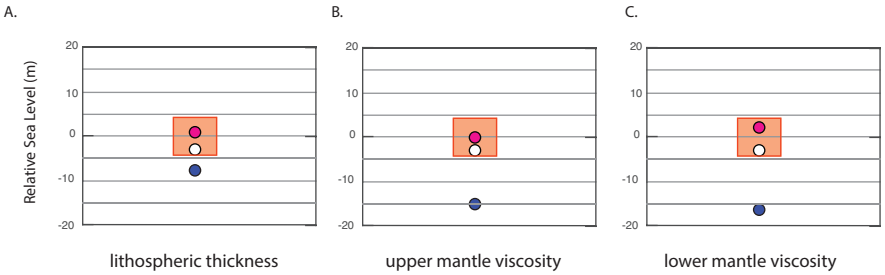

FIGURE B.5: Relative sea level predictions at location shown by white star (Figure 1) are based on the ice history ICEPC2 (Figure 2A) with seven different Earth models (including that adopted in main text). A. Lithospheric thickness is increased to 127 km (pink) and decreased to 72 km (dark blue). B. Upper mantle viscosity is increased to 1 x10^{21}Pa s (pink) and decreased to 0.3x10^{21} Pa s (dark blue). C. Lower mantle viscosity is increased to 30 x10^{21} Pa s (pink) and decreased to 5 x10^{21} Pa s (dark blue). The Earth model adopted in the main text is shown by the white circle, and the observational constraints on the MIS 3 sea-level highstand is shown by the orange box (Figure 1).

B.5 Supplementary References

Best, K. M. (2010) (2010) Quaternary geologic evolution of the Croatan beach ridge complex, Bogue Sound, and Bogue Banks, Carteret County, NC. Department of Geological Sciences, East Carolina University, Greenville, NC, 265 pp. Blackwelder.

Cronin, T. M., Szabo, B. J., Ager, T. A., Hazel, J. E. and Owens, J. P. (1981) 'Quaternary climates and sea levels of the u.s. Atlantic coastal plain.', Science (New York, N.Y.), 211(4479), pp. 233–40. doi: 10.1126/science.211.4479.233.

Culver, S. J., Farrell, K. M., Mallinson, D. J., Willard, D. A., Horton, B. P., Riggs, S. R., Thieler, E. R., Wehmiller, J. F., Parham, P., Snyder, S. W. and Hillier, C. (2011) 'Micropaleontologic record of Quaternary paleoenvironments in the Central Albemarle Embayment, North Carolina, U.S.A.', Palaeogeography, Palaeoclimatology, Palaeoecology, 305(1–4), pp. 227–249. doi: 10.1016/j.palaeo.2011.03.004.

Hill, D. F., Griffiths, S. D., Peltier, W. R., Horton, B. P. and T??rnqvist, T. E. (2011) 'High-resolution numerical modeling of tides in the western Atlantic, Gulf of Mexico, and Caribbean Sea during the Holocene', Journal of Geophysical Research: Oceans, 116(10), pp. 1–16. doi: 10.1029/2010JC006896.

Mallinson, D., Burdette, K., Mahan, S. and Brook, G. (2008) 'Optically stimulated luminescence age controls on late Pleistocene and Holocene coastal lithosomes, North Carolina, USA', Quaternary Research, 69(1), pp. 97–109. doi: 10.1016/j.yqres.2007.10.002.

Mixon, R. ., Szabo, B. J. and Owens, J. P. (1982) 'Uranium-Series Dating of Mollusks and Corals , arid Age of Pleistocene Deposits Chesapeake Bay Area , Virginia and Maryland Uranium-Series Dating of Mollusks and Corals , and Age of Pleistocene Deposits , Chesapeake Bay Area , Virginia and Maryland', Geological Survey Professional Paper 1067-E. Surface and shallow subsurface geologic studies in the emerged coastal plain of the Middle Atlantic States), United States Government Printing Office, Washington.

Moore, C. (2009) Geoarchaeological Investigations of Stratified Holocene Aeolian Deposits

along the Tar River in North Carolina. Coastal Resources Management, East Carolina University, Greenville, NC, 307 pp. Murray.

Parham, P. R., Riggs, S. R., Culver, S. J., Mallinson, D. J., Jack Rink, W. and Burdette, K. (2013) 'Quaternary coastal lithofacies, sequence development and stratigraphy in a passive margin setting, North Carolina and Virginia, USA', Sedimentology, 60(2), pp. 503–547. doi: 10.1111/j.1365-3091.2012.01349.x.

Scott, T. W. (2006) (2006) Correlating late Pleistocene Deposits on the Coastal Plain of Virginia with the Glacial-Eustatic Sea-Level. Old Dominion University, Norfolk, VA, 111.

Scott, T. W., Swift, D. J. P., Whittecar, G. R. and Brook, G. A. (2010) 'Glacioisostatic influences on Virginia's late Pleistocene coastal plain deposits', Geomorphology. Elsevier B.V., 116(1–2), pp. 175–188. doi: 10.1016/j.geomorph.2009.10.017.

Titus, J., & Wang, J. (no date) 'Maps of Lands Close to Sea Level along the Middle Atlantic Coast of the United States. United States Environmental Protection Agency.', 2008. Wehmiller, J. F., Edwards, R. L. and Martin-McNaughton, J. (2004) 'Uranium-series coral ages from the US Atlantic Coastal Plain – the "' 80 ka problem '" revisited', Quaternary International, 120, pp. 3–14.

C

Chapter 3 Supplement

Table C.1: Observational data presented in text and Figure 4/5.

Latitude	Longitude	Age (ka)	Age error (kyr) 1σ	Method	Elevation (m)	Indicator	ID/Reference
50.87	84.85	42.8	3.75	OSL	130	terrestrial	12-PJB-109 Dalton et al., 2016
55.43	88.2	52.5	5.05	OSL	55	marine	BG3807 Dalton et al., 2016
55.43	88.2	42.2	4	OSL	marine	BG3808 Dalton et al., 2016	
44.28	79.62	45.4	1.8	^{1}4C	168.65	fluvial	A2447 Mulligan & Bajc, 2017
44.28	79.62	49.5	3.1	^{1}4C	168.65	fluvial	A2392 Mulligan & Bajc, 2017
47.27	61.70	55	5	OSL	30	shallow marine	OSL53 Remillard et al., 2017
47.27	61. 70	51	4	OSL	37	beach	OSL55 Remillard et al., 2017
47.22	61.99	47.1	2.3	^{1}4C	15	terrestrial	UCIAMS-84792 Remillard et al., 2016
47.22	61.99	47.8	2.5	^{1}4C	15	terrestrial	UCIAMS-84793 Remillard et al., 2016
47.22	61.99	41	4	OSL	14.8	beach	OSL03 Remillard et al., 2016
47.22	61.99	44	4	OSL	15.6	beach	OSL04 Remillard et al., 2016
48.10	69.71	29.28	0.68	^{1}4C	30	marine	Beta-54140 Dionne & Occhietti, 1996
48.10	69.71	34.51	0.38	^{1}4C	30	marine	TO-3990 Dionne & Occhietti, 1996
45.70	74.17	31.27	0.2	^{1}4C	14.6	fluvial	Parent et al., 2015
45.70	74.17	33.25	0.24	^{1}4C	13.8	fluvial	Parent et al., 2015

C.1 Finite Difference Approximation

We use the flux form for the finite difference approximation. We use forward Euler and second order centered difference, where n denotes the time step, i the node in the x direction, and j the node in the y direction:

$$\frac{H_{i,j}^{n+1}-H_{i,j}^{n}}{\Delta t}=\frac{D_{i+\frac{1}{2},j}^{n}\left(\frac{H_{i+1,j}^{*n}-H_{i,j}^{*n}}{\Delta x_i}\right)+D_{i-\frac{1}{2},j}^{n}\left(\frac{H_{i,j}^{*n}-H_{i-1,j}^{*n}}{\Delta x_{i-1}}\right)}{\frac{1}{2}(\Delta x_i+\Delta x_{i-1})}+\frac{D_{i,j+\frac{1}{2}}^{n}\left(\frac{H_{i,j+1}^{*n}-H_{i,j}^{*n}}{\Delta y_j}\right)+D_{i,j-\frac{1}{2}}^{n}\left(\frac{H_{i,j}^{*n}-H_{i,j-1}^{*n}}{\Delta y_{j-1}}\right)}{\frac{1}{2}(\Delta y_j+\Delta y_{j-1})}+G \tag{C.1}$$

Next, the numerical expression for the diffusivity is:

$$D_{i+\frac{1}{2},j}^{n}=AH_{i+\frac{1}{2},j}^{m+2}\left[\left(\frac{H_{i+1,j}^{*}-H_{i,j}^{*}}{\Delta x_i}\right)^2+\left(\frac{1}{2}\left(\frac{H_{i+1,j+1}^{*}-H_{i+1,j-1}^{*}}{\Delta y_{j-1}+\Delta y_j}+\frac{H_{i,j+1}^{*}-H_{i,j-1}^{*}}{\Delta y_{j-1}+\Delta y_j}\right)\right)^2\right]^{(m-1)/2}D_{i-\frac{1}{2},j}^{n}=AH_{i-\frac{1}{2},j}^{m+2} \tag{C.2}$$

Finally, our use of flux form requires the following expressions:

$$H_{i+\frac{1}{2},j}^{m+2}=\left(\frac{H_{i+1,j}+H_{i,j}}{2}\right)^{m+2}H_{i-\frac{1}{2},j}^{m+2}=\left(\frac{H_{i,j}+H_{i-1,j}}{2}\right)^{m+2}H_{i,j+\frac{1}{2}}^{m+2}=\left(\frac{H_{i,j+1}+H_{i,j}}{2}\right)^{m+2}H_{i,j-\frac{1}{2}}^{m+2}=\left(\frac{H_{i,j}+H_{i}\right. \tag{C.3}$$

This model uses a 0.25 yr time step. At each time step, a new ice thickness is calculated based on the equations above. Then with the new ice thickness and basal topography known, a new surface elevation is calculated (H*=B+H). The edge and center of the ice sheet can lead to a situation in which D=0, which is unrealistic behavior. Thus, we set a minimum D; as noted by Oerlemans (1981), and as confirmed in our simulations, the ice model does not depend strongly on this choice.

C.2 Supplementary Figures

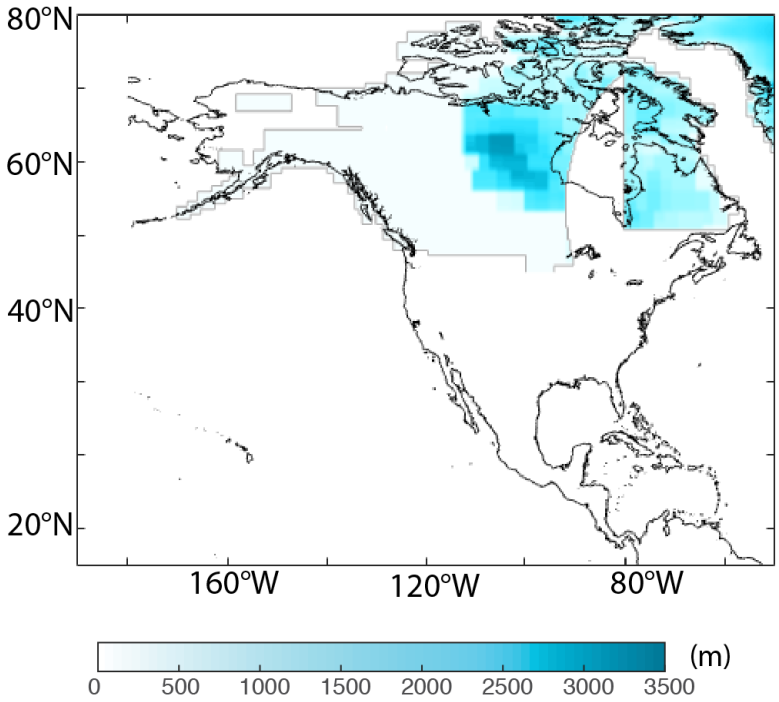

Figure C.1: Ice thickness at 44 ka for ice history ICE-PC3.

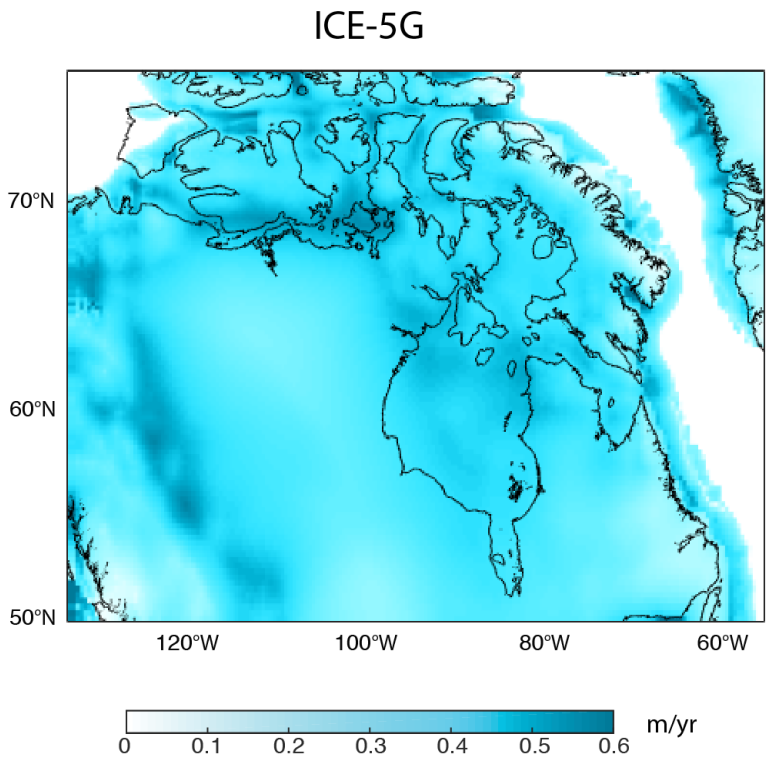

FIGURE C.2: Ice growth rates averaged over 4.5 kyr using an initial ice configuration governed by ICE-5G at 44 ka and the paleotopography shown in Figure 3A.

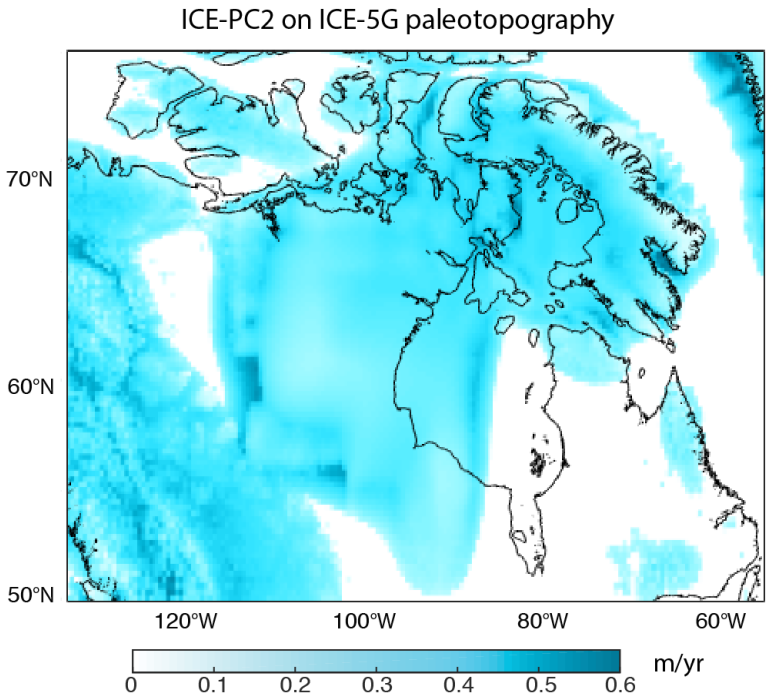

FIGURE C.3: Ice growth rates averaged over 4.5 kyr using an initial ice configuration governed by ICE-PC2 at 44 ka and the paleotopography shown in Figure 3A associated with the ICE-5G ice history.

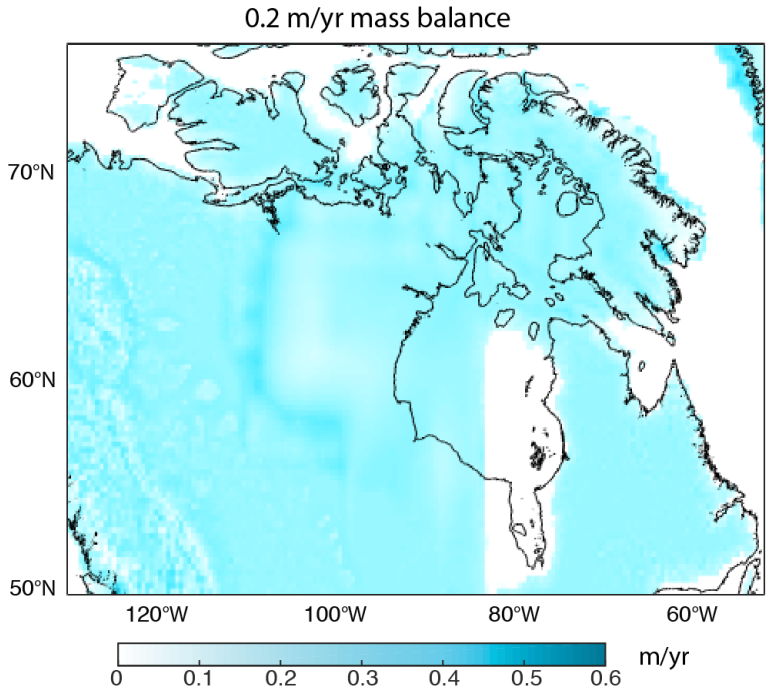

FIGURE C.4: Ice growth rates averaged over 4.5 kyr using an initial ice configuration governed by ICE-PC2 at 44 ka and the paleotopography shown in Figure 3B adopting a mass balance of 0.2 m/yr.

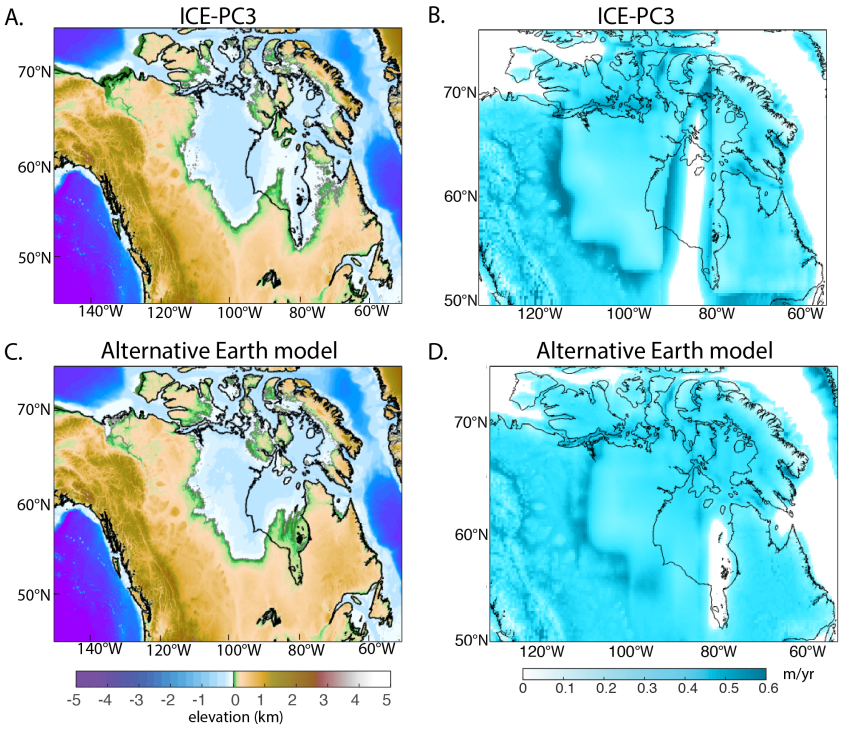

FIGURE C.5: A. Paleotopography at 44 ka predicted using ice history ICE-PC3. B. Ice growth rates averaged over 4500 yr period predicted with basal topography in (A) and initial ice thickness shown in Appendix Figure 1 associated with ice history ICE-PC3. C. Paleotopography at 44 ka predicted using ice history ICE-PC2 and the alternate viscoelastic Earth model described in the text. D. Ice growth rates averaged over 4500 yr period predicted with basal topography in (C) and initial ice thickness shown in Figure 2C associated with ice history ICE-PC2 (as in main text).

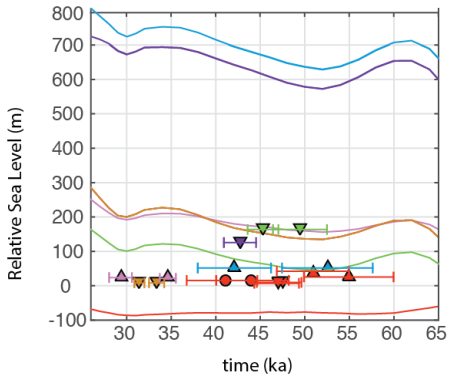

FIGURE C.6: Relative sea level predictions using ICE-5G (Figure 2A; dotted black; Figure 2B) and Earth model VM2 (as in main text). Colors correspond to the sites shown in Figure 4.

D

Chapter 4 Supplement

D.1 Supplementary Note 1: Additional ice histories

We construct three additional ice histories that adopt the same GMSL history as ICE-PC2 (as in main text, Figure 2A) but vary the geographic extent of ice. In ICE-PC, ice sheets grow in the same geometry as they decay (that is, as in our modified ICE-5G history, the ice geometry during the glaciation phase is assumed to be identical to the post-LGM geometry when the eustatic sea-level value is the same; Supplementary Figure 1E). In ICE-PC3, the eastern sector of the LIS is ice-free (as in ICE-PC2) from 80-44 ka except for northern Quebec, which remains glaciated, according to retrodicted patterns of snow accumulation (e.g. Löfverström et al. 2014; Supplementary Figure 1F). Lastly, ICE-PC4 has the same ice extent as ICE-PC2 at 44 ka, but the ice configuration at the LGM is modified to match the moraine limits in Braun (2004) (Supplementary Figure 1B). We calculate the west-east gradient predicted by GIA simulations for each of these ice histories, when paired with the Earth model adopted in the main text, on a 202 km segment between (40°N, 73.2°W) and (40°N,

75.6°W). In the case of modified ICE-5G the gradient is 1.8 mm km-1 ky-1. For ICE-PC, ICE-PC2, ICE-PC3, and ICE-PC4, the gradients are 2.5 mm km-1 ky-1, 2.0 mm km-1 ky-1, 3.0 mm km-1 ky-1, and 0.2 mm km-1 ky-1, respectively.

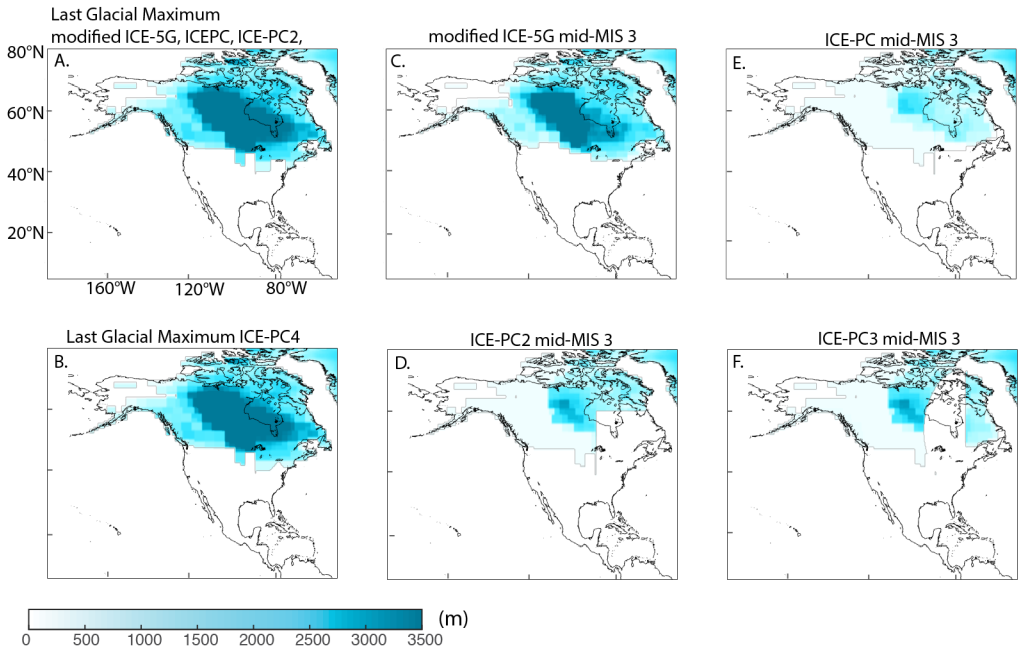

FIGURE D.1: A. Ice thickness at the Last Glacial Maximum (26 ka) for the modified ICE-5G, ICE-PC, ICE-PC2, ICE-PC3 histories, B. Ice thickness at the Last Glacial Maximum for ICE-PC4. C-F. Ice thickness at mid-MIS 3 (44 ka) for the modified ICE-5G (C), ICE-PC2 (and ICE-PC4) (D), ICE-PC (E), ICE-PC3 (F) histories.

D.2 SUPPLEMENTARY NOTE 2: TIME-VARIABLE UPLIFT

In Supplementary Figure 2, vertical displacement rates are plotted at 1 kyr time intervals from 32-26 ka. These fields are input to the CHILD landscape evolution model. The pattern of vertical displacement, especially the amplitude of the west-east gradient, varies substantially over this time period. Inspection of these time frames reveals that the vertical displacement field across the time step 28-27 ka is likely the largest control on the number of eastward diversions noted at the final time step 26 ka. Here, as elsewhere, we use the term "diversion" as a synonym for "avulsion", indicating a shift

in a river's course without implications for the cause of the shift.

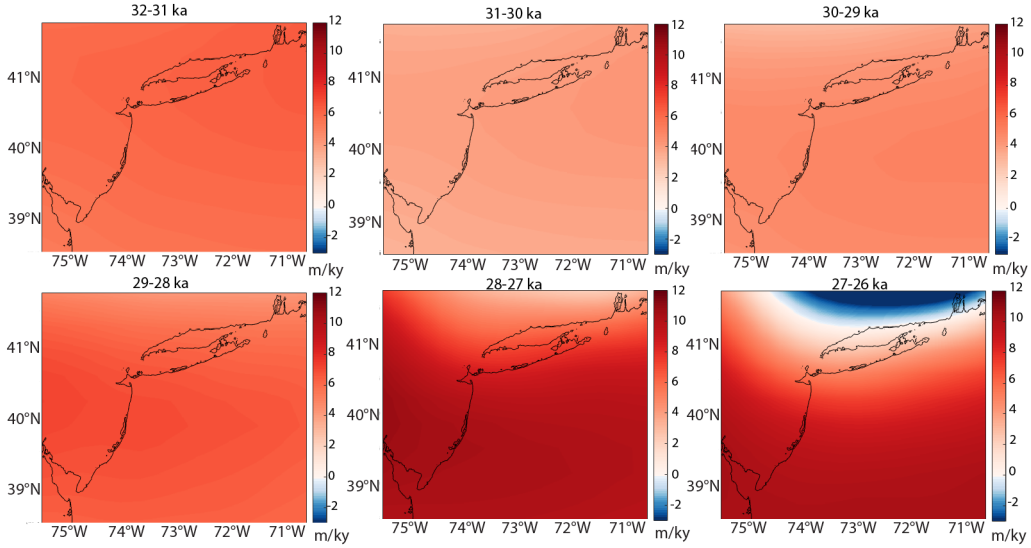

FIGURE D.2: Vertical displacement rates computed using ICE-PC2 from 32-26 ka at 1 ky time intervals. Note the differences in color scales among panels.

D.3 SUPPLEMENTARY NOTE 3: SENSITIVITY TO MANTLE VISCOSITY

We assess the sensitivity of our results to Earth structure by varying the upper and lower mantle viscosities in the ranges of (0.2-1.0) × 10^{21} Pa s and (5-30) × 10^{21} Pa s, respectively. Each of these simulations was driven with the erodibility parameters adopted in the main text (Supplementary Note 5) and ice model ICE-PC2. The number of predicted river diversions is primarily sensitive to the upper mantle viscosity. In particular, the west-east gradient predicted in the GIA calculation increases as one weakens the upper mantle, which leads to more river diversions. Supplementary Figure 3 shows the predicted rate of change in elevation from 32-26 ka for each of these Earth models, including the Earth model adopted in the main text. Supplementary Figure 4 shows the river channel locations predicted by the landscape evolution simulation at 26 ka.

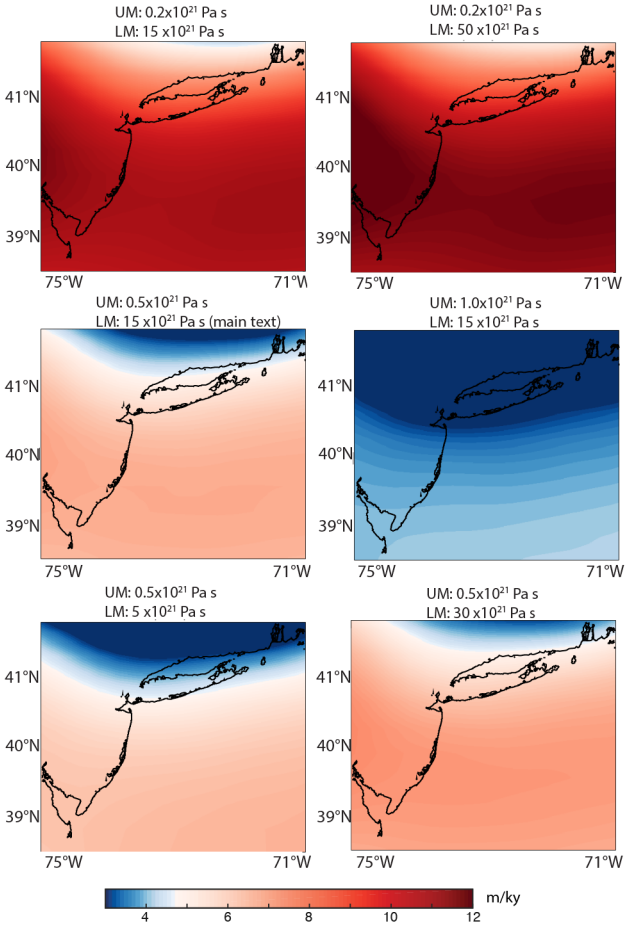

FIGURE D.3: Predicted rate of change in elevation from 32-26 using ice history ICE-PC2 (as in main text) in a GIA simulation paired with a variety of upper (UM) and lower (LM) mantle viscosities.

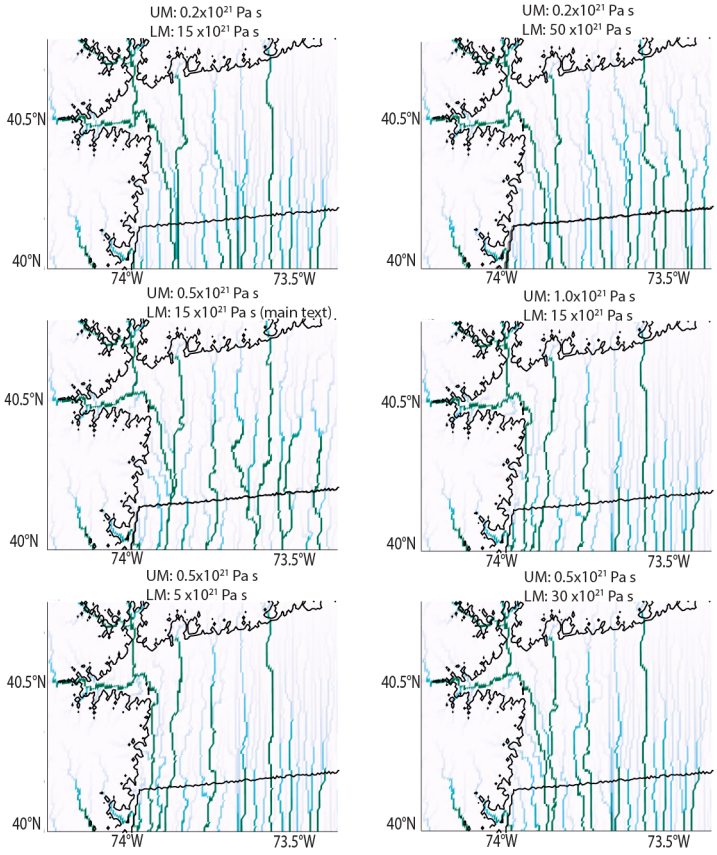

FIGURE D.4: Predicted path of rivers using simulations forced by a GIA calculation in which the ice history ICE-PC2 is paired with Earth models sampling a variety of upper (UM) and lower (LM) mantle viscosities (see text). Parameters adopted in the landscape evolution simulation are the same as those adopted in main text. Darker colors are used to highlight relatively larger rivers.

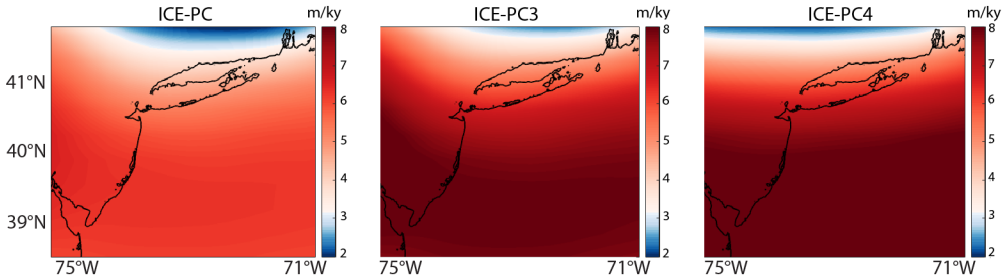

FIGURE D.5: Average rates of vertical displacement (as in Figure 2 of the main text) for ice histories ICE-PC, ICE-PC3, and ICE-PC4.

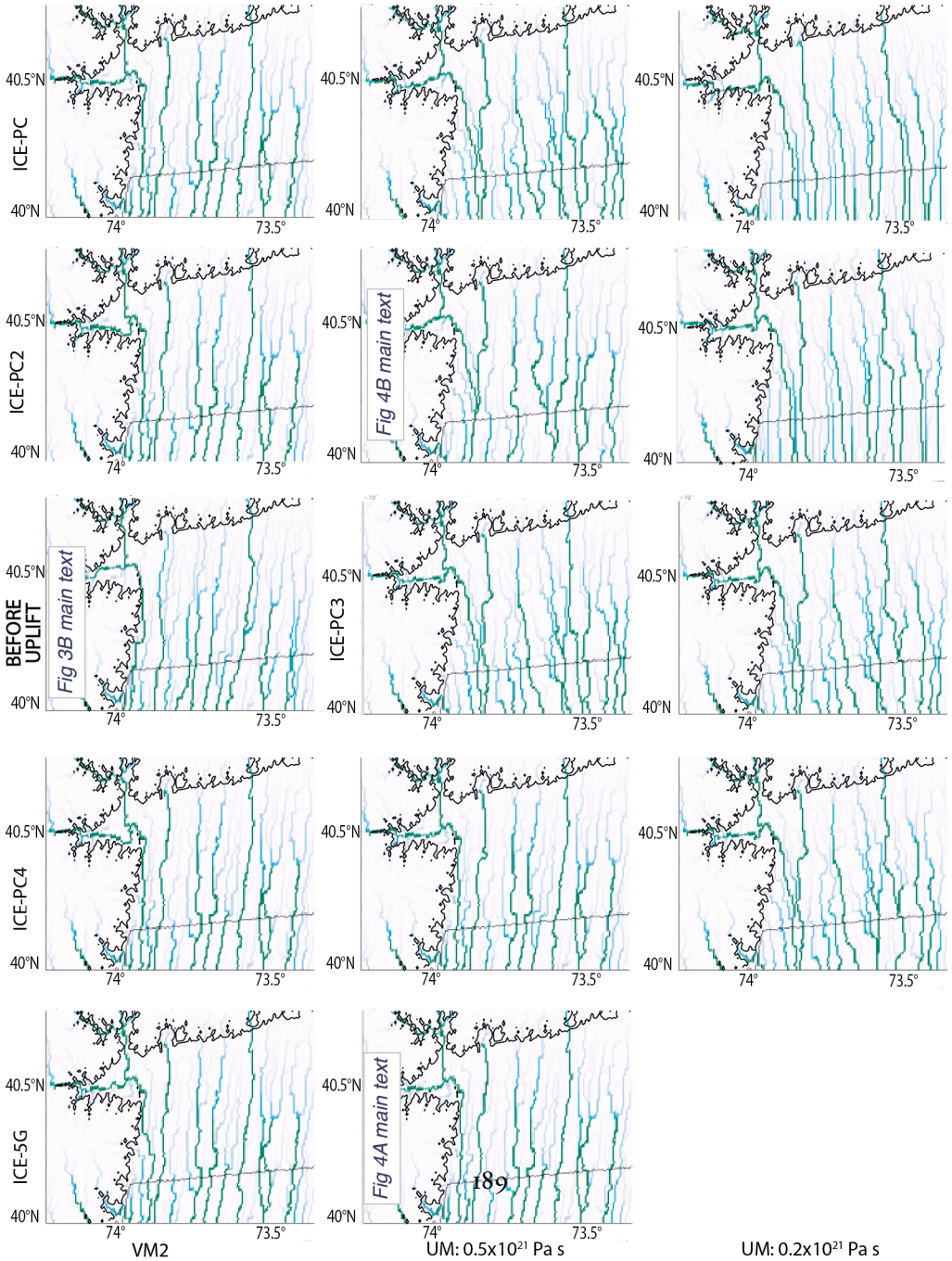
ICE-PC
ICE-PC2
ICE-PC3
ICE-PC4
ICE-5G
BEFORE UPLIFT
Fig 3B main text
Fig 4B main text
Fig 4A main text
40.5°N
40°N
74°
73.5°
VM2
UM: 0.5x10^21 Pa s
LM: 15 x10^21 Pa s
(as in main text)
UM: 0.2x10^21 Pa s
LM: 50 x10^21 Pa s

D.4 Supplementary Note 4: Construction of synthetic topography at 32 ka

The initial topography adopted in landscape evolution models can strongly influence predicted erosional and depositional histories. To explore the influence of GIA on river diversions in a generalized landscape, we created a simplified topographic field at 32 ka to represent the initial topography in a region similar to the Hudson shelf, which was subaerial before LGM. Our goal here is not to exactly reproduce the paleotopography on the Hudson shelf, which is not precisely known, but rather to explore the frequency of river diversions in a simplified landscape that captures the most important drivers of diversions: the regional shelf gradient, the initial north-south orientation of the river, and a realistic ice history. For comparisons of model predictions to field sites like the Hudson Shelf, it is preferable to begin with roughened topography that mimics the irregularity of real topography (Perron & Fagherazzi 2012). In order to create a synthetic map to represent a simplified topography at 32 ka on the Hudson shelf region, we first run a simulation over 100 ky by applying two separate uplift functions to a randomly-generated topography with amplitudes between 0 and 1 m elevation. We outline the present-day continents on this generated topography, and apply one uplift function here and another to the present-day ocean areas (shown in Figure 3A). In continental areas (above present-day sea level) we apply uplift rates that decrease from north to south from 2 m/ky to 0.5 m/ky. A smaller uplift function is applied to the present-day ocean regions to simulate the lower topographic gradients on the continental shelf (uplift rate gradient decreases from 0.5 m/ky to 0 m/ky from north to south). We simulate bedrock river incision by solving the stream power law, given the uplift rates described above, using the Fastscape algorithm over 100 ky, using 1 ky time steps and an erodibility parameter k of $3x10^{-4}$ $m^{-0.8}$ (Braun & Willett 2013) . This method generates topography where elevations are higher toward the north, similar to the actual present-day topography in this region. We ensure that shelf gradients on the reconstructed topography are similar to present-day gradients (1 m/km) by adding an additional tilt with a decreasing north-to-south gradient of

0.03 m/arc-second. Finally, in order to establish a location of the coastline at 32 ka consistent with predicted shorelines on present-day bathymetry (Figure 2C) we uniformly subtract a value of 25 m from the topography established in the last step. The pattern of river drainage on this topographic reconstruction is shown in Figure 3B, where relatively larger rivers (measured by drainage area) are shown in green. In the region depicted in Figure 3B there are 9 large rivers and 10 intermediate rivers. These rivers drain in a general north-south direction, consistent with the paleo-flow direction of the ancestral Hudson River. While this reconstruction yields a simplified version of the regional paleotopography, we believe that the synthetic topography captures the topographic features that are most important in determining whether an eastward diversion occurs, in particular the shelf gradient, the initial north-south orientation of the river, and a realistic ice history.

D.5 Supplementary Note 5: Landscape Evolution Model: CHILD

We adopt the landscape evolution model Channel-Hillslope Integrated Landscape Development (CHILD) to simulate physical erosion in the synthetic reconstruction of Hudson Shelf topography. This open-source model provides process-based simulations of both bedrock and alluvial rivers, which provide the flexibility to simulate the ancestral Hudson River channel in both detachment-limited and transport-limited fluvial regimes. We drive the landscape evolution simulations by inputting to CHILD an initial topography (Supplementary Note 4) and a time series of vertical displacement fields from 32-26 ka (Supplementary Figure 2). Here we briefly describe our adopted values for key model parameters in CHILD, and refer the reader to the CHILD User Guide for model details (Tucker 2010). Transport-limited fluvial transport in CHILD is modeled as a function of sediment transport capacity, Qc, which itself is a function of excess shear stress: $Q_c = K_F W(\tau_0 - \tau_c)^{P_F}$. Here KF is a transport coefficient, W is channel width, τ_0 is the bed shear stress, τ_c is the critical shear stress, and PF is a constant scaling exponent. We adopt a value of τ_c = 1 Pa for both bedrock and regolith in our simulations, consistent with field and laboratory measurements

implying non-dimensional critical shear stresses τ_c* of 0.01 to 0.1 (Lamb et al., 2008). For simplicity, we adopt a value of PF = 1, such that the sediment transport capacity is linearly dependent on the shear stress. We note that other sediment transport relations use different values for these parameters (e.g., an exponent of 2.5 on shear stress in Engelund and Hansen, 1967), and that our adopted value of PF = 1 may underestimate the likelihood of GIA-drive avulsion. Future work will explore the sensitivity of GIA-driven avulsions to alternative sediment transport relations. We adopt a value of KF = 5.0 m2 yr-1 Pa 1. Bed shear stress is modeled as a function of the water discharge Q and channel gradient S, as in $\tau_0 = K_T(W^{-1}Q)^{M_F}S^{N_F}$, where KT is a scaling coefficient and MF and NF are constant exponents. MF and NF are poorly constrained, but the ratio MF /NF typically falls between 0.35-0.6 (Whipple & Tucker 1999). We adopt values of NF = 1 and MF = 0.4, consistent with global datasets that show a best fit ratio of ∼0.5 (Harel et al., 2016). Lastly, we adopt a value of KT = 10-6 Pa (m2/s)-0.4, such that we obtain an erosional scaling coefficient (KFKT) consistent with values adopted in previous studies (Whipple et al. 2017; Whipple & Tucker 2002). Detachment-limited fluvial transport in CHILD is modeled as a function of detachment capacity Dc, which itself is a function of excess bed shear stress: $D_c = K_B(\tau_0 - \tau_c)^{P_B}$. Here KB is a rate coefficient, PB is a constant exponent, and bed shear stress has the same form as it does in transport-limited conditions: $\tau_0 = K_T(W^{-1}Q)^{M_B}S^{N_B}$. We adopt values of PB = 1 and KB = 1, such that the erosional scaling coefficient is a function of KTKF. We adopt the same values for the exponents as the analogous exponents in transport-limited conditions: NB = 1 and MB = 0.4. Hillslope soil flux qc is modeled as a nonlinear function of topographic gradient: $q_c = K_D\nabla z[1 - (\mid \nabla z \mid /S_c)^2]^{-1}$, where KD is a soil transport coefficient, z is elevation, and Sc is a critical hillslope gradient. Here we adopt a value of KD = 0.01 m^2/yr, consistent with a global compilation of field measurements (Perron 2017), and a value of Sc = 0.5774, consistent with values used in example simulations included in the 2011 CHILD release.

By restricting our simulations to fluvial and hillslope processes, our simulations neglect coastal

Table D.1: Supplementary Table 1. Parameter values adopted in CHILD simulations.

Name	Value	Description
KB	1 m^2 s/kg	Bedrock erodibility coefficient
KD	0.01 m^2/yr	Hillslope soil transport coefficient
KF	5.0 $m^2 yr^{-1}$ Pa 1	Fluvial sediment transport coefficient
KR	0.0005 m yr^{-1} Pa 1	Regolith erodibility coefficient
KT	10-6 Pa (m^2/s)-0.4	Bed shear stress coefficient
MB	0.4	Discharge exponent in detachment capacity equation
MF	0.4	Discharge exponent in transport capacity equation
NB	1	Slope exponent in detachment capacity equation
NF	1	Slope exponent in transport capacity equation
PB	1	Excess shear stress exponent in detachment capacity equation
PF	1	Excess shear stress exponent in transport capacity equation
Sc	0.5774	Threshold gradient for nonlinear creep
τ_c	1 Pa	Detachment threshold for bedrock and regolith

processes such as backwater effects and delta deposition.

D.5.1 Supplementary Note 6: Sensitivity to erodibility parameters

We ran several simulations to assess the sensitivity of our results to the erodibility parameters adopted in CHILD. In particular, we ran simulations using the ice history ICE-PC2, paired with the Earth model adopted in the main text, and varied τ_c and KF. For both KF and τ_c we varied values by two orders of magnitude: KF from 0.5 to 50 (the value adopted in main text is 5) and τ_c from 0.1 to 10 (the value adopted in main text is 1). When driven by the same GIA-induced deformation field as in main text, these simulations produced the same number of river diversions as in Figure 3B. Thus these simulations suggest that the number of modeled river diversions is primarily sensitive to changes in the imposed field of GIA-induced deformation, rather than to the assumed values of KF and τ_c within the above ranges. We also performed simulations adopting the detachment-only option in CHILD to assess the influence of transport-limited conditions on the modeled river diversions. We found that simulations ignoring alluvial processes resulted in predicted river drainage patterns identical to that shown in the main text for both ICE-PC2 and ICE-5G. Thus these simulations suggest that the modeled predictions of river evolution are largely sensitive to changes in slope, which in our simulations is primarily determined by GIA-induced crustal deformation. This may be

a consequence of the slope-dependence of both transport-limited and detachment-limited processes, such that GIA-induced changes in slope strongly affect both transport-limited and detachment-limited conditions.

D.6 Supplementary Note 7: Results of landscape evolution simulation over an extended time interval

Although the focus of this study is on the diversion of the ancestral Hudson River at ~30 ka, we also explore the evolution of the Hudson River forced by GIA simulations over a longer time interval. Specifically, we ran the simulation for an additional 8 ky, to 18 ka. While rates of vertical displacement from 26-18 ka are much smaller than those over the 32-26 ka interval, a west-east gradient persists, and 4 more rivers are diverted eastward by 18 ka (Supplementary Figure 7). Because the present-day submarine channel is deeply incised, and this incision is thought to be coincident with the catastrophic drainage of pro-glacial Lake Iroquois, the Hudson River must have been at this position at the time of flooding ~13 ka (Rayburn et al. 2005). Thus, simulations of river evolution forced with GIA vertical displacement histories must predict a river that is east of the ancestral channel at this time. By running our simulations until 18 ka we note that more eastward diversions are predicted, and rates of crustal deformation decrease sharply after this time. Future studies aimed at continuing simulations through the entire deglaciation phase should include realistic changes in the depositional regime of the river channel. In particular, as base level fell, the Hudson River may have shifted from a depositional to an incisional environment, explaining the entrenchment in the channel after it was diverted eastward.

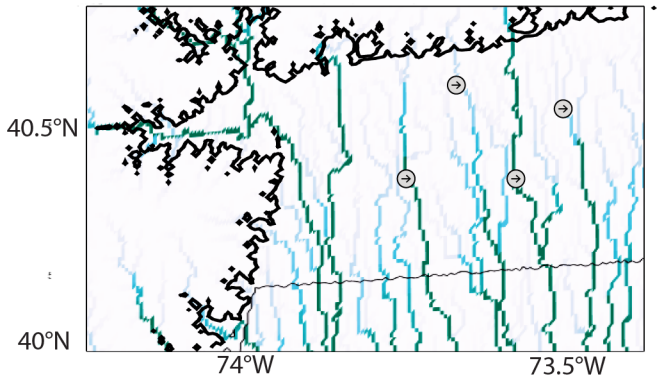

FIGURE D.7: Landscape evolution simulation with ICE-PC2 (as in main text) at 18 ka. River channels are colored in green and blue as in Supplementary Figure 2. Additional diversions that occurred after 26 ka are highlighted in gray circles.

D.7 SUPPLEMENTARY REFERENCES

Braun, J. & Willett, S.D., 2013. A very efficient O(n), implicit and parallel method to solve the stream power equation governing fluvial incision and landscape evolution. Geomorphology, 180–181, pp.170–179.

Engelund, F., & Hansen, E. (1967). A monograph on sediment transport in alluvial streams. Technical University of Denmark ostervoldgade 10, Copenhagen K.

Harel, M., Mudd, S.M. & Attal, M., 2016. Global analysis of the stream power law parameters based on worldwide Be denudation rates. Geomorphology, 268, pp.184–196. Lamb, M.P., Dietrich, W.E. & Venditti, J.G., 2008. Is the critical shields stress for incipient sediment motion dependent on channel-bed slope? Journal of Geophysical Research: Earth Surface, 113(2), pp.1–20.

Löfverström, M., Caballero, R., Nilsson, J., & Kleman, J. (2014). Evolution of the large-scale atmospheric circulation in response to changing ice sheets over the last glacial cycle. Climate of the Past, 10, 1453–1471. http://doi.org/10.5194/cp-10-1453-2014

Perron, J.T., 2017. Climate and the Pace of Erosional Landscape Evolution. Annual Review of Earth and Planetary Sciences, 45(1), p.annurev-earth-060614-105405.

Perron, J.T. & Fagherazzi, S., 2012. The legacy of initial conditions in landscape evolution. Earth Surface Processes and Landforms, 63(August 2011), pp.52–63.

Rayburn, J.A., Knuepfer, P.L.K. & Franzi, D.A., 2005. A series of large , Late Wisconsinan melt-water floods through the Champlain and Hudson Valleys , New York State , USA. Quat. Sci. Reviews, 24, pp.2410–2419.

Tucker, G.E., 2010. CHILD users guide for version R9.4.1.

http://csdms.colorado.edu/mediawiki/images/Child_users_guide.pdf.

Whipple, K. X., Forte, A. M., DiBiase, R. A., Gasparini, N. M., & Ouimet, W. B. (2017). Timescales of landscape response to divide migration and drainage capture: Implications for the role of divide mobility in landscape evolution. Journal of Geophysical Research: Earth Surface, 122(1), 248–273. http://doi.org/10.1002/2016JF003973

Whipple, K.X. & Tucker, G.E., 1999. Dynamics of stream-power river incision model. Journal of Geophysical Research, 104(August), pp.661–674.

Whipple, K.X. & Tucker, G.E., 2002. Implications of sediment-flux-dependent river incision models for landscape evolution. Journal of Geophysical Research, 107.

E

Chapter 5 Supplement

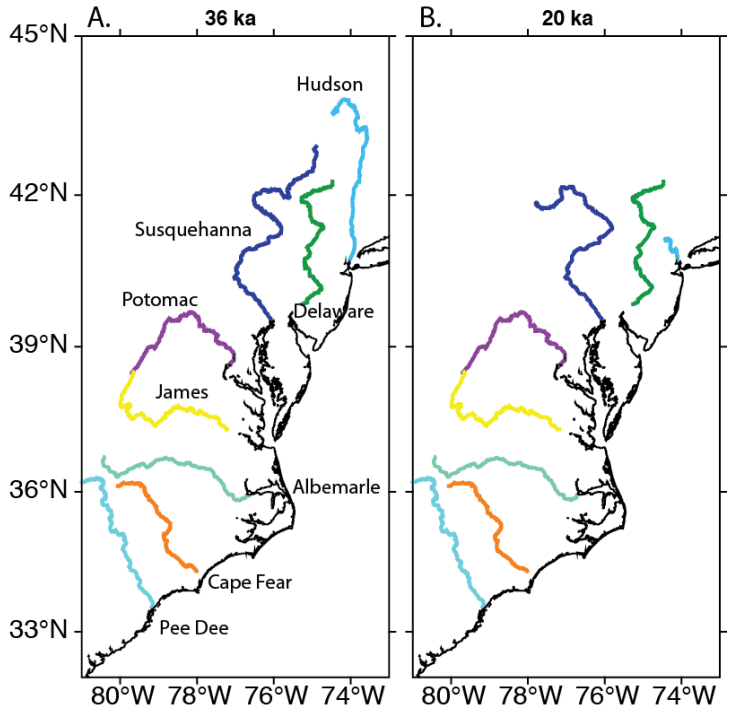

FIGURE E.1: River channel locations at 36 ka (A) and at 20 ka (B). Black line shows modern coastline.

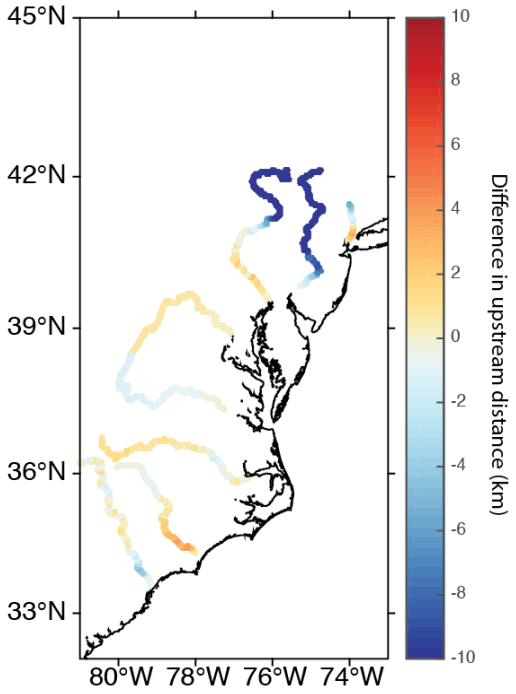

FIGURE E.2: Difference in upstream distance measured from modern coastline in river channels between 36 and 20 ka, where upstream distance for 20 ka channels was subtracted from the upstream distance along 36 ka channels.

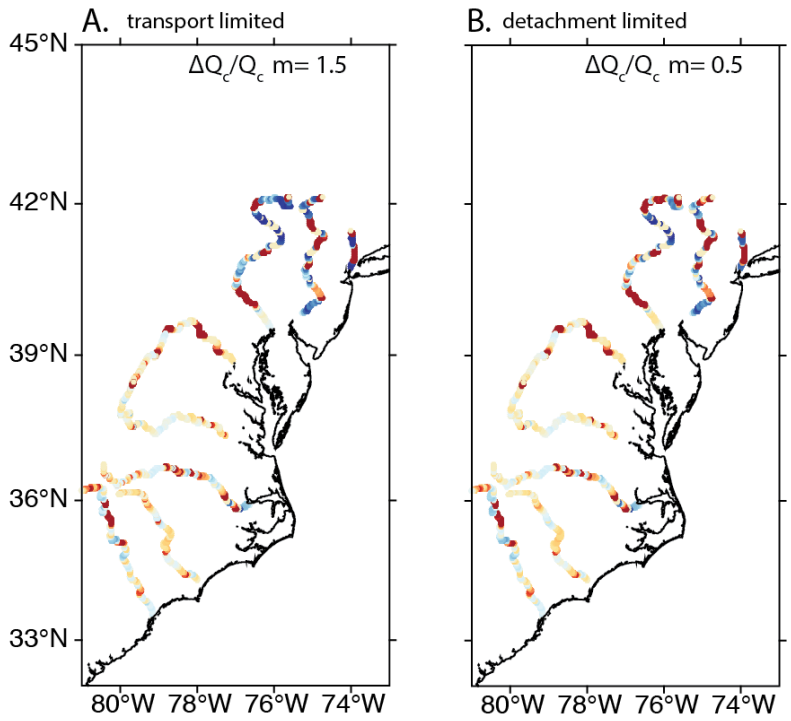

FIGURE E.3: Modeled percent change in Qc using m = 1.5, the case for transport-limited, (A), and using m = 0.5, as in main text, (B), the case for detachment-limited. Changes to Qc in the transport-limited case are only substantially different from the detachment-limited case in rivers with significant changes in drainage area.

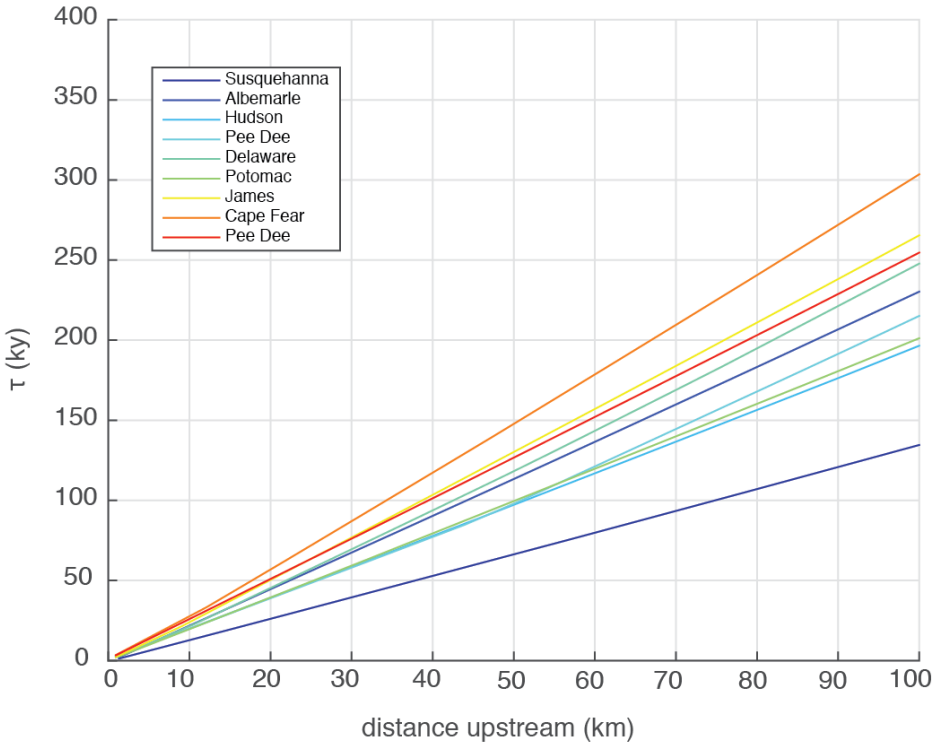

FIGURE E.4: Calculated τ values, the transit time required for a knickpoint to propagate from base level to a distance x upstream, for each river system adopting k = 2.5x10^{-6}/yr (2σ confidence interval from 2.08 x10^{-6} /yr to 2.99 x10^{-6} /yr) and m = 0.5, n = 1, as in Miller et al. (2013). Dotted lines show the upper and lower bound on the estimate of k values in Miller et al., 2013.

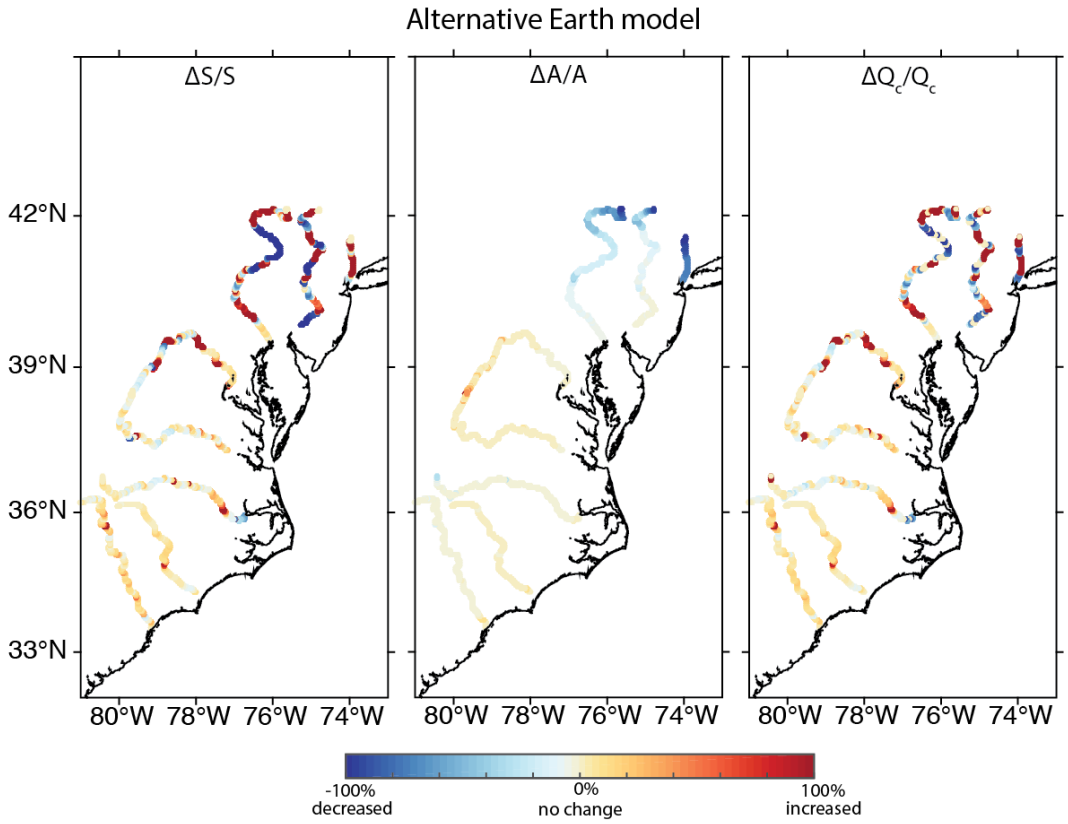

FIGURE E.5: GIA-induced percent changes from 36 to 20 ka in (A) channel slope, (B) drainage area, and (C) transport capacity. Here GIA responses are governed by the alternate Earth model described in the main text (upper mantle: 0.2 x10^{21} Pa s, lower mantle: 50 x10^{21} Pa s).

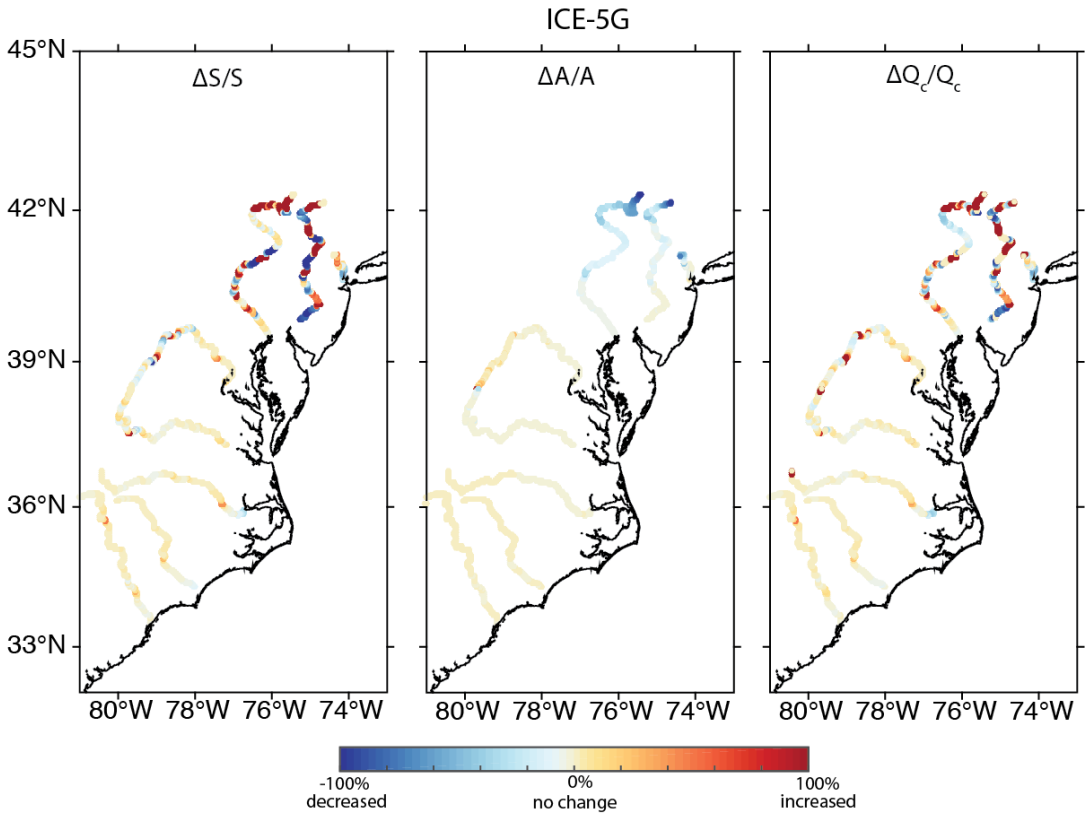

FIGURE E.6: GIA-induced percent changes on the standard Earth model from 36 to 20 ka in (A) channel slope (B) drainage area and (C) sediment transport capacity Qc, driven by the ice history ICE-5G.

Table E.1: Drainage area for river systems highlighted in Figure 2 at 36 ka and 20 ka. Drainage areas are calculated at the 36 ka shoreline predicted from GIA simulations driven by the ice history ICE-PC2.

River	36 ka drainage area (km^2)	20 ka drainage area (km^2)
Hudson	$5.3x10^4$	$1.1\ x10^4$
Delaware	$4.25\ x10^4$	$4.1\ x10^4$
Susquehanna	$10.1\ x10^4$	$9.4\ x10^4$
Potomac	$4.8\ x10^4$	$4.8\ x10^4$
James	$3.5\ x10^4$	$3.4\ x10^4$
Albemarle	$6.3\ x10^4$	$6.2\ x10^4$
Cape Fear	$3.0\ x10^4$	$2.9\ x10^4$
Pee Dee	$5.2x10^4$	$5.3x10^4$
Savannah	$2.6\ x10^4$	$2.7\ x10^4$

F

Chapter 6 Supplement

F.1 Uncertainty on elevation of Bering Strait sill at 13-11.5 ka

In this study we assume that in order for the Pacific and Arctic oceans to be connected relative sea level must reach -53 m, the present-day elevation at the Bering Strait sill. We further assume that minimal vertical displacements to the Bering Strait sill have occurred since 13 ka other than those associated with glacio-isostatic adjustment. However, a variety of processes besides glacio-isostatic adjustment can affect the paleoelevation of the sill, including tectonic activity, sedimentation and erosion, and changes in tidal or storm-surge regime. Estimates of tectonic activity suggest that less than 3-4 m of vertical displacement have occurred since 20 ka(Brigham-Grette, 2017). Given the absence of dated sediment cores directly on the sill, it is challenging to determine sedimentation rates at this site since 13 ka, nevertheless the core 85-69 cited in this study (Figure 1) accumulated 1-4 m of sediment since flooding. At present-day the channel experiences relatively high current speeds, and therefore likely does not accumulate significant sedimentation(Woodgate, 2018). An additional

uncertainty is related to bathymetric resolution on the Bering Shelf. While present elevation at the Bering Strait sill is -53 m, the ARDEM bathymetry dataset suggests that there are partial sills to the north and south at -47 m elevation(Danielson et al., 2015). The effective sill depth for purposes of water transport may be somewhat shallower than the deepest passage through the sill. The effective sill depth for marine species dispersal may be similarly complex and species dependent.

In our simulations we show that varying the Earth model can modulate the absolute value of relative sea level. However, such changes do not affect whether a sea-level stillstand is predicted from 13-11.5 ka, which (given the constraint of global eustatic sea level rise at the time) is largely a response to the gravitational effects of ice melt in the CIS/western LIS region. This is independent of the absolute value of RSL obtained with different Earth models.

F.2 Local observations of flooding as sea-level markers

In this study we synthesize published data including marine and terrestrial markers in addition to geochemical proxies for changes in water depth. While these datasets address the issue of the timing of initial Bering Strait flooding, our primary interest is reconstructing regional sea level rather than precisely dating the flooding surface at each site. While certain data sets we used were published including an interpolated or extrapolated age for the flooding surface (i.e. Hill & Driscoll(Hill and Driscoll, 2008)), we are primarily interested in these data as sea-level limiting indicators. Therefore, we use the calibrated dates of each sample and its observed elevation, rather interpolating or extrapolating an age for regional flooding based on individual locations. A key finding is that the apparent timing of local inundation is expected to vary between locations because of glacio-isostatic effects, so no single location is best suited to defining the timing at which sea level rose above the sill.

F.3 Contributions to relative sea level: gravitational vs. deformational effects

Relative sea level at the Bering Strait is calculated as the sum of globally uniform sea-surface height variations and regional changes in relative sea level due to crustal deformation (including the impact of these changes on local sea-surface height) and the direct gravitational effects of the changing surface mass load. To assess the relative contribution of each process, we decomposed the RSL prediction based on ice models ICE-6G (dotted lines, Supplementary Figure 4) and GI-31 (solid lines, Supplementary Figure 4) into these two components: crustal deformation (red lines, Supplementary Figure 4) and direct gravitational effects (blue lines, Supplementary Figure 4). A large sea-level fall due to gravitational effects associated with the GI-31 model in the period 13-11.5 ka is a result of the contemporaneous loss of ice mass in the region at the border of the CIS and western LIS (henceforth the CIS-LIS zone). In the case of the ICE-6G simulation this sea level occurs over a longer period and earlier, during MWP-1a.

Supplementary Figure 5 shows a map of the difference between RSL predictions for GI-31 and ICE-6G at 13 ka. RSL is higher in the region surrounding the CIS, western LIS and Bering Strait region for GI-31 from 15-13 ka because there is a larger ice mass in the CIS-LIS zone during this time compared with ICE-6G, and this exerts a gravitational pull on nearby oceans. The relative sea-level fall associated with the gravitational loss to this sector of the ice sheet from 13-11.5 ka occurs rapidly in the GI-31 simulation. It is this component of RSL fall that results in the net sea-level stillstand predicted at the Bering Strait.

F.4 Sensitivity to ice model

For the series of tests assessing sensitivity to the adopted ice model, we construct a simplified ice history GI-15, which has not been designed to as closely match geochronological constraints as GI-31,

but rather consists of an ice-melting scenario from 13-11.5 ka in which the region west of 110°W in the CIS-LIS zone is retained from the ICE-6G history from 15 ka to 13 ka, and is then melted from 13-11.5 ka. Simulations using this ice history and adopting the Earth model in the main text results in a RSL rise of 1.2 m from 13-11.5 ka. We use this simplified ice melting scenario in order to assess sensitivity to the regional sources of melt, geometry of melt, and duration of melt.

F.4.1 Regional sources of meltwater from 13-11.5 ka

We assess the sensitivity of our results to regional distributions of ice melt. As an example, we shift the geographic limit of ice melt further east to 100° W (GI-19, purple line, Supplementary Figure 7A), so as to broaden the zone of ice mass flux, and this results in an additional 1 m of sea-level rise across the 13-11.5 ka time window (2.2 m of sea-level rise compared with 1.2 m for GI-15).

We explore the sensitivity of sea-level in the Bering Strait to the location of ice melt by constructing alternative ice models where the southern or western region of the CIS-LIS zone melts from 13-12.25 ka, and the northern or eastern region melts in the remaining period from 12.25-11 ka. We find that during the period when the southern or eastern region is melting, sea level at the Bering Strait rises rapidly, resulting in a total sea-level change of 4.85 m (GI-23, blue line, Supplementary Figure 7B) and 6.28 m (GI-26, light blue line, Supplementary Figure 7B), respectively. Therefore, we conclude that a sea-level stillstand at the Bering Strait from 13-11.5 ka can be explained by melting from the northwestern section of the CIS-LIS zone over this entire interval, as this has the largest control on gravitational effects in the Bering Strait region.

We next consider how varying the timing of melting over the total CIS-LIS zone within the 13-11.5 ka period impacts RSL predictions. We modified the duration of melting to be longer (13-11 ka, GI-14, green line, Supplementary Figure 7A) or shorter (12.5-11.5 ka, GI-18, blue line, Supplementary Figure 7A), and this yielded an average rate of sea-level rise of 1.5 m/ky and 0.2 m/ky, respectively, compared with 0.8 m/ky for GI-15. By melting the majority of this ice in the first 0.5 ky we predict

a sea-level fall of .7 m from 13-12.5 ka followed by a SL rise of 2.2 m until 11.5 ka (GI-12, orange line, Supplementary Figure 7A).

F.4.2 Total GMSL required for sea-level stillstand

We construct additional ice models similar to GI-15, distinguished by smaller amounts of GMSL melt (50%, 75%, and 80%) from the CIS-LIS zone, where the remaining GMSL melt was sourced from the eastern sector of LIS (GI-24, purple, yellow, orange lines, Supplementary Figure 7B), and find that these result in a sea level rise of 5.1 m, 3.0 m, and 2.6 m, respectively. If (for example) 3 m is an accepted value of sea-level rise over the 13-11.5 ka interval, we conclude that it is possible to source up to 25% of the total North American GMSL in the period 13-11.5 ka from the eastern LIS section. We construct two additional ice models that source 75% of the GMSL in CIS-LIS zone that melted in GI-15. In this case the remaining 25% of GMSL is sourced from the AIS (GI-28, magenta line, Supplementary Figure 7B) or FIS (GI-27, crimson line, Supplementary Figure 7B), to explore how the source of additional meltwater affects relative sea level in the Bering Strait. We find that latter results in a sea-level rise of 4.3 m, while the former predicts a sea-level rise of 3.7 m.

F.4.3 Saddle collapse vs. margin retreat

Ice modeling performed by Gregoire et al.(Gregoire, Payne and Valdes, 2012) suggest a rapid saddle collapse of the CIS-LIS zone. The mechanism for this collapse involves rapid thinning of the larger region of the ice saddle, as surface melting lowers the ice surface causing an additional feedback of surface melting. Other authors have instead suggested an ice margin retreat(Dyke, 2004), characterized by a separation between the two ice sheets, followed by a retreat of the CIS and LIS ice margins. The model GI-15 (and GI-31, adopted in the main text) is based on the ice margin retreat associated with ICE-6G following the interpretation suggested by Dyke(Dyke, 2004). We construct an alternative model that adopts the saddle collapse (characterized by ice thinning, rather than margin retreat)

using predictions by Gregoire et al(Gregoire, Payne and Valdes, 2012). We force total GMSL to be the same as GI-15 from the CIS-LIS region from 13-11.5 ka. This results in a total sea-level rise of 0.9 m (GI-25, green line, Supplementary Figure 7B), which is smaller than the 1.2 m predicted by GI-15. We conclude that both these ice-melting hypotheses are consistent with observational data that suggests a sea-level stillstand or fall from 13-11.5 ka.

F.4.4 Sources of melt at MWP-1a

The meltwater sources for the rapid rise in sea level during MWP-1a are highly debated(Clark et al., 2002; Bassett et al., 2005; Liu et al., 2015). For purposes of a sensitivity test, we construct an additional ice model that tests whether our predictions of a sea-level stillstand at the Bering Strait are sensitive to where meltwater is sourced during MWP-1a. Similar to GI-15, this additional hypothetical ice model is based on ICE-6G. Instead of forcing the AIS and FIS to contribute to MWP1a, as in GI-15, we adopt the same AIS model as ICE-6G, and only modify the FIS component of the ICE-6G ice model. We require that ice melt from the FIS section of ICE-6G from 13-11.5 ka is sourced earlier at 14.5 ka. In this variation of GI-15, ice volumes in the CIS-LIS zone are preserved from 15 ka until 13 ka. In order to fit total global ice volumes, we require that the primary source for MWP-1a is the eastern sector of the LIS. Half of the ice volume lost from 14.5-13 ka in the eastern LIS sector in the ICE-6G model is forced to melt earlier from 14.5-14.25, so that this melt contributes to MWP-1a. This ice model, when paired with the Earth model adopted in the main text, yields RSL predictions in which sea level increases from -51.6 to -51.0 m from 13-11.5 ka (GI-22, red line, Supplementary Figure 7B), with a total sea level rise of $\sim$0.7 m (compared with 1.2 m for GI-15, solid black line, Supplementary Figure 7).

This test indicates that a contribution of the AIS to MWP-1a, although possible(Golledge et al., 2014), is not an essential factor in our construction of an ice history. Rather, our results rely solely on a small contribution from the CIS-LIS zone during MWP-1a (14.5-14.0 ka), and a large contribution

during the Younger Dryas interval (13.0-11.5 ka).

F.5 Sensitivity to Earth model

We assessed the sensitivity of the RSL predictions in the Bering Strait region to variations in the adopted Earth model by varying the lithospheric thickness as well as the upper and lower mantle viscosities. We increased the lithospheric thickness to 96 km and found that RSL at 13 ka was shifted by 2.1 m (blue line, Supplementary Figure 8). We next considered three Earth models in which the upper mantle viscosity was decreased to 3 x 1020 Pa s or the lower mantle viscosity was changed to either 7 x 1021 Pa s or 3 x 1021 Pa s. These three models perturbed RSL at 13 ka by 0.3 m, 1.9 m and -1.5 m, respectively (Supplementary Figure 8).

F.6 Meltwater flux volumes to Arctic Ocean

We can estimate the flux of freshwater created by melting ice in our various reconstructed ice histories. Ice model GI-31 (adopted in main text) sources 14.3 m GMSL from the CIS-LIS zone in 1.5 ky, resulting in a flux of 0.11 Sv ($10^6 m^3$/s). As a comparison, the duration of melt in ice model GI-18 is shortened to 0.5 ky, leading to a flux 0.33 Sv, melting the same volume in 2 ky results in a flux of 0.082 Sv. According to previously published estimates, this range of meltwater fluxes is sufficient to lead to a reduction in the strength of the Atlantic Meridional Overturning Circulation(Tarasov and Peltier, 2006; Ivanovic et al., 2017).

F.7 Meltwater pulses recorded in Arctic

Our inference that ice loss in the CIS/western LIS region during the Younger Dryas interval predicts meltwater input directly the Arctic Ocean in the area of the modern Mackenzie River delta. We find support for this prediction in foraminiferal δ^{18}Odata reported from sediment cores P189AR-P45

recovered from this region (700 33.03'N, 1410 52.08'W, 405 m water depth west of the Mackenzie River(Andrews and Dunhill, 2004)) and HLY1302-JPC 15 and JPC27 (JPC15: 71°06.222'N, 135°08.129'W; JPC27: 71°06.360'N, 135°09.640'W, 690 m water depth, east of the Mackenzie River24). We recalibrated ^{14}C measurements based on the reservoir age approach noted below in Supplementary Material 8, and calculated an age model that addresses analytical error, uncertainties in reservoir ages, and increased uncertainty between dated levels in 10,000 BCHRON simulations(Parnell, 2014). Both sites document relatively low Δ 18O of the planktonic foraminifera left-coiling Neogloboquadrina pachyderma (implying lower salinity likely forced by freshwater runoff) relative to a reconstruction of the global average marine Δ 18O ice-volume component(Waelbroeck et al., 2002) between about 12,800 and 11,900 cal yr BP (Supplementary Figure 9). The low- Δ 18O (presumed meltwater) event is much stronger in the sites east of the Mackenzie River. The potential existence of older events is unconstrained in core P45, given the basal age of the core, but appear to be present (though less accurately dated) based on extrapolation of dates and a splice between two cores.

F.8 On-land geologic data constraining CIS and LIS retreat

The on-land deglaciation chronology of the late North American ice sheets is largely comprised of dates using ^{14}C, OSL, and cosmogenic methods. Radiocarbon dates on biological material provide a minimum age of ice retreat, as the location must have been ice-free to host vegetation. While the time required for a recently deglaciated area to harbor life is debated, some researchers have estimated as little as a 30 yr period(Fisher et al., 2009). OSL dates on aeolian dune deposits also involve a time lag, including the time required for a pro-glacial lake to retreat(Munyikwa, Rittenour and Feathers, 2017). Supplementary Figure 6 shows the 2σ uncertainty minimum and maximum on ages, and the corresponding ice melting scenarios for each (GI-34; GI-30).

Cosmogenic ages record the time duration of exposure, since ice sheets (as well as snow cover) block cosmic flux radiation from penetrating the underlying rocks. These ages provide information

on the last time that ice retreated from the region of observation. The type of moraine sampled contains important information on the style of glaciation. For instance, in Menounos et al.(Menounos, Goehring, et al., 2017) the authors argue that dates on cirque and valley glacier moraines indicate that the style of ice cover had changed from extensive ice sheets to small alpine glaciers by 14 ka. These authors suggest that ages on cirque and valley glaciers indicate the CIS had fully deglaciated in this region, possibly thousands of years before alpine glaciation built cirque and valley glacier moraines.

We consider the sites presented in Menounos et al.18 which are most relevant to our ice-melting scenario construction GI-31. In particular, the cirque moraine Site 9 has a mean age of ∼14.3 ka (Supplementary Figure 10; circle dot). If this age represents the timing of a total deglaciation of the Cordilleran Ice Sheet, then our ice history GI-31 can be ruled out. However, the actual set of dates obtained at this site show a large spread, ranging from 17.7 to 11.7 ka. The adjacent valley moraine Site 8 (Supplementary Figure 10; triangle dot) includes a 40.84 ka age, suggesting this site may be prone to inheritance, opening the possibility that some of the older cirque dates at Site 9 include some inherited exposure.

A series of valley glacier sites (triangle dots; Supplementary Figure 10) in the same vicinity, sites 10, 11, and 12, similarly show a large spread in ages, ranging from 10.24-14.81 ka, 10.16-19.45 ka, and 10.38-17.87 ka, respectively. However, because ^{10}Be was measured on small boulders, these samples may have been snow-covered and therefore should be corrected for this effect, suggesting that the snow and erosion corrected ages calculated in Menounos et al.(Menounos, Clarke, et al., 2017), which are older than uncorrected dates, may be most accurate.

F.9 Radiocarbon reservoir age corrections

Reservoir corrections to radiocarbon dates in the Bering Strait region are challenging and have been applied differently in various publications. Here we review available constraints and outline a frame-

work for consistent application of reservoir age anomalies (ΔR) when correcting measured radiocarbon ages to calendar ages in this region.

F.9.1 "Portlandia" Effect

Many of the dates used to calibrate ^{14}C reservoir ages in the region are based on shallow-water mollusks. England et al.(England et al., 2013) note that infaunal deposit-feeding bivalves such as Portlandia arctica yield ^{14}C ages as much as a few thousand years (uncertainty-weighted average recalculated here as 800 $\pm$ 700 yr) older than co-existing epifaunal filter feeders. They refer to this as the "Portlandia Effect", but this issue can also apply to deposit feeders such as Macoma sp., Nuculana sp., and likely others. Suspension feeders such as Astarte borealis, Musculus discors, Hiatella arctica, Mytilus sp., bivalves and Balanus barnacles appear to give more reliable dates. The Portlandia Effect is most severe in carbonate terranes where ^{14}C-free bedrock erodes to comprise a significant fraction of the ambient sediment and its subsequent diagenesis adds ^{14}C-free (aka "dead") carbon to the porewaters. Even in non-carbonate terranes the dates on infaunal taxa can be influenced by older organic matter and porewater effects. We have excluded infaunal taxa from our analysis to the extent possible, or make corrections as noted below.

F.9.2 Canadian Arctic reservoir age

Mollusk calibrations in the western Canadian Arctic(Coulthard et al., 2010) use corrections from the Intcal09 atmosphere(Reimer et al., 2009), and exclude deposit feeders. They recommend a modern ΔR value of 335 $\pm$ 85 years. We recalculate these values based on Marine13(Reimer et al., 2013) using the ΔR tool in CALIB-7.1(Stuiver, Reimer and Reimer, 2017), which calculates the Δ R value between a measured date and the Marine13 nominal ocean ^{14}C history. We only use samples collected prior to 1950, to avoid potential contamination with bomb radiocarbon, and we calculate an uncertainty-weighted average ΔR of 320 $\pm$50 yr for the western Canadian Arctic.

F.9.3 Siberian Arctic reservoir age

On the Siberian Arctic margin, radiocarbon content of pre-bomb mollusks (excluding Portlandia sp.) in the Barents and Kara seas yield ΔR, recalculated here based on uncertainty-weighted averages, of -40 ± 40 yr (Forman and Polyak, 1997). In the Laptev Sea, a similar study yields ΔR, recalculated here based on uncertainty-weighted averages as 60 ± 40 yr(Bauch et al., 2001).

F.9.4 Bering Sea reservoir age

Radiocarbon reservoir effects are much larger in the Bering Sea, south of Bering Strait, because of the dominance of upwelled Pacific water, and limited gas exchange. Cook et al.(Cook, Keigwin and Sancetta, 2005) assumed ΔR values there of 300 yr based on published pre-bomb shell estimates ranging from 40-360 yr, but did not specify an uncertainty and stated that values may be higher in the past. Dumond and Griffin(Dumond and Griffin, 2002) reported apparent reservoir ages of marine shells relative to terrestrial carbon (charcoal, wood, or grass) of 460 ±35 yr (i.e., ΔR of about 50 ± 45 yr) and between marine mammal residue and terrestrial carbon of 735 ±20 yr (ΔR of about 325 ±30 yr). Although uncertain, these authors considered the larger value from the marine mammals to be more representative of the Bering Sea, and that the low values from shells may represent local effects.

Larger values from the Bering Sea are consistent with estimated Holocene values from the subpolar North Pacific in the Alaska Current (which flows into the Bering Sea), e.g., ΔR of 470 ± 80 yr(Davies-walczak et al., 2014) based on average benthic-planktonic age differences and modern deep-water ages, which are generally consistent with paleomagnetic correlations(Walczak et al., 2017). Regional correlations of deglacial paleoclimate records suggest a ΔR of 390±50 yr at the same site(Praetorius et al., 2014). Tephrochronology constraints along the southeastern Alaska margin during the deglacial interval yield a ΔR of 190 ±50 yr(Praetorius et al., 2016), while nearby com-

parisons of the age differences between terrestrial plant materials and marine bivalves yield a ΔR of 330$\pm$50 years(Addison et al., 2010). The data from the Alaska margin and the Bering Sea together allow for variations in reservoir ages of a few hundred years, with ΔR values generally in the range of 350 $\pm$ 120 yr.

F.9.5 Reservoir ages adopted in this study

In this study we follow a strategy similar to Jakobsson et al.(Jakobsson et al., 2017) in correcting marine radiocarbon dates for changing reservoir ages during the opening event, however we update calculations of these effects. We apply this strategy consistently to other published data. For radiocarbon dates on the Arctic side of Bering Strait, if clearly older than the inundation event or with ^{14}C dates > 12000 yr BP, we use the Laptev Sea ΔR of 60 $\pm$ 40 yr. For ^{14}C dates clearly younger than the inundation events with a substantially open Bering Strait or with ^{14}C dates < 10,000 yr BP we use the North-Pacific and Bering ΔR composite value of 350 $\pm$120 yr. For times intermediate between a fully closed and open Bering Strait (the majority of the data included in Table 1 and Figure 2), we are less certain about reservoir ages, and use an intermediate value of 250 $\pm$ 200 yr, acknowledging that this is not fully constrained.

For dating the initial occurrence of Pacific mollusk taxa in the Arctic we use the modern ΔR from the western Canadian archipelago of 320$\pm$50 years. For mollusks identified as infaunal deposit feeders (Portlandia sp., Macoma sp., or Nuculana sp.) we subtract 800$\pm$700 yr from the measured radiocarbon date prior to applying a ΔR value. We calculate all calendar ages for marine materials based on the Marine13 database and Calib 7.1 software(Stuiver, Reimer and Reimer, 2017).

For calibrating calendar ages in terrestrial peats, we use the Intcal13 database and Calib 7.1 software, considering only wet-sieved peats that minimize contamination with older bulk carbon(Elias et al., 1996). No reservoir age is applied to the peat samples. Note however, that different fractions of peat samples may yield different dates, either too young due to root penetration, or too old due

to respired CO_2 from older deposits contributing to peat growth(Nilsson, Klarqvist and Bohlin, 2001), implying that analytical uncertainties may underestimate geological uncertainty.

F.9.6 Calibrating ages with additional uncertainty

In addition to calibrating raw ^{14}C ages with the reservoir ages described above, we also calibrated ages using a reservoir age with a large uncertainty ($\Delta R = 300 \pm 200$ yr). These calibrated ages are shown in Supplementary Table 1 and Supplementary Figure 11.

F.10 Fitting relative sea level constraints in far-field

The reconstructed ice histories adopted in this study are characterized by GMSL histories that closely match the ICE-6G GMSL history. We predict RSL histories at Tahiti and Barbados for GI-31 and ICE-6G, adopting Earth model VM2 (Peltier & Fairbanks 2006) and find that differences between these predicted RSL histories from 13-11.5 ka are less than 1.5 m. Therefore our modifications to the ICE-6G ice history in constructing GI-31 are well within the uncertainties associated with the well-established sea-level records at these sites (~5-10 m(Peltier and Fairbanks, 2006; Deschamps et al., 2012)).

F.11 Fitting glacial lake shoreline tilts and local relative sea level histories

Glacial lake shorelines constitute an important geologic constraint on glacial isostatic adjustment, and recently published ice models have begun to incorporate such datasets in modeling of the GIA process(Gowan et al., 2016; Lambeck, Purcell and Zhao, 2017). The ice model NAICE39, as an example, was constructed to yield predictions consistent with differential lake level changes and strandline tilts for glacial lakes throughout central and northwestern Canada. As a test, we construct a new ice model NAICE-D where we adopt a modified version of the NAICE ice model in which ice melting

in the CIS- LIS region is delayed from 15 to 13 ka (as in GI-31, main text). We compared predictions based on the NAICE and NAICE-D ice histories, both coupled to an Earth model characterized by a 96 km thick elastic lithosphere, and upper and lower mantle viscosities of $4x10^{20}$ Pa s and 10^{22} Pa s, respectively (similar to Gowan et al.(Gowan et al., 2016)).

We focused this test on data from Glacial Lake Agassiz because its shoreline features have been most reliably dated (Lepper et al., 2013, Yang and Teller, 2012). Since the Upper Campbell shoreline ($\sim$10.5 ka) contains the most extensive record of all the Glacial Lake Agassiz shorelines, we compare the tilt of the shorelines predicted using the NAICE and NAICE-D models to observations (Supplementary Figure 14; compare to Figure 4 in Gowan et al.(Gowan et al., 2016)). The NAICE model results are shown in green and the results based on the modified NAICE-D model are shown in blue. There are small differences in the predicted tilt, and both models perform well in fitting the measured tilt of the Upper Campbell strandline. Next, we can compare the predicted paleotopography at any relevant shoreline with the observed measured elevation. Supplementary Figure 15 compares the paleotopography predicted using the two ice histories for the following Lake Agassiz shorelines: Upper Campbell (10.5 ka), Norcross (13.5 ka), and Herman (14 ka). To compare these predictions in more quantitative terms, we plot below the misfit between the predicted and observed elevations (Supplementary Figure 16). Although these misfits show some variation between the predictions for the NAICE to NAICE-D models of ice history, these misfits are of the same magnitude.

Finally, we show relative sea level predictions using these two ice models and compare these predictions to observations of relative sea level in the Canadian Arctic dated to > 11 ka (Supplementary Figure 17). The results in Supplementary Figures 15-17 demonstrate that introducing a delayed melting of ice from within the CIS-LIS region does not impact the fit to the local glacial lake and relative sea level data sets when one begins with a local ice history that fits these data.

F.12 Supplementary References

Addison, J. A., Beget, J. E., Ager, T. A. and Finney, B. P. (2010) 'Marine tephrochronology of the Mt . Edgecumbe Volcanic Field , Southeast', Quaternary Research. Elsevier Inc., 73(2), pp. 277–292. doi: 10.1016/j.yqres.2009.10.007.

Andrews, J. T. and Dunhill, G. (2004) 'Early to mid-Holocene Atlantic water influx and deglacial meltwater events , Beaufort Sea slope , Arctic Ocean', Quaternary Research, 61, pp. 14–21. doi: 10.1016/j.yqres.2003.08.003.

Bassett, S. E., Milne, G. A., Mitrovica, J. X. and Clark, P. U. (2005) 'Ice Sheet and Solid Earth Influences on Far-Field Sea-Level Histories', Science, 309(August), pp. 925–929. doi: 10.1029/2002GL016722.

Bauch, H. A., Mueller-lupp, T., Taldenkova, E., Spielhagen, R. F. and Kassens, H. (2001) 'Chronology of the Holocene transgression at the North Siberian margin', Global and Planetary Change, pp. 125–139.

Brigham-Grette, J. (2017) Online Review (WWW source) https://www.clim-past-discuss.net/cp-2017-11/cp-2017-11-RC1.pdf, Climate of the Past.

Clark, P. U., Mitrovica, J. X., Milne, G. a and Tamisiea, M. E. (2002) 'Sea-level fingerprinting as a direct test for the source of global meltwater pulse IA.', Science (New York, N.Y.), 295(5564), pp. 2438–2441. doi: 10.1126/science.1068797.

Cook, M. S., Keigwin, L. D. and Sancetta, C. A. (2005) 'The deglacial history of surface and intermediate water of the Bering Sea', Deep-Sea Research Part II, 52, pp. 2163–2173. doi: 10.1016/j.dsr2.2005.07.004.

Coulthard, R. D., Furze, A. J., Piewnkowski, F. C., Nixon and England, J. (2010) 'New marine DeltaR values for Arctic Canada', Quaternary Geochronology, 5, pp. 419–434.

Danielson, B. S. L., Dobbins, E. L., Jakobsson, M., Johnson, M. A. and Thomas, J. (2015) 'Sounding the Northern Seas', Eos, (December 2015), pp. 1–8.

Davies-walczak, M., Mix, A. C., Stoner, J. S., Southon, J. R., Cheseby, M. and Xuan, C. (2014)

'Late Glacial to Holocene radiocarbon constraints on North Pacific Intermediate Water ventilation and deglacial atmospheric CO 2 sources', Earth and Planetary Science Letters. Elsevier B.V., 397, pp. 57–66. doi: 10.1016/j.epsl.2014.04.004.

Deschamps, P., Durand, N., Bard, E., Hamelin, B., Camoin, G., Thomas, A. L., Henderson, G. M., Okuno, J. and Yokoyama, Y. (2012) 'Ice-sheet collapse and sea-level rise at the Bølling warming 14 , 600 years ago', Nature. Nature Publishing Group, 483(7391), pp. 559–564. doi: 10.1038/nature10902. Dumond, D. O. N. E. and Griffin, D. G. (2002) 'Measurements of the Marine Reservoir Effect on Radiocarbon Ages in the Eastern Bering Sea', Arctic, 55(1), pp. 77–86.

Dyke, A. S. (2004) 'An outline of North American Deglaciation with emphasis on central and northern Canada', in J.Ehlers and P.L.Gibbard (eds) Quaternary Glaciations-Extent and Chronology: Part II: North America, pp. 373–424.

Elias, S., Short, S., Nelson, H. and Birks, H. (1996) 'Life and times of the Bering land bridge', Nature, 382(July).

England, J., Dyke, A. S., Coulthard, R. O. Y. D., Mcneely, R. and Aitken, A. (2013) 'The exaggerated radiocarbon age of deposit-feeding molluscs in calcareous environments', Boreas, 2013. doi: 10.1111/j.1502-3885.2012.00256.x.

Fisher, T. G., Waterson, N., Lowell, T. V and Hajdas, I. (2009) 'Deglaciation ages and meltwater routing in the Fort McMurray region , northeastern Alberta and northwestern Saskatchewan , Canada', Quaternary Science Reviews. Elsevier Ltd, 28(17–18), pp. 1608–1624. doi: 10.1016/j.quascirev.2009.02.003.

Forman, S. L. and Polyak, L. (1997) 'Radiocarbon content of pre-bomb marine mollusks and variations in the ^{14}C Reservoir age for coastal areas of the Barents and Kara Seas, Russia', Geophysical Research Letters, 24(8), pp. 885–888.

Golledge, N. R., Menviel, L., Carter, L., Fogwill, C. J., England, M. ., Cortese, G. and Levy, R. . (2014) 'Antarctic contribution to meltwater pulse 1A from reduced Southern Ocean overturning Antarctic contribution to meltwater pulse 1A from reduced Southern Ocean overturning', Nature

Communications. Nature Publishing Group, 5(September), pp. 1–10. doi: 10.1038/ncomms6107.

Gowan, E. J., Tregoning, P., Purcell, A., Montillet, J. and Mcclusky, S. (2016) 'A model of the western Laurentide Ice Sheet , using observations of glacial isostatic adjustment', Quaternary Science Reviews. Elsevier Ltd, 139, pp. 1–16. doi: 10.1016/j.quascirev.2016.03.003.

Gregoire, L. J., Payne, A. J. and Valdes, P. J. (2012) 'Deglacial rapid sea level rises caused by ice-sheet saddle collapses.', Nature. Nature Publishing Group, 487(7406), pp. 219–22. doi: 10.1038/nature11257.

Hill, J. C. and Driscoll, N. W. (2008) 'Paleodrainage on the Chukchi shelf reveals sea level history and meltwater discharge', Marine Geology, 254, pp. 129–151. doi: 10.1016/j.margeo.2008.05.018.

Ivanovic, R. F., Gregoire, L. J., Wickert, A. D., Valdes, P. J. and Burke, A. (2017) 'Collapse of the North American ice saddle 14,500 years ago caused widespread cooling and reduced ocean overturning circulation', Geophysical Research Letters, 44(1), pp. 383–392. doi: 10.1002/2016GL071849.

Jakobsson, M., Pearce, C., Cronin, T. M., Backman, J., Anderson, L. G., Björk, G., Coxall, H., Boer, A. De, Mayer, L. A., Mörth, C., Rattray, J. E., Stranne, C., Semilietov, I. and Regan, M. O. (2017) 'Post-glacial flooding of the Beringia Land Bridge dated to 11 , 000 cal yrs BP based on new geophysical and sediment records', Climate of the Past. doi: 10.5194/cp-2017-11.

Lambeck, K., Purcell, A. and Zhao, S. (2017) 'The North American Late Wisconsin ice sheet and mantle viscosity from glacial rebound analyses', Quaternary Science Reviews. Elsevier Ltd, 158, pp. 172–210. doi: 10.1016/j.quascirev.2016.11.033.

Liu, J., Milne, G. A., Kopp, R. E., Clark, P. U. and Shennan, I. (2015) 'Sea-level constraints on the amplitude and source distribution of Meltwater Pulse 1A', Nature Geoscience, 9(2), pp. 130–134. doi: 10.1038/ngeo2616.

Menounos, B., Clarke, G. K. C., Clague, J. J., Lakeman, T., Koch, J., Caffee, M. W. and Gosse, J. (2017) 'Cordilleran Ice Sheet mass loss preceded climate reversals near the Pleistocene Termination', Science, (November), pp. 1–5.

Menounos, B., Goehring, B. M., Osborn, G., Margold, M., Ward, B., Bond, J., Clarke, G. K. C., Clague, J. J., Lakeman, T., Koch, J., Caffee, M. W., Gosse, J., Stroeven, A. P., Seguinot, J. and Heyman, J. (2017) 'Supplement: Cordilleran Ice Sheet mass loss preceded climate reversals near the Pleistocene Termination', Science, 358(6364), pp. 781–784. doi: 10.1126/science.aan3001.

Munyikwa, K., Rittenour, T. M. and Feathers, J. K. (2017) 'Temporal constraints for the Late Wisconsinan deglaciation of western Canada using eolian dune luminescence chronologies from Alberta', Palaeogeography, Palaeoclimatology, Palaeoecology. Elsevier B.V., 470, pp. 147–165. doi: 10.1016/j.palaeo.2016.12.034.

Nilsson, M., Klarqvist, M. and Bohlin, E. (2001) 'Variation in 14 C age of macrofossils and different fractions of minute peat samples dated by AMS', The Holocene, 5, pp. 579–586.

Parnell, A. (2014) 'Bchron: Radiocarbon dating, age-depth modelling, relative sea level rate estimation, and non-parametric phase modelling. R package version, 4(1).'

Peltier, W. R. and Fairbanks, R. G. (2006) 'Global glacial ice volume and Last Glacial Maximum duration from an extended Barbados sea level record', Quaternary Science Reviews, 25, pp. 3322–3337. doi: 10.1016/j.quascirev.2006.04.010.

Praetorius, S. K., Mix, A. C., Pacific, N. and Atlantic, N. (2014) 'Synchronization of North Pacific and Greenland climates preceded abrupt deglacial warming', Science, 345(6195).

Praetorius, S., Mix, A., Jensen, B., Froese, D., Milne, G., Wolhowe, M., Addison, J. and Prahl, F. (2016) 'Interaction between climate , volcanism , and isostatic rebound in Southeast Alaska during the last deglaciation', Earth and Planetary Science Letters. Elsevier B.V., 452, pp. 79–89. doi: 10.1016/j.epsl.2016.07.033.

Reimer, P. J., Baillie, Bard and Bayliss, A. (2009) 'IntCal09 and Marine09 radiocarbon age calibration curves, 0–50,000 years cal BP', Radiocarbon, 51, pp. 1111–1150.

Reimer, P. J., Bard, E., Bayliss, A., Beck, J. W., Blackwell, P. G., Bronk, C., Caitlin, R., Hai, E. B. and Edwards, R. L. (2013) 'Intcal13 and marine13 radiocarbon age calibration curves 0 – 50,000 years

cal bp', Radiocarbon, 55(4).

Stuiver, M., Reimer, P. J. and Reimer, R. W. (2017) CALIB 7.1 [WWW program] at http://calib.org.

Tarasov, L. and Peltier, W. R. (2006) 'A calibrated deglacial drainage chronology for the North American continent□: evidence of an Arctic trigger for the Younger Dryas A calibrated deglacial drainage chronology for the North American continent□: evidence of an Arctic trigger for the Younger D', Quaternary Science Reviews, 25(September 2014), pp. 659–688. doi: 10.1016/j.quascirev.2005.12.006.

Waelbroeck, C., Labeyrie, L., Michel, E., Duplessy, J. C., McManus, J. F., Lambeck, K., Balbon, E. and Labracherie, M. (2002) 'Sea-level and deep water temperature changes derived from benthic foraminifera isotopic records', Quaternary Science Reviews, 21(1–3), pp. 295–305. doi: 10.1016/S0277-3791(01)00101-9.

Walczak, M. H., Stoner, J. S., Mix, A. C., Jaeger, J., Rosen, G. P., Channell, J. E. T., Heslop, D. and Xuan, C. (2017) 'A 17 , 000 yr paleomagnetic secular variation record from the southeast Alaskan margin□: Regional and global correlations', Earth and Planetary Science Letters. Elsevier B.V., 473, pp. 177–189. doi: 10.1016/j.epsl.2017.05.022.

Woodgate, R. A. (2018) 'Increases in the Pacific inflow to the Arctic from 1990 to 2015, and insights into seasonal trends and driving mechanisms from year-round Bering Strait mooring data', Progress in Oceanography. Elsevier, 160(December 2017), pp. 124–154. doi: 10.1016/j.pocean.2017.12.007.

Table F.1: Supplementary Table 1 | Calibrated radiocarbon ages using a larger uncertainty on reservoir ages than in main text (ΔR = 300±200 yr).

Reference	Site name	Latitude	Longitude	Material	Marker depth (m)	Raw ^{14}C age (yrs)	Raw age uncertainty (1σ)	ΔR	ΔR uncertainty(yr)	Calendar Yr	1σ - yr	1σ + yr	Calibration curve
Jakobsson et al., 2017	4PC-1	72.8	175.7	mollusc	124.07	10200	30	300	200	10850	230	260	Marine13
Keigwin et al., 2016	JPC02	67.4	165.6	E. excavatum	53.455	10900	140	300	200	11870	470	390	Marine13
Hill et al., 2008	VBC03*	70.7	165.4	marine bivalve (Portlandia)	60.42	11500	765	300	200	12520	1100	910	Marine13
JPC10	70.8	165.5	marine bivalve	59.2	10200	55	300	200	10850	230	260	Marine13	
Elias et al., 1996	85-69	70	165.7	screened peat	44.95	11000	60	0	0	12870	90	80	Intcal13
Dyke & Savelle, 2001	Bowhead whale bone	10210	70	300	200	10860	240	260	Marine13				
Dyke et al., 1996	M. Balthica	11400	100	300	200	12570	280	530	Marine13				
England & Furze, 2008	C. kurriana	12,380	110	300	200	13560	240	500	Marine13				
England & Furze, 2008	C. kurriana	12,170	25	300	200	13340	210	440	Marine13				
England & Furze, 2008	C. kurriana	11,800	70	300	200	12980	220	380	Marine13				

* Portlandia Arctica raw ^{14}C age includes correction (800±700 yr subtracted from published raw ^{14}C age).

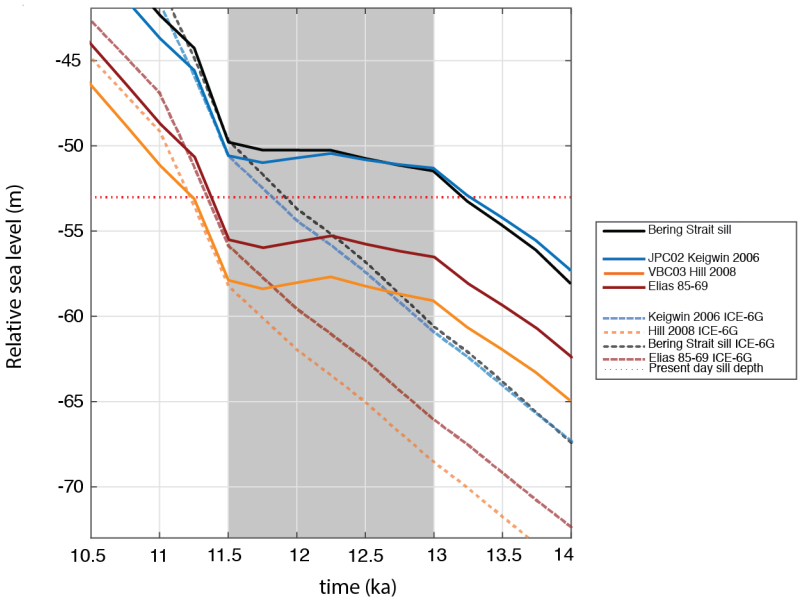

FIGURE F.1: Relative sea-level predictions at each site of observation for ice model GI-31 (solid) and ICE-6G (dashed) adopting the Earth model described in main text. The horizontal dotted red line represents present-day depth of the Bering Strait sill at -53 m.

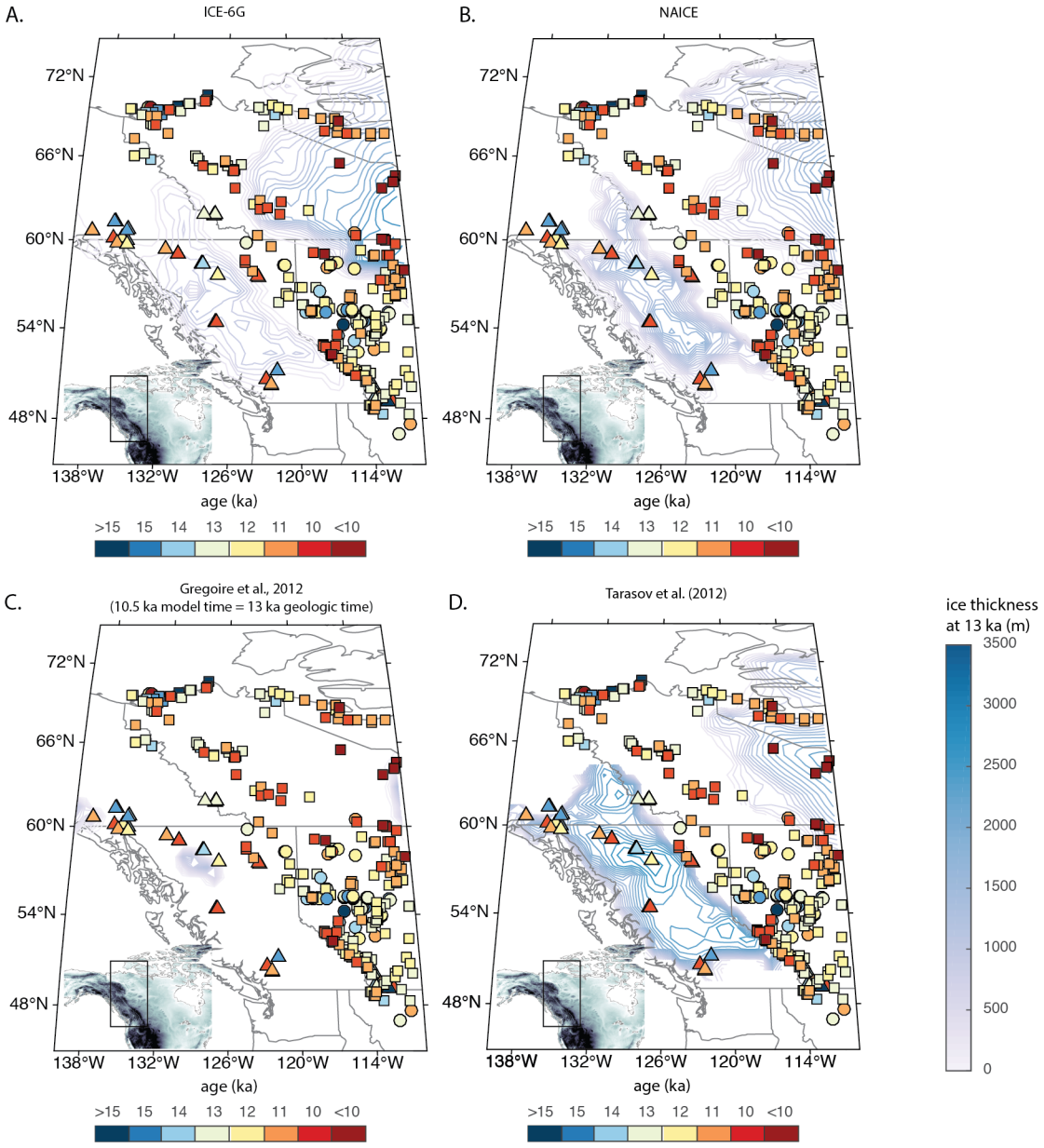

FIGURE F.2: Ice thickness at 13 ka, analogous to Figure 4 in the main text, except for the following ice histories: ICE-6G (A), NAICE (B), Gregoire et al., 2012 (C), and Tarasov et al., 2012(D).

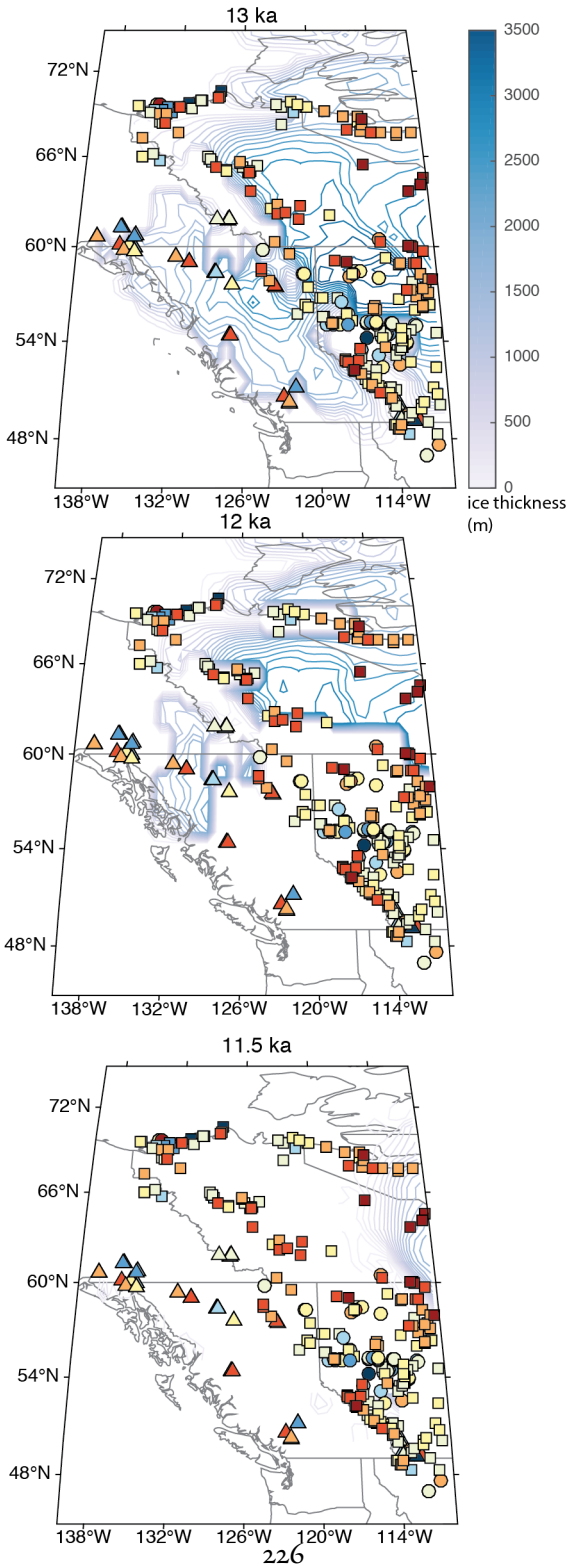

FIGURE F.3: Snapshots of ice thickness from 13 to 11.5 ka for ice history GI-31 (ice history adopted in main text).

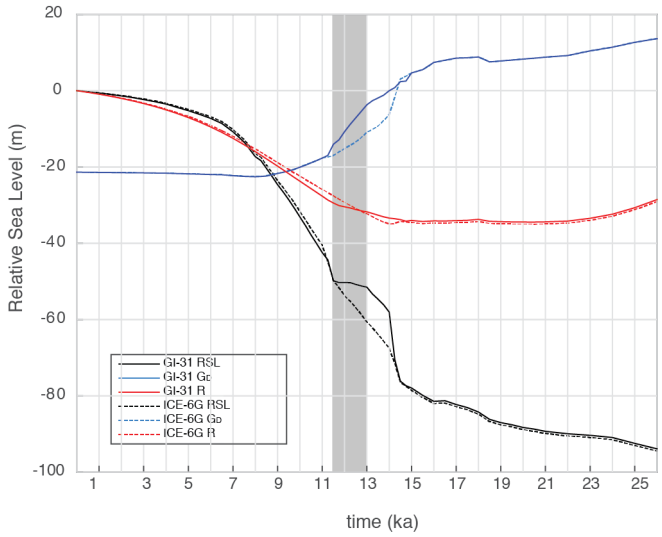

FIGURE F.4: Decomposition of total RSL at the Bering Strait sill (black lines) into components associated with the direct gravitational effect of the surface load (GD, blue lines) and crustal deformation, including the local gravitational effect of this deformation (R, red lines). Dashed lines are computed by adopting ice model ICE-6G and solid lines adopt GI-31, as in main text. The gray rectangle highlights the 13-11.5 ka interval.

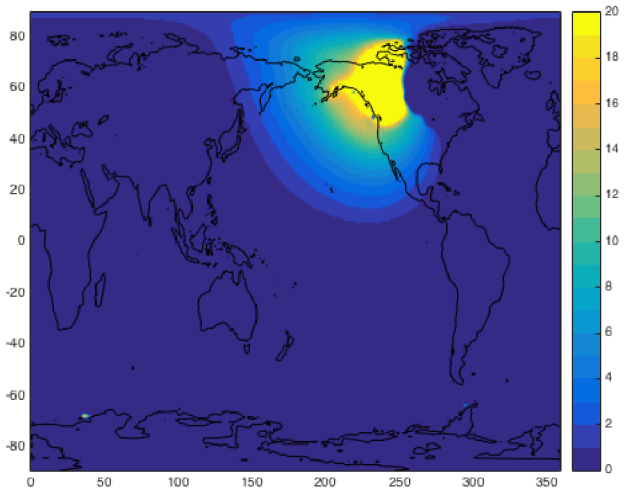

FIGURE F.5: Map of the difference in relative sea-level predictions at 13 ka BP predicted using the GI-31 and ICE-6G ice histories (i.e., GI-31 result minus ICE-6G result) and the Earth model described in the main text.

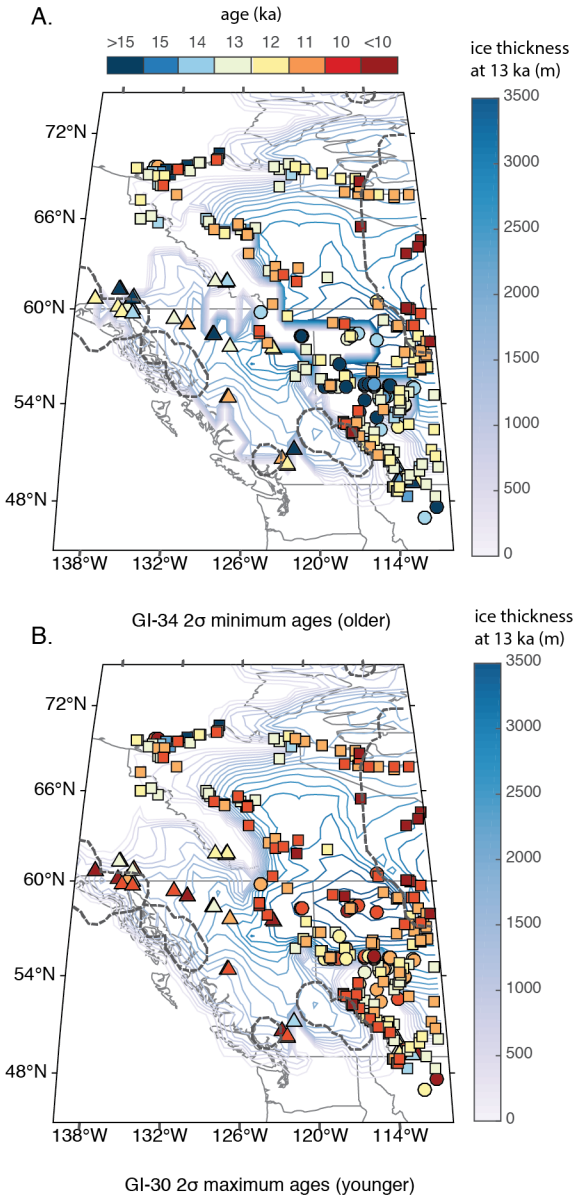

FIGURE F.6: Ice melting scenario from 13-11.5 ka for GI-34 (A) and GI-30 (B). Contours represent ice thickness at 13 ka (right-hand colorbar). Squares represent calibrated radiocarbon ages, circles represent luminescence ages, and triangles represent cosmogenic ages. Interior colors represent ages rounded to nearest integer (top colorbar). Dotted gray lines represent the limits of ice extent at 11.5 ka.

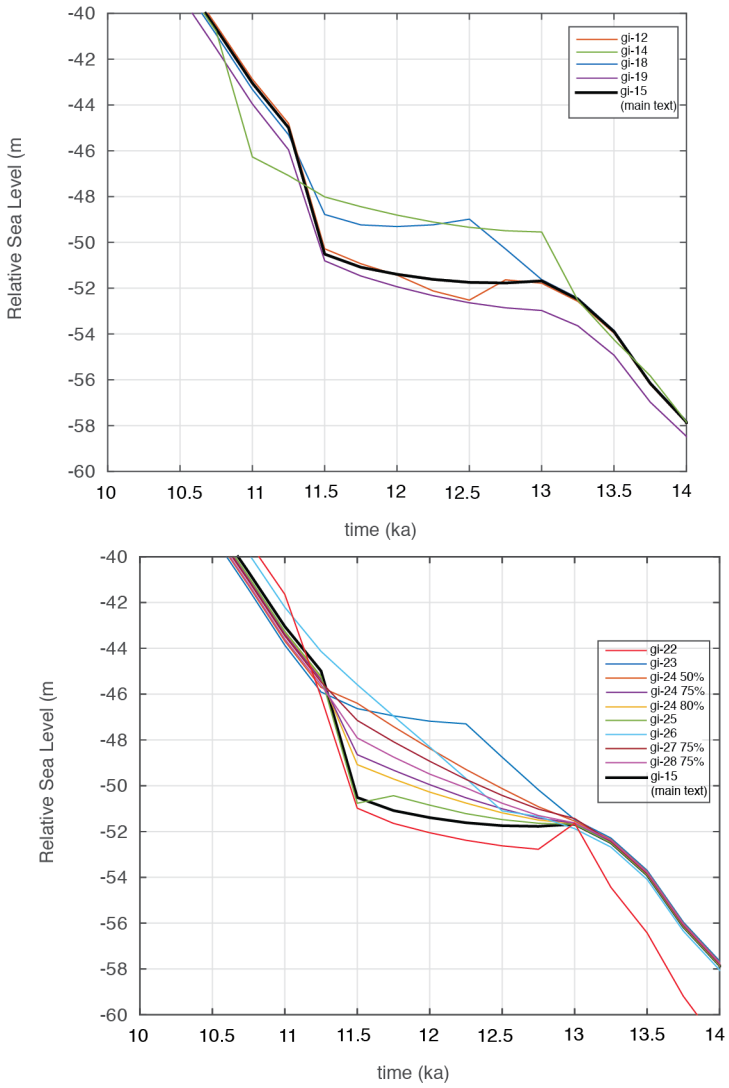

FIGURE F.7: Relative sea level predictions based on a suite of ice models, testing the sensitivity of the predictions to changes in the regional distribution and duration of ice melt. (See text for a full description of the different ice models.) A. Ice models GI-12, GI-14, GI-18, GI-19, GI-15. B. Ice models GI-22, GI-23, GI-24 (50%,75%,80%), GI-25, GI-26, GI-27, GI-28, and GI-15).

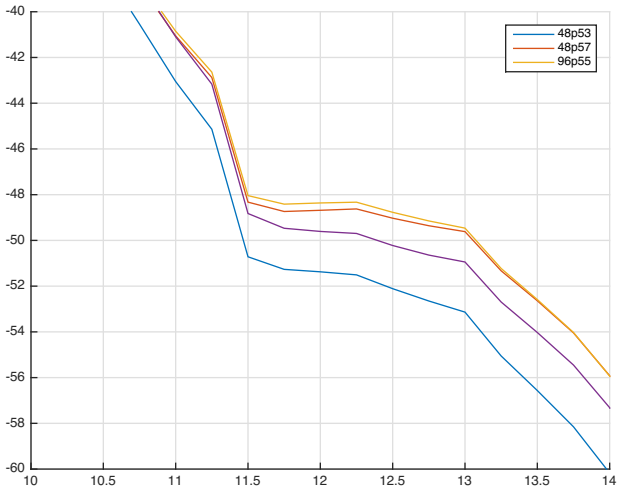

FIGURE F.8: Earth model sensitivity. Relative sea-level predictions based on ice model GI-31 using a suite of Earth models. Solid black line is the prediction based on the Earth model adopted in main text. Yellow, blue, orange, and purple lines are based on Earth models with a lithospheric thickness, upper mantle viscosity and lower mantle viscosity of: (96 km, 5 x10^{20} Pa s, 5x10^{21}); (48 km, 5 x10^{20} Pa s, 3x10^{21} Pa s); (48 km, 5 x10^{20} Pa s, 7x10^{21}); (48 km, 3 x10^{20}Pa s, 5x10^{21}).

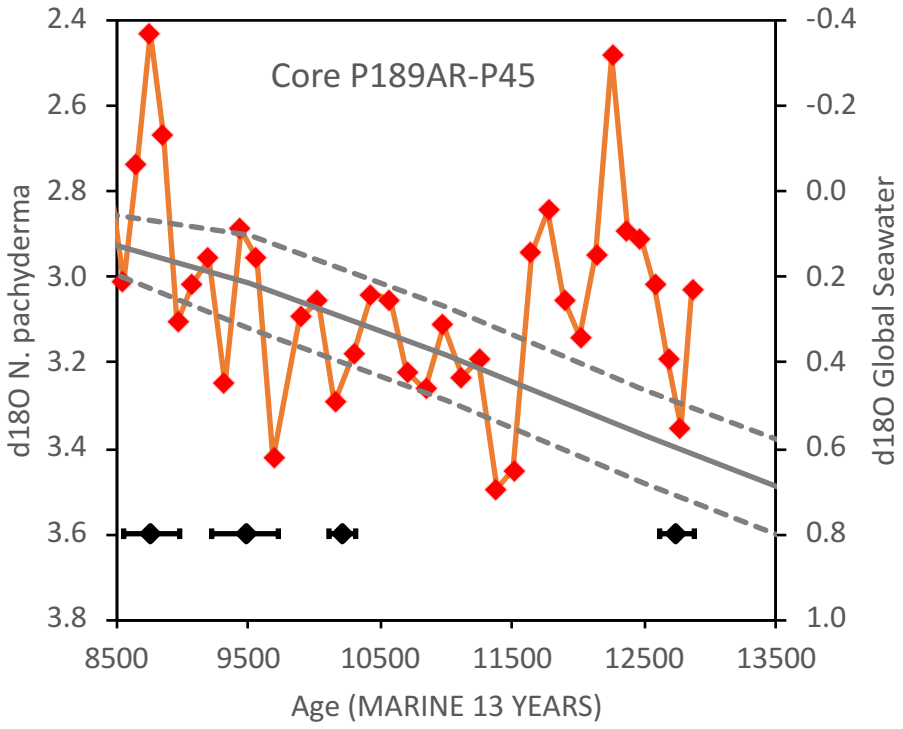

FIGURE F.9: Oxygen isotope record from planktonic foraminifera left-coiling N. pachyderma (red symbols and lines) from the Mackenzie River delta region of the Arctic Ocean in a) sediment core P189AR-P45 (Andrews and Dunhill, 2004) and b) sediment core HLY1302-JPC15,29 24. For comparison, a reconstruction of the global average ice-volume component of δ^{18}O(global seawater) is shown as a gray line (uncertainty envelope represented by dashed lines)(Waelbroeck et al., 2002). Vertical bar demarcates the Younger Dryas (YD) interval. Age models are recalculated here using ^{14}C dates calendar corrected based on our adopted reservoir age constraints (black bars span 2σ uncertainty). Age uncertainties of BCHRON Bayesian age model applied to the δ^{18}Osamples in the intervals of anomalously low δ^{18}O(i.e., high freshwater runoff) are shown as red horizontal bars. Low values of δ^{18}Orelative to the global trend are consistent with increased flux of freshwater from melting continental ice. The apparent freshwater anomalies are relatively subdued in P189AR-P45, yet strong in HLY1302-JPC15,29, which also suggests a series of earlier events. The two cores agree that an interval of relatively high δ^{18}O (implying cessation or re-routing of freshwater runoff to the region) occurred between ~12,000 and ~9000 yr BP.

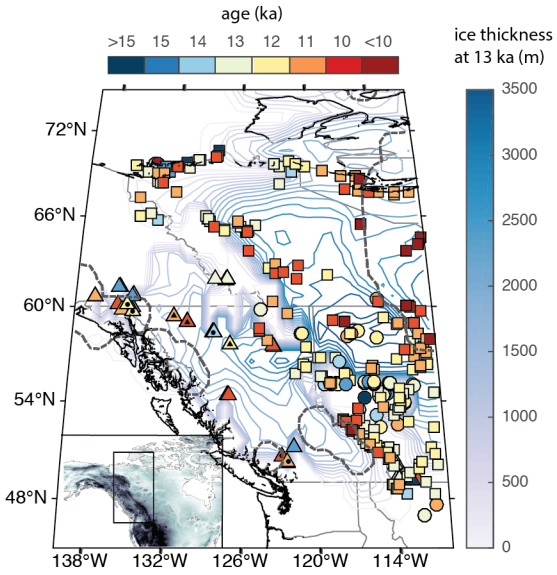

FIGURE F.10: The location of cirque (dots) and valley (triangle) glacier moraines in the Menounos et al.(Menounos, Clarke, et al., 2017) study is shown on Figure 4 from main text. See Supplementary Material 7 for a discussion of these ages.

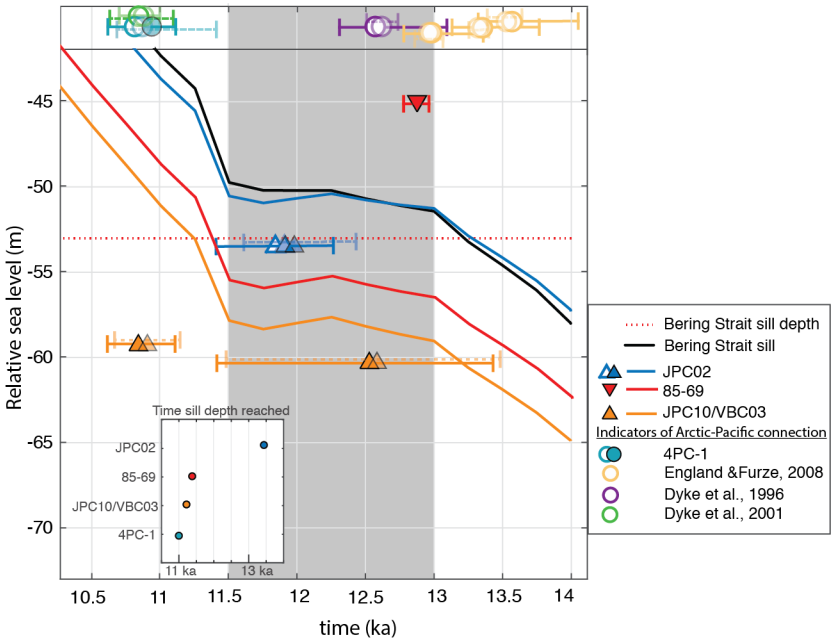

FIGURE F.11: Relative sea-level predictions for sites in the Bering Strait region compared with observations using radiocarbon dates calibrated with additional uncertainty. Translucent markers with dotted uncertainty bars represent ages adopted in main text (as in Figure 2), solid markers and uncertainty bars are ages calibrated with $\Delta R = 300 \pm 200$ yr. Horizontal bars denote 1σ uncertainties.

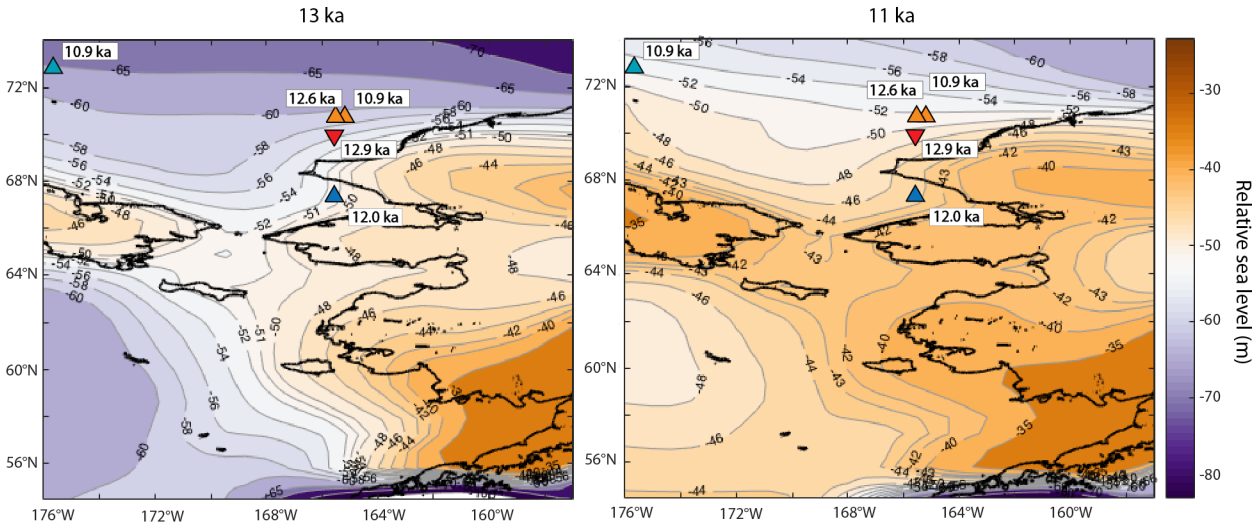

FIGURE F.12: Map of relative sea-level predictions at 13 and 11 ka. Sites with observations on resubmergence of the Bering Strait are shown by upward and downward pointing triangles, which denote marine or terrestrial deposits, respectively. Adjacent white boxes show dates associated with each observable. At 13 ka, relative sea level at the Bering Strait sill is higher than the -53 m threshold, however relative sea level is lower at other sites on the Bering Shelf.

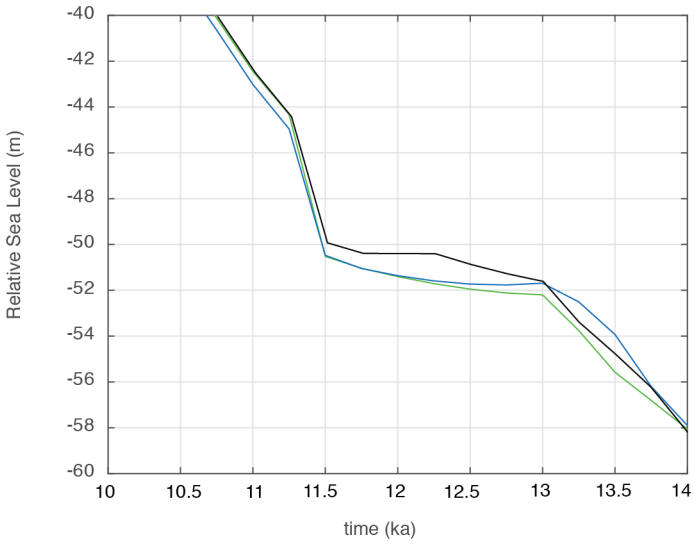

FIGURE F.13: RSL predictions using ice history GI-31 (as in main text; black), GI-30 (2σ uncertainty maximum ages; blue), and GI-34 (2σ uncertainty minimum ages; green). See Supplementary Figure 4 for ice-melting scenarios for GI-30 and GI-34. All simulations adopt the Earth model described in the main text.

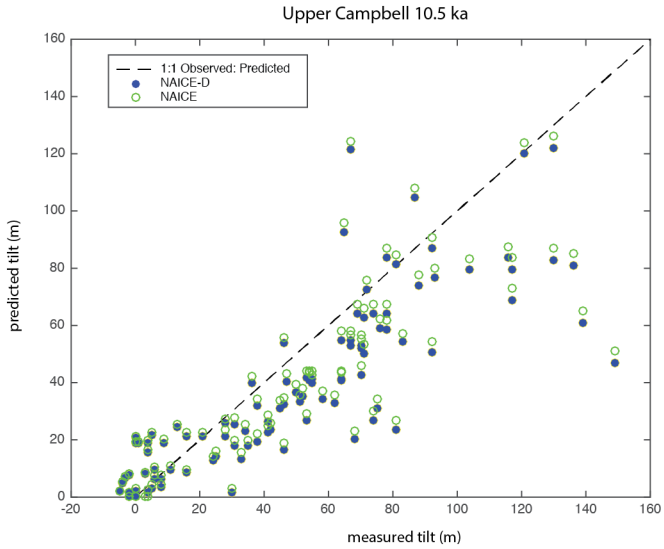

FIGURE F.14: Comparison of measured and predicted tilt using ice history NAICE-D (blue filled circles) and NAICE (green circles).

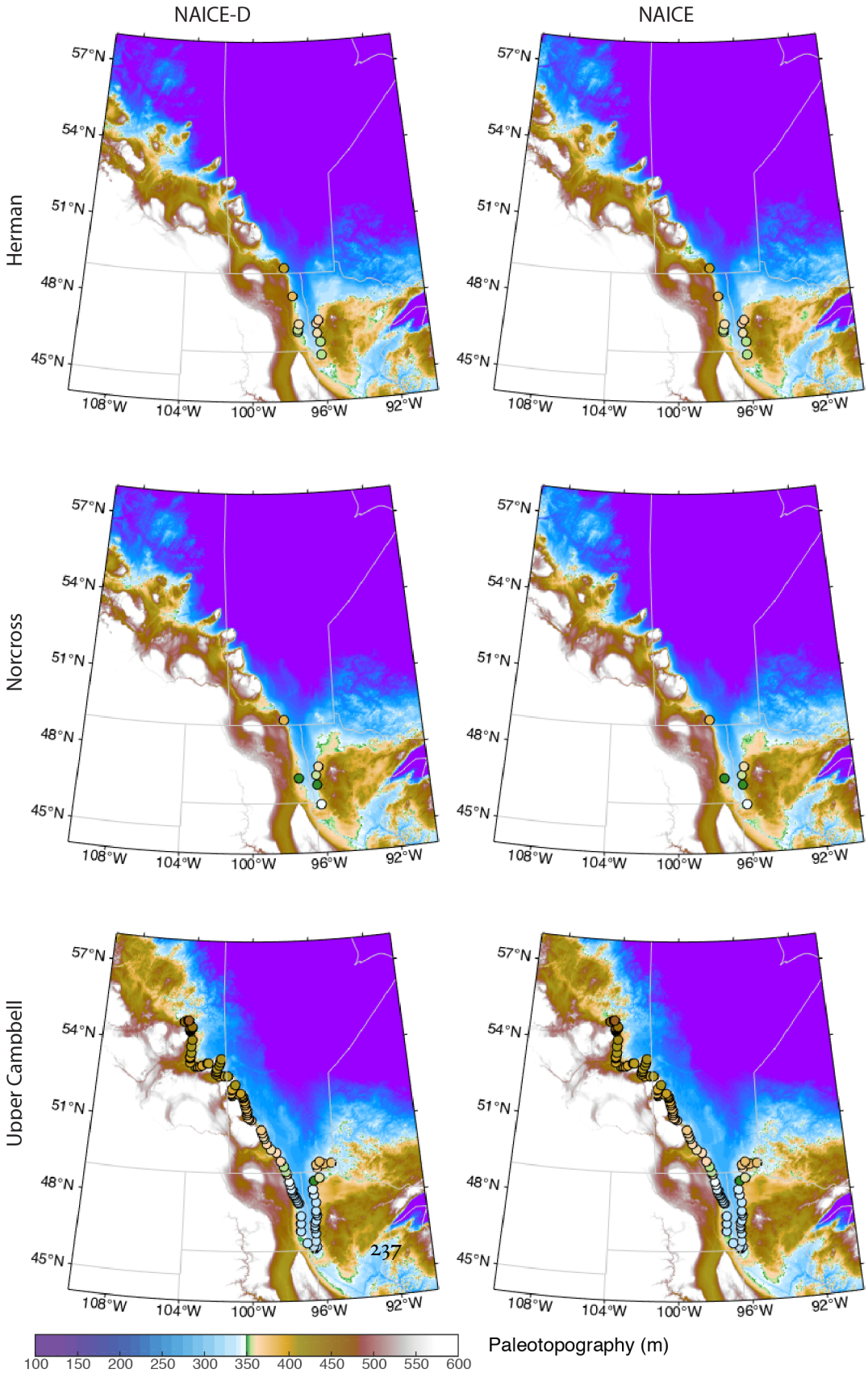

FIGURE F.15: Paleotopography predicted using NAICE-D (left) and NAICE(right) compared with observed elevation of strandline (circles).

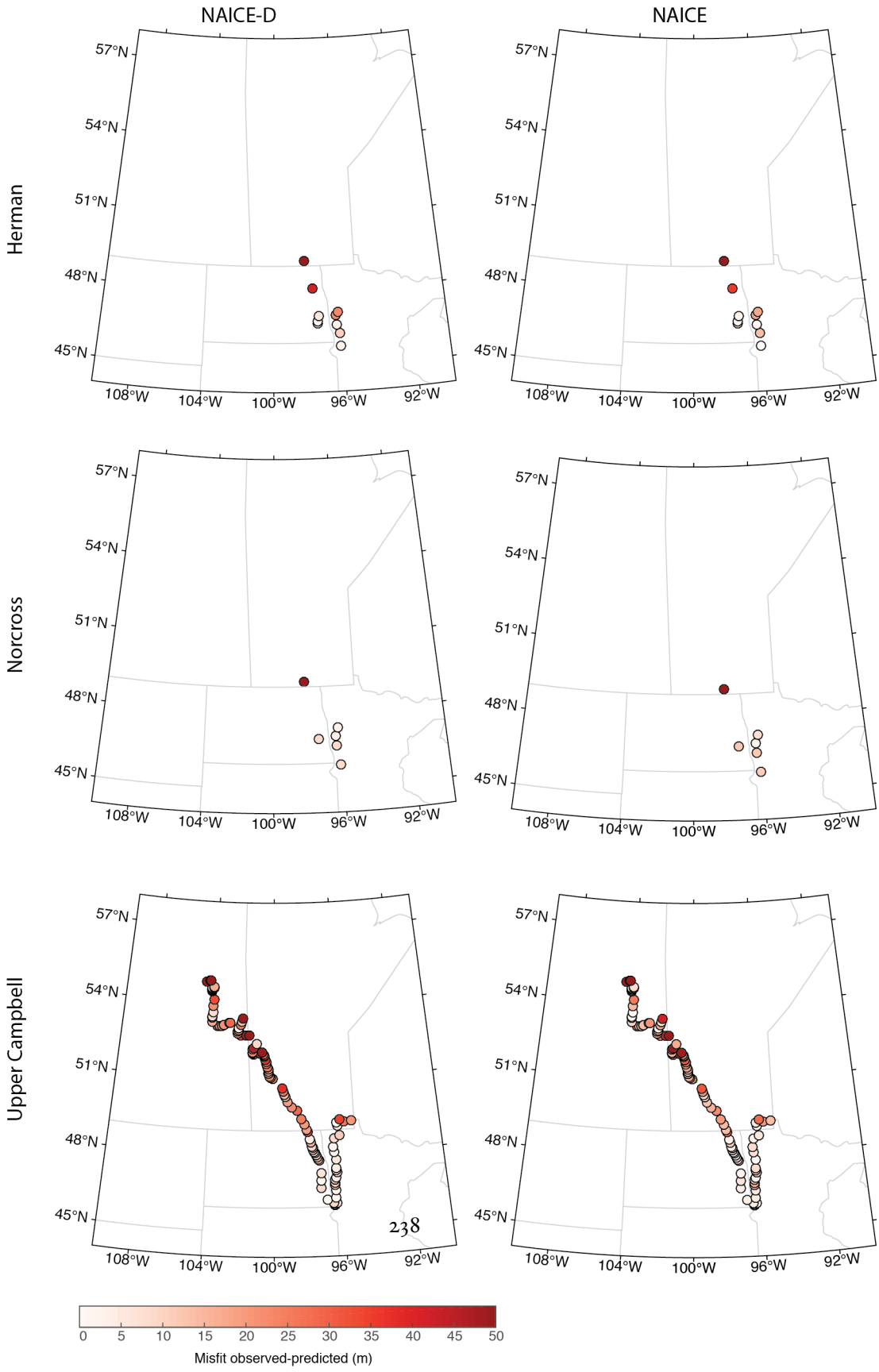

FIGURE F.16: Misfit between the observed and predicted paleotopography for each glacial Lake Agassiz shoreline for NAICE-D (left) and NAICE (right).

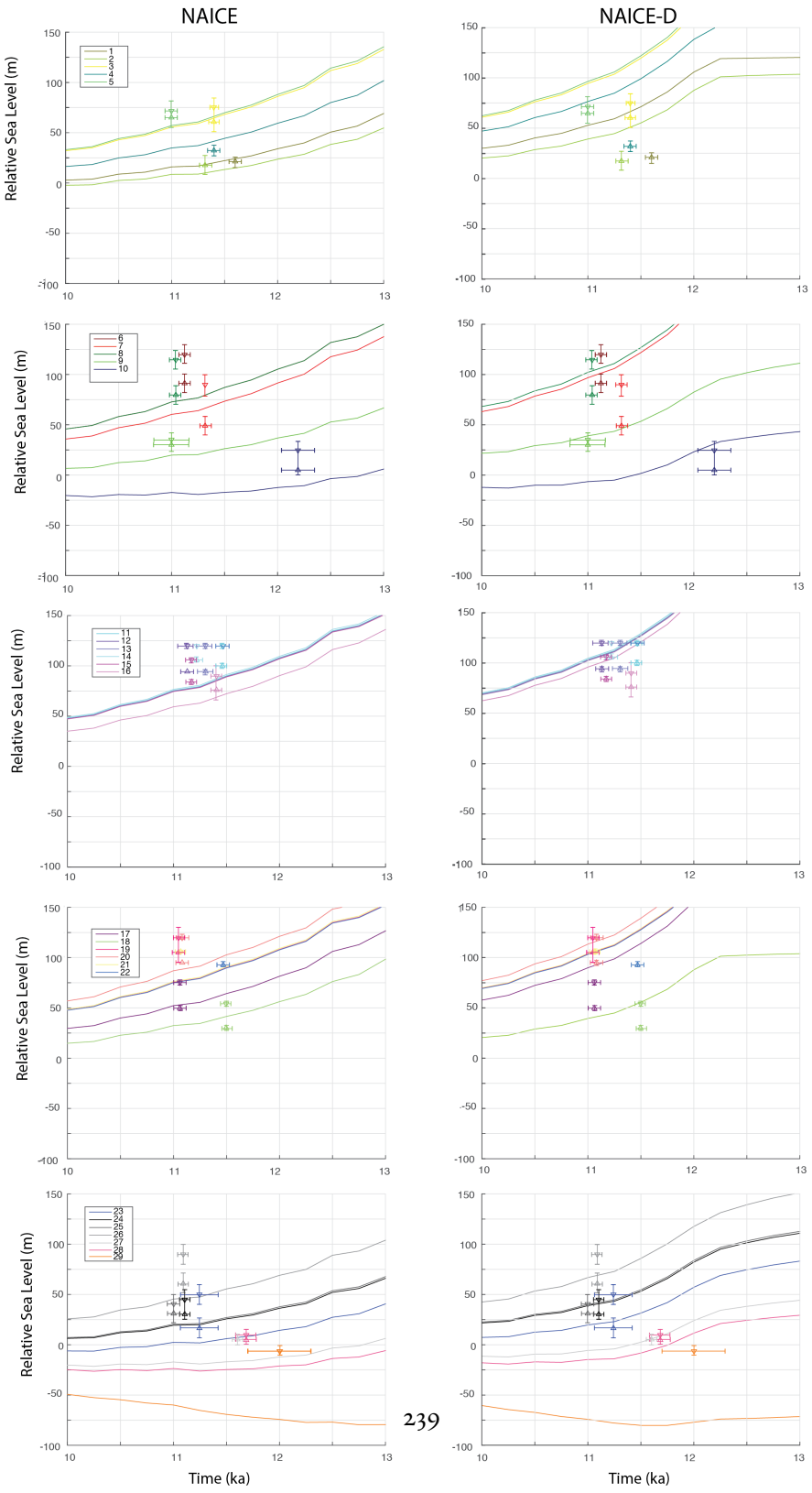

FIGURE F.17: Relative sea level predictions adopting NAICE (left) and NAICE-D (right) compared with relative sea level markers in the Canadian Arctic older than 11 ka (sites labeled 1-29 from Gowan et al.(Gowan et al., 2016)).

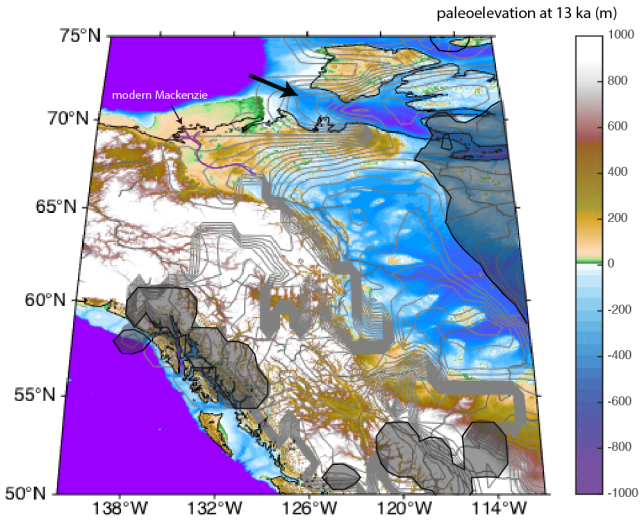

FIGURE F.18: Possible marine retreat of ice sheet. Modeled paleoelevation at 13 ka using GI-31 ice history. Contours show the margin and thickness of ice at 13 ka. Shaded regions show ice margin at 11.5 ka. Region with reverse bedrock slope (1m/km) is highlighted by black arrow. This region of ice may have been subject to a marine ice sheet instability, where water at the base of the ice sheet induces melting, causing a rapidly retreating grounding line to induce a large mass loss in this region.

G

Chapter 7 Supplement

G.1 Accounting for glacial isostatic adjustment signal

In the regression model we construct variable X_{GIA} to account for the change in vertical elevation due to glacial isostatic adjustment since the Last Interglacial. We calculate the value for this variable by averaging the value predicted at the LIG sea-level marker sites for 70 GIA models, characterized by the thickness of the elastic lithosphere, and the viscosity of the upper and lower mantle. These three parameters were respectively varied over the following ranges: 71-96 km, 2-5 x 10^{20} Pa s, and 3-50 x 10^{21} Pa s. To construct a two-cycle ice history, we adopted the ICE-6G model (Peltier, Argus and Drummond, 2015)for both the last and penultimate deglacial period, and the glaciation phase in each cycle was modeled to follow the eustatic curve inferred by Waelbroeck et al.(2002).

G.2 Sensitivity to uncertainty in sea-level marker elevation

We assessed the sensitivity of our resulting regression coefficients to the upper and lower uncertainty bounds associated with the LIG sea-level marker database. We performed an analysis where we adopted the upper bound (observed marker elevation+ indicative range), and found that the resulting β coefficients similarly showed there is not a statistically significant relationship between predicted sediment loading and observed elevation of LIG SL marker (Appendix Table 2). For the lower bound case (observed marker elevation – indicative range), we found a similar relationship (Appendix Table 3).

Table G.1: Appendix Table 1 | Coefficients for main text analysis (Figure 5)

main text results	β Estimate	Std. Error	t value	Pr(>|t|)
(Intercept)	7.095	0.459	15.475	< 2e-16
X_{SLsed}	-0.138	0.305	-0.453	0.651
X_{active}	8.344	1.090	7.658	3.72E-14
X_{GIA}	-1.102	0.453	-2.433	0.0151
X_{ac}	0.028	0.004	6.459	1.49E-10
$X_{interact}$	1.307	0.434	3.011	0.00265
Adjusted R-squared:	0.164			

Table G.2: Appendix Table 2 | Upper bound

upper bound results	β	Estimate	Std. Error	t value	Pr(>|t|)
(Intercept)	9.176	0.525	17.481	< 2e-16	
X_{SLsed}	-0.238	0.356	-0.667	0.50508	
X_{active}	9.495	1.092	8.695	< 2e-16	
X_{GIA}	-1.141	0.490	-2.328	0.02007	
X_{ac}	0.030	0.004	7.203	1.00E-12	
$X_{interact}$	1.504	0.496	3.035	0.00245	
Adjusted R-squared:	0.156				

Appendix Table 4-8 (Earth model variations)

Table G.3: Appendix Table 3 | Lower bound

lower bound results	β Estimate	Std. Error	t value	Pr(>|t|)
(Intercept)	4.987	0.467	10.668	< 2e-16
X_{SLsed}	-0.090	0.304	-0.297	0.7668
X_{active}	8.545	1.041	8.207	5.48E-16
X_{GIA}	-1.136	0.445	-2.555	0.0107
X_{ac}	0.029	0.005	6.205	7.38E-10
$X_{interact}$	0.972	0.406	2.395	0.0168
Adjusted R-squared:	0.158			

Table G.4: Appendix Table 4 | VM2 Fluid lovenumbers

VM2 fluid	β Estimate	Std. Error	t value	Pr(>|t|)
(Intercept)	7.127	0.408	17.49	< 2e-16
X_{SLsed}	-0.051	0.077	-0.661	0.508669
X_{active}	5.664	1.193	4.747	2.30E-06
X_{GIA} -1.037	0.444	-2.336	0.019638	
X_{ac}	0.028	0.004	6.327	3.44E-10
$X_{interact}$	-1.150	0.295	-3.898	0.000102
Adjusted R-squared:	0.1648			

Table G.5: Appendix Table 5 | 48p55

48p55	β Estimate	Std. Error	t value	Pr(>|t|)
(Intercept)	7.124	0.409	17.434	< 2e-16
X_{SLsed}	-0.051	0.077	-0.661	0.5088
X_{active}	5.606	1.197	4.683	3.13E-06
X_{GIA}	-1.032	0.443	-2.328	0.0201
X_{ac}	0.028	0.004	6.334	3.31E-10
$X_{interact}$	-1.153	0.295	-3.908	9.81E-05
Adjusted R-squared:	0.1645			

Table G.6: Appendix Table 5 | 72p515

72p515	β Estimate	Std. Error	t value	Pr(>|t|)
(Intercept)	7.121	0.411	17.316	< 2e-16
X_{SLsed}	-0.051	0.077	-0.661	0.509
X_{active}	5.531	1.208	4.578	5.15E-06
X_{GIA}	-1.033	0.444	-2.329	0.02
X_{ac}	0.028	0.004	6.334	3.30E-10
$X_{interact}$	-1.152	0.295	-3.906	9.87E-05
Adjusted R-squared:	0.1646			

Table G.7: Appendix Table 5 | 48p515

48p515	β Estimate	Std. Error	t value	Pr(>|t|)
(Intercept)	7.125	0.409	17.413	< 2e-16
X_{SLsed}	-0.051	0.077	-0.661	0.508669
X_{active}	5.609	1.200	4.674	3.27E-06
X_{GIA}	-1.037	0.444	-2.336	0.019638
X_{ac}	0.028	0.004	6.327	3.44E-10
$X_{interact}$	-1.150	0.295	-3.898	0.000102
Adjusted R-squared:	0.1648			

Table G.8: Appendix Table 9 | Effect of sediment loading sea-level change on inferred tectonic uplift rates on west coast of United States

Latitude	Longitude	LIG terrace elevation (m)	Inferred uplift rate in Simms et al.(m/ky)	Updated uplift rate (sediment load correction) (m/ky)	Change in uplift rate (%)
44.63	124.05	109	0.82	0.84	2.69
43.69	124.39	98	0.72	0.74	3.31
43.12	124.42	105	0.78	0.81	3.26
42.05	124.28	111	0.83	0.86	3.45
39.61	123.79	40	0.23	0.24	4.61
37.9	122.69	142	1.08	1.09	0.61
36.96	122.09	170	1.32	1.38	4.74
35.64	121.19	25	0.1	0.11	8.34
35.45	120.95	7	-0.05	-0.04	-16.25
35.26	120.9	30	0.14	0.15	6.29
34.47	120.23	35	0.19	0.20	4.92
33.96	119.71	5	-0.07	-0.06	-14.43
33.96	120.05	24	0.09	0.10	12.24
34.02	120.33	22.5	0.08	0.09	14.34
34.03	118.71	58	0.38	0.39	1.50
33.74	118.28	75	0.52	0.53	1.00
33.61	117.86	34	0.18	0.18	2.02
33.25	119.48	36	0.19	0.20	5.94
32.93	118.54	31	0.15	0.16	5.98
33.17	117.35	22	0.08	0.08	3.77
32.67	117.24	23	0.09	0.09	4.21
31.74	116.74	35.5	0.19	0.19	1.69
31.33	116.44	17	0.04	0.04	5.72
27.69	114.86	22.5	0.12	0.12	2.34

Table G.9: Appendix Table 10 | Effect of sediment loading sea-level change on inferred tectonic uplift rates in Barbados

Latitude	Longitude	LIG terrace elevation (m)	Inferred uplift rate in Creveling et al. (m/ky)	Updated uplift rate (sediment load correction) (m/ky)	Change in uplift rate (%)
13.1330	59.6330	60.0000	0.4805	0.5279	6.5626
13.1380	59.6310	60.0000	0.4805	0.5278	6.5445
13.1400	59.6340	60.0000	0.4156	0.4566	6.5379

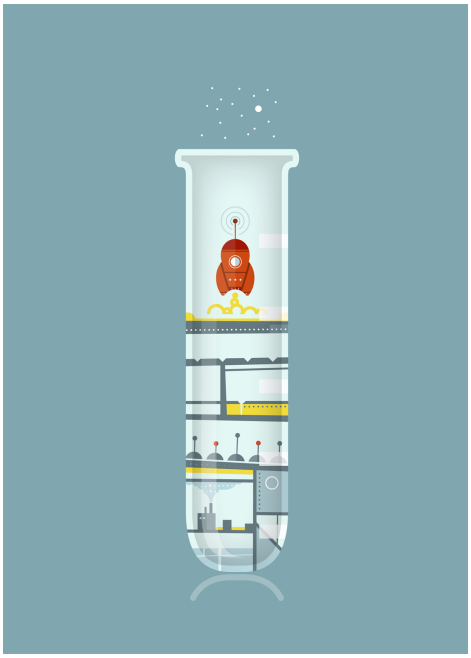

This thesis was typeset using LaTeX, originally developed by Leslie Lamport and based on Donald Knuth's TeX. The body text is set in 11 point Egenolff-Berner Garamond, a revival of Claude Garamont's humanist typeface. The above illustration, *Science Experiment 02*, was created by Ben Schlitter and released under CC BY-NC-ND 3.0. A template that can be used to format a PhD dissertation with this look & feel has been released under the permissive AGPL license, and can be found online at github.com/suchow/Dissertate or from its lead author, Jordan Suchow, at suchow@post.harvard.edu.